QUANTUM LIQUIDS AND QUANTUM CRYSTALS

On the classification of equilibrium superfluid states with scalar and tensor order parameters

M. Yu. Kovalevsky,* S. V. Peletminsky, and N. N. Chekanova

Kharkov Physicotechnical Institute National Research Center, Akademicheskaya 1, 61108 Kharkov, Ukraine
(Submitted November 6, 2001)
Fiz. Nizk. Temp. **28**, 327–337 (April 2002)

A classification of the equilibrium states of superfluid liquids with scalar and tensor order parameters, based on the concept of quasi-averages, is presented. The condition of unbroken symmetry is generalized to inhomogeneous equilibrium states. The admissible conditions of spatial symmetry are found in terms of integrals of the motion. A connection between these symmetry conditions and the helicoidal structure of the spin and spatial anisotropy vectors is established. Under certain restrictions it is shown that the equilibrium structure of the order parameter can be represented as a product of a homogeneous part of the order parameter and a part that depends on the spatial coordinates. © *2002 American Institute of Physics.*
[DOI: 10.1063/1.1476575]

1. INTRODUCTION

Research on superfluidity phenomena in ^{3}He has led to the prediction and discovery of a number of superfluid phases. Among these is the isotropic state described by Balian and Werthamer,[1] which has come to be called the *B* phase. The stability of the state predicted by Anderson and Morel,[2] corresponding to the *A* phase, is explained by the influence of spin fluctuations, which stabilize the anisotropic state of the superfluid liquid. When a magnetic field is applied, a stable A_1 phase is observed.[3] A number of other phases states that have been predicted previously, such as the polar phase,[4] the α, β, δ, and ε phases,[5] and the 2D phase,[6] have not been observed experimentally. A common property of the states mentioned above is their translational invariance. Analysis and classification of such states in ^{3}He have been carried out in Refs. 5, 7–10, and 11 on the basis of the Ginzburg–Landau theory or with the use of group-theoretical methods. The relation between the collective modes and the irreducible representations of the symmetry group of the equilibrium state was studied in Ref. 12. It is known that in a certain region of variation of the thermodynamic parameters the homogeneous state loses stability and the superfluid phase undergoes a transition to an inhomogeneous state. The inhomogeneous equilibrium states in superfluid ^{3}He were considered in Refs. 13–16. In those studies the stability conditions of the helicoidal structures were investigated using model expressions for the free energy. A refinement of the stability conditions for the states over a wider range of temperatures was made in Refs. 17 and 18. Interest in this problem has risen in view of its intimate connection with the problem of critical velocities in superfluid ^{3}He. However, a classification of the equilibrium inhomogeneous states has not been done.

The goal of the present study is to classify the superfluid phases for singlet or triplet pairing on the basis of the concept of quasi-averages[19] with allowance for the possibility that inhomogeneous equilibrium structures can arise. In a microscopic approach, in Refs. 20–23 the equilibrium state of magnetic and superfluid systems with broken symmetry with respect to spin rotations and phase transitions was investigated, and the thermodynamics of helicoid structures in condensed media of this kind was examined. In the present paper a condition of unbroken symmetry of the equilibrium state and a compatible condition of spatial symmetry are formulated. A physical interpretation of the additional thermodynamic parameters arising as a result of this generalization of the symmetry conditions is given. Inhomogeneous structures of the order parameter are found, and it is shown that under certain restrictions such a structure can be represented in the form a product of a homogeneous part of the order parameter and an inhomogeneous part that depends on the spatial coordinates. Here the problem of classification of the homogeneous part of the order parameter effectively reduces to that for a translationally invariant case.

2. EQUILIBRIUM. NORMAL PHASE OF A FERMI LIQUID

Let us consider the equilibrium state of normal condensed matter, a state describable by the density matrix (Gibbs statistical operator)

$$\hat{w} = \exp(\Omega - Y_0 \hat{\mathcal{H}} - Y_4 \hat{N}). \tag{2.1}$$

Here $\hat{\mathcal{H}}$ is the Hamiltonian, and $\hat{N}$ is the particle number operator. The thermodynamic potential Ω is determined from the normalization condition $\mathrm{Tr}\,\hat{w} = 1$. The set of thermodynamic forces includes the temperature $T \equiv Y_0^{-1}$ and the chemical potential $\mu_k \equiv -Y_4/Y_0$. For convenience we consider the condensed medium in the rest frame and we assume that the effective magnetic field is equal to zero. The extremum properties of the equilibrium density matrix (2.1) have the form

$$[\hat{w}, \hat{\boldsymbol{\mathcal{P}}}_k] = 0, \quad [\hat{w}, \hat{\mathcal{H}}] = 0, \quad [\hat{w}, \hat{N}] = 0,$$

 © 2002 American Institute of Physics

$$[\hat{w},\hat{S}_\alpha]=0, \quad [\hat{w},\hat{\boldsymbol{\mathcal{L}}}_i]=0, \tag{2.2}$$

where $\hat{\boldsymbol{\mathcal{P}}}_k$ is the momentum operator, and $\hat{\boldsymbol{\mathcal{S}}}_\alpha$ and $\hat{\boldsymbol{\mathcal{L}}}_i$ are the spin and orbital angular momentum operators, respectively. The first three relations reflect the spatial translational invariance and the phase invariance. The properties of symmetry with respect to rotations in spin space and configuration space mean that we are neglecting the weak dipole and spin–orbit interactions in the characteristic of the equilibrium state. The total symmetry group of the normal equilibrium state of a Fermi liquid has the form

$$G=[SO(3)]_S\times[SO(3)]_{\mathcal{L}}\times[U(1)]_\varphi \times[T(3)]\times[T(1)]. \tag{2.3}$$

Here $[SO(3)]_S$ and $[SO(3)]_{\mathcal{L}}$ are the symmetry groups with respect to rotations in spin space and configuration space, $[T(3)]$ and $[T(1)]$ are the translation groups in space and time, and $[U(1)]_\varphi$ is the phase symmetry group. Each element of a group is a unitary operator $U\equiv\exp i\hat{G}g$ (g is a parameter of the transformation) which leaves the Gibbs distribution invariant:

$$U\hat{w}U^+=\hat{w}. \tag{2.4}$$

The generators of the transformations (2.4) are linear combinations of the operators $\{\hat{\boldsymbol{\mathcal{S}}},\hat{\boldsymbol{\mathcal{L}}},\hat{N},\hat{\boldsymbol{\mathcal{P}}},\hat{\boldsymbol{\mathcal{H}}}\}$. Averages of the form $\mathrm{Tr}\,\hat{w}[\hat{G},\hat{b}(x)]$ vanish for an arbitrary quasilocal operator $\hat{b}(x)$ for $\hat{G}\varepsilon(\hat{\boldsymbol{\mathcal{P}}}_k,\hat{N},\hat{S}_\alpha,\hat{\boldsymbol{\mathcal{L}}}_k)$. This, in particular, is valid for the order parameter operators $\hat{b}(x)\equiv\hat{\Delta}_a(x)$, which do not commute with the integrals of the motion $\hat{G}$. The subscript a reflects the tensor dimension of the order parameter. As we shall see below, the commutators $[\hat{G},\hat{\Delta}_a(x)]$ are linear and homogeneous with respect to the order parameter operators $\hat{\Delta}_a(x)$, and that leads to the vanishing of the equilibrium averages of the order parameters in the normal state: $\mathrm{Tr}\,\hat{w}\hat{\Delta}_a(x)=0$.

3. EQUILIBRIUM. SINGLET PAIRING OF A SUPERFLUID FERMI LIQUID

The quasi-average value of a quantity, $a(x)=\langle\hat{a}(x)\rangle$, in a state of statistical equilibrium with broken symmetry is defined by the formula[19]

$$\langle\hat{a}(x)\rangle=\lim_{\nu\to0}\lim_{V\to\infty}\mathrm{Tr}\;\hat{w}_\nu\hat{a}(x), \tag{3.1}$$

where

$$\hat{w}_\nu\equiv\exp(\Omega_\nu-Y_0\hat{\boldsymbol{\mathcal{H}}}-Y_4\hat{N}-\nu Y_0\hat{F}) \tag{3.2}$$

and in general depends on the structure of the source $\hat{F}$ breaking the symmetry; this source is chosen in the form of a linear functional of the order parameter operator. For a superfluid Fermi liquid with singlet pairing the equilibrium state is characterized by a scalar order parameter,

$$\hat{\Delta}(x)\equiv(i/2)\hat{\psi}(x)\sigma_2\hat{\psi}(x), \tag{3.3}$$

where $\hat{\psi}(x)$ is the Fermi field operator for annihilation of a particle at point x, and σ_2 is a Pauli matrix. The order parameter operator satisfies the commutation relations:

$$[\hat{N},\hat{\Delta}(x)]=-2\hat{\Delta}(x), \quad i[\hat{S}_\alpha,\hat{\Delta}(x)]=0,$$
$$i[\hat{\boldsymbol{\mathcal{P}}}_k,\hat{\Delta}(x)]=-\nabla_k\hat{\Delta}(x), \quad i[\hat{\boldsymbol{\mathcal{L}}}_i,\hat{\Delta}(x)] =-\varepsilon_{ikl}x_k\nabla_l\hat{\Delta}(x). \tag{3.4}$$

The operator $\hat{F}$ has the symmetry of the given phase of the condensed medium and lifts the degeneracy of the equilibrium state:

$$\hat{F}=\int d^3x(f(x,t)\hat{\Delta}(x)+\mathrm{h.c.})=\hat{F}(t). \tag{3.5}$$

Here $f(x,t)$ is some function of the coordinates and time which is conjugate to the order parameter operator and which specifies its equilibrium averages in the sense of quasi-averages $\Delta(x,t)=\langle\hat{\Delta}(x)\rangle$. The coordinate and time dependence $\Delta=\Delta(x,t)$ is due to the fact that the introduction of a source $\hat{F}$ breaks the invariance of the equilibrium density matrix with respect to translations in space and time, i.e., $[\hat{w},\hat{\boldsymbol{\mathcal{P}}}]\neq0$, $[\hat{w},\hat{\boldsymbol{\mathcal{H}}}]\neq0$. The equilibrium density matrix $\hat{w}(Y,\hat{F}(t))\equiv\hat{w}(t)$ satisfies the von Neumann condition, and, as a result,

$$e^{-i\hat{\boldsymbol{\mathcal{H}}}\tau}\hat{w}(t)\mathrm{e}^{-i\hat{\boldsymbol{\mathcal{H}}}\tau}=\hat{w}(t+\tau) \tag{3.6}$$

(for normal systems the operator $\hat{w}$ is independent of the time t).

Let us consider the translationally invariant subgroups H of the total symmetry group G and establish the possible equilibrium structures of the scalar order parameter. Translational invariance means that the equilibrium density matrix satisfies the symmetry relation

$$[\hat{w},\hat{\boldsymbol{\mathcal{P}}}_k]=0. \tag{3.7}$$

Analysis of the translationally invariant subgroups of the unbroken symmetry of the equilibrium states is done in accordance with Ref. 7 by proceeding from the relation

$$[\hat{w},\hat{T}]=0, \tag{3.8}$$

where the generator $\hat{T}$ of the unbroken symmetry is a linear combination of integrals of the motion (generators of the subgroup H)

$$\hat{T}\equiv a_i\hat{\boldsymbol{\mathcal{L}}}_i+b_\alpha\hat{S}_\alpha+c\hat{N}\equiv\hat{T}(\xi) \tag{3.9}$$

with certain real numerical parameters $(a_i,b_\alpha,c\equiv\xi)$. The unitary transformations $U(\xi)=\exp i\hat{T}(\xi)$ form a continuous subgroup of the unbroken symmetries $U(\xi)U(\xi')=U(\xi''(\xi,\xi'))$ of the equilibrium state. For translationally invariant equilibrium states the order parameter and the function f are, by virtue of (3.4), independent of the coordinate:

$$\Delta(x)=\mathrm{Tr}\;\hat{w}\hat{\Delta}(x)=\Delta(0,Y_0,Y_4), \quad f(x)=f(0). \tag{3.10}$$

According to (3.2), (3.4), and (3.8) we have $[\hat{w},\hat{S}_\alpha]=0$, $[\hat{w},\hat{\boldsymbol{\mathcal{L}}}_i]=0$. Therefore $c=0$ and thus $\Delta(x)\neq0$. The generator of the unbroken symmetry takes the form

$$\hat{T}\equiv a_i\hat{\boldsymbol{\mathcal{L}}}_i+b_\alpha\hat{S}_\alpha. \tag{3.11}$$

Hence we find the order parameter in the equilibrium state for this case:

$$\langle\hat{\Delta}(x)\rangle=\eta(Y_0,Y_4)\exp i\varphi.$$

Here η is the modulus of the order parameter, and φ is the superfluid phase.

For further refinement of the symmetry properties of the equilibrium state it is necessary to invoke order parameters that do not possess the property of invariance with respect to rotations in spin or configuration space. By doing an analogous procedure of classification with these order parameters, one can determine the possible equilibrium states distinguished by anisotropic properties and investigate the question of the coexistence of several nonzero order parameters. However, we shall not discuss that topic here.

Consider the equilibrium states that do not possess the property of translational invariance (3.8). In a degenerate condensed medium there can exist various physical possibilities for breaking the translational invariance of the equilibrium state. This can occur as a result of breaking of the phase invariance (if the superfluid momentum is nonzero). Other possible mechanisms for the breaking of translational invariance are also possible. These include breaking of the symmetry with respect to rotations of the spins (a nonzero magnetic-helix vector) and of the symmetry with respect to rotations in configuration space (nonzero cholesteric-helix vector). Let us consider all of the indicated mechanisms for the onset of spatially inhomogeneous structures and ascertain the consequences of each in the equilibrium structure of the order parameter. We assume that the spatial symmetry of equilibrium states of this kind can be specified by the relation

$$[\hat{w},\hat{P}_k]=0,\quad \hat{P}_k\equiv\hat{\boldsymbol{\mathcal{P}}}_k-p_k\hat{N}-q_{k\alpha}\hat{S}_\alpha-t_{kj}\hat{\boldsymbol{\mathcal{L}}}_j,\qquad(3.12)$$

where p_k, $q_{k\alpha}$, and t_{kj} are certain real parameters. The generator of the unbroken symmetry of such states now includes a momentum operator

$$\hat{T}\equiv a_i\hat{\boldsymbol{\mathcal{L}}}_i+b_\alpha\hat{S}_\alpha+c\hat{N}+d_i\hat{\boldsymbol{\mathcal{P}}}_i.\qquad(3.13)$$

According to (3.4) and (3.12), we arrive at the equations relating the parameters of the generator of the spatial symmetry:

$$t_{kj}\varepsilon_{juv}p_v=0,\quad \nabla_k\Delta(x)=2ip_k\Delta(x).\qquad(3.14)$$

Identity (3.9) with Eqs. (3.4) and (3.13) taken into account will lead to an equation relating the parameters of the generator of the unbroken symmetry:

$$a_i\varepsilon_{ikl}x_k2ip_l\Delta(x)+2ic\Delta(x)+d_i2ip_i\Delta(x)=0.$$

From this we obtain the relations

$$a_i\varepsilon_{ikl}p_l=0,\quad c+\mathbf{d}\cdot\mathbf{p}=0,\qquad(3.15)$$

which are compatible with a nonzero equilibrium value of the order parameter $\Delta(x)$.

Using the Jacobi identity, we establish additional relations between the parameters introduced by relations (3.12) and (3.13). Taking relations (3.12) and (3.13) into account, we find that the operators $\hat{w}$, $\hat{T}$, and $\hat{\mathbf{P}}$ satisfy the relation $\mathrm{Tr}[\hat{w},[\hat{T},\hat{P}_k]]\hat{\Delta}(x)=0$. Hence, taking (3.15) into account, we obtain

$$p_ip_lt_{kl}-p^2t_{ik}=0.\qquad(3.16)$$

Using the Jacobi identity, we obtain for the operators $\hat{w}$, $\hat{P}_i$, and $\hat{P}_k$ the relation $\mathrm{Tr}[\hat{w},[\hat{P}_i,\hat{P}_k]]\hat{\Delta}(x)=0$. This implies the relation

$$(t_{ij}t_{kl}-t_{il}t_{kj})p_l=0.\qquad(3.17)$$

We seek t_{kj} in the form $t_{kj}=t\delta_{kj}+t_i\varepsilon_{ikj}+t^s_{kf}$, where t^s_{kj} is a symmetric and traceless tensor. Multiplying (3.16) by δ_{ik}, we find $t=l_il_jt^s_{ij}/2$, where $\mathbf{l}\equiv\mathbf{p}/p$. Further multiplying (3.16) by $\varepsilon_{ikj}l_j$, we see that $\mathbf{t}\perp\mathbf{l}$. Multiplying the first relation in (3.14) by $\varepsilon_{ku\lambda}$, we obtain $t_i=l_i(\mathbf{l}\cdot\mathbf{t})$, and therefore $\mathbf{t}=0$. We parametrize the symmetric and traceless matrix t^s_{ik} by the relation

$$t^s_{ik}=An_in_k+Bm_im_k-(A+B)\delta_{ik}/3,\qquad(3.18)$$

where $\mathbf{n}$ and $\mathbf{m}$ are mutually orthogonal unit vectors. Using this representation and relation (3.14), we easily see that $\mathbf{l}=\mathbf{m}\times\mathbf{n}$. Further, by virtue of (3.16) and (3.18) it is easily shown that $A=B$ and, hence, $t=-A/3$. Thus the matrix t_{ik} has the form

$$t_{ik}=Al_il_k.\qquad(3.19)$$

Formulas (3.14)–(3.17) and (3.19) establish the admissible structure of the generators of the unbroken and spatial symmetry of a quantum liquid with singlet pairing:

$$\hat{T}\equiv al_i\hat{\boldsymbol{\mathcal{L}}}_i+b_\alpha\hat{S}_\alpha+d_i(\hat{\boldsymbol{\mathcal{P}}}_i-pl_i\hat{N}),$$

$$\hat{P}_k\equiv\hat{\boldsymbol{\mathcal{P}}}_k-pl_k\hat{N}-q_{k\alpha}\hat{S}_\alpha-Al_kl_j\hat{\boldsymbol{\mathcal{L}}}_j.\qquad(3.20)$$

We see that the structure of the commutation relations for the scalar order parameter (3.4) and the symmetry properties (3.9), (3.12) retain considerable arbitrariness in the parameters of the generators of the unbroken and spatial symmetry. To narrow down this arbitrariness one must consider either the order parameters that relate to the spin or orbital degrees of freedom or the simultaneous existence of order parameters connected with the degrees of freedom indicated above in addition to the singlet pairing order parameter.

The particular case $q_{k\alpha}=0$ and $A=0$ was considered in Ref. 20. The generator of the unbroken symmetry takes the form (3.11). In accordance with the idea of Bose condensation, the thermodynamic parameter p_k has the meaning of superfluid momentum. The condition of spatial symmetry,

$$[\hat{w},\hat{P}_k]=0,\quad \hat{P}_k\equiv\hat{\boldsymbol{\mathcal{P}}}_k-p_k\hat{N}\qquad(3.21)$$

means that a macroscopically large number of particles can be found in a state with momentum $\mathbf{p}$. The symmetry of the equilibrium state with respect to rotations in configuration space and spin space is not broken and is specified by the formulas

$$[\hat{w},\hat{\boldsymbol{\mathcal{L}}}_k]=0,\quad [\hat{w},\hat{S}_\alpha]=0.\qquad(3.22)$$

We note further that $[\hat{w}_\nu,Y_0\hat{\boldsymbol{\mathcal{H}}}+Y_4\hat{N}+\nu\hat{F}]=0$. Since by virtue of the canonical commutation relations the operator $[\hat{F},\hat{a}(x)]$ is also quasilocal, and the average of a quasilocal operator is assumed finite, we have

$$\lim_{\nu\to0}\lim_{V\to\infty}\nu\mathrm{Tr}\ \hat{w}_\nu[\hat{F},\hat{a}(x)]=0.$$

Thus we arrive at the condition of stationarity:

$$[\hat{w}_\nu, \hat{H}] = 0, \quad \hat{H} \equiv \hat{\boldsymbol{\mathcal{H}}} + p_0 \hat{N}, \quad p_0 \equiv Y_4 / Y_0 . \tag{3.23}$$

The subgroup of unbroken symmetry of the superfluid state of a Fermi liquid with singlet pairing has the form

$$H = [SO(3)]_s \times [SO(3)]_{\mathcal{L}} \times [T(3)] \times [T(1)] \subset G. \tag{3.24}$$

Here the generators of the unitary transformations should be understood to be operators defined in the sense of relations (3.21) and (3.23).

The density matrix $\hat{w}$ satisfies the von Neumann condition (3.6). Using the stationarity condition (3.23), we obtain

$$\hat{w}(1+\tau) = e^{ip_0 \hat{N} \tau} \hat{w}(t) e^{-ip_0 \hat{N} \tau}. \tag{3.25}$$

The conditions of spatial homogeneity (3.21) and stationarity (3.23) lead to the following coordinate and time dependence of the function $f(x,t)$:

$$f(x,t) = \exp i 2\varphi(x,t), \quad \varphi(x,t) = \mathbf{p}\cdot\mathbf{x} - p_0 t + \varphi(0,0). \tag{3.26}$$

Relations (3.21) and (3.23) also permit one to find the coordinate and time dependence of the equilibrium value of the order parameter:

$$\Delta(x,t) = \mathrm{Tr}\ \ \hat{w}(t)\hat{\Delta}(x) = \eta(Y,\mathbf{p}) \exp 2i\varphi(x,t). \tag{3.27}$$

4. TRANSLATIONALLY INVARIANT EQUILIBRIUM STATES OF SUPERFLUID ^{3}He

The order parameter of a superfluid liquid with triplet pairing contains the spin index $\alpha = 1,2,3$, which corresponds to the spin angular momentum $s = 1$, and the vector index $k = 1,2,3$, which corresponds, by virtue of the Pauli exclusion principle, to an orbital angular momentum $l = 1$. Furthermore, the triplet order parameter operator should be complex. This fact reflects the circumstance that in the case under discussion the symmetry with respect to phase transformations is lost on account of the formation of Cooper pairs. It is convenient to choose the operator $\hat{\Delta}_{\alpha k}(x)$ in the form[20]

$$\hat{\Delta}_{\alpha k}(x) \equiv \hat{\psi}(x)\sigma_2\sigma_\alpha \nabla_k \hat{\psi}(x) - \nabla_k \hat{\psi}(x)\sigma_2\sigma_\alpha \hat{\psi}(x). \tag{4.1}$$

Here σ_α are the Pauli matrices. The matrices $(\sigma_2\sigma_\alpha)_{\mu\nu} = (\sigma_2\sigma_\alpha)_{\nu\mu}$ are symmetric with respect to indices μ and ν. In accordance with this definition and the canonical commutation relations for Fermi operators, we see that the following relations are valid:

$$\begin{aligned}
&i[\hat{S}_\alpha, \hat{\Delta}_{\beta i}(x)] = -\varepsilon_{\alpha\beta\gamma}\hat{\Delta}_{\gamma i}(x),\\
&[\hat{N}, \hat{\Delta}_{\beta i}(x)] = -2\hat{\Delta}_{\beta i}(x),\\
&i[\hat{\boldsymbol{\mathcal{P}}}_k, \hat{\Delta}_{\alpha i}(x)] = -\nabla_k \hat{\Delta}_{\alpha i}(x),\\
&i[\hat{\boldsymbol{\mathcal{L}}}_k, \hat{\Delta}_{\alpha i}(x)] = -\varepsilon_{kjl} x_j \nabla_l \hat{\Delta}_{\alpha i}(x) - \varepsilon_{kil}\hat{\Delta}_{\alpha l}(x).
\end{aligned} \tag{4.2}$$

In terms of the concept of quasi-averages, the equilibrium density matrix of the Fermi liquid under discussion is determined by equation (3.2). The operator that breaks the symmetry of the equilibrium state is a linear functional of the order parameter operator:

$$\hat{F} = \int d^3x (\hat{\Delta}_{\alpha k}(x) f_{k\alpha}(x,t) + \text{h.c.}). \tag{4.3}$$

The quasi-average value of the order parameter is a function of the thermodynamic parameters and a functional of $f_{k\alpha}(x,t)$:

$$\Delta_{\alpha k}(x,t) = \mathrm{Tr}\, \hat{w}(t)\hat{\Delta}_{\alpha k}(x) = \Delta_{\alpha k}(Y, f(x,t)). \tag{4.4}$$

In the case when the thermodynamic forces conjugate to the additive integrals of the motion $\hat{\boldsymbol{\mathcal{P}}}_i$ and $\hat{\mathcal{S}}_\alpha$ vanish, i.e., $Y_i = 0$ and $Y_\alpha = 0$, the translationally invariant ($[\hat{w}, \hat{\boldsymbol{\mathcal{P}}}_i] = 0$) density matrix and the source $\hat{F}$ have the same unbroken symmetry properties:

$$[\hat{w}, \hat{T}] = 0, \quad [\hat{F}, \hat{T}] = 0. \tag{4.5}$$

By virtue of the algebra (4.2) and relations (3.8)–(3.10), we obtain an equation determining the equilibrium structure of the order parameter parameter:

$$a_k \varepsilon_{kil}\Delta_{\beta l} + b_\alpha \varepsilon_{\alpha\beta\gamma}\Delta_{\gamma i} + 2ic\Delta_{\beta i} = 0. \tag{4.6}$$

We see that under such conditions there can be nonzero values of the order parameter in the equilibrium state. Let us consider a subgroup of the unbroken symmetry, the generator of which is an operator of the form $\hat{T} \equiv a_i \hat{\boldsymbol{\mathcal{L}}}_i + c\hat{N}$. Without loss of generality we assume that $a_i^2 = 1$, $a_i = l_i$. From the symmetry condition (4.6) we find $(a_i \varepsilon_{ikj} + 2ic\delta_{kj})\Delta_{\beta j} = 0$. A nonzero solution for the order parameter is contingent on the vanishing of the determinant:

$$\begin{aligned}
\det|a_i \varepsilon_{ikj} + 2ic\delta_{kj}| &= 2ic(a^2 - 4c^2) \equiv F_3(\mathbf{a}, c)\\
&= 2ic(1 - 4c^2) = 0.
\end{aligned} \tag{4.7}$$

The solutions $c = 0, \pm 1/2$ of this equation lead to an operator $\hat{T}$ of the form

$$\hat{T} \equiv l_i \hat{\boldsymbol{\mathcal{L}}}_i - \frac{m_l}{2}\hat{N}, \quad m_l = 0, \pm 1. \tag{4.8}$$

Let us consider another particular case of the operator $\hat{T}$: $\hat{T} \equiv b_\alpha \hat{S}_\alpha + c\hat{N}$. As in the previous case, we assume that $b_\alpha^2 = 1$, $b_\alpha = d_\alpha$. In accordance with condition (4.6) and the algebraic relations (4.2), we obtain the equation $(b_\alpha \varepsilon_{\alpha\beta\gamma} + 2ic\delta_{\beta\gamma})\Delta_{\beta j} = 0$, from which we find the value of the determinant

$$\begin{aligned}
\det|b_\alpha \varepsilon_{\alpha\beta\gamma} + 2ic\delta_{\beta\gamma}| &= 2ic(b^2 - 4c^2) \equiv F_3(\mathbf{b}, c)\\
&= 2ic(1 - 4c^2.
\end{aligned}$$

From the condition that this determinant vanish we obtain the values $c = 0, \pm 1/2$ and, hence, in this case the operator $\hat{T}$ has the form

$$\hat{T} \equiv d_\alpha \hat{S}_\alpha - \frac{m_s}{2}\hat{N}, \quad m_s = 0, \pm 1. \tag{4.9}$$

Let us explore the physical meaning of the unbroken-symmetry conditions generated by the operators (4.8) and (4.9).[20] For this we introduce the "wave function" of a Cooper pair of particles of the system:

$$\Psi_{\alpha_1\alpha_2}(x_1, x_2) = \mathrm{Tr}\ \ \hat{w}\hat{\psi}_{\alpha_1}(x_1)\hat{\psi}_{\alpha_2}(x_2). \tag{4.10}$$

By virtue of the unbroken-symmetry conditions (3.9) we have

$$\mathrm{Tr}\left[\hat{w}, \mathbf{1}\cdot\hat{\boldsymbol{\mathcal{L}}} - \frac{m_l}{2}\hat{N}\right]\hat{\psi}_{\alpha_1}(x_1)\hat{\psi}_{\alpha_2}(x_2) = 0,$$

$$\mathrm{Tr}\left[\hat{w}, \mathbf{d}\cdot\hat{\mathbf{S}} - \frac{m_s}{2}\hat{N}\right]\hat{\psi}_{\alpha_1}(x_1)\hat{\psi}_{\alpha_2}(x_2) = 0. \tag{4.11}$$

Since

$$[\hat{\mathcal{L}}_i, \hat{\psi}_\alpha(x)] = -l_i\hat{\psi}_\alpha(x),$$

$$[\hat{S}_i, \hat{\psi}_\alpha(x)] = -(\sigma_i)_{\alpha\beta}\hat{\psi}_\beta(x)/2,$$

we have

$$\mathbf{1}\cdot(\hat{\mathbf{l}}^{(1)} + \hat{\mathbf{l}}^{(2)})\Psi_{\alpha_1\alpha_2}(x_1, x_2) = m_l\Psi_{\alpha_1\alpha_2}(x_1, x_2),$$

$$\mathbf{d}\cdot(\hat{\mathbf{s}}^{(1)} + \hat{\mathbf{s}}^{(2)})\Psi_{\alpha_1\alpha_2}(x_1, x_2) = m_s\Psi_{\alpha_1\alpha_2}(x_1, x_2),$$

where $\hat{l}_i^{(a)} = -i\varepsilon_{ikl}x_k^{(a)}\nabla_l^{(a)}$, $s_i^{(a)}$ $(a = 1,2)$ are the angular momentum and spin operators, which act respectively on the first and second arguments of the "wave function." The state of statistical equilibrium, for which relation (4.11) holds, corresponds to the state in which the projection of the orbital angular momentum of the Cooper pair on the **l** direction is equal to m_l and the projection of the spin of the Cooper pair on the **d** direction is equal to m_s. The choice of order parameter operator in the form of a vector with respect to the spin and orbital indices (4.1) corresponds to the situation that the spin and angular momentum of the Cooper pair are assumed equal to unity. It follows from relations (4.11) that the function $f_{\alpha k}$ appearing in the source $\hat{F}$ is given by the formula

$$f_{\alpha k} = d_\alpha(m_s)\xi_k(m_l), \tag{4.12}$$

where

$$d_\alpha(m_s) = \begin{cases} d_\alpha^+, & m_s = -1 \\ d_\alpha^-, & m_s = 1 \\ d_\alpha, & m_s = 0 \end{cases}, \quad \xi_k(m_l) = \begin{cases} \xi_k^+, & m_l = -1 \\ \xi_k^-, & m_l = 1 \\ l_k, & m_l = 0 \end{cases}. \tag{4.13}$$

Here $\mathbf{d}^\pm = (\mathbf{e} \pm i\mathbf{f})/\sqrt{2}$ and $\xi^\pm = (\mathbf{m} \pm i\mathbf{n})/\sqrt{2}$, where **m** and **n** (**e** and **f**) are mutually orthogonal real unit vectors orthogonal to the vector **l** (**d**).

The equilibrium structure of the order parameters of ^{3}He for the different phase states can be represented in the unified form

$$\Delta_{\alpha k} = \sum_{m_s m_l} a_{m_s m_l} d_\alpha(m_s)\xi_k(m_l).$$

The symmetry properties of the equilibrium state lead to certain relations between the amplitudes of the order parameter $a_{m_s m_l}$. The superfluid states, the generators of the unbroken symmetry of which have the form (4.8), (4.9), have been given the name "inert phases."[5] In particular, for the A phase the quantum numbers of the Cooper pairs take the values $m_l = \pm 1$, $m_s = 0$.[2] The order parameter in equilibrium has the form

$$\Delta_{\alpha k} = a_{0\mp} d_\alpha \xi_k^\mp, \tag{4.14}$$

where from now on we will be using a Cartesian coordinate system for which the vectors d_α and l_k have the projections $d_\alpha = (0,0,1)$ and $l_k = (0,0,1)$. The polar phase of ^{3}He corresponds to a state with quantum numbers $m_l = 0$, $m_s = 0$.[4] In this case the order parameter becomes

$$\Delta_{\alpha k} = a_{00} d_\alpha l_k. \tag{4.15}$$

The values of the quantum numbers $m_l = 0$, $m_s = \pm 1$ correspond to the β phase.[5] For this state we find the order parameter

$$\Delta_{\alpha k} = a_{\mp 0} d_\alpha^\mp l_k. \tag{4.16}$$

The case $m_l = \pm 1$, $m_s = \pm 1$ corresponds to the A_1 phase.[3] The order parameter in equilibrium has the form

$$\Delta_{\alpha k} = a_{\mp\mp} d_\alpha^\mp \xi_k^\mp. \tag{4.17}$$

The equilibrium structure of the order parameters (4.14)–(4.17) of ^{3}He gives four anisotropic phase states, each of which is characterized by one independent amplitude.

For the set of possible anisotropic states of superfluid ^{3}He relations (4.11) with the generators (4.8) and (4.9) are not necessarily satisfied simultaneously. Four additional anisotropic equilibrium states arise in cases when the unbroken-symmetry condition holds only with one of these generators. If relation (3.9) with generator (4.8) holds, then for a value of the quantum number $m_l = 0$ we arrive at a state with order parameter

$$\Delta_{\alpha k} = V_{\alpha 0} l_k, \tag{4.18}$$

where its spin component

$$V_{\alpha 0} = Ae_\alpha + Bf_\alpha + Cd_\alpha \equiv \sum_{m_s} a_{m_s 0} d_\alpha(m_s)$$

is an arbitrary complex vector. For values $m_l = \pm 1$ the order parameter, in accordance with (3.9), has the form

$$\Delta_{\alpha k} = V_{\alpha\mp}\xi_k^\mp. \tag{4.19}$$

Here

$$V_{\alpha\mp} = A_\mp e_\alpha + B_\mp f_\alpha + C_\mp d_\alpha \equiv \sum_{m_s} a_{m_s\mp} d_\alpha(m_s)$$

is the spin structure of the order parameter.

The unbroken-symmetry relation (3.9) with generator (4.9) for the value $m_s = 0$ leads to an equilibrium state with the order parameter

$$\Delta_{\alpha k} = d_\alpha \Psi_{0k}. \tag{4.20}$$

where its spatial part

$$\Psi_{0k} = Am_k + Bn_k + Cl_k \equiv \sum_{m_l} a_{0m_l}\xi_k(m_l)$$

is an arbitrary complex vector. Analogously, for the values $m_s = \pm 1$ the order parameter at equilibrium has the form

$$\Delta_{\alpha k} = d_\alpha^\mp \Psi_{\mp k}, \tag{4.21}$$

where

$$\Psi_{\mp k}=A_{\mp}m_k+B_{\mp}n_k+C_{\mp}l_k\equiv\sum_{m_l}a_{\mp m_l}\xi(m_l)$$

is the corresponding spatial structure of the order parameter. These four anisotropic states (4.18)–(4.21) have a lower unbroken symmetry than do (4.14)–(4.17) and therefore contain a greater arbitrariness in the structure of the order parameter parameter. Each of these states is characterized by three independent amplitudes.

Let us now consider the generator of the unbroken symmetry (3.10) and find the remaining anisotropic states. For this we write out the corresponding determinant of the 9×9 matrix:

$$\det\left|a_i\varepsilon_{ikj}\delta_{\gamma\beta}+b_\alpha\delta_{kj}\varepsilon_{\alpha\beta\gamma}+2ic\,\delta_{kj}\delta_{\beta\gamma}\right|=F_9(\mathbf{a},\mathbf{b},c).$$

Without loss of generality, by virtue of of the invariance of the determinant with respect to rotations in spin space and configuration space, we can choose the coordinate system such that $\mathbf{b}\equiv(0,0,b)$ in spin space and $\mathbf{a}\equiv(0,0,a)$ in coordinate space. Then the evaluation of the determinant $F_9(a,b,c)$ of the matrix reduces to calculation of the third- and sixth-order determinants:

$$F_g(a,b,c)=F_3(a,c)F_6(a,b,c). \tag{4.22}$$

Here the matrix $\hat{F}_6(a,b,c)$ has the block form

$$\hat{F}_6(a,b,c)=\begin{vmatrix}\hat{F}_3(a,c) & b\hat{I}_3\\ -b\hat{I}_3 & \hat{F}_3(a,c)\end{vmatrix},$$

where $\hat{I}_3$ is a 3×3 unit matrix and the matrix $\hat{F}_3(a,c)$ is defined by Eq. (4.7). Taking the explicit form of the matrix (4.7) into account, we see that the following relation holds:

$$F_6(a,b,c)=F_3(a,c+b/2)F_3(a,c-b/2). \tag{4.23}$$

According to (4.22), (4.23), we obtain the following expression for the determinant $F_9(a,b,c)$:

$$\begin{aligned}F_9(a,b,c)=F_3(a,c)F_3(a,c+b/2)F_3(a,c-b/2)=2ic\\ \times(a^2-4c^2)(b^2-4c^2)[(a-b)^2-4c^2]\\ \times[(a+b)^2-4c^2].\end{aligned} \tag{4.24}$$

The system of linear and homogeneous equations (4.6) has a nonzero solution if the determinant (4.24) vanishes. The vanishing of each of the five cofactors individually will lead to the cases already considered, (4.14)–(4.21). By considering them in combination we can obtain four more states.

1. When the 1st and 4th or 1st and 5th cofactors vanish, the unbroken-symmetry condition (3.9) takes the form $[\hat{w},l_i\hat{\boldsymbol{\mathcal{L}}}_i\pm d_\alpha\hat{S}_\alpha]=0$. In this case the ζ-phase state[5] arises, with the order parameter

$$\Delta_{\alpha k}=\begin{vmatrix}A & B & 0\\ -B & A & 0\\ 0 & 0 & C\end{vmatrix}. \tag{4.25}$$

2. The combination of the cases $c=\pm b/2$ and $c=\pm a/2$ describes the ε state.[5] The unbroken-symmetry generator $\hat{T}=l_i\hat{\boldsymbol{\mathcal{L}}}_i+d_\alpha\hat{S}_\alpha\pm\hat{N}/2$ leads to the order parameter

$$\Delta_{\alpha k}=\begin{vmatrix}0 & 0 & A\\ 0 & 0 & \pm iA\\ B & \pm iB & 0\end{vmatrix}. \tag{4.26}$$

3. The solution $c=\pm a/2$ in combination with $c=\pm(a-b)/2$ or $c=\pm(a+b)/2$ (the order of the signs is arbitrary) leads to an equilibrium state with an unbroken-symmetry generator $\hat{T}=l_i\hat{\boldsymbol{\mathcal{L}}}_i+2d_\alpha\hat{S}_\alpha\pm\hat{N}/2$ and the following structure of the order parameter:[7,8]

$$\Delta_{\alpha k}=\begin{vmatrix}A & -iA & 0\\ -iA & -A & 0\\ B & iB & 0\end{vmatrix}. \tag{4.27}$$

4. By combining the values $c=\pm b/2$ with $c=\pm(a+b)/2$ or $c=\pm(a-b)/2$ one can obtain an unbroken-symmetry generator of the form $\hat{T}=2l_i\hat{\boldsymbol{\mathcal{L}}}_i+d_\alpha\hat{S}_\alpha\pm\hat{N}/2$ and an order parameter[7,8]

$$\Delta_{\alpha k}=\begin{vmatrix}A & -iA & B\\ -iA & -A & iB\\ 0 & 0 & 0\end{vmatrix}. \tag{4.28}$$

Formulas (4.14)–(4.21), (4.25)–(4.28) describe 12 anisotropic phases of superfluid ^{3}He, corresponding to translationally invariant states.

Let us now consider the state, corresponding to an isotropic superfluid phase, that arises as a result of the vanishing of determinant (4.24) at the parameter values $c=0$, $a=b$. We introduce an orthogonal rotation matrix describing the rotation of the spatial coordinate system with respect to the spin equality $b_\alpha=a_iR_{i\alpha}$. Taking (3.9) into account, we obtain $a_i[\hat{w},\hat{\boldsymbol{\mathcal{L}}}_i+R_{i\alpha}\hat{S}_\alpha]=0$. The isotropy condition means that the latter relation is valid for arbitrary directions of the vector **a**. Therefore, the symmetry property of the state has the form[20]

$$[\hat{w},\hat{\boldsymbol{\mathcal{L}}}_i+R_{i\alpha}\hat{S}_\alpha]=0. \tag{4.29}$$

This state describes the B phase of superfluid ^{3}He. For states with symmetry (4.29) the average value of the order parameter has the form

$$\Delta_{\alpha k}=a_BR_{k\alpha}, \tag{4.30}$$

where a_B is the amplitude of the order parameter.

5. INHOMOGENEOUS EQUILIBRIUM STATES OF SUPERFLUID PHASES OF ^{3}He

As in the matter of the classification of translationally invariant states, it is advisable to start by considering the subgroups of the spatial symmetry which have a generator consisting of two operators. Let

$$\hat{P}_k\equiv\hat{\boldsymbol{\mathcal{P}}}_k-p_k\hat{N}. \tag{5.1}$$

According to this definition and the algebra (4.2), we obtain the following equation for the order parameter:

$$\nabla_i\Delta_{\beta k}(x)=2ip_i\Delta_{\beta k}(x), \tag{5.2}$$

the solution of which has the form

$$\Delta_{\beta k}(x)=e^{2i\varphi(\mathbf{x})}\Delta_{\beta k}(0),\quad \varphi(\mathbf{x})=\varphi+\mathbf{p}\cdot\mathbf{x}, \tag{5.3}$$

where $\underline{\Delta}_{\beta k}(0)$ is the homogeneous, coordinate-independent part of the order parameter. By virtue of the explicit form of the unbroken-symmetry generator (3.13) and Eq. (5.2), the relations

$$a_k\varepsilon_{kil}\Delta_{\beta l}+b_\alpha\varepsilon_{\alpha\beta\gamma}\Delta_{\gamma i}+a_i\varepsilon_{imn}x_m p_n\Delta_{\beta k}(x)+2ic\underline{c}\Delta_{\beta i}=0,$$

are valid, where $\underline{c}\equiv c+\mathbf{p}\cdot\mathbf{d}$. The requirement that the term linear in the coordinate in this equation be zero leads to relations determining the equilibrium structure of the order parameter parameter:

$$a_k\varepsilon_{kil}\underline{\Delta}_{\beta l}+b_\alpha\varepsilon_{\alpha\beta\gamma}\underline{\Delta}_{\gamma i}+2i\underline{c}\underline{\Delta}_{\beta i}=0,\quad \mathbf{a}\times\mathbf{p}=0. \tag{5.4}$$

We see that for the homogeneous part of the order parameter, $\underline{\Delta}_{\beta k}(0)$ (5.3), the classification procedure set forth above is valid. In Refs. 13–15 the question of the stability of the inhomogeneous configurations in A-^{3}He was investigated by starting from a model Hamiltonian, and the stability of the configuration for $\mathbf{a}\|\mathbf{p}$ was demonstrated.

Consider the case when the spatial symmetry operator has the form

$$\hat{P}_k\equiv\hat{\boldsymbol{\mathcal{P}}}_k-q_{k\alpha}\hat{S}_\alpha. \tag{5.5}$$

This condition leads to an equation for the order parameter:

$$\nabla_i\Delta_{\beta k}(x)=q_{i\alpha}\varepsilon_{\alpha\beta\gamma}\Delta_{\gamma k}(x). \tag{5.6}$$

Using the Jacobi identity for the operators $\hat{w}$, $\hat{P}_i$, and $\hat{P}_k$, one can obtain the relation

$$\mathrm{Tr}[\hat{w},[\hat{P}_i,\hat{P}_k]]\hat{\Delta}_{\beta l}(x)=(q_{i\beta}q_{k\alpha}-q_{i\alpha}q_{i\beta})\Delta_{\alpha l}(x)=0,$$

which implies the following restriction on the structure of the parameter $q_{i\alpha}$:

$$q_{i\alpha}=q_i n_\alpha. \tag{5.7}$$

Here q_k is the magnetic-helix vector, and n_α is the axis of anisotropy in spin space. The solution of equation (5.6) together with (5.7) gives the explicit structure of the order parameter for this state:

$$\Delta_{\beta k}(x)=a_{\beta\gamma}(\mathbf{n}\theta(x))\underline{\Delta}_{\gamma k}(0),\quad \theta(x)=\theta+\mathbf{q}\cdot\mathbf{x}, \tag{5.8}$$

where $a_{\beta\gamma}$ is an orthogonal rotation matrix in spin space. The unbroken-symmetry condition (3.9) with allowance for the form of the generator of the spatial symmetry (5.5) and Eq. (5.6) leads to the equation

$$a_k\varepsilon_{kil}\Delta_{\beta l}(x)+\underline{b}_\alpha\varepsilon_{\alpha\beta\gamma}\Delta_{\gamma i}(x)+a_j\varepsilon_{jmn}x_m q_n n_\alpha\varepsilon_{\alpha\beta\gamma}\Delta_{\gamma i}(x)+2ic\Delta_{\beta i}(x)=0, \tag{5.9}$$

where $\underline{b}_\alpha\equiv b_\alpha+\mathbf{d}\cdot\mathbf{q}n_\alpha$. Hence, taking into account the requirement that there be no term linear in the coordinate, we obtain the equations

$$a_k\varepsilon_{kil}\Delta_{\beta l}(x)+\underline{b}_\alpha\varepsilon_{\alpha\beta\gamma}\Delta_{\gamma i}(x)+2ic\Delta_{\beta i}(x)=0,$$

$$a_j\varepsilon_{jmn}q_{il}=0,$$

which specify the equilibrium structure of the order parameter. Taking formula (5.8) into account, we can easily obtain an equation for only the homogeneous, coordinate-independent part of the order parameter:

$$a_k\varepsilon_{kil}\underline{\Delta}_{\beta l}+\underline{b}_\alpha\varepsilon_{\alpha\beta\gamma}\underline{\Delta}_{\gamma i}+2ic\underline{\Delta}_{\beta i}=0,$$

under the condition that $\mathbf{b}\times\mathbf{n}=0$. As a result, the analysis of the possible states for the homogeneous part of the order parameter, $\underline{\Delta}_{\beta k}$, reduces to the case already considered.

Let us investigate the case when the spatial symmetry is determined by the equation

$$\hat{P}_k\equiv\hat{\boldsymbol{\mathcal{P}}}_k-t_{kj}\hat{\boldsymbol{\mathcal{L}}}_j. \tag{5.10}$$

The symmetry condition (3.12) and the algebra (4.2) reduce to the system of equations

$$\nabla_i\Delta_{\beta k}(x)=t_{ij}\varepsilon_{jkl}\Delta_{\beta l}(x),\quad t_{ij}\varepsilon_{ju\upsilon}\nabla_\upsilon\Delta_{\beta k}(x)=0, \tag{5.11}$$

from which we obtain the following condition on the admissible structure of the parameter t_{ij}:

$$t_{ij}\varepsilon_{ju\upsilon}t_{\upsilon\lambda}\varepsilon_{\lambda kl}=0. \tag{5.12}$$

We seek the quantity t_{kj} in the form $t_{kj}=t\delta_{kj}+t_i\varepsilon_{ikj}+t^2_{kj}$, where t^s_{kj} is a symmetric and traceless tensor. We substitute this expression into relation (5.12) and take into account that this relation is valid for any values of the indices. Therefore, by contracting it with the tensor $(\delta_{ki}\delta_{lu}-\delta_{ku}\delta_{li})$, we obtain an equation relating the parameters of the matrix t_{kj}:

$$6t^2-t_n^2-t^s_{i\lambda}t^s_{i\lambda}=0. \tag{5.13}$$

Contracting relations (5.12) with the tensor ε_{klu}, we arrive at another equation:

$$t_j(t\delta_{ij}+t^s_{ij})=0. \tag{5.14}$$

A consequence of equations (5.13) and (5.14) is that $t_j=0$. Let us now turn to the Jacobi identity for the operators $\hat{w}$, $\hat{P}_i$, and $\hat{P}_k$. We note that $[\hat{P}_i,\hat{P}_k]\neq 0$. In accordance with the explicit form (5.10), we find the following conditions on the structure of the matrix elements t_{ij}:

$$t_{ii}t^2_{kl}-t_{ik}t_{kl}t_{li}=0,\quad t_{ik}t_{ki}-t_{ii}t_{kk}=0. \tag{5.15}$$

It is easy to obtain the explicit form of the matrix t_{ij} satisfying (5.13)–(5.15):

$$t_{ik}=tl_il_k. \tag{5.16}$$

The spatially homogeneous part of the order parameter can be found from Eq. (5.11) together with (5.16). The solution has the form

$$\Delta_{\gamma i}(x)=a_{ik}(\mathbf{l}\psi(x))\underline{\Delta}_{\gamma k}(0), \tag{5.17}$$

where $a_{ik}(\mathbf{l}\psi(x))$ is an orthogonal matrix of rotation about axis $\mathbf{l}$ in configuration space by an angle $\psi(x)=\psi+t\mathbf{l}\cdot\mathbf{x}$. This solution describes a helicoidal structure. The quantity $2\pi t^{-1}$ determines the pitch of the helicoid, the direction of which is specified by the unit vector $\mathbf{l}$. The unbroken-symmetry condition, with allowance for (5.10) and (5.17), leads to the equation

$$\underline{a}_k(\varepsilon_{kil}\Delta_{\beta l}+\varepsilon_{iu\upsilon}x_u\nabla_\upsilon\Delta_{\beta l})+b_\alpha\varepsilon_{\alpha\beta\gamma}\Delta_{\gamma i}+2ic\Delta_{\beta i}=0, \tag{5.18}$$

where $\underline{a}_i\equiv a_i+tl_i\mathbf{l}\cdot\mathbf{d}$. Hence we obtain the relation $\mathbf{a}\times\mathbf{l}=0$, which is a restriction on the structure of the order parameter stemming from the requirement that there be no term linear in the coordinate in Eq. (5.18), and an equation for the homogeneous part of the order parameter,

$$\underline{a}_k\varepsilon_{kil}\underline{\Delta}_{\beta l}+b_\alpha\varepsilon_{\alpha\beta\gamma}\underline{\Delta}_{\gamma i}+2ic\underline{\Delta}_{\beta i}=0.$$

The general structure of the spatial symmetry operator, according to (5.1), (5.5), and (5.10), has the form

$$\hat{P}_k\equiv\hat{\boldsymbol{\mathcal{P}}}_k-p_k\hat{N}-q_kn_\alpha\hat{S}_\alpha-tl_jl_k\hat{\boldsymbol{\mathcal{L}}}_j. \tag{5.19}$$

The condition of spatial symmetry of the equilibrium state of the Fermi liquid under consideration should be supplemented by the condition of unbroken symmetry of the equilibrium state, (3.9), where the generator $\hat{T}$ is given by Eq. (3.13). In accordance with these symmetry conditions we write the equations

$$i\mathrm{Tr}\ [\hat{w},\hat{T}]\hat{\Delta}_{\beta k}(x)=0,\quad i\mathrm{Tr}[\hat{w},\hat{P}_i]\hat{\Delta}_{\beta k}(x)=0.$$

Hence we obtain equations establishing the equilibrium structure of the order parameter and find the restrictions on the parameters a_i, b_α, c, and d_i of the generator $\hat{T}$ and the parameters p_k, q_k, n_α, t, and l_k of the spatial symmetry operator $\hat{P}_k$:

$$\begin{aligned}&\underline{a}_i[\varepsilon_{ikl}\Delta_{\beta l}(x)+\varepsilon_{iuv}x_u\nabla_v\Delta_{\beta l}(x)]+\underline{b}_\alpha\varepsilon_{\alpha\beta\gamma}\Delta_{\gamma l}(x)\\&\qquad+2i\underline{c}\Delta_{\beta k}(x)=0,\\&\nabla_i\Delta_{\beta k}(x)=2ip_i\Delta_{\beta k}(x)+q_in_\alpha\varepsilon_{\alpha\beta\gamma}\Delta_{\gamma k}(x)\\&\qquad+tl_il_j[\varepsilon_{jkm}\Delta_{\beta m}(x)+\varepsilon_{juv}x_u\nabla_v\Delta_{\beta m}(x)].\end{aligned} \tag{5.20}$$

The parameters $\underline{a}_i$, $\underline{b}_\alpha$, and $\underline{c}$ are related to a_i, b_α, and c by the relations

$$\underline{a}_i\equiv a_i+tl_i\mathbf{1}\cdot\mathbf{d},\quad \underline{b}_\alpha\equiv b_\alpha+\mathbf{d}\cdot\mathbf{q}n_\alpha,\quad \underline{c}\equiv c+\mathbf{p}\cdot\mathbf{d}.$$

The requirement that there be no terms linear in the coordinate in the two equations (5.20) leads to the relations

$$\begin{aligned}&l_j\varepsilon_{juv}[2ip_v\Delta_{\beta k}(x)+q_vn_\alpha\varepsilon_{\alpha\beta\gamma}\Delta_{\gamma k}(x)]=0,\\&\underline{a}_j\varepsilon_{juv}[2ip_v\Delta_{\beta k}(x)+q_vn_\alpha\varepsilon_{\alpha\beta\gamma}\Delta_{\gamma k}(x)\\&\qquad+tl_vl_m\varepsilon_{mkn}\Delta_{\beta n}(x)]=0.\end{aligned} \tag{5.21}$$

which enable us to relate the directions of the vectors **p**, **q**, and **l** relative to one another and to the vector $\underline{\mathbf{a}}$. Equations (5.20) and (5.21) provide a basis for analysis of the classification of equilibrium states of the superfluid phases of ^{3}He with spatial symmetry generator (5.19). The solution of the second equation in (5.20) has the form

$$\Delta_{\beta i}(x)=e^{2i\varphi(x)}a_{\beta\gamma}(\mathbf{n}\theta(\mathbf{x}))a_{ik}(\mathbf{1}\psi(x))\underline{\Delta}_{\gamma k}(0). \tag{5.22}$$

Relation (5.21) holds if the vectors **p**, **q**, **l**, and $\underline{\mathbf{a}}$ are collinear. In this case the first equation of (5.20) lets one reduce the equation for the homogeneous part of the order parameter $\underline{\Delta}_{\gamma k}(0)$ (5.22), under the condition $\mathbf{b}\times\mathbf{n}$, to the standard form

$$\underline{a}_i\varepsilon_{ikl}\underline{\Delta}_{\beta l}(0)+\underline{b}_\alpha\varepsilon_{\alpha\beta\gamma}\underline{\Delta}_{\gamma l}(0)+2i\underline{c}\underline{\Delta}_{\beta k}(0)=0.$$

Let us examine the condition of stationarity of the superfluid states of ^{3}He. For the equilibrium density matrix the relation $[\hat{w},\hat{H}]=0$ holds [see (3.23)]. The von Neumann equation, together with the stationarity condition, permits determination of the time dependence of the equilibrium averages. In particular, for the order parameter we obtain

$$\begin{aligned}\mathrm{Tr}\ \hat{w}(t)\hat{\Delta}_{\alpha k}(x)&=\mathrm{Tr}\ \hat{w}(0)e^{i\hat{N}p_0t}\hat{\Delta}_{\alpha k}(x)e^{-i\hat{N}p_0t}\\&=e^{2ip_0t}\mathrm{Tr}\ \hat{w}(0)\hat{\Delta}_{\alpha k}(x).\end{aligned} \tag{5.23}$$

Relations (5.22) and (5.23) determine the space–time dependence of the order parameter in the equilibrium state.

CONCLUSION

We have used the concept of quasi-averages to generalize the classification of equilibrium states of quantum liquids with scalar and tensor order parameters with allowance for the possibility of inhomogeneous equilibrium structures. We have formulated the conditions of unbroken and spatial symmetry. We have shown that inhomogeneous spatial structures such as the magnetic helix and helicoidal liquid-crystal ordering can exist in quantum liquids.

*E-mail: mik@kipt.kharkov.ua

[1] R. Balian and N. R. Werthamer, Phys. Rev. **131**, 1553 (1963).
[2] P. W. Anderson and P. Morel, Phys. Rev. **123**, 1911 (1961).
[3] V. Ambegaokar and N. D. Mermin, Phys. Rev. Lett. **30**, 81 (1973).
[4] Z. M. Galasiewicz, Bull. Acad. Pol. Sci., Ser. Sci., Math., Astron. Phys. **9**, 605 (1961).
[5] G. Barton and M. Moore, J. Phys. C **7**, 4220 (1974).
[6] C. M. Varma and N. R. Werthamer, Phys. Rev. A **9**, 1465 (1974).
[7] V. P. Mineev, Soviet Scientific Reviews, Phys. Rev. **2**, 173 (1980).
[8] F. W. Nijhoff, H. W. Capel, and A. den Breems, Physica **130**, 375 (1985).
[9] C. Bruder and D. Vollhardt, Phys. Rev. B **34**, 131 (1986).
[10] A. M. J. Schakel and F. A. Bais, J. Phys.: Condens. Matter **1**, 1743 (1989).
[11] D. Vollhardt and P. Wolfle, *The Superfluid Phases of Helium-3*, Taylor and Francis, London–New York–Philadelphia (1990).
[12] G. E. Volovik, M. V. Khazan, Zh. Éksp. Teor. Fiz. 85, 948 (1983) [Sov. Phys. JETP **58**, 551 (1983)].
[13] A. Fetter, Phys. Rev. B **20**, 303 (1979).
[14] Y. R. Lin-Liu, D. Vollhardt, and K. Maki, Phys. Rev. B **20**, 159 (1979).
[15] A. Fetter, Phys. Rev. B **23**, 218 (1981).
[16] J. N. Kotzev and D. V. Shopova, Phys. Lett. A **187**, 264 (1994).
[17] V. M. Ruutu, J. Kopu, M. Krusius, U. Parts, B. Placais, E. V. Thuneberg, and W. Xu, Phys. Rev. Lett. **79**, 5058 (1997).
[18] J. Kopu, R. Hanninen, and E. V. Thuneberg, Phys. Rev. B **62**, 12374 (2000).
[19] N. N. Bogolyubov, Preprint D-78 [in Russian], Dubna (1961).
[20] N. N. Bogolyubov Jr., M. Yu. Kovalevskiĭ, A. M. Kurbatov, S. V. Peletminskiĭ, and A. N. Tarasov, Usp. Fiz. Nauk. **154**, 585 (1989) [Sov. Phys. Usp. **32**, 1041 (1989)].
[21] M. Yu. Kovalevskiĭ and S. V. Peletminskiĭ, Teor. Mat. Fiz. **100**, 59 (1994).
[22] M. Yu. Kovalevskiĭ and A. A. Rozhkov, Fiz. Nizk. Temp. **21**, 1138 (1995) [Low Temp. Phys. **21**, 873 (1995)].
[23] M. Yu. Kovalevskiĭ and A. A. Rozhkov, Teor. Mat. Fiz. **127**, 317 (2001).

Translated by Steve Torstveit

Equation of state of an equimolar ^{3}He–^{4}He mixture

L. V. Karnatsevich, R. M. Sibileva, M. A. Khazhmuradov,* and I. N. Shapoval

Kharkov Physicotechnical Institute National Research Center, ul. Akademicheskaya 1, 61108 Kharkov, Ukraine

A. V. Meriuz

Kharkov Polytechnical Institute National Engineering University, ul. Frunze 21, Kharkov 61002, Ukraine
(Submitted November 26, 2001)
Fiz. Nizk. Temp. **28**, 338–343 (April 2002)

Analytical forms of the empirical equations of state of the system are obtained for an equimolar ^{3}He–^{4}He mixture in the homogeneous liquid and dense fluid phases at temperatures 1.5–14 K and pressures 0–10 MPa on the basis of the existing experimental $P-V-T$ data. This is done by choosing approximating expressions, setting up a computer program, and calculating the fitting coefficients of the expressions. The quality of the approximation corresponds to the accuracy of the experimental determinations and is on average 0.5%. © *2002 American Institute of Physics.* [DOI: 10.1063/1.1476576]

1. INTRODUCTION

Liquid and gaseous isotopes of helium are unique refrigerants that are widely used in modern cryogenic technique. The use of liquid ^{4}He can provide a temperature level from 4.2 to 0.8 K. Still lower temperatures (down to 0.3 K) can be obtained by pumping on the vapor over liquid ^{3}He. Dilution refrigerators in which ^{3}He is dissolved in ^{4}He have reached a high degree of development;[1] these use ^{3}He–^{4}He isotopic mixtures to provide temperatures down to a few thousands of a kelvin. The development of cryostats of this kind requires detailed data tables for the thermodynamic properties of the mixtures over a wide range of parameters—temperature and pressure—made up of data obtained on the basis of experimental measurements in the form of an empirical equation of state in analytical form.

The helium isotopes (^{3}He and ^{4}He), while being practically identical substances chemically, are substantially different in their thermodynamic properties, especially at low temperatures in dense phases.[2] This difference is a manifestation of quantum effects of both a diffractional and a statistical nature. The helium isotopes in the solid, liquid, and dense fluid phases behave as essentially different substances. Their equations of state are substantially different.

For pure ^{4}He there are several empirically chosen equations of state based on the plentiful experimental $P-V-T$ data in different temperature and pressure intervals. It seems to us that the most complete correlation is that which was carried out by McCarty at the National Bureau of Standards (USA)[3] for temperatures from 2 to 1500 K and at pressures up to 100 MPa. This correlation describes well the liquid, vapor, and fluid phases of ^{4}He. For pure ^{3}He the semiempirical equations of state were proposed for the liquid and fluid phases separately by Taran[4] on the basis of the quantum theorem of corresponding states. For the liquid phase the equation given in Ref. 4 contains errors in the coefficients, but for the fluid phase it turns out to be quite successful.[5] Graphical correlation of the experimental $P-V-T$ data for ^{3}He (Refs. 6–8) was carried out previously with the participation of one of the authors[5,9] for the liquid and dense fluid phases in the interval interval 1.5–14 K, but the equation of state in analytical form was not determined.

For ^{3}He–^{4}He solutions in the liquid and dense fluid phases the $P-V-T$ data cannot be obtained from the corresponding data for the pure isotopes, since these solutions are substantially nonideal.[10] Experimental determinations of the $P-V-T$ relations for ^{3}He–^{4}He solutions have been made in the temperature interval 1.5–14 K.[6,10,11] In the present paper we attempt to use these determinations as a basis for finding an empirical equation of state in analytical form for an equimolar ^{3}He–^{4}He solution (the exact value of the concentration of the mixture investigated experimentally was 50.7% ^{3}He) in the liquid and dense fluid phases.

2. CHOICE OF THE ANALYTICAL FORM OF THE APPROXIMATING EXPRESSIONS FOR THE EQUATION OF STATE OF THE SYSTEM IN DIFFERENT $P-T$ REGIONS

After several attempts to use various analytical forms of the approximating expressions for the equation of state of ^{3}He–^{4}He mixtures, we chose as the best form for the dense fluid phase an expression close to that proposed by McCarty in Ref. 3. The McCarty expression has the form

$$P=\rho RT[1+B(T)\rho]+\sum_{i=1}^{8} n_{1i}\rho^3 T^{(1.5-i/2)} + \sum_{i=1}^{4} n_{2i}\rho^4 T^{(1.5-i)}+\sum_{i=1}^{6} n_{3i}\rho^5 T^{(0.75-i/4)} + \sum_{i=1}^{3} n_{4i}\rho^3 e^{\gamma\rho^2} T^{(1.0-i)}+\sum_{i=1}^{3} n_{5i}\rho^5 e^{\gamma\rho^2} T^{(1.0-i)} + \sum_{i=1}^{2} n_{6i}\rho^6 T^{(1.0-i)}, \quad (1)$$

where P is the pressure, T is the temperature, $\rho=1/V$ is the molar density of the substance (V is the molar volume), R is

 © 2002 American Institute of Physics

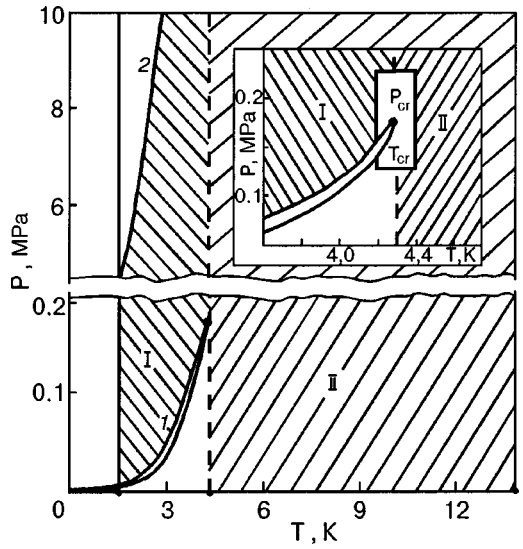

FIG. 1. Regions of states an equimolar ^{3}He–^{4}He mixture in which the equations of state of were determined in analytical form: the vapor pressure line (*1*); the line of the onset of solidification (*2*). The inset shows the region of the critical point of the mixture.

the gas constant, equal to 8.3143 J/mole·K, and $B(T)$ is the second virial coefficient of the substance; all of the n's and γ's are adjustable parameters of the model.

Figure 1 shows two regions in which calculations were done on the $P-T$ plane. Region I is a homogeneous liquid state of the solutions at pressures above the vapor-pressure line of the liquid equimolar mixture. This region is bounded from above by the line on which solidification of the liquid equimolar solution begins and by the maximum pressure level (10 MPa) reached in the experiments. The lowest temperature in this region is the lowest temperature of the experiment, 1.5 K. The highest temperature is the temperature of the critical point of the equimolar mixture, $T_{cr}=4.29$ K.[12] Region II is the fluid region above the temperature T_{cr}. This region is bounded from above in pressure by the 10 MPa level and in temperature by 14 K. At higher temperatures, as is shown in Ref. 13, the equimolar ^{3}He–^{4}He mixture is an ideal solution, and its thermodynamic quantities can be obtained from the corresponding quantities for the pure components in an additive manner. It is important to note that the upper pressure level of 10 MPa is not accidental. It has been shown experimentally that at higher pressures ^{3}He–^{4}He mixtures behave as ideal solutions to a high degree of accuracy at all temperatures, i.e., their equation of state can be obtained on the basis of the equations of state of the pure components.

In region I we have used the approximating expression

$$P=\sum_{i=1}^{4}\left[\sum_{j=1}^{6} c_{ij}T^{(j-1)}\right]V^{-(i+2)}. \tag{2}$$

Here the coefficients c_{ij} are adjustable parameters of the model. This expression is close to the McCarty form but without the virial terms, since it pertains to the liquid phase.

In region II we have used expression (1) in the form

$$\begin{aligned}P=&\frac{RT}{V}\left[1+\frac{B(T)}{V}\right]+\frac{1}{V^3}\sum_{i=1}^{8} C_{1i}T^{(1.5-i/2)}\\&+\frac{1}{V^4}\sum_{i=1}^{4} C_{2i}T^{(1.5-i)}+\frac{1}{V^5}\sum_{i=1}^{6} C_{3i}T^{(0.75-i/4)}\\&+\frac{1}{V^3}e^{(\gamma/V^2)}\sum_{i=1}^{3} C_{4i}T^{(1.0-i)}\\&+\frac{1}{V^5}e^{(\gamma/V^2)}\sum_{i=1}^{3} C_{5i}T^{(1.0-i)}+\frac{1}{V^6}\sum_{i=1}^{2} C_{6i}T^{(1.0-i)}.\end{aligned} \tag{3}$$

It is especially necessary to discuss the region of states near the critical point of the equimolar mixture. The critical parameters of ^{3}He–^{4}He mixtures were determined in Ref. 12. For an equimolar mixture they are

$$T_{cr}=4.29\ \text{K};\quad P_{cr}=0.175\ \text{MPa}.$$

In this region the equation of state of any system is described in a particularly universal manner in the framework of the scaling theory of critical phenomena.[14] Any approximating expression for the equation of state which is valid over a wide range of temperatures and pressures will lack sufficient accuracy in the critical region, but for practical purposes one doesn't need the values of the thermodynamic quantities for mixtures of helium isotopes in the critical region anyway. Therefore, in a narrow region of temperatures and pressures near the critical point it does not make sense to use the approximating expressions obtained. The width of this region in our experiment is 0.2 K in temperature and 0.05 MPa in pressure (see the inset to Fig. 1).

3. CALCULATION OF THE ADJUSTABLE PARAMETERS OF THE APPROXIMATING EXPRESSIONS

Let us consider in turn the two indicated regions of states of the system. In region I we used the data file obtained in the experiments of Ref. 6 (around 200 experimental points). Also included in the initial data file were the experimental

TABLE I. Parameters of Eq. (2) (Region I).

$c_{11}=-7.456122378\cdot10^{6}$	$c_{21}=7.27735020623\cdot10^{8}$	$c_{31}=-2.3215336056102\cdot10^{10}$	$c_{41}=2.43471678431716\cdot10^{11}$
$c_{12}=9.542853976\cdot10^{6}$	$c_{22}=-1.012836928180\cdot10^{9}$	$c_{32}=3.415175713913\cdot10^{10}$	$c_{42}=-3.71590188805814\cdot10^{11}$
$c_{13}=-4.477159806\cdot10^{6}$	$c_{23}=5.30224198179\cdot10^{8}$	$c_{33}=-1.9095031516872\cdot10^{10}$	$c_{43}=2.17233637584717\cdot10^{11}$
$c_{14}=9.0966847\cdot10^{5}$	$c_{24}=-1.29936776404\cdot10^{8}$	$c_{34}=5.121344952174\cdot10^{9}$	$c_{44}=-6.1503269396509\cdot10^{10}$
$c_{15}=-6.569338\cdot10^{4}$	$c_{25}=1.4531882507\cdot10^{7}$	$c_{35}=-6.57262537325\cdot10^{8}$	$c_{45}=8.458395819068\cdot10^{9}$
$c_{16}=-3.439784\cdot10^{2}$	$c_{26}=-5.62331094\cdot10^{5}$	$c_{36}=3.2183971566\cdot10^{7}$	$c_{46}=-4.53498324226\cdot10^{8}$

TABLE II. Parameters of Eq. (3) (Region II).

$c_{11} = -2.52324 \cdot 10^5$	$c_{22} = -2.87265 \cdot 10^7$	$c_{41} = 9.28786 \cdot 10^9$
$c_{12} = 3.48459 \cdot 10^6$	$c_{23} = 7.07832 \cdot 10^7$	$c_{42} = 2.22045 \cdot 10^9$
$c_{13} = -9.30782 \cdot 10^9$	$c_{24} = -8.07302 \cdot 10^7$	$c_{43} = -2.01159 \cdot 10^6$
$c_{14} = 6.06168 \cdot 10^7$	$c_{31} = 1.46698 \cdot 10^{10}$	$c_{51} = 3.42303 \cdot 10^{13}$
$c_{15} = -2.32286 \cdot 10^9$	$c_{32} = -1.1864 \cdot 10^{11}$	$c_{52} = -7.20941 \cdot 10^{10}$
$c_{16} = 9.55869 \cdot 10^7$	$c_{33} = -3.38525 \cdot 10^{13}$	$c_{53} = 9.0026 \cdot 10^9$
$c_{17} = -4.32729 \cdot 10^7$	$c_{34} = -5.81274 \cdot 10^{11}$	$c_{61} = 2.47022 \cdot 10^9$
$c_{18} = 8.64864 \cdot 10^6$	$c_{35} = 3.95108 \cdot 10^{11}$	$c_{62} = -5.33779 \cdot 10^9$
$c_{21} = 2.11562 \cdot 10^6$	$c_{36} = -2.37165 \cdot 10^{10}$	$\gamma = -0.0005$

results on the $P-V-T$ relations for an equimolar ^{3}He–^{4}He mixture in the liquid phase along the saturated vapor line (the vapor-pressure line in Fig. 1) from Refs. 15 and 16 and also the analogous data for a liquid equimolar mixture along the line of the onset of solidification (Fig. 1) from Ref. 17 (a total of 18 experimental points). The statistical weights of the points used in the calculation were determined by the accuracy of the experimental results given in the original sources. The results of the calculation of the adjustable fitting parameters are given in Table I (for P in MPa, T in K, and V in cm^3/mole).

For calculations in region II it is necessary to know the values of the second virial coefficient $B(T)$ of the equimolar mixture for the temperature interval 4.29–14 K. These values were taken from an experimental paper.[18] For convenience in the calculation the first term, that containing the virial coefficients, in expression (3) was represented in the following analytical form:

$$\frac{RT}{V}\left[1+\frac{B(T)}{V}\right] = -\frac{41180.6}{V^2} - \frac{73859}{T^2V^2} + \frac{217604}{T^{1.5}V^2} - \frac{248654}{TV^2} + \frac{138296}{\sqrt{T}V^2} + \frac{4586.93\sqrt{T}}{V^2} + \frac{8.3143T}{V}. \quad (4)$$

The calculations were based on the experimental measurements of the density of the mixture in Ref. 10 (about 350 experimental points in all).

The results of the calculations of the adjustable parameters of the model are presented in Table II (for P in MPa, T in K, and V in cm^3/mole).

For illustration of the quality of the approximation, Fig. 2 shows the experimental $P(V)$ curves for several isotherms for states in region I. The corresponding calculated curves are shown by the solid curves. The average distance between the calculated and experimental curves is 0.5%, while the real scatter of the experimental points from the smoothed curves reaches 1%. Figure 3 shows the analogous comparison for region II, but in the more convenient coordinates $\rho-P$. We see that the agreement is quite good. It should be kept in mind that the accuracy of the measurements in this region depends substantially on the density of the system (see Ref. 10). For example, at $\rho = 0.001$ mole/cm^3 it is 3%, while the discrepancy between the calculated and experimental data does not exceed 1%.

The calculations showed that both approximating expressions for regions I and II are in good agreement in a $P-T$ strip of width ± 0.1 K around the critical temperature of the equimolar mixture.

CONCLUSION

In summary, this study has permitted us to choose approximating expressions, to set up a computer program, and

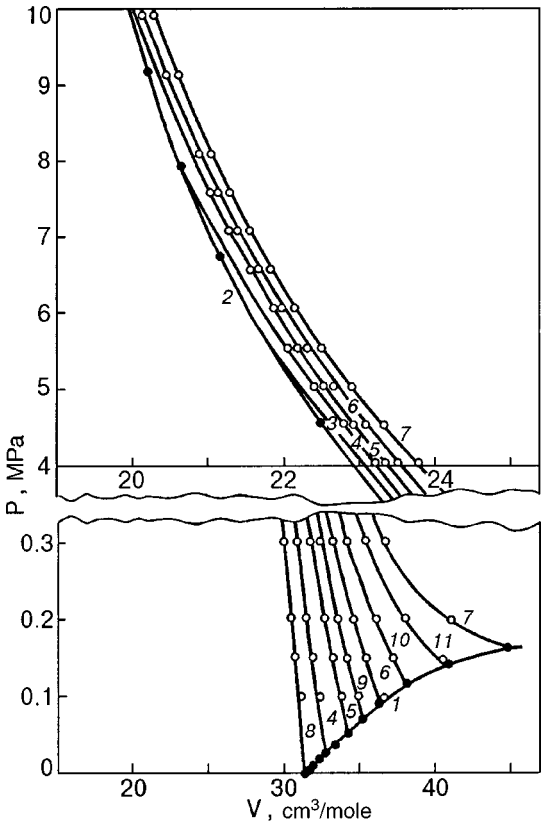

FIG. 2. Comparison of the experimental and calculated $P-V$ points for an equimolar ^{3}He–^{4}He mixture in the region of the homogeneous liquid state along the following isotherms: the vapor-pressure line (*1*), the line of the onset of solidification (*2*), $T=2$ (*3*), 2.5 (*4*), 3.0 (*5*), 3.5 (*6*), 4.2 (*7*), 1.5 (*8*), 3.25 (*9*), 3.75 (*10*), and 4.0 K (*11*). The filled dots are the data of other authors.[15–17]

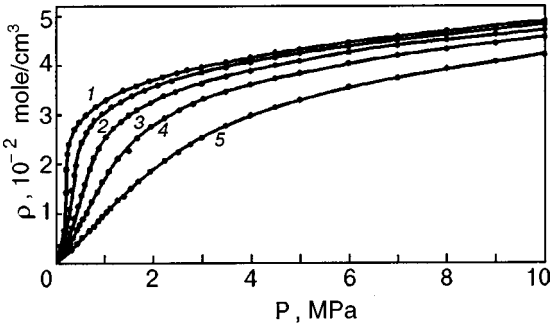

FIG. 3. Comparison of the experimental and calculated $\rho-P$ curves for an equimolar ^{3}He–^{4}He mixture in the dense fluid region along the isotherms for $T=4.52$ (*1*), 5.42 (*2*), 6.94 (*3*), 8.99 (*4*), and 13.00 K (*5*).

to calculate the adjustable parameters of the expressions giving an adequate empirical description of the equation of state of an equimolar ^{3}He–^{4}He mixture in the region of the homogeneous liquid state and in the region of the dense fluid, i.e., in the entire part of the $P-T$ plane in which this mixture is substantially different from the ideal solution. The expressions obtained in this study provide a means for calculating the various thermodynamic quantities for an equimolar mixture of helium isotopes: the isothermal compressibility, isochoric coefficient of volume expansion, entropy, enthalpy, etc. The approximating expressions obtained also permit comparison of the detailed engineering tables of the quantities mentioned, which are needed for constructing ultralow-temperature cryostats. Finally, the equimolar mixture is basic to practical applications of the mixtures. However, for certain problems it is also important to know the concentration dependence of some thermodynamic quantities. This study provides a basis for extending the method and software developed here to other ^{3}He–^{4}He mixtures for which experimental $P-V-T$ data are available.

This study was done with the support of the Ukrainian Government Scientific–Industrial Center for Standardization, Metrology, and Certification.

*E-mail: khazhm@kipt.kharkov.ua

[1] O. V. Lounasmaa, *Experimental Principles and Methods Below One Degree Kelvin* [Academic Press, New York (1974); Mir, Moscow (1977)].
[2] B. N. Esel'son, V. N. Grigor'ev, V. G. Ivantsov, É. Ya. Rudavskiĭ, D. D. Sanikidze, and I. A. Serbin, *Solutions of* ^{3}He–^{4}He *Quantum Liquids* [in Russian], Nauka, Moscow (1973).
[3] R. D. McCarty, J. Phys. Chem. Ref. Data **2**, 923 (1973).
[4] V. N. Taran, Teplofizicheskie Svoĭstva Veshchestv i Materialov **7**, 31 (1973).
[5] V. G. Konareva, L. V. Karnatsevich, and I. V. Bogoyavlenskiĭ, Ukr. Fiz. Zh. **27**, 675 (1982).
[6] I. V. Bogoyavlenskiĭ and S. I. Yurchenko, Fiz. Nizk. Temp. **2**, 1379 (1976) [Sov. J. Low Temp. Phys. **2**, 672 (1976)].
[7] R. N. Sherman and F. J. Edeskuty, Ann. Phys. (N.Y.) **9**, 522 (1960).
[8] I. V. Bogoyavlenskiĭ, L. V. Karnatsevich, and V. G. Konareva, Fiz. Nizk. Temp. **4**, 549 (1978) [Sov. J. Low Temp. Phys. **4**, 265 (1978)].
[9] L. V. Karnatsevich, V. G. Konareva, and I. V. Bogoyavlenskiĭ, *Tables of Recommended Handbook Data for Helium-3. Thermodynamic Properties. Bibliographic Index*, Vol. 12 [in Russian], VINITI, Moscow (1988), 120.
[10] I. V. Bogoyavlenskiĭ, L. V. Karnatsevich, and V. G. Konareva, Fiz. Nizk. Temp. **6**, 1241 (1980) [Sov. J. Low Temp. Phys. **6**, 601 (1980)].
[11] I. V. Bogoyavlenskiĭ, L. V. Karnatsevich, and V. G. Konareva, Fiz. Nizk. Temp. **6**, 5 (1980) [Sov. J. Low Temp. Phys. **6**, 1 (1980)].
[12] B. Wallace Jr. and H. Meyer, Phys. Rev. A **5**, 953 (1972).
[13] A. I. Karnus, N. S. Rudenko, E. I. Vinokurov, Ukr. Fiz. Zh. **20**, 1729 (1975).
[14] H. E. Stanley, *Introduction to Phase Transitions and Critical Phenomena* [Clarendon Press, Oxford (1971); Mir, Moscow (1973)].
[15] E. C. Kerr, *Proceedings LT-5*, Madison (1958).
[16] B. N. Esel'son, V. G. Ivantsov, P. S. Novikov, and R. I. Shcherbachenko, Ukr. Fiz. Zh. **14**, 1837 (1969).
[17] R. C. Pandorf, E. M. Ifft, and D. O. Edwards, Phys. Rev. **163**, 175 (1967).
[18] L. V. Karnatsevich, I. V. Bogoyavlenskiĭ, and A. A. Sheĭnina, Fiz. Nizk. Temp. **14**, 1230 (1988) [Sov. J. Low Temp. Phys. **14**, 680 (1988)].

Translated by Steve Torstveit

Spin–lattice relaxation in the bcc phase of phase-separated ^{3}He–^{4}He solid mixtures

N. P. Mikhin,* V. A. Maidanov, and A. V. Polev

B. Verkin Institute for Low Temperature Physics and Engineering, National Academy of Sciences of Ukraine, pr. Lenina 47, 61103 Kharkov, Ukraine

(Submitted December 7, 2001)
Fiz. Nizk. Temp. **28**, 344–348 (April 2002)

The spin–lattice relaxation time in two samples of ^{3}He–^{4}He solid mixtures with initial concentrations of 0.5% ^{3}He in ^{4}He and 0.5% ^{4}He in ^{3}He is measured by the pulsed NMR method. As a result of phase separation, in both cases two-phase crystals form, having the same helium concentration in the concentrated bcc phase. However, in the first sample the bcc phase forms as small inclusions in an hcp matrix, while in the second sample the bcc phase is the matrix. It is established that in the second case the spin–lattice relaxation occurs in the same way as in pure bulk ^{3}He, while in the first case one observes anomalous behavior of the spin–lattice relaxation time at low temperatures. Experiments have shown that this anomaly is due not to the possible influence of the small ^{4}He impurity but to the small dimensions of the inclusions of the of the bcc phase. In this case the main contribution to the relaxation is apparently due to defects formed at the boundaries of the bcc inclusions and the hcp matrix. © *2002 American Institute of Physics.* [DOI: 10.1063/1.1476577]

1. INTRODUCTION

Spin–lattice relaxation in solid helium has been studied[1,2] in detail experimentally and theoretically only for bulk solid ^{3}He. The observed temperature dependence of the spin–lattice relaxation time T_1 is well explained in the framework of the well-developed Garwin–Landesman model, which describes the process of energy transfer from the nuclear spins to the lattice via multiply connected subsystems—Zeeman, ^{3}He–^{3}He exchange, vacancy, and, in the presence of impurities, ^{4}He–^{3}He exchange.

Developments in experimental technique make it possible to expand the temperature region of investigation to a range in which the homogeneous solid mixtures of helium isotopes undergo a first-order phase transition, decaying into two daughter phases with different ^{3}He concentrations. The two-phase crystals that are formed in this case are an interesting quantum system. For example, a dilute solid mixture of ^{3}He in ^{4}He after phase separation at sufficiently low temperatures consists of disperse inclusions of almost pure ^{3}He with the bcc lattice embedded in an hcp matrix of practically pure ^{4}He. Studies of the spin–lattice relaxation in such systems have shown[3–5] that the properties of the matrix are no different from those of homogeneous solid mixtures of the corresponding concentration. However, unlike the case for bulk ^{3}He, in the disperse concentrated phase T_1 is independent of temperature down to temperatures of the order of 1 mK,[3] and the value of T_1 corresponds to the region of the "^{3}He–^{3}He exchange plateau" for bulk ^{3}He of the corresponding density. It should be noted that in bulk ^{3}He the indicated regions of the exchange plateau is observed only for temperatures above $\sim$200 mK. Upon cooling below this temperature the time T_1 in bulk ^{3}He increases exponentially because of the disruption of equilibrium of the exchange system with the lattice owing to the decrease in the number of vacancies, and then, in the presence of ^{4}He impurities, it increases by a T^{-9} power law. These strong differences in the behavior of T_1 in a bulk sample and in a fine disperse phase can be attributed to the following main causes.

1. The presence of ^{4}He impurities is known to be effective[1,2,6] in suppressing the growth of T_1 in bulk ^{3}He; the same situation may exist in the ^{3}He inclusions after phase separation.

2. The small sizes of the inclusions (1–3 μm) can also affect the value of T_1. In the case of small inclusions the main site of such rapid relaxation will be the boundary between the bcc inclusions and the hcp matrix, which can serve as a source of a large number of defects.

The goal of this study is to investigate the influence of these factors on the temperature dependence of the spin–lattice relaxation time in solid ^{3}He. Here it is convenient to investigate two samples, corresponding to the left and right sides of the diagram, with initial concentrations such that after phase separation the concentration of one of the substances in the matrix of one sample will be practically the same as the concentration of the same substance in the inclusions of the other sample.

2. EXPERIMENTAL TECHNIQUE

In this study we have accordingly investigated samples of ^{3}He–^{4}He solid mixtures with two initial concentrations: 0.5% ^{3}He and 0.5% ^{4}He. For simplicity we shall call these samples A and B, respectively. When samples A and B are cooled below the phase separation temperature, two daughter phases are formed in them: a bcc phase with a high concentration of ^{3}He, and an hcp phase, with a low concentration. In sample A the phase with the high concentration of ^{3}He consists of fine disperse bcc inclusions of almost pure ^{3}He 1–3 μm in size,[5,8,9] surrounded by a bulk hcp matrix of almost pure ^{4}He. In sample B it is hcp inclusions of ^{4}He surrounded by a bcc matrix of almost pure ^{3}He. An important point is that after separation the ^{4}He concentration in the bcc daughter phase (like the ^{3}He concentration in the hcp

 © 2002 American Institute of Physics

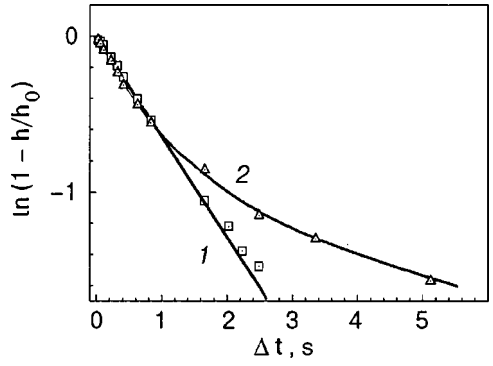

FIG. 1. Recovery of the equilibrium magnetization of sample B: $T = 110$ mK (1), $T = 60$ mK (2).

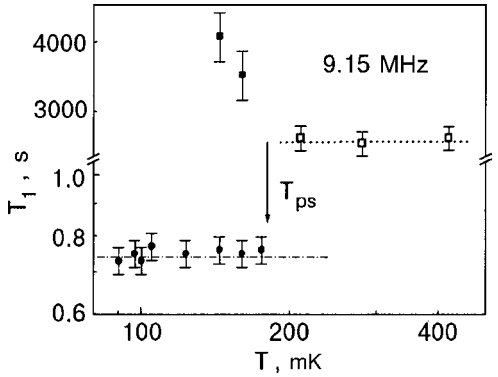

FIG. 2. Temperature dependence of the spin–lattice relaxation time in sample A: □—T_1^0, ●—T_1^c, ■—T_1^d. The arrow indicates the phase-separation temperature. The dotted line shows the calculated value of T_1^0, while the dot-and-dash line shows the calculated value of T_1 for the "exchange plateau" in solid ^{3}He.

daughter phase) is the same for both types of samples at the same temperature, since the phase separation process occurs in accordance with the same phase diagram. A comparison of the results of experiments done with samples of such "symmetric" initial concentrations makes it possible to separate out the contribution of the spin–lattice relaxation coming from the small sizes of the solid inclusions of ^{3}He.

The samples were grown in the cell described in Ref. 8 by the capillary-blocking method. The final pressure in homogeneous samples annealed at a pre-melting temperature was around 32 atm, corresponding to molar volumes $V_m = 20.55 \pm 0.05$ cm^3/mole for sample A and $V_m = 24.6 \pm 0.05$ cm^3/mole for sample B.

The change of the pressure in the samples as a result of the phase separation was estimated to be not more than a few hundredths of an atmosphere, which is less than the real scatter of the pressure in the prepared samples after annealing. Therefore, it can be assumed that to within the experimental accuracy, even the parameters that depend strongly on pressure (the Debye temperature, exchange integral, and diffusion coefficient) are the same for the corresponding phases in the phase-separated samples of both types.

The cell holding the sample was in good thermal contact with the mixing chamber of the refrigerator.[8] The spin–lattice relaxation time was measured by the pulsed NMR method with the use of the standard pulse technique: $90° - \tau - 180° - \tau - \text{echo1} - \Delta T - 90° - \tau - 180° - \tau - \text{echo2}$. Since $\tau = 200\ \mu\text{s} \ll \Delta t$, the amplitude h of the echo signal was proportional to the magnetization recovered over a time Δt:

$$\frac{h}{h_0} = 1 - \exp\left(-\frac{\Delta t}{T_1}\right), \tag{1}$$

where h_0 is the amplitude of the echo signal for $\Delta t \gg T_1$.

3. EXPERIMENTAL RESULTS AND DISCUSSION

Figure 1 shows typical data obtained from experimental measurements on sample B (0.5% ^{4}He in ^{3}He). At sufficiently high temperatures (110 mK, curve *1*) the results are well described by a single-exponential function of the form (1). Since solid ^{3}He at 32 atm begins to melt at temperatures below 88 mK and the liquid already amounts to around 40% of the sample at 60 mK, the recovery of the magnetization can be described by two exponentials, corresponding to the relaxation in the liquid and in the crystal (see curve 2 in Fig. 1).

The data of the measurements for sample A are qualitatively similar to those described for sample B. However, the low ^{3}He concentration in them leads to a low "signal-to-noise" ratio and the large scattering of the h values, so that one cannot say for certain whether features analogous to those observed on curve *2* of Fig. 1, for example, are present in this case. As to the liquid phase with a high ^{3}He concentration, regular measurements of T_1 have not been made in it. We note only that at 60 mK the values of T_1 in the liquid lies between 10 and 20 s in both types of samples. These values agree with the results of Refs. 4 and 9 for samples of the corresponding density.

The temperature dependence of T_1 obtained for samples of type A is shown in Fig. 2. It should be noted immediately that this dependence is qualitatively similar to that obtained previously at frequencies of 250 kHz (Ref. 3) and 1 MHz (Refs. 4 and 5) on analogous samples. It has three branches, corresponding to the initial homogeneous sample with the hcp structure and to two daughter phases of the separated mixture—the dilute hcp matrix and the concentrated bcc disperse phase. In the initial homogeneous sample T_1^0 is unchanged on cooling, and its value corresponds to those known from published data for T_1 under similar conditions[10] and from calculations according to the Torrey theory[1] (the "exchange plateau" region). Below the phase separation temperature T_{ps} one observes two values of T_1, corresponding to phases with large (T_1^c) and small (T_1^d) ^{3}He concentrations. The decrease of the ^{3}He concentration in the dilute hcp phase in accordance with the phase-separation diagram leads to growth of T_1^d on cooling.[10] These two factors—the growth of T_1^d and the decrease of the ^{3}He concentration in the hcp phase—make it different to distinguish the echo signal from the background of instrument noise below 150 mK, even with a several-hour wait. The long duration Δt makes measurements difficult and lowers their accuracy. We note that in the low-frequency measurements,[3] when T_1^d does not exceed 1 min, by averaging the values of h obtained in several tens of measurements the spin–lattice relaxation time in the dilute phase could be measured down to a temperature of 100 mK.

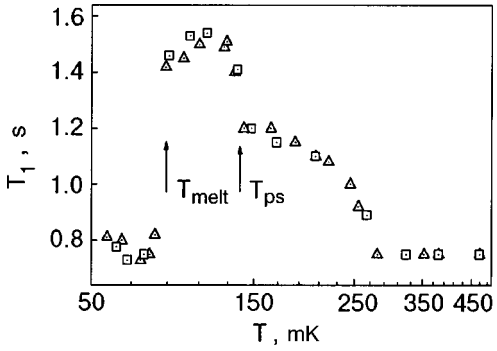

FIG. 3. Temperature dependence of T_1 in sample B: the data obtained on cooling (△) and heating (□). The arrows indicate the phase-separation temperature T_{ps} and the melting temperature $T_{\rm melt}$.

On the other hand, thanks to the large T_1^d values in the present study, by choosing an interval of around 1 min between measurements we were able to obtain a signal for the concentrated phase alone, since the magnetization of the dilute hcp phase at the time of the measurements and, hence, its contribution to the spin echo, are practically zero.

As we see in Fig. 2, in the concentrated phase the time T_1^c is practically independent of temperature and has a value that agrees with the experimental value of T_1 obtained in bulk solid ^{3}He under similar conditions and with the value obtained from theoretical calculations[1] for temperatures in the so-called ''exchange plateau'' region, where T_1 is determined mainly by the relaxation of the Zeeman subsystem to the ^{3}He–^{3}He exchange subsystem. As can be seen in Fig. 2, the deviation of T_1^c from the calculated values does not exceed the measurement error.

The results of measurements for sample B are presented in Fig. 3. We note, first, that both the small amount of the dilute phase and the low ^{3}He concentration in it make it impossible to distinguish the contribution of the dilute phase to the signal amplitude. The absence of noticeable hysteresis on cooling and heating indicates that a half-hour wait after a temperature change of 5–10 mK is sufficient for the phases coexisting in the sample to come to equilibrium. At high temperatures one observes a plateau with $T_1=0.75$ s. The agreement of this value with the known data[1] for pure ^{3}He in the ''exchange plateau'' region and the coincidence of the temperature region in which this plateau exists indicate that in this case the coupling of the Zeeman and exchange subsystems is a ''bottleneck'' on the path for energy to leak from the Zeeman subsystem to the lattice. The temperature $\sim$260 mK below which appreciable growth of T_1 is observed also agrees with the data of Refs. 1, 2, and 7. In accordance with the concepts of the Garwin–Landesman theory[1] this growth is due to a shifting of the role of the ''bottleneck'' over to the vacancy–exchange mechanism of relaxation on account of the decrease of the number of vacancies during cooling. Here $T_1 \propto \exp(E_v/T)$, where E_v is the activation energy of the vacancies. From the experimental data one can not only estimate E_v but even distinguish the exponential growth from the power-law growth ($T_1 \propto T^{-9}$ for the bcc lattice) that is due to the successive appearance of another possible relaxation path via the ^{4}He–^{3}He exchange mechanism.[1] The smooth approach to saturation of the growth of T_1 on further cooling is apparently analogous to that observed in Ref. 6 for bulk solid ^{3}He containing a 0.5% ^{4}He impurity at high pressures. Below $T_{ps}=144$ mK, which is indicated by an arrow in Fig. 3, phase separation of the sample occurs, according to the phase diagram, and one observes a growth of T_1.

Finally, below $\sim$88 mK, at which solid ^{3}He at a pressure of around 32 atm begins to melt, one observes a sharp decrease in T_1 (see Fig. 3). This is apparently due to the wall relaxation mechanism, which operates efficiently in the liquid: liquid ^{3}He in this temperature region is already a degenerate Fermi liquid with a spin diffusion coefficient $D_s \propto T^{-2}$, ensuring a rather rapid transport of ^{3}He toward the wall.

Thus we have shown in this paper that T_1^c is independent of temperature in the disperse bcc daughter phase of a phase-separated dilute solid mixture of ^{3}He in ^{4}He (samples A). At the same time, the temperature dependence of T_1 in samples with an initial ^{4}He concentration of 0.5% (samples B) under analogous conditions exhibits practically all the previously known features due to the various spin–lattice relaxation mechanisms in bulk solid ^{3}He. A comparison of the two results obtained (see Figs. 2 and 3) leads one to conclude that the temperature dependence of T_1^c (in the case of sample A) is not due directly to the ^{4}He impurities but is determined by the small sizes of the inclusions of the ^{3}He-rich phase.

In closing the authors thank V. N. Grigor'ev and É. Ya. Rudavskii for their interest in this study and for some stimulating discussions.

This study was supported by the Ukrainian Government Foundation for Basic Research 02.07/00391 (Project F7/286-2001) and was carried out as part of the Young Scientists Project FM12-1.

*E-mail: mikhin@ilt.kharkov.ua

[1] R. A. Guyer, R. C. Richardson, and L. I. Zane, Rev. Mod. Phys. **43**, 532 (1971).
[2] M. Bernier and G. Guerrier, Physica **121**, 202 (1983).
[3] N. P. Mikhin, A. V. Polev, É. Ya. Rudavskiĭ, and V. A. Shvarts, Fiz. Nizk. Temp. **23**, 807 (1997) [Low Temp. Phys. **23**, 455 (1997)].
[4] S. C. J. Kingsley, I. Kosarev, L. Roobol, V. Maidanov, J. Sauders, and B. Cowan, J. Low Temp. Phys. **110**, 34 (1998).
[5] S. C. J. Kingsley, V. Maidanov, J. Sauders, and B. Cowan, J. Low Temp. Phys. **113**, 1017 (1998).
[6] M. Bernier and G. Deville, J. Low Temp. Phys. **16**, 349 (1974).
[7] M. Chapellier, M. Basson, M. Devort, J. M. Delrien, and N. S. Sullivan, J. Low Temp. Phys. **59**, 45 (1985).
[8] V. A. Mikhev, V. A. Maĭdanov, N. P. Mikhin, S. E. Kal'noĭ, and N. F. Omelaenko, Fiz. Nizk. Temp. **14**, 564 (1988) [Sov. J. Low Temp. Phys. **14**, 309 (1988)].
[9] N. Alikasem, Ph.D. Thesis, University of Sussex (1989).
[10] Y. Hirayoshi, T. Mizusaki, S. Maekava, and A. Hirai, J. Low Temp. Phys. **30**, 137 (1978).

Translated by Steve Torstveit

SUPERCONDUCTIVITY, INCLUDING HIGH-TEMPERATURE SUPERCONDUCTIVITY

Steady state diagram of current-carrying layered superconductors

A. N. Artemov and Yu. V. Medvedev*

A. A. Galkin Donetsk Physicotechnical Institute, ul. R. Lyuksemburg 72, 83114 Donetsk, Ukraine
(Submitted September 25, 2001; revised November 19, 2001)
Fiz. Nizk. Temp. **28**, 349–354 (April 2002)

The stability of the nonisothermal state of a layered superconductor carrying a current is investigated in a model based on the heat production in an electrical circuit with nonlinear resistance, which adequately reflects the features of the quasi-two-dimensional behavior of the system. The state diagrams of the layered superconductor are plotted in the following coordinates: heat removal coefficient (which depends on the substrate properties) versus current, and nonlinearity parameter (which characterizes the superconductor material) versus current. The velocity of the resistive-zone motion as a function of the value of the transport current is calculated for different values of the nonlinearity parameter. © *2002 American Institute of Physics.* [DOI: 10.1063/1.1477355]

1. INTRODUCTION

The problem of the stability of a superconducting current state has long been the subject of intensive research (see, e.g., Refs. 1 and 2). The theoretical study of instability is based mainly on simple phenomenological models that take into account the balance of the production and removal of heat in the superconductor–thermostat system. Nevertheless, these simple models have proved extremely useful for formulating the main relationships in the development of instabilities of the critical state of bulk,[1–4] thin-film,[5–8] and composite[1,2,9,10] superconductors both in the presence and absence of a varying external magnetic field. In the absence of such a field the thermal instability of a superconducting sample is conditional on the nonisothermal dynamics of the sample-penetrating field lines of the self-magnetic field of the current.

For high-T_c superconductors (HTCSs), which have a layered structure, the basic relationships governing the thermal stability of a superconducting current state remain as before. The only difference is in the character of the heat-producing processes, which is determined by the nonlinearity of the current–voltage (I–V) characteristics of HTCS materials; we shall refer to this by the term ''nonlinear heat production.''

Physically the nonlinearity of the I–V characteristics of HTCS systems is a manifestation of the quasi-two-dimensional character of these materials. As in two-dimensional superconductors, in the copper-oxide superconducting layers of HTCS systems, topological defects in the form of neutral two-dimensional vortex–antivortex pairs (bound 2D vortices) can arise as a result of thermal fluctuations.[11–13] Under the influence of the transport current, sufficiently long vortex dipoles will be broken apart, and the free 2D vortices that appear will move along the superconductor. This mechanism of resistivity leads to nonlinear behavior of the I–V characteristic, since the number of free vortices depends on the value of the current. In this case the theory predicts a power-law dependence of the voltage on current:[14] $V \sim I^{a(T)+1}$. The exponent $a = K(T_c/T - 1)$ depends on temperature and the phenomenological parameter K. In the framework of the Lawrence–Doniach model[15] this parameter can be written in the form $K = \Phi_2^2 s/(16\pi^2 \lambda^2(0) T_c)$, where T_c is the critical temperature of the superconductor, s is the period of the layered structure, Φ_0 is the magnetic flux quantum, and $\lambda(0)$ is the London penetration depth at $T = 0$. The phase transition in the sample (the Berezinskii–Kosterlitz–Thouless (BKT) transition)[16,17] does not materially affect the heat production in such a system, since at currents that can lead to thermal instability of the superconducting state the number of free vortices produced by the current is much greater than the number arising under the influence of thermal fluctuations.

In real HTCSs the situation is complicated by the fact that a Josephson link exists between the superconducting layers. The vortex dipoles of fluctuational origin arising in the layers consist of two 2D vortices whose magnetic flux is closed by two Josephson vortices situated between superconducting layers. The presence of Josephson vortices in the dipole will lead to linear growth of the dipole energy with increasing distance between 2D vortices.[18] The behavior of these materials, because of the weak superconductivity in the direction perpendicular to the superconducting layers, differs from the behavior of ideal 2D systems in the low-temperature region but becomes typically two-dimensional above a certain temperature which we shall denote T_{KT}, having in mind that the instability manifested at this temperature is the same as that which leads to the BKT transition in 2D systems. The behavior becomes two-dimensional because near T_{KT}, fluctuations causing dissociaiton of the dipoles destroy the correlation between superconducting layers. Such behavior is observed in the experimental study of the I–V characteristics of HTCS single crystals in the direction of the c axis[19] and follows from the results of numerical simulations using an anisotropic 3D XY model.[20]

The character of the I–V characteristics of such systems

 © 2002 American Institute of Physics

is different, since the current breaking apart the dipole must now overcome the tension of the Josephson vortices. As a consequence, an internal critical current $I_c(T)$ appears in the superconductor. In this case the I–V characteristic of the superconductor is well described by a function of the form $V \propto I(I-I_c(T))^a$ (Ref. 21). The critical current goes to zero at the temperature T_{KT}, and its temperature dependence can be approximated by the expression $I_c(T)=I_{c0}(1-T/T_{KT})^{3/2}$ (Ref. 19).

The influence of the nonlinear heat production in layered superconductors on the velocity of the normal-phase motion was first studied in Ref. 22. In that paper the expression $\dot{Q}(T)=\rho(j,T)j^2$ was used for the power of heat production in the sample, with an expression of the form $\rho(j,T)=\rho_n(1-j_c(T)/j)^{a(T)}$ for the effective nonlinear resistivity of the superconductor in the resistive state, where ρ_n is the resistivity of the superconductor in the normal state, $j_c(T)=j_{c0}(1-T/T_c)$, and T_c is the temperature of the transition to the superconducting state. Formally the use of this expression implements the idea of a nonlinear character of the heat production in layered superconductors and suggests that the resistive state might also be stable in addition to the superconducting and normal states.

However, the model of heat production in Ref. 22 does not fully reflect the main behavioral features of such materials. In particular, it does not allow one to take into account the fact that the critical current goes to zero at a temperature $T_{KT}<T_c$, while the I–V characteristic remains nonlinear all the way up to the transition of the sample to the normal state. Another important feature of superconductors is the presence of a decoupling current I_{GL}, which goes to zero at the temperature T_c. When the transport current becomes equal to I_{GL}, the superconductor will undergo a transition to the normal state, for which the I–V characteristic is linear.

These features of the nonlinear heat production in the resistive state of layered superconductors are taken into account in the phenomenological model proposed in the present paper. This model is used to study the stable steady states of layered superconductors and also the stability of the superconducting state and the motion of the normal phase along the sample. Phase diagrams are constructed which clearly show the regime of existence of the various current states of the superconductor in relation to the parameters of the model.

2. MODEL

The dynamics of thermal processes of a thin-film superconductor is investigated on the basis of a numerical solution of the one-dimensional heat transfer equation

$$D_s C_s \frac{\partial T}{\partial t} = D_s \frac{\partial}{\partial x} k_s \frac{\partial T}{\partial x} + d_f \dot{Q}(T) - W(T). \tag{1}$$

Here D_s is the thickness of the substrate, C_s and k_s are the heat capacity and thermal conductivity of the substrate material, d_f is the thickness of the superconducting film, and the heat removal function is written in the form

$$W(T)=h(T-T_0), \tag{2}$$

where $h=k_s/D_s$ is the effective coefficient of heat removal, and T_0 is the temperature of the thermostat.

As in Ref. 22, we assume that the specific power of heat production is given by the expression $\dot{Q}(T)=\rho(j,T)j^2$, in which the effective nonlinear resistivity,

$$\rho(j,T) = \begin{cases} \rho_n & (T>T_c)\cup(j\geqslant j_{GL}(T)) \\ \rho_n\left(\dfrac{j-j_c(T)}{j_{GL}(T)-j_c(T)}\right)^{a(j,T)} & (T_r\geqslant T<T_c)\cap(j<j_{GL}(T)) \\ 0 & T<T_r \end{cases} \tag{3}$$

approximates the main features of the behavior of a layered superconductor. Here T_r is the temperature of the transition of the superconductor to the resistive state, which is determined from the condition $j_c(T_r)=j$, and $j_{GL}=j_{GL}(0)(1-T/T_c)^{3/2}$ is the decoupling current that destroys the superconducting state.

In writing $\rho(j,T)$ in the form (3), we have taken into account the breaking of already existing vortex pairs of fluctuational origin by the Lorentz force. The expression for the exponent $a(j,T)$ proposed in Ref. 22 is, strictly speaking, valid only at currents much less than the decoupling current. It goes to zero, corresponding to a transition of the superconductor to the normal state, at the temperature T_c. However, if a transport current is flowing in the superconductor, then it will go into the normal state at a temperature $T_n<T_c$ at which the current becomes equal to the pair-breaking current, $j=j_{GL}(T_n)$. To take this fact into account in our model, we multiply the expression for $a(j,T)$ by an even function of the current which is equal to unity for $j=0$ and to zero for $j=j_{GL}$. The simplest expression for the exponent of the I–V characteristic satisfying all of these requirements can be written as $a(j,T)=K(T_c/T-1)[1-(j/j_{GL})^2]$. The last term in the expression for $a(j,T)$ takes into account the saturation of the concentration of free vortices when the current approaches the decoupling value, where the exponent goes to zero and $\rho(j,T)$ approaches ρ_n. The critical current due to the internal tension of the Josephson components of the vortex rings goes to zero at the temperature T_{KT} of the BKT transition, which is determined from the condition $K(T_c/T_{KT}-1)=2$. It is given by the expression[19]

$$j_c(T)=j_{c0}\left(1-\frac{T}{T_{KT}}\right)^{3/2}. \tag{4}$$

The proposed phenomenological model of nonlinear conductivity adequately reflects all of the limiting behavior associated with the critical currents and temperatures of layered superconductors. Thus we can suggest that their properties in the region of intermediate parameters are also adequately described by the model.

3. STEADY STATES OF A CURRENT-CARRYING SUPERCONDUCTOR

The character of the steady solutions of the nonlinear heat transfer equation (1) is known[1,2,23] to depend on the number and character of its critical points, which are determined by the condition

$$d_f\dot{Q}(T)-W(T)=0. \tag{5}$$

Depending on the parameters and the value of the current, there can be either one such point or three of them. In the first case one has a stable superconducting state (SS), resistive state (RS), or normal state (NS). The stability criterion is the inequality $\partial W/\partial T > d_f \partial \dot{Q}/\partial T$. The only stable steady solutions that can exist in this case are homogeneous solutions.

In the case when Eq. (1) has three critical points, the two outer points (T_1, T_2) correspond to stable states, and the temperature T_3 $(T_1 < T_3 < T_2)$ to an unstable state. This is the region of bistability (BSS) of the superconductor. Here, besides the homogeneous solutions indicated there can also exist an inhomogeneous stable steady solution which we shall call the switching wave between states T_1 and T_2. The switching wave is a self-similar solution of equation (1). It is a nonuniform temperature distribution moving at a constant velocity v which is an eigenvalue of the equation. The features of solutions of this kind will be explored in the next Section.

The model contains a number of phenomenological parameters. The parameter K depends on the period of the superconducting structure and the London depth $\lambda(0)$ and is determined by the structure and properties of the superconductor material. It can be varied by choosing different types of HTCSs or creating artificial superlattices having different periods. In real samples this parameter can be varied over rather wide limits. For example, using the published data of various authors we obtain in the framework of the Lawrence–Doniach model a value $K \approx 32$ for YBCO[24] and a value $K \approx 3-5$ for the more anisotropic thallium HTCSs.[25] Estimating this parameter from the value of the BKT transition temperature gives higher values (>100 for YBCO). The difference in the values of this parameter may be due to the imperfection of the technique used to process the results of measurements of the I–V characteristics, the data from which the temperature T_{KT} is most often found.

Other parameters of the model are determined by the conditions of heat production and removal. The effective heat-removal coefficient h can be varied by changing the material, thickness, and quality of the substrate surface. It also can be varied over wide limits. For example, using the data obtained in Ref. 26, for a substrate thickness $D_s = 5 \times 10^{-5}$ m one obtains $h = 9 \times 10^4$ W/(m^{2}K) in the case of a $SrTiO_3$ substrate and $h = 1.4 \times 10^7$ W/(m^{2}K) for an Al_2O_3 substrate.

These parameters have a qualitative influence on the character of the stability of the superconducting state. By varying them, one can create and alter the width of the region of bistability of the superconductor. In this Section we investigate the influence of the nonlinearity parameter K and effective heat-removal coefficient h on the character of the steady states of the superconductor.

We adopt the following values of the parameters of the superconducting film:

$$K=30, \quad d_f=10^{-7}\ \text{m} \quad \rho=3.5\cdot 10^{-5}\ \Omega\cdot\text{m},$$

$$j_c(0)=10^{10}\ \text{A/m}^2, \quad j_{GL}(0)=10^{11}\ \text{A/m}^2,$$

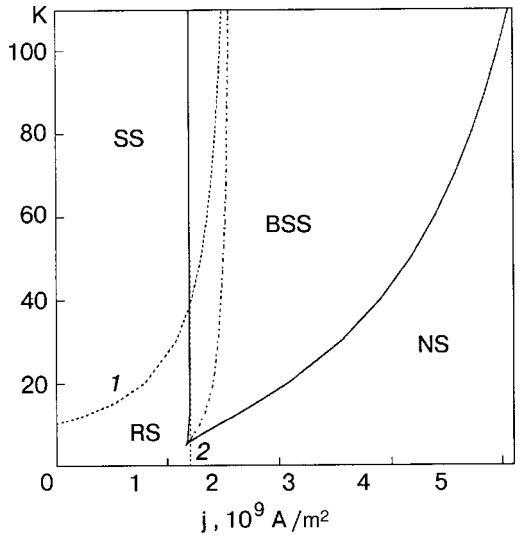

FIG. 1. State diagram of a superconductor in the plane of the nonlinearity parameter K versus current j: SS is the superconducting, RS the resistive, NS the normal, and BSS the bistable state.

$$T_{c0}=92\ \text{K}$$

and substrate

$$D_s=5\cdot 10^{-5}\ \text{m}, \quad k_s=250\ \text{W/(m}\cdot\text{K)},$$

$$C_s=10^5\ \text{J/(m}^3\text{K)},$$

which correspond to a value of the parameter $h = 5 \times 10^5$ W/(m^{2}K) and a thermostat temperature $T_0 = 77$ K.

Figure 1 shows the state diagram of a superconductor in the space of the parameter K and transport current j. The dashed line separates the regions in which the superconductor can be found in one of three homogeneous states: superconducting (SS), resistive (RS), and normal (NS). The solid lines bound the regions of the diagram within which the superconductor has two stable states (BSS). Inside this region the superconductor can be found either in one of two homogeneous states or in an inhomogeneous state of the switching-wave type. Changing the other parameters of the model alters the position of the BSS region without affecting the qualitative form of the diagram. Increasing the resistivity ρ of the film or decreasing the parameter h shifts the BSS region downward and to the left. On line *1* the condition $T_r = T_0 = T_1$ holds. Crossing this line means a transition of the system between the SS and RS. If this line lies inside the BSS region, then the character of the low-temperature (T_1) state changes at this line. Line *2* is found from the condition $T_2 = T_n$, where the temperature T_n is determined by the equation $j = j_{GL}(T_n)$. Inside the BSS region the high-temperature (T_2) state changes on crossing this line. The dot-and-dash line corresponds to values of the model parameters for which the velocity of the switching wave is zero. Above this line the wave moves in the direction of the high-temperature phase, bringing the sample to a homogeneous state with temperature T_1. It could be superconducting or resistive, depending on the its position with respect to line *1*. Below the dot-and-dash line the wave moves in the opposite direction, bringing the sample to a state with temperature T_2, which can be resistive or normal.

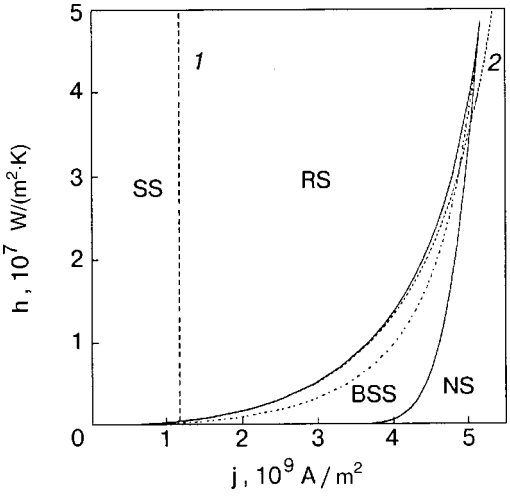

FIG. 2. State diagram of a superconductor in the plane of the effective heat-removal coefficient h versus current j. The notation is the same as in Fig. 1.

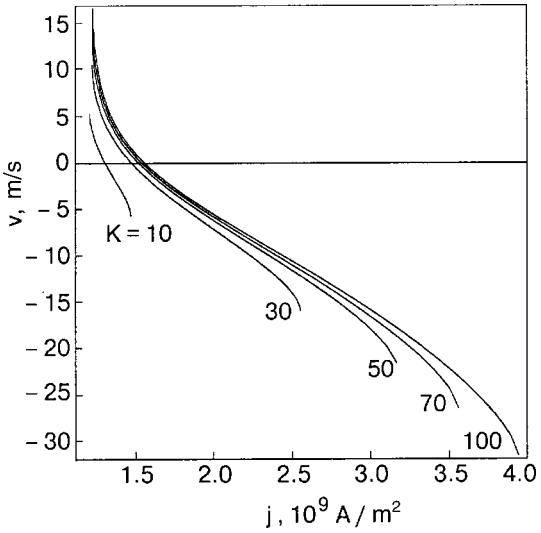

FIG. 3. Velocity of the switching wave in the superconductor as a function of current for different values of the nonlinearity parameter K.

As can be seen from the diagram, increasing the parameter K with the remaining parameters of the model unchanged can significantly widen the stability region of the superconducting state.

The state diagram of the superconductor in the space of effective heat-removal coefficient h and current j is shown in Fig. 2. All of the lines of this diagram have the same meaning as in Fig. 1. It is clear that with improving heat-removal conditions (increasing h) the boundary of the stability region of the superconducting state is shifted in the direction of increasing current.

4. THERMAL STABILITY OF THE SUPERCONDUCTING STATE

Let us consider the inhomogeneous stationary solution of equation (1). This solution can exist in the region of model parameters and currents in which Eq. (5) has three solutions. In this case the two outer critical points (T_1, T_2) are stable saddles, and the third (T_3) is an unstable node.[15] Let us discuss the stationary self-similar solution of equation (1) of the form $T(x,t)=T(x-vt)$ with the boundary conditions

$$T(x=-\infty,t)=T_1, \quad T(x=+\infty,t)=T_2,$$

$$\frac{\partial T}{\partial x}(x=\pm\infty,t)=0,$$

which is a nonuniform temperature distribution propagating with velocity v. The lowest-temperature point T_1 corresponds to a stable superconducting or resistive state, depending on the relationships among the parameters. The second stable critical point T_2 corresponds to a normal or resistive state of the superconductor.

It is known[23,27] that the only stable stationary solution of this form is the solution corresponding to the separatrix going from one saddle to the other. This solution corresponds to a nonuniform temperature distribution moving at a constant velocity v.

Figure 3 shows the dependence of the velocity of the boundary between the superconducting and normal phases on the current density flowing along the superconductor. At small j the boundary moves in the positive x direction from the superconducting phase T_1 to the normal phase T_2. Here the region occupied by the superconducting phase expands. This may be interpreted as absolute stability of the superconducting at low currents phase is absolutely stable, i.e., a normal region arising in a fluctuational manner will collapse after some time. At a certain value of the current the velocity of the boundary can change sign. This means that the interface will now move in the direction of the superconducting phase, bringing the entire sample to the normal state. The influence of the parameters K and h on the value of the current at which the wave velocity $v=0$ can be seen in Figs. 1 and 2.

CONCLUSION

Generally speaking, the model parameters used in calculating the phase diagrams and velocities of the switching wave do not reflect the properties of any particular material. They were chosen so as to obtain a general sort of system demonstrating the maximum possible number of variants of behavior while remaining within the realm of physically reasonable values.

This study was supported by the Ministry of Education and Science of Ukraine (Project 2M/71-2000).

*E-mail: medvedev@kinetic.ac.donetsk.ua

[1] R. G. Mints and A. L. Rakhmanov, *Instabilities in Superconductors* [in Russian], Nauka, Moscow (1989).
[2] A. V. Gurevich, R. G. Mints, and A. L. Rakhmanov, *Physics of Composite Superconductors* [in Russian], Nauka, Mosva (1987).
[3] I. L. Maksimov, Yu. N. Mastakov, and N. A. Taĭlanov, Fiz. Tverd. Tela (Leningrad) **28**, 2323 (1986) [Sov. Phys. Solid State **28**, 610 (1986)].
[4] N. A. Taĭlanov and U. G. Yakhshiev, Pis'ma Zh. Tekh. Fiz. **26**, 8 (2000) [Tech. Phys. Lett. **26**, 897 (2000)].
[5] V. G. Volotskaya, I. M. Dmitrenko, L. E. Musienko, and A. G. Sivakov, Fiz. Nizk. Temp. **7**, 383 (1981) [Sov. J. Low Temp. Phys. **7**, 188 (1981)].
[6] Yu. M. Ivanchenko, P. N. Mikheenko, and V. F. Khirnyĭ, Zh. Éksp. Teor. Fiz. **80**, 171 (1981) [Sov. Phys. JETP **53**, 86 (1981)].

[7] Yu. M. Ivanchenko and P. N. Mikheenko, Zh. Éksp. Teor. Fiz. **83**, 684 (1982) [Sov. Phys. JETP **56**, 380 (1982)].
[8] I. M. Dmitrenko, Fiz. Nizk. Temp. **22**, 849 (1996) [Low Temp. Phys. **22**, 648 (1996)].
[9] V. V. Lysenko, Zh. Tekh. Fiz. **70**, 67 (2000) [Tech. Phys. **45**, 736 (2000)].
[10] V. R. Romanovskiĭ, JETP Lett. **23**, 94 (1997).
[11] S. N. Artemenko and A. N. Kruglov, Phys. Lett. A **143**, 485 (1990).
[12] J. R. Clem, Bull. Am. Phys. Soc. **35**, 260 (1990); Phys. Rev. B **43**, 7837 (1991).
[13] L. I. Glazman and A. E. Koshelev, Zh. Éksp. Teor. Fiz. **97**, 1371 (1990) [Sov. Phys. JETP **70**, 774 (1990)].
[14] P. Minnhagen, Rev. Mod. Phys. **59**, 1001 (1987).
[15] W. E. Lawrence and S. Doniach, in *Proceedings of the 12th International Conference on Low Temperature Physics*, Kyoto, 1970, edited by E. Kanda, Keigaku, Tokyo (1971), p. 361.
[16] V. L. Berezinskiĭ, Zh. Éksp. Teor. Fiz. **61**, 1144 (1971) [Sov. Phys. JETP **34**, 610 (1972)].
[17] J. M. Kosterlitz and D. G. Thouless, J. Phys. C **6**, 1181 (1973).
[18] V. Cataudella and P. Minnhagen, Physica C **166**, 442 (1990).
[19] N.-C. Yeh and C. C. Tsuei, Phys. Rev. B **39**, 9708 (1989).
[20] P. Minnhagen and P. Olsson, Phys. Rev. B **44**, 4503 (1991).
[21] H. J. Jensen and P. Minnhagen, Phys. Rev. Lett. **66**, 1630 (1991).
[22] I. L. Maksimov and D. Yu. Vodolazov, Pis'ma Zh. Tekh. Fiz. **24**(21), 1 (1998) [Tech. Phys. Lett. **24**, 829 (1998)].
[23] V. A. Vasil'ev, Yu. M. Romanovskiĭ, and V. G. Yakhno, *Autowave Processes* [in Russian], Nauka, Moscow (1987).
[24] Wang Jun, Mao Xiang Lei, Chen Lin, Wu Bai Mei, Chen Zhao Jia, Chen Jin Seng, Le De Fen, Zhang Yu Heng, Cao Xiao Wen, Wen Hai Hu, and Zhang Ting Yu, J. Low Temp. Phys. **66**, 1125 (1994).
[25] A. Wahl, A. Maignan, C. Martin, V. Hardy, J. Provost, and Ch. Simon, Phys. Rev. B **51**, 9123 (1995).
[26] A. M. Grishin, Yu. V. Medvedev, and Yu. M. Nikolaenko, Fiz. Tverd. Tela (St. Petersburg) **41**, 1377 (1999) [Phys. Solid State **41**, 1260 (1999)].
[27] Ya. I. Kanel', Mat. Sbornik **59**, 245 (1962).

Translated by Steve Torstveit

Flux-line pinning by columnar magnetic defects in a type-II superconductor

S. A. Krivenko and N. M. Suleĭmanov*

E. K. Zavoiskiĭ Kazan Physicotechnical Institute, Russian Academy of Sciences, Sibirskiĭ Trakt 10/7, 420029 Kazan, Russia
(Submitted November 14, 2001)
Fiz. Nizk. Temp. **28**, 355–359 (April 2002)

The interaction of a magnetic vortex in a type-II superconductor with a cylindrical (columnar) defect filled with a nonconducting magnetic material is investigated for the first time. Analytical expressions are obtained for the vortex pinning force at such a defect. It is shown that if the material filling the cylinder has a small magnetization, then the attractive force it exerts on a vortex is determined mainly by the interaction of the vortex with the surface of the defect. In the case of a material with a large magnetization the interaction of the magnetic field of the vortex with the magnetic moments throughout the volume of the defect becomes substantial. This can serve as a good resource for enhancing the pinning efficiency. © *2002 American Institute of Physics.* [DOI: 10.1063/1.1477356]

INTRODUCTION

The low critical current density substantially limits the practical application of high-T_c superconductors (HTSCs). At the present time, by employing various technical means it has been possible to obtain polycrystalline HTSC materials (which are the most attractive from the standpoint of applications by virtue of the simplicity of preparation and amenability to large-scale production) with conducting properties close to those for single crystals. Moreover, the problem of superconducting transport has another extremely important aspect. This is due to the fact that the magnetic flux lines arising in a type-II superconductor when it is placed in a sufficiently high external magnetic field should be rigidly pinned in the volume of the superconductor in order not to create an additional resistance to superconducting currents. This problem is particularly urgent for HTSC materials with high values of T_c, at which the probability of random thermal hops of the flux lines in the material increase significantly.

It has been established experimentally (see, e.g., Refs. 1–3) that columnar defects extending in the same direction are efficient pinning centers for flux lines, as the vortices interact with them along their entire length. Such defects can be obtained, e.g., by irradiating the superconductor with high-energy particles, which create linear tracks of amorphized material along their paths. The interaction of the vortices with such defects in HTSC systems is analyzed in the framework of the solution of differential equations of the Ginzburg–Landau type for a superconductor bordering another medium (the contents of the track). Their solution is complicated by the necessity of taking into account the boundary conditions for the superconducting currents and the superconducting order parameter at the boundary of the defect, which in general can have a complex geometry. A consistent calculation of the pinning force has been successfully carried out only for hollow cylindrical channels.[4–6] The attraction of the vortices to them occurs on account of deformation of their currents upon interaction with the surface of the defects. However, the matter of how a real physical medium (conductor, insulator, or magnet) will affect the pinning mechanism and pinning force remains an open question.

In this paper we investigate how filling a cylindrical columnar defect of finite length with a nonconducting magnetic material will be reflected in the vortex pinning force. For the HTSC system we used the London approximation, as for a type-II superconductor. We assumed that the vortex–defect distance is smaller than the London penetration depth λ. This is the situation that is of greatest practical interest, since otherwise the interaction is exponentially small. The expressions obtained for the attractive force on a vortex recovers the results of Refs. 4–6 in the limit when the material filling the cylinder is nonmagnetic. In the case of a track made of a material with a large magnetization it is found that a new pinning mechanism appears, due to the interaction of the nonuniform magnetic field of the vortex with the magnetic moments throughout the volume of the defect.

MODEL

Consider a cylindrical defect in a type-II superconductor. The defect consists of a magnetic material in the form of an infinitely long cylinder with a radius R much greater than the coherence length ξ. We shall assume that the medium filling this cylinder is an insulator, and we shall neglect the exchange of current carriers between the superconductor and defect. We assume that the magnet filling the cylinder has a uniform magnetization $\mathbf{m}$ parallel to the axis of the cylinder, which we take as the z axis of the coordinate system. Let the axis z be oriented perpendicular to the copper planes of the HTSC, and let the magnetic field be directed along this axis. The field distribution depends only on the coordinates x and y. Therefore, it is sufficient to describe it in any plane cross section of the superconductor perpendicular to the z axis. We consider a vortex whose axis passes through the point $\mathbf{r}_0 = (x_0, y_0)$ and lying a distance r_0 from the axis of the cylinder (it is assumed that $r_0 > R$). To describe the magnetic field $\mathbf{h} = h\mathbf{e}_z$ ($\mathbf{e}_z$ is the unit vector along the z axis) generated by the vortex currents $\mathbf{j} = (c/4\pi)\text{curl}\ \mathbf{h}$ at any point $\mathbf{r} = (x,y)$ of the superconductor, we use the London equation

 © 2002 American Institute of Physics

$$\Delta\mathbf{h}-\frac{\mathbf{h}}{\lambda^2}=-\frac{\Phi_0}{\lambda^2}\,\delta(|\mathbf{r}-\mathbf{r}_0|)\mathbf{e}_z\,, \tag{1}$$

where Δ is the Laplacian operator, Φ_0 is the magnetic flux quantum, and λ is the penetration depth of the magnetic field into the type-II superconductor. When a vortex approaches a nonconducting cylinder, its magnetic field $\mathbf{h}_{\rm in}=h_{\rm in}\mathbf{e}_z$ penetrates into the cylinder. Since the vortex currents do not penetrate into the insulator, and curl $\mathbf{h}_{\rm in}=0$ inside it, the value of $h_{\rm in}$ is a constant over the volume of the defect. By virtue of the continuity condition for the tangential component of the magnetic field of the currents at the interface,[7] on the surface of the cylinder $|\mathbf{r}|=R$ the relation $h_{\rm in}=h(|\mathbf{r}|=R)$ should hold, where $h(|\mathbf{r}|=R)$ denotes the magnetic field of the vortex at the boundary of the defect.

As a result of the interaction of the superconducting currents with the magnetic field, the magnetization $\mathbf{m}=m(h_{\rm in})\mathbf{e}_z$ of the cylinder becomes dependent on $h_{\rm in}$ but remains uniform. The total magnetic field inside the cylinder will be equal to $\mathbf{B}(\mathbf{r})=\mathbf{h}_{\rm in}+\mathbf{H}(\mathbf{r})$, where $\mathbf{H}(\mathbf{r})$ is the magnetic field of the molecular currents. From the standpoint of macroscopic electrodynamics the magnetic field $\mathbf{H}(\mathbf{r})$ of the molecular currents of the cylinder are exactly the same as for an infinite cylindrical solenoid with a completely surface current $\mathbf{i}=c\mathbf{m}\times\mathbf{n}$, where $\mathbf{n}$ is the outer normal to the surface of the cylinder.[8] It has a discontinuity at the boundary and has the form[8]

$$\mathbf{H}(\mathbf{r})=\mathbf{H}_0\,,\quad r\in\ \text{in};\quad \mathbf{H}(\mathbf{r})=0,\quad r\in\ \text{ex}, \tag{2}$$

where ''in'' and ''ex'' denote the interior and exterior regions of space with respect to the cylinder, and $\mathbf{H}_0=(4\pi/c)\mathbf{n}\times\mathbf{i}=4\pi\mathbf{m}$. In this approximation it can be assumed that the magnetic field created by the molecular currents of the magnetized cylinder are concentrated inside it and do not penetrate into the superconductor. Consequently, it does not influence the distribution of the vortex currents and the magnetic field $\mathbf{h}$ due to them. Thus the magnetic field distribution of a vortex interacting with a cylinder of nonconducting material does not depend on whether or not the material is magnetic. Since we are neglecting the diffusion of superconducting pairs through the boundary of the defect, the superconducting currents on this surface will satisfy the same condition $\mathbf{j}\cdot\mathbf{n}=0$ as for a superconductor–vacuum boundary. Therefore, in the given case the field $\mathbf{h}$ will be the same as for a vortex interacting with a hollow cylinder. It was calculated for the latter in Refs. 5 and 6 by the methods of electrostatics, and for $\xi<|\mathbf{r}|$, $|\mathbf{r}_0|<\lambda$ it has the form

$$\mathbf{h}(|\mathbf{r}|)=[h_0(|\mathbf{r}-\mathbf{r}_0|)+h_0(|\mathbf{r}|)-h_0(|\mathbf{r}-\mathbf{r}_0'|)]\mathbf{e}_z\,. \tag{3}$$

Here $\mathbf{r}_0'=(R/r_0)^2\mathbf{r}_0$, and the function $h_0(x)=(\Phi_0/2\pi\lambda^2)\ln|\lambda/x|$ describes the value of the field of a vortex at a distance x from its center. Then from the value of the magnetic field at the boundary of the defect it is found, with allowance for expression (3), that the magnetic field due to the vortex currents has the value $h_{\rm in}=h_0(r_0)$ inside the cylinder.

PINNING FORCE

The pinning force $\mathbf{f}=-\partial E/\partial\mathbf{r}_0$ exerted by the cylinder on the vortex is determined by their interaction energy $E=E(r_0)$. As we have shown, the field $\mathbf{h}$ penetrates into the defect and induces a magnetization $\mathbf{m}(\mathbf{h})$ in the cylinder, but here there is no ''back'' effect of this magnetization on the vortex field. This circumstance makes it possible in calculating the energy of the system to separate the two contributions to it, the first being related to the geometry of the surface of the defect and the second to its magnetization:

$$E=E_1+E_2\,. \tag{4}$$

The first term in relation (4) is

$$E_1=\frac{1}{8\pi}\int_V d\mathbf{r}[\mathbf{h}^2+\lambda^2(\text{rot}\ \ \mathbf{h})^2], \tag{5}$$

where V is the volume of the sample and $\mathbf{h}$ is given by expression (3). It corresponds to the interaction energy of a vortex with a hollow cylinder.[4–6] When the superconducting vortex approaches the boundary of a nonconducting defect, the current streamlines of the vortex are deformed by the surface of the defect. As a result, an imbalance of forces acting on the core of the vortex arises. Since the current density increases in the boundary region, this causes an attraction of the vortex core toward the defect.[9] The corresponding ''surface'' pinning force is given by

$$\mathbf{f}_1(\mathbf{r}_0)=-\left(\frac{\Phi_0}{4\pi\lambda}\right)^2\frac{2R^2}{r_0^3}\,\frac{\mathbf{e}_0}{1-(R/r_0)^2}, \tag{6}$$

where $\mathbf{e}_0=\mathbf{r}_0/r_0$, and it corresponds to an attraction of the vortex toward the cylinder. As to the contribution E_2, it is the interaction energy of a cylinder magnetized to a value $\mathbf{m}(\mathbf{h}_{\rm in})$ with the vortex magnetic field $\mathbf{h}_{\rm in}$ penetrating into it. According to Ref. 7, the energy of a magnet in an external magnetic field, the role of which in this case is played by $\mathbf{h}_{\rm in}$, is given by the expression

$$E_2=-\int_{V_{\rm in}}\int_0^{h_{\rm in}}\mathbf{m}(\mathbf{h})\cdot d\mathbf{h}d\mathbf{r}, \tag{7}$$

where $V_{\rm in}$ is the volume of the defect. Since the value of the field $\mathbf{h}_{\rm in}$ increases as the vortex approaches the boundary of the cylinder, the energy E_2 (7) increases or decreases depending on the direction of $\mathbf{m}$ with respect to $\mathbf{h}$. This circumstance leads to a second contribution to the pinning force, equal to

$$\mathbf{f}_2(\mathbf{r}_0)=\pi R^2\mathbf{m}(\mathbf{h}_{\rm in})\partial\mathbf{h}_{\rm in}/d\partial\mathbf{r}_0\,. \tag{8}$$

The dependence of $\mathbf{f}_2$ on the distance r_0 to the vortex is determined, first, by its field gradient $\partial\mathbf{h}_{\rm in}/\partial\mathbf{r}_0=-(\Phi_0/2\pi\lambda^2)\mathbf{e}_0/r_0$, and, second, by the fact that in each particular case the magnetization $\mathbf{m}(\mathbf{h}_{\rm in})$ of the contents of the defect is due to the field $\mathbf{h}_{\rm in}$ applied to it, since the latter is itself a function of r_0. We also note that if the vectors $\mathbf{m}$ and $\mathbf{h}_{\rm in}$ are parallel, then the direction of the force (8) corresponds to attraction of the vortex toward the cylinder, while if $\mathbf{m}$ and $\mathbf{h}_{\rm in}$ are oriented antiparallel, then the contribution $\mathbf{f}_2$ corresponds to repulsion of the vortex.

The saturation magnetization for a typical ferro- or ferrimagnet is of the order of 100 Oe, i.e., is relatively small compared to the vortex fields (the critical field in high-T_c superconductors is $H_{c1}\approx 1$ kOe). Therefore, as a result of the interaction with those fields a cylinder of such a material can be magnetized to the saturation value $\mathbf{m}=m_0\mathbf{e}_z(m_0>0)$.

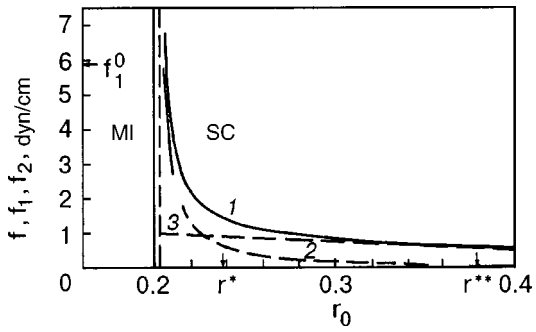

FIG. 1. Absolute values of the total pinning force **f** (*1*), its component $\mathbf{f}_1$ (*2*), given by formula (6), and its component $\mathbf{f}_2$ (*3*), formula (9), as functions of the distance r_0 between the axis of the vortex in the superconductor (SC) and the axis of a cylinder of magnetic insulator (MI) in the region $R+\xi < r_0 < \lambda$ for $m_0 = 1000$ G, $R = 400$ Å, and $\xi = 10$ Å. The vertical dashed line corresponds to the value $r_0 = R+\xi$. The distances are given in units of λ ($\lambda = 2000$ Å). If the cylinder were hollow, then with distance of the vortex core from its boundary the modulus of the pinning force, equal to f_1, would fall off from $f_1^0 \approx 5.8$ dyn/cm (denoted by an arrow on the vertical axis) to $f_1(r^*) = 10^{-1} f_1^0$ at a distance $r^* \approx 0.24\lambda$. In the case of a magnetic cylinder the pinning force f will reach the same value $f(r^{**}) = f_1(r^*)$ at a considerably greater distance $r^{**} \approx 0.37\lambda \approx 1.5 r^*$. The scales of r^* and r^{**} are indicated by arrows on the horizontal axis.

Then expression (8)—the contribution to the force of attraction of the vortex toward the track—takes the form

$$\mathbf{f}_2 = -\frac{\Phi_0}{2\lambda^2}\frac{R^2}{r_0}\mathbf{m}_0\mathbf{e}_0. \tag{9}$$

If the magnetization of a unit volume has the typical value for a ferro(ferri)magnet $m_0 \approx 1000$ G, then the pinning force component $\mathbf{f}_2$ at large distances ($r_0 \gg R$) will be significantly greater in modulus than the force $\mathbf{f}_1$ given by formula (6), since the function (9) falls off much more slowly with distance (see Fig. 1). For example, in the case of a cylinder of radius $R = 400$ Å and a vortex at a distance $r_0 = 800$ Å in a superconductor with $\xi = 10$ Å and $\lambda \approx 2000$ Å we obtain $f_2/f_1 \approx 10$. As a result of this, for a magnetized cylinder not only does the pinning force increase on account of the contribution $\mathbf{f}_2$ but it also has a considerably longer range. Thus if the cylinder in the example just considered were hollow, then with increasing distance of the vortex core from the boundary of the defect the modulus of the pinning force, which would be equal to the force (6), would fall off from the value $f_1^0 \approx f_1(r_0 = R+\xi) \approx 5.8$ dyn/cm to $f_1(r^*) = 10^{-1} f_1^0$ at a distance $r^* \approx 0.24\lambda$ (see Fig. 1). Consequently, the force of attraction of the vortex toward the defect, due solely to the contribution $\mathbf{f}_1$, should fall much more rapidly with distance, vanishing not far from the cylinder boundary R (in this example $R = 0.2\lambda$). In contrast, in the case of a magnetic cylinder, as can be seen in Fig. 1, the value of the pinning force f reaches the same value $f(r^{**}) = f_1(r^*)$ at a distance r^{**} which is considerably larger than r^* ($r^{**} \approx 0.37\lambda \approx 1.5 r^*$).

It should be noted that in Ref. 10 it was also shown that magnetic pinning centers are more efficient than hollow cylinders. There they investigated formations in the form of droplets of magnetized material (magnetic dots) deposited on the surface of a superconducting film. The pinning occurred as a result of the interaction of the vortex currents with the magnetic field lines penetrating into the superconductor from these defects. However, the mechanism of attraction of vortices toward the pinning centers investigated in the present paper is qualitatively different, since the magnetic defect is located not on the surface of the superconducting film but inside a bulk superconductor. Therefore, in addition to the component due to the magnetization of the defect, the component of the pinning force due to deformation of the vortex currents by its boundary will also have a substantial value. This latter component is what determines the value of the pinning force when the vortex core approaches the surface of a nonconducting magnetic cylinder (see Fig. 1).

In the case when the conductivity of the medium filling the cylinder is nonzero, the superconductor can exchange current carriers with it: Cooper pairs will penetrate into the defect from outside, and unpaired electrons will come back out. As a result, the density of superconducting pairs and, with it, the vortex current density in the superconductor will decrease near a defect. This will tend to decrease the ''surface'' component of the pinning force for conducting defects. At the same time, the magnetic component remains the same in magnitude as in the case of an insulating defect.

CONCLUSION

In summary, we have investigated the mechanism of vortex pinning by a magnetic defect located in the bulk of a superconductor. The defect considered had the form of an infinitely long cylinder of a nonconducting material lying parallel to the flux line. An analytical expression was obtained for the force of interaction of the vortex with such a defect. It was shown that an additional contribution to this force arises due to the interaction of the magnetic cylinder with the vortex field penetrating into it, which leads to a substantial enhancement of the pinning efficiency.

This study was done with the support of the Russian Foundation for Basic Research (Grant No. 99-02-18064).

*E-mail: suleiman@dionis.kfti.kcn.ru

[1] L. Krusin-Elbaum, L. Givale, G. Blatter, A. D. Marwick, F. Holtzberg, and C. Feild, Phys. Rev. Lett. **72**, 1914 (1994).
[2] J. A. Fendrich, W. K. Kwok, J. Giapintzakis, C. J. van der Beek, V. M. Vinokur, S. Freshler, U. Welp, H. K. Viswanathan, and G. W. Grabtree, Phys. Rev. Lett. **74**, 1210 (1995).
[3] L. M. Paulius, R. E. Shamu, S. Ferguson, M. C. de Andrade, and M. B. Maple, Appl. Phys. Lett. **71**, 3415 (1997).
[4] G. S. Mkrtchyan and V. V. Schmidt, Zh. Éksp. Teor. Fiz. **61**, 367 (1971) [Sov. Phys. JETP **34**, 195 (1972)].
[5] A. Buzdin and D. Feinberg, Physica C **256**, 303 (1996).
[6] A. Buzdin and M. Daumens, Physica C **294**, 257 (1998).
[7] L. D. Landau and E. M. Lifshitz, *Electrodynamics of Continuous Media*, 2nd ed., rev. and enl. by E. M. Lifshitz and L. P. Pitaevskii [Pergamon Press, Oxford (1984); Nauka, Moscow (1982)].
[8] I. E. Tamm, *Principles of the Theory of Electricity* [in Russian], Nauka, Moscow (1966).
[9] G. S. Mkrtchyan, V. V. Shmidt, Usp. Fiz. Nauk **112**, 355 (1974) [Sov. Phys. Usp. **17**, 460 (1975)].
[10] R. Sášik and T. Hwa, cond-mat/0003462 (2000).

Translated by Steve Torstveit

Reinforcement of pinning by surface magnetic microparticles in high-T_c superconductors

P. N. Togulev, V. V. Bazarov,* I. B. Khaĭbullin, and N. M. Suleĭmanov

E. K. Zavoiskiĭ Kazan Physicotechnical Institute, Russian Academy of Sciences, Sibirskiĭ Trakt 10/7, 420029 Kazan, Russia

(Submitted November 14, 2001)
Fiz. Nizk. Temp. **28**, 360–364 (April 2002)

A reinforcement of pinning in high-T_c superconducting materials by surface magnetic microparticles obtained by ion implantation is observed. Measurements are made by the method of magnetically modulated microwave absorption. In single crystals of $Bi_2Sr_2CaCu_2O_8$ an ensemble of magnetic particles is formed directly in a subsurface layer of the superconductor by the implantation of Fe^+ ions followed by annealing. In experiments with $YBa_2Cu_3O_7$ the magnetic microparticles of iron were formed individually in SiO_2 films which were then applied to the surface of a thin film of $YBa_2Cu_3O_7$, and measurements were made on the composite structure. In both cases reinforcement of the pinning is observed. In the limits of the chosen implantation regimes the pinning effect becomes stronger with increasing fluence of implanted iron atoms. © *2002 American Institute of Physics.* [DOI: 10.1063/1.1477357]

INTRODUCTION

Finding ways of increasing the critical current density in high-T_c superconductors (HTSCs) is becoming one of the most topical problems in the physics of high-temperature superconductivity in connection with the practical application of these materials. It is known that the critical current density can be increased by creating regions of suppressed superconducting order parameter (pinning centers) in the bulk of the superconducting material. Regions of this kind arise at the sites of structural defects or in places where the chemical composition of the host material is locally disrupted. The standard way of creating such defects is to irradiate the HTSC materials by a flux of high-energy particles: ions, neutrons, or protons (see, e.g., Ref. 1). Such irradiation gives rise not only to ''point'' defects randomly distributed in the HTSC but also to columnar defects, which are linear regions of amorphized material along the particle trajectories (tracks). An interaction of flux lines (fluxons) with these linear formations arises because of the deformation of the vortex current when a vortex approaches a defect.[2–4]

Thus the main focus of attention has been on research on the influence of the geometric parameters of the defects on the pinning efficiency. At the same time, the electronic and magnetic states of the defects can no doubt play an important role in the pinning of magnetic flux lines in superconducting materials. From this standpoint it is of interest to create defects having a magnetic moment and to study their interaction with vortices in a superconductor.

At the present time there is particular interest in studying how the pinning of flux lines can be influenced by surface magnetic formations produced in a controlled manner. For example, in Ref. 5 a reinforcement of the pinning was observed in a thin film of superconducting niobium deposited on submicron magnetic formations which had been prepared by electron lithography. The fabrication of such films is a rather complicated technical problem, particularly in the case of multicomponent HTSC materials. At the same time, magnetic particles can be created in a surface layer by implantation of magnetic ions. In the present study we investigate how the presence of surface magnetic formations obtained by the implantation of iron ions will influence the pinning of the flux lines in HTSC materials: $Bi_2Sr_2CaCu_2O_8$ single crystals and $YBa_2Cu_3O_7$ films.

Two methods were used to create the pinning centers. In the case of $Bi_2Sr_2CaCu_2O_8$ the magnetic pinning centers were created by implantation of low-energy iron ions directly into the bismuth superconductor. In the $YBa_2Cu_3O_7$ films the magnetic particles of iron were formed by ion implantation separately in a thin nonconducting film of the silicon oxide SiO_2. Then this film, with the magnetic particles formed in it, was laid on the superconducting film, and the measurements were made on the composite structure. As far as we know, this approach was used here for the first time. This original idea is attractive in that the superconductor is not subjected to the effects of ion bombardment, and the research process is substantially simplified.

EXPERIMENT

Single crystals of the bismuth HTSC $Bi_2Sr_2CaCu_2O_8$ with dimensions of $3\times2\times0.1$ mm were grown by the Bridgman–Stockbarger method.[6] Their superconducting transition temperature was 84 K. Iron ions with an energy of 40 keV were implanted to a fluence of 6.6×10^{16} ions/cm^2 on an ILU-3 accelerator. With the goal of creating magnetic particles of iron the samples were subjected to post-implantation annealing at a temperature of 600 °C.

The effect of stacking (composite structures) was studied with the use of a thin ($\sim$100 nm) film of the HTSC $YBa_2Cu_3O_7$ (YBCO) with a superconducting transition temperature of 88 K, prepared by magnetron sputtering on an Al_2O_3 substrate.

Magnetic particles were formed in the SiO_2 by the tech-

 © 2002 American Institute of Physics

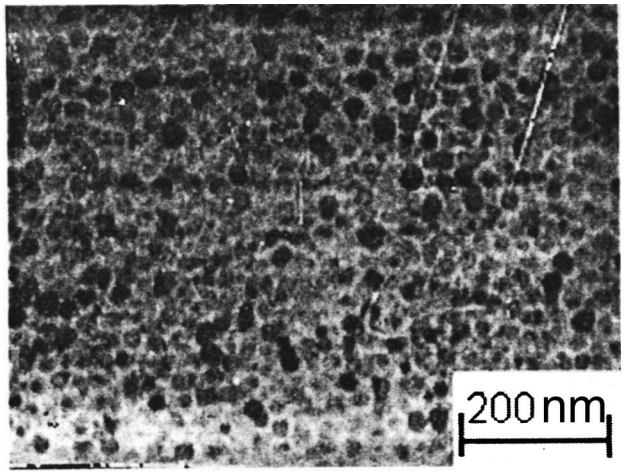

FIG. 1. Electron microscope image of a portion of a SiO_2/Si film implanted with Fe^+ ions to a fluence of 1.2×10^{17} ions/cm^2.

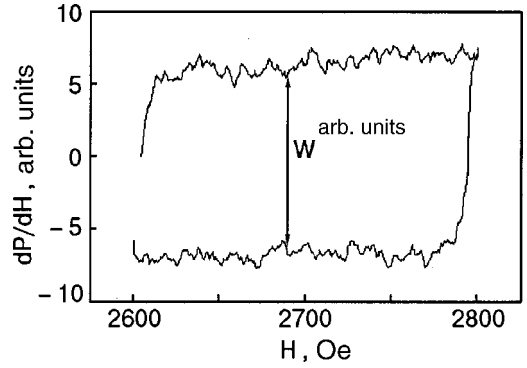

FIG. 2. Experimentally observed microwave absorption loops of an yttrium–barium film at a temperature of 25 K. P is the power of the microwave radiation absorbed by the sample.

nique described in Ref. 7. The authors of that paper showed that after a silicon oxide film was bombarded by iron atoms, ferromagnetic particles of iron, 5 to 60 nm in size, depending on the implantation fluence, had formed in the subsurface layer of the film. The magnetization of the particles was oriented parallel to the surface of the film. This was confirmed by ferromagnetic resonance measurements. The single-crystal silicon wafers used had a SiO_2 film 250 nm thick formed on the surface by oxidation in an atmosphere of dry oxygen. As in the case of the bismuth HTSC samples, the implantation of 40-keV Fe^+ ions to fluences of from 3×10^{16} to 3×10^{17} ions/cm^2 was done on an ILU-3 ion accelerator. This irradiation resulted in silicon oxide films containing magnetic particles with dimensions ranging from several nanometers to several tens of nanometers. Figure 1 shows an electron microscope image of a portion of a SiO_2/Si film containing Fe particles for an implantation fluence of 1.2×10^{17} ions/cm^2.

We have also made ferromagnetic resonance measurements on the Fe–SiO_2/Si samples for two orientations of the magnetic field, parallel and perpendicular to the plane of the sample. In the case of the parallel orientation the resonance was observed at field values of 1–2 kOe, depending on the implantation fluence, whereas for the perpendicular orientation the resonance field varied from 6 to 10 kOe for the same fluences of implanted ions. This behavior of the ferromagnetic resonance indicates that the particles created are in the form oblate ellipsoids lying in the plane of the film and that the particles are larger for higher implantation fluences.[7]

To estimate the pinning efficiency we used the method of magnetically modulated microwave absorption (MWA). In this method a superconductor is placed in a microwave cavity and a magnetic field is swept in the forward and reverse directions. In the presence of a modulation of the magnetic field one records a so-called microwave absorption loop, the width of which is determined by the expression (see, e.g., Ref. 8):

$$W=\sqrt{2\mu\omega\rho_n}\left(\frac{2\pi}{a}\right)^3\frac{\Phi_0}{\eta^2\omega^2}\left(\frac{B}{B_{c2}}\right)^{1/2}U_{p0}\frac{J_0}{J_c}K\left(\frac{J_0}{J_c}\right),$$

where U_{p0} is the pinning potential, J_0 is the current caused by the sweeping of the magnetic field, J_c is the critical current, η is the viscosity of a fluxon, ω is the frequency of the microwave field, Φ_0 is the magnetic flux quantum, and a is the distance between pinning centers.

Thus by making relative measurements of the width of the hysteresis loop before and after the magnetic particles are created on the surface of the superconductor, one can assess the participation of these particles in the pinning of the flux lines. MWA measurements were made on a Bruker BER 418s EPR spectrometer at a frequency of 9.2 GHz in a magnetic field of 2600 Oe directed perpendicular to the plane of the sample. The modulation frequency was 100 kHz. The sweeping of the field was done in an interval of 200 Oe at a rate of change of the field equal to 3.3 Oe/s. Low temperatures were achieved with a helium cryostat. The experimentally observed MWA hysteresis loop is shown in Fig. 2.

RESULTS AND DISCUSSION

Figure 3 shows the temperature dependence of the width W of the hysteresis loop for a bismuth HTSC sample in which iron ions had been implanted. One can see from the figure that the width of the MWA hysteresis loop for the $Bi_2Sr_2CaCu_2O_8$ superconducting single crystals increases after the implantation of iron ions and a subsequent annealing. This indicates that the pinning potential has increased, since all of the experimental parameters were the same in the measurements of the initial and treated samples. Estimates of the distribution of the implanted ions and their embedding depth (TRIM code, version SRIM 98.01) showed that the concentration of implanted ions is maximum at a depth of 20–40 nm, i.e., it actually does lie in a subsurface layer of the sample.

Figure 4 shows the temperature dependence of the width of the MWA hysteresis loop of an initial YBCO superconducting film and a YBCO film to which different films containing magnetic particles were applied. We see that the MWA hysteresis loop is wider for composite structures consisting of the superconductor and a nonconducting film laid on it. This indicates that there is an efficient interaction between the ensemble of magnetic particles and the magnetic

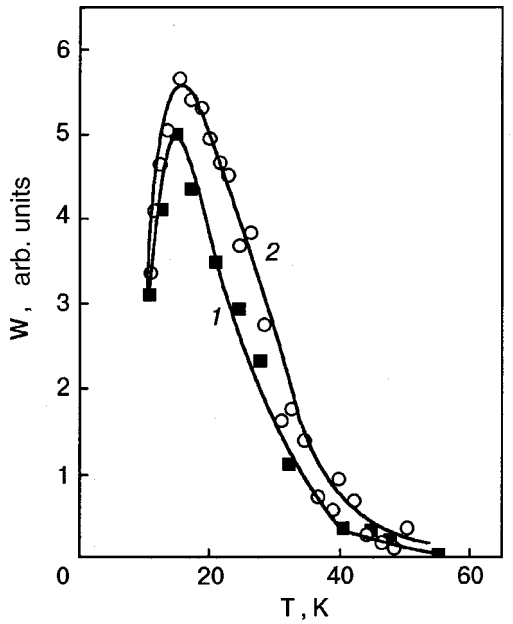

FIG. 3. Temperature dependence of the width of the microwave absorption hysteresis loop of the initial $Bi_2Sr_2CaCu_2O_8$ sample (*1*) and of a $Bi_2Sr_2CaCu_2O_8$ sample implanted with iron ions (*2*). The experimental error corresponds to the size of the symbols.

flux lines in the superconductor. The width of the hysteresis loop increases with increasing irradiation fluence.

The pinning mechanism in such a system can be understood in the framework of the following model. Magnetic particles of iron forming in the SiO_2 film have dimensions lying in a range from a few nanometers to several tens of nanometers. These ferromagnetic formations can be regarded as elementary magnetic dipoles. The magnetic field lines of these elementary magnetic dipoles can penetrate into the superconductor, since their magnetization is greater than the value of the first critical field. As a result, an effective interaction will arise between the vortices in the superconductor and the magnetic field lines of the microparticles, which are fixed to the magnetic particle. We note that at the present time, theoretical papers describing the pinning mechanism in such composite structures have only begun to appear; we can cite Ref. 9 as an example.

In addition to films containing magnetic particles obtained by ion implantation, composite structures formed by laying ''continuous'' magnetic films on a superconductor, e.g., iron garnet films and films cut from a magnetic floppy disk have also been studied (these data are also shown in Fig. 4). It turns out that in such composite structures one observes a substantial decrease of the width of the hysteresis loop; it becomes even smaller than in the superconductor itself. This indicates the importance of the sizes of the particles and the distance between them for efficient pinning in such a system.

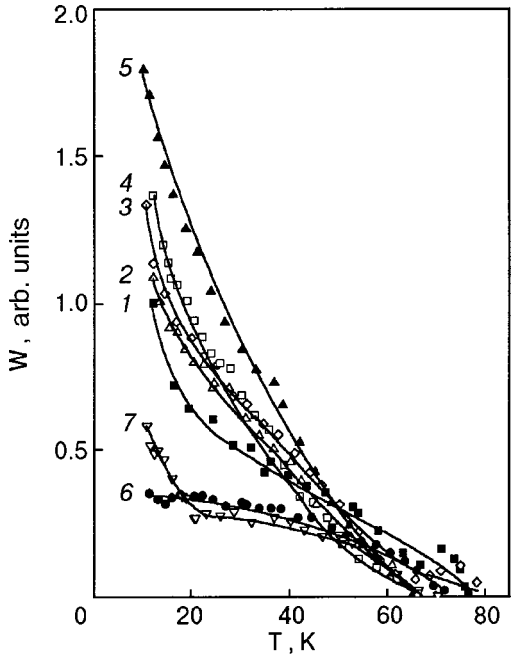

FIG. 4. Temperature dependence of the width of the microwave absorption hysteresis loop of an initial $YBa_2Cu_3O_7$ (YBCO) sample (*1*) and of $YBa_2Cu_3O_7$ samples with applied-on films in which magnetic particles have been formed: YBCO+(Fe−SiO_2), for irradiation doses D [ions/cm^2]: 3×10^{16} (*2*), 1.2×10^{17} (*3*), 1.8×10^{17} (*4*), 3×10^{17} (*5*); YBCO+iron garnet (*6*); YBCO+piece of magnetic floppy disk (*7*). The experimental error corresponds to the size of the symbols.

CONCLUSION

In summary, in this study we have investigated samples of $Bi_2Sr_2CaCu_2O_8$ superconducting crystals containing a subsurface layer of magnetic particles of iron. Our measurements showed that the pinning potential is higher in such a system. We observed reinforcement of the pinning in a HTSC thin film of YBCO when a thin nonconducting silicon oxide film containing magnetic microparticles of iron formed by ion implantation was applied to its surface. We observed an increase in the pinning potential with increasing fluence of iron implanted in the silicon oxide. We found that ''continuous'' magnetic films, in contrast, suppress the pinning in this sort of composite system. This indicates that the sizes of the magnetic particles and the distances between them have an effect on the pinning mechanism. The results obtained open up new possibilities for studying the properties of pinning by surface magnetic formations by the technique of applying to the surface of the superconductor a nonconducting film in which an ensemble of magnetic microparticles has been formed.

This study was performed as part of Projects Nos. 99-02-18064 and 00-15-96615 of the Russian foundation for Basic Research. The single-crystal samples of $Bi_2Sr_2CaCu_2O_8$ were prepared at the Institute of Experimental Physics IV of the Ruhr University (Bochum, Germany) in connection with a study of the pinning effect in hydrogen-doped HTSC materials. The authors thank Prof. K. Westerholt for the samples and for discussions that stimulated this study.

*E-mail: bazarov@dionis.kfti.kcn.ru

[1] L. M. Paulius, R. E. Shamu, S. Ferguson, M. C. de Anrade, and M. B. Maple, Appl. Phys. Lett. **71**, 3415 (1997).
[2] G. S. Mkrtchyan and V. V. Schmidt, Éksp. Teor. Fiz. **61**, 362 (1971) [Sov. Phys. JETP **34**, 195 (1971)].
[3] M. L. Kulic, A. Kramer, and K. D. Schotte, Solid State Commun. **2**, 541 (1992).
[4] A. Buzdin and M. Daumens, Physica C **294**, 257 (1998).
[5] J. I. Martin, M. Veléz, J. Nogués, and Ivan K. Shuller, Phys. Rev. Lett. **79**, 1929 (1997).
[6] B. vom Hedt, W. Lisseck, K. Westerholt, and H. Bach, Phys. Rev. B **49**, 9898 (1994).
[7] A. Bukharaev, A. V. Kazakov, R. A. Manapov, and I. B. Khaĭbullin, Fiz. Tverd. Tela (Leningrad) **33**, 1018 (1991) [Phys. Solid State **33**, 578 (1991)].
[8] C. Kessler, B. Nebendahl, D.-N. Peligrad, M. Mehring, A. Dulcic, and H.-U. Habermeier, Appl. Magn. Reson. **8**, 147 (1995).
[9] R. Šášik and T. Hwa, cond-mat/0003462 (2000).

Translated by Steve Torstveit

Anisotropy of the critical current and the guided motion of vortices in a stochastic model of bianisotropic pinning. I. Theoretical model

V. A. Shklovskij*

Institute of Theoretical Physics, National Research Center "Kharkov Physicotechnical Institute", ul. Akademicheskaya 1, 61108 Kharkov, Ukraine; V. N. Karazin Kharkov National University, pl. Svobody 4, 61077 Kharkov, Ukraine

A. A. Soroka

Institute of Theoretical Physics, National Research Center "Kharkov Physicotechnical Institute", ul. Akademicheskaya 1, 61108 Kharkov, Ukraine

(Submitted November 30, 2001; revised December 21, 2001)
Fiz. Nizk. Temp. **28**, 365–373 (April 2002)

A planar stochastic model of bianisotropic pinning created by two different mutually orthogonal systems of periodic ''washboard'' potentials is examined. Possible implementations of this model, both naturally occurring and artificially created, are proposed. Unlike the stochastic model of uniaxial anisotropic pinning by a system of parallel planes, where the critical current density j_c is actually equal to zero for all directions because the motion of vortices along the planes is unpinned, in the proposed model an anisotropic critical current exists for all directions. Theoretical formulas for calculating the anisotropic current-and temperature-related depinning of vortices are interpreted in terms of two basic nonlinear temperature-dependent resistive XY responses, having the physical meaning of the probabilities of a vortex overcoming the XY components of the pinning potential. © *2002 American Institute of Physics.* [DOI: 10.1063/1.1477358]

1. INTRODUCTION

An important research topic in the physics of superconductors in the mixed state, from both the applied and theoretical standpoints, involves investigating the anisotropy of their resistive properties due to anisotropy of the pinning.[1–18] The simplest example of this is uniaxial pinning anisotropy, which in layered anisotropic high-T_c superconductors (HTSCs) arises either as a consequence of their layered structure in the form of intrinsic pinning or as a result of the presence of a system of unidirectional (parallel) planar defects (primarily twins) in the sample. Thus the growth of HTSC crystals based on Y, La, and Nd is accompanied by the formation of twins oriented with their plane parallel to the c axis. The physical cause of the pinning at twins in HTSCs is the reliably established fact[19] that the order parameter is slightly suppressed at a twin. Because of this, the boundary of an isolated twin attracts vortices and pins them. Since the pinning force produced by a twin is directed perpendicular to its plane, the vortices will move preferentially in this plane if the driving force (the Lorentz force in the case of a transport current) has a nonzero component in the direction of the twin. This ''guided'' motion of the vortices (which is known as the guiding or **G** effect[1–3,14–16]) gives rise to an even (with respect to inversion $\mathbf{H}\rightarrow-\mathbf{H}$, where $\mathbf{H}$ is the external magnetic field) contribution to the transverse (to the current) magnetoresistivity $\rho_{\perp}^{+}$. In Ref. 16 for a geometry in which $\mathbf{H}\|\mathbf{c}$ while the transport current density $\mathbf{j}$ flows along the crystalline layers, rather simple formulas were obtained for the longitudinal and transverse magnetoresistivities $\rho_{\|,\perp}(j,\tau,\alpha,\varepsilon)$ as functions of j, the temperature τ, the angle α between the direction of the current and the twins, and the relative fraction ε of the volume occupied by twins.

From a mathematical standpoint the problem solved in Ref. 16 reduces to the Fokker–Planck equation for the one-dimensional dynamics of a vortex,[14,20,21] since pinning is absent for motion of the vortices in the direction parallel to the planes of the twins. Consequently, a critical current density j_c exists only for the direction strictly perpendicular to the planes of the twins ($\alpha=0$); $j_c(\alpha)=0$ for any other direction ($0<\alpha\leqslant\pi/2$). From a physical standpoint this is typical for the response of a vortex liquid.[16,22] Nevertheless, measurements of the resistive response for a solid vortex phase always show[7,8] that $j_c(\alpha)>0$ for any angles α (although $j_c(\alpha)$ may be anisotropic). Thus, although the model with a single system of unidirectional twins does have some merit, it cannot take into account the anisotropy of j_c in a solid vortex phase.[7,8]

In the present paper we propose the simplest model in which anisotropy of j_c is realized for any angles α in the presence of a planar pinning potential—a bianisotropic pinning model with a composite potential formed by a superposition of two periodic planar pinning potentials acting in mutually perpendicular directions. The model can be implemented experimentally both in naturally occurring and in artificially created pinning structures. For example, parallel nanocracks perpendicular to the planes of unidirectional twins were recently observed in $YBa_2Cu_3O_{7-\delta}$ films oriented along the **c** axis on $NdGaO_3$ substrates.[10] An artificial bianisotropic pinning structure in the form of a network of narrow magnetic stripes (rather than a regular lattice of magnetic dots) can be created by the method used in Refs. 23 and 24. In addition, it is possible to create different bianisotropic pinning structures in which the naturally grown structure of parallel planar defects is combined with artificially created pinning structures with planar pinning potentials perpendicular to them. For example, in a twin-free YBCO film[25] ori-

 © 2002 American Institute of Physics

ented along the **a** axis, covered with a magnetic tape on which a periodic signal had been recorded,[26] one can study the bianisotropic competition between the intrinsic pinning by the layered structure of YBCO and an artificially programmable magnetic pinning.

Thus, possible experimental implementations of anisotropic pinning include pre-existing systems of unidirectional planar pinning centers or two such mutually orthogonal systems of unidirectional planar pinning centers—bianisotropic pinning. The first of these cases has been studied intensively both experimentally[1–8] and theoretically,[11–17] while the bianisotropic case has as yet been little studied experimentally[9,10] and not at all theoretically.

This paper is devoted to a study of the resistive properties of a superconductor in the mixed state in the presence of bianisotropic pinning in neglect of the Hall effect and the anisotropy of the electronic viscosity. The resistive response of the system is obtained in the approximation of noninteracting vortices in the framework of a two-dimensional stochastic model of bianisotropic pinning on the basis of the Fokker–Planck equations. The two-dimensional bianisotropic pinning potential, modeling two mutually orthogonal systems of unidirectional planar defects, is assumed additive and periodic in the directions of anisotropy. For such a potential of general form we obtain formulas for the main resistive characteristics of the system—the longitudinal and transverse (to the current) magnetoresistivities as functions of the current density, temperature, and the angle α specifying the direction of the current density vector with respect to the anisotropy axes (see Fig. 1). Thanks to the neglect of the Hall effect the expressions for the magnetoresistivities are even with respect to inversion of the magnetic field direction.

The most important features of the problem are the nonlinear behavior of the observed magnetoresistivities as functions of the transport current density and temperature and the anisotropy of the critical current due to the anisotropy of the

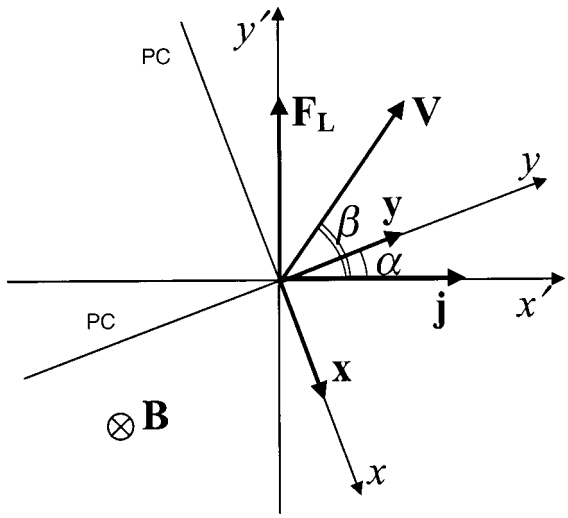

FIG. 1. Coordinate system xy tied to two mutually orthogonal systems of pinning centers PC (their positions are specified by anisotropy vectors **x** and **y**, which are perpendicular to their planes), and the coordinate system $x'y'$ tied to the current direction (the current density vector is directed along the $0x'$ axis); α is the angle between the vectors **y** and **j**, β is the angle between the velocity vector **v** of the vortices and the vector **j**; **B** is the magnetic field vector, and $\mathbf{F}_L$ is the Lorentz force.

pinning. This gives rise, in a certain parameter region, to guided motion of the vortices, an effect nonlinear in both current and temperature wherein the vortex system has a tendency to move along the planes of the pinning centers under the influence of pinning forces perpendicular to these planes. The main nonlinear component of the problem is the probability function ν for a vortex to overcome the potential barrier of a planar pinning center. The behavior of ν as a function of the external force or temperature reflects the nonlinear transition between the thermally activated flux flow (TAFF) and the free flux flow (FF) regimes for the motion of vortices with respect to the corresponding system of planar pinning centers. For the system as a whole, depending on the values of the parameters, there can be a regime of guided motion of vortices along the planes of the pinning centers of one of the mutually orthogonal systems, a regime of weak pinning of vortices at pinning centers (these two types of regimes correspond to a resistive response linear in the current) and various intermediate regimes corresponding to a nonlinear transition (with respect to current) in the resistive response of the system. The use of a concrete form of the bianisotropic pinning potential allows one to reduce the problem to final analytical formulas and to analyze both quantitatively and qualitatively all of the effects of interest to us as functions of the dimensionless parameters of the problem.

The topical problem that is considered theoretically for the first time has to do with the study of the polar diagrams of the total magnetoresistivity $\rho(\alpha)$. The motivation for framing the problem in this way comes from the possibility of measuring the anisotropic resistive response using a so-called ''rotating current'' experimental scheme, which was recently implemented in Refs. 7 and 8 in a study of the vortex dynamics in $YBa_2Cu_3O_{7-\delta}$ crystals containing a system of unidirectional twins. In this paper we present a theoretical analysis of the polar diagrams of the magnetoresistivity $\rho(\alpha)$ in the general nonlinear case. The characteristic form of the current dependence and temperature dependence of $\rho(\alpha)$ due to the evolution of the vortex dynamics with changing angle α can be analyzed qualitatively and quantitatively with the aid of the diagram of the dynamic states of the vortex system on the (j_x, j_y) plane, which gives a clear connection between the anisotropy of the critical current and the guided motion of the vortices along pinning planes.

Thus in the framework of the stochastic model of bianisotropic pinning considered here, one can study the anisotropy of the critical currents of the system and the nonlinear G effect and to establish directly the interrelationship of these aspects of the vortex dynamics and the resistive properties of the system. We also note that the stochastic model of bianisotropic pinning used here is a generalization of the model of uniaxial anisotropic pinning used previously,[16] since in the latter the only one system of unidirectional planar pinning centers was considered as a source of pinning; this situation corresponds to having one of the components of the general bianisotropic form of the pinning potential equal to zero. Here we set forth a theoretical model for the stated problem. In Sec. 2 we set forth a two-dimensional stochastic model of bianisotropic pinning based on the Fokker–Planck equations and obtain expressions for the av-

erage velocity of the vortex system in the framework of this model. In Sec. 3 we obtain formulas in general form for the nonlinear conductivity and resistivity tensors and the main observable characteristics of the system—the longitudinal and transverse (to the current) magnetoresistivities. In Sec. 4 the general form of the bianisotropic pinning potential is particularized to some possible experimental implementations, exact particular expressions for the probability functions ν_x and ν_y are discussed, and the critical currents and saturation currents are introduced for the entire region of angles α, including, in particular, the principal (basis) critical currents and saturation currents along the directions of anisotropy of the pinning in the system.

2. FOKKER–PLANCK METHOD IN THE MODEL OF BIANISOTROPIC PINNING

We consider the problem of the dynamics of vortices in a two-dimensional superconducting sample (film, thin layer) in the presence of bianisotropic pinning. By ''bianisotropic'' we mean pinning created by two orthogonal systems of planar, unidirectional, equally spaced pinning centers, in general with different concentrations of pinning centers and forms of pinning potentials in these systems. The preferred (basis) directions along which the pinning forces are exerted by the corresponding systems of pinning centers are characterized by pinning anisotropy vectors **x** and **y** (see Fig. 1). The two-dimensional pinning potential of such a system of planar defects is assumed additive and periodic in the anisotropy directions, i.e.,

$$U_p(x,y)=U_{pa}(x)+U_{pb}(y), \tag{1}$$

where $U_{pa}(x)=U_{pa}(x+a)$ and $U_{pb}(y)=U_{pb}(y+b)$; a and b are constant periods.

The resistive properties of the superconductor are considered in neglect of the Hall effect. With such an assumption the problem simplifies substantially and it becomes possible to directly assess the role of the guided motion effects for vortices in the presence of bianisotropic pinning in the general nonlinear case.

The Langevin equation for a vortex moving with velocity **v** in a magnetic field $\mathbf{B}=\mathbf{n}B$ (where $B\equiv|\mathbf{B}|$, $\mathbf{n}=n\mathbf{z}$, $\mathbf{z}$ is a unit vector along the z axis, and $n=\pm 1$) has the form[14–18]

$$\eta\mathbf{v}=\mathbf{F}_L+\mathbf{F}_p+\mathbf{F}_{\rm th}, \tag{2}$$

where $\mathbf{F}_{\rm L}=n(\Phi_0/c)\mathbf{j}\times\mathbf{z}$ is the Lorentz force (Φ_0 is the magnetic flux quantum, c is the speed of light, and $\mathbf{j}$ is the current density); $\mathbf{F}_p=-\nabla U_p$ is the pinning force (U_p is the pinning potential); $\mathbf{F}_{\rm th}$ is the force of thermal fluctuations, and η is the electronic viscosity constant. The fluctuational force $\mathbf{F}_{\rm th}(t)$ is Gaussian white noise, the stochastic properties of which are given by the relations

$$\langle F_{{\rm th},i}(t)\rangle=0, \quad \langle F_{{\rm th},i}(t)F_{{\rm th},j}(t')\rangle=2\tilde{T}\eta\delta_{ij}\delta(t-t'), \tag{3}$$

where $\tilde{T}$ is the temperature in energy units. Using relation (3), we can reduce Eq. (2) to a system of Fokker–Planck equations:

$$\eta\mathbf{S}=(\mathbf{F}_L+\mathbf{F}_p)P-\tilde{T}\nabla P, \tag{4}$$

$$\frac{\partial P}{\partial t}=-\nabla\mathbf{S}, \tag{5}$$

where $P(\mathbf{r},t)$ is the probability density for a vortex to be located at the point $\mathbf{r}=(x,y)$ at time t, and $\mathbf{S}(\mathbf{r},t)\equiv P(\mathbf{r},t)\mathbf{v}(\mathbf{r},t)$ is the flux density of the vortex probability. By definition the average velocity of the vortices is

$$\langle\mathbf{v}\rangle=\frac{\int\int\mathbf{S}d^2\mathbf{r}}{\int\int Pd^2\mathbf{r}}. \tag{6}$$

In the steady-state case, Eq. (4) for the functions $P=P(x,y)$ and $\mathbf{S}=(S_x(x,y),S_y(x,y))$ reduces to the equations

$$\begin{cases}\eta S_x=F_xP-\tilde{T}(\partial P/\partial x)\\ \eta S_y=F_yP-\tilde{T}(\partial P/\partial y)\end{cases}, \tag{7}$$

where $F_x=F_{Lx}-dU_{pa}/dx$ and $F_y=F_{Ly}-dU_{pb}/dy$. The condition of stationarity for Eq. (5) leads to the equation

$$\partial S_x/\partial x+\partial S_y/\partial y=0. \tag{8}$$

In view of the additivity of the pinning potential the probability density function for the location of vortices can be written in the factorized form $P(x,y)=P_a(x)P_b(y)$. Introducing the notation

$$\begin{cases}a_x\equiv F_xP_a-\tilde{T}(dP_a/dx)\\ b_y\equiv F_yP_b-\tilde{T}(\partial P_b/dy)\end{cases} \tag{9}$$

and using formulas (7) and (8), we obtain the equation $P_b da_x/dx=-P_a db_y/dy$. Its integration with respect to x and y with allowance for the positivity of the functions a_x and b_y gives $a_x=a_0=\text{const}$, $b_y=b_0=\text{const}$. Then from Eq. (9) we find the functions $P_a(x)$ and $P_b(y)$; their integrals (which give the quantities a_0 and b_0) in the corresponding periods of the potential have the values

$$\int_0^a P_a(x)dx=aa_0/\tilde{\nu}_x(F_{Lx}),$$

$$\int_0^b P_b(y)dy=bb_0/\tilde{\upsilon}_y(F_{Ly}), \tag{10}$$

where

$$1/\tilde{\nu}_i(F)\equiv 1/(F\nu_i(F))=\{l\tilde{T}[1-\exp(-Fl/\tilde{T})]\}^{-1}\times\int_0^l dx\exp(-Fx/\tilde{T})\times\int_0^l dx'\exp\{[U_{pl}(x+x')-U_{pl}(x')]/\tilde{T}\}. \tag{11}$$

Here $i=x,y$, $l=a,b$, and the function $\nu_i(T)$ has the physical meaning of the probability of vortices overcoming the potential barriers of the pinning centers in the x and y directions under the influence of an effective force F (see Ref. 16 for more detail). As a result, using formulas (10) and (11) we obtain, according to formula (6), the following expressions for the components of the average velocity of a vortex:

$$\langle\upsilon_x\rangle=\tilde{\nu}_x(F_{Lx})/\eta, \quad \langle\upsilon_y\rangle=\tilde{\nu}_y(F_{Ly})/\eta. \tag{12}$$

3. NONLINEAR CONDUCTIVITY AND RESISTIVITY TENSORS AND THE OBSERVABLE RESISTIVE CHARACTERISTICS—THE LONGITUDINAL AND TRANSVERSE MAGNETORESISTIVITIES $\rho_{\parallel}$ AND $\rho_{\perp}$

The average electric field induced by the moving vortex system is given by

$$\mathbf{E}=(1/c)\mathbf{B}\times\langle\mathbf{v}\rangle=n(B/c)(-\langle v_y\rangle\mathbf{x}+\langle v_x\rangle y). \tag{13}$$

From formulas (12) and (13) we find the magnetoresistivity tensor $\hat{\rho}$ (having components measured in units of the flux-flow resistivity $\rho_f\equiv(\Phi_0 B/\eta c^2)$) for the nonlinear Ohm's law $\mathbf{E}=\hat{p}(\boldsymbol{j})\boldsymbol{j}$:

$$\hat{\rho}=\begin{pmatrix}\rho_{xx} & \rho_{xy}\\ \rho_{yx} & \rho_{yy}\end{pmatrix}=\begin{pmatrix}\nu_y(F_{Ly}) & 0\\ 0 & \nu_x(F_{Lx})\end{pmatrix}, \tag{14}$$

where F_{Lx} and F_{Ly} are the external force components acting along the vectors **x** and **y**, respectively. As we see from Eq. (14), an obvious consequence of the neglect of the Hall effect is the vanishing of the off-diagonal components of the tensor $\hat{\rho}$. The diagonal components of the tensor $\hat{\rho}$ are functions of the current density j, temperature $\tilde{T}$, and angle α.

The conductivity tensor $\hat{\sigma}$ (the components of which are measured in units of $1/\rho_f$), which is the inverse of the tensor $\hat{\rho}$, has the form

$$\hat{\sigma}=\begin{pmatrix}\sigma_{xx} & \sigma_{xy}\\ \sigma_{yx} & \sigma_{yy}\end{pmatrix}=\begin{pmatrix}\nu_y(F_{Ly})^{-1} & 0\\ 0 & \nu_x(F_{Lx})^{-1}\end{pmatrix}. \tag{15}$$

The experimentally measurable values refer to a coordinate system tied to the current (see Fig. 1). The longitudinal and transverse (with respect to the direction of the current) components of the electric field, $E_{\parallel}$ and $E_{\perp}$, are related to E_x and E_y by the simple expressions

$$\begin{cases}E_{\parallel}=E_x\sin\alpha+E_y\cos\alpha,\\ E_{\perp}=-E_x\cos\alpha+E_y\sin\alpha\end{cases}. \tag{16}$$

Consequently, according to (16), the expressions for the experimentally observable longitudinal and transverse (with respect to the current) components of the magnetoresistivity, $\rho_{\parallel}=E_{\parallel}/j$ and $\rho_{\perp}=E_{\perp}/j$, have the form:

$$\begin{cases}\rho_{\parallel}=\rho_{xx}\sin^2\alpha+\rho_{yy}\cos^2\alpha,\\ \rho_{\perp}=(\rho_{yy}-\rho_{xx})\sin\alpha\cos\alpha\end{cases}. \tag{17}$$

Formulas (17) are written formally in a manner analogous to the linear case,[11] but with the important difference that in the nonlinear case both of the diagonal components of the resistivity tensor, which are in general different, depend not only on the the current density and temperature but also on the angle α (and also, as will be seen below, on the respective concentrations of pinning centers): $\rho_{xx}=\nu_y(F_{Ly},\tilde{T})$, $\rho_{yy}=\nu_x(F_{Lx},\tilde{T})$.

The dimensionless functions $\nu_x(F_{Lx},\tilde{T})$ and $\nu_y(F_{Ly}\tilde{T})$ in the cases $F_{Lx}\to 0$, $F_{Ly}\to 0$ are the same as the analogous quantities introduced in Ref. 14, and one of them, viz., $\nu_x(F_{Lx},\tilde{T})$, in view of the asymmetry of the problem of vortex dynamics in the presence of a uniaxial anisotropic pinning, was originally used in Ref. 16 for describing the dynamics of the vortices over the entire interval of the corresponding external force component perpendicular to the pinning center (and, hence, in the entire interval of current densities). They have the physical meaning of the probability of a vortex overcoming the potential barriers U_{0x} and U_{0y} (their characteristic value is denoted U_0 and the indices x and y will be dropped, since the analysis will pertain equally to the functions ν_x and ν_y). This can be seen by considering the limiting cases of high ($\tilde{T}\gg U_0$) and low ($\tilde{T}\ll U_0$) temperatures. In the case of high temperatures one has $\nu\approx 1$, and expressions (11) correspond to the regime of free flux flow (the FF regime). Indeed, in this case the effect of pinning can be neglected. In the case of low temperatures, ν is a function of the current density. At high currents ($Fa\gg U_0$) the potential barrier vanishes, $\nu\approx 1$, and the FF regime is again realized. In low currents ($Fa\ll U_0$) one has $\nu\propto\exp(-U_0/\tilde{T})$, which corresponds to the TAFF regime.[19] The transition from the TAFF to the FF regime is due to a lowering of the potential barrier with increasing current. In Ref. 16 it is shown that for a periodic potential having the property of evenness ($U_p(-x)=U_p(x)$), the function $\nu(F)$ is even with respect to F, i.e., $\nu(-F)=\nu(F)$.

We know that it is generally necessary to separate the magnetoresistivity components which are even and odd in the magnetic field. Clearly, as a consequence of our having neglected the Hall effect the components which are odd with respect to the magnetic field, $\rho_{\parallel}^{-}$ and $\rho_{\perp}^{-}$, are identically equal to zero. The magnetoresistivity components which are even with respect to the magnetic field and longitudinal ($\rho_{\parallel}^{+}$) and transverse ($\rho_{\perp}^{+}$) with respect to the current are directly measurable quantities. From formulas (14) and (17) we obtain for them the following expressions:

$$\begin{cases}\rho_{\parallel}^{+}\equiv\rho_{\parallel}=\nu_y(F_{Ly})\sin^2\alpha+\nu_x(F_{Lx})\cos^2\alpha\\ \rho_{\perp}^{+}\equiv\rho_{\perp}=[\nu_x(F_{Lx})-\nu_y(F_{Ly})]\sin\alpha\cos\alpha\end{cases}. \tag{18}$$

We introduce the X and Y geometries, in which $\mathbf{j}\|\mathbf{x}(\alpha=\pi/2)$ and $\mathbf{j}\|\mathbf{y}(\alpha=0)$. In both cases only longitudinal magnetoresistivities exist, $\rho_{\parallel}^{x}(j,\tilde{T})=\rho_{xx}=\nu_y(j,\tilde{T})$, $\rho_{\parallel}^{y}(j,\tilde{T})=\rho_{yy}=\nu_x(j,\tilde{T})$, while $\rho_{\perp}^{x}=\rho_{\perp}^{y}\equiv 0$. Thus, measurements of the longitudinal magnetoresistivities in the XY geometries, corresponding to the diagonal components of the magnetoresistivity tensor, will yield the current dependence and temperature dependence of the functions $\nu_{x,y}$, which are the main nonlinear components of the problem. Knowledge of the dependences $\rho_{\parallel}^{x,y}(j,\tilde{T})$ is sufficient for obtaining the resistivities $\rho_{\parallel,\perp}(j,\tilde{T})$ at arbitrary angles α, since the functions $\nu_{x,y}$ appearing in formula (18) can be written as $\nu_x(j_y,\tilde{T})=\rho_{\parallel}^{y}(j_y,\tilde{T})$ and $\nu_y(j_x,\tilde{T})=\rho_{\parallel}^{x}(j_x,\tilde{T})$.

We note that the probability functions ν_x and ν_y are inversely proportional to the effective nonlinear pinning viscosities introduced in Ref. 12, where a phenomenological approach was developed. In regions of nonlinearity of the functions ν_x and ν_y with respect to current and temperature (or, in other words, in regions of nonlinearity of the pinning viscosities) a pronounced nonlinearity can appear in the current dependence and temperature dependence of the magnetoresistivities (18), and, on account of the anisotropy of the pinning viscosity, a nonlinear G effect with respect to both current and temperature can appear in the dynamics of the vortex system. In the nonlinear case the functions $\nu_{x,y}$ correspond to a smoothed steplike resistive transition (see be-

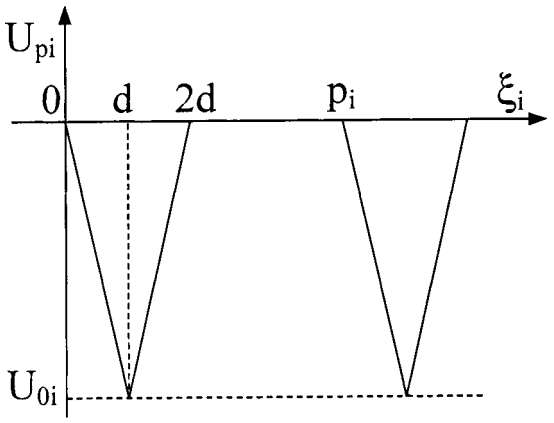

FIG. 2. Pinning potentials of two mutually orthogonal systems of pinning centers $U_{pi}(\xi_i)$, $i=x,y$, $\xi_i \leftrightarrow i$, U_{0i} are the depths of the potential wells of the pinning centers, p_i are the periods of the respective potentials, and $2d$ is the width of the potential wells of both potentials. The concentration of pinning centers of each system is specified by the parameter $\varepsilon_i = 2d/p_i$.

low), and the resistivities $\rho_{\parallel,\perp}(j,\tilde{T})$ are combinations of the corresponding functions. We see from formula (18) that the magnetoresistivity $\rho_\parallel$ is always positive, while the sign of $\rho_\perp$ can vary.

We also note that, in contrast to the anisotropic pinning with asymmetric xy dynamics,[16] in the case of bianisotropic pinning the x and y directions are symmetric in the sense that now they are, in principle, equivalent.

4. DISCUSSION OF THE MODEL AND ANALYSIS OF THE NONLINEAR BEHAVIOR OF THE PROBABILITIES $\nu_{x,y(j,\tau,\alpha,p,\varepsilon,K)}$ OF OVERCOMING PERIODIC PINNING POTENTIALS

The nonlinear properties of the magnetoresistivity tensor $\hat{\rho}$, as is seen from formula (14), are completely determined by the behavior of the functions $\nu_x(F_{Lx},\tilde{T})$ and $\nu_y(F_{Ly},\tilde{T})$, which, according to formulas (11), depend on the form of the pinning potential. We particularize this potential to HTSCs of the YBaCuO type, for which the experimental realizations of the anisotropic pinning centers might be twins, nanocracks, or gaps between planes of the layered superconductor.[1,10,18] For each of these cases the order parameter is depressed in the region of the pinning center, and, consequently, it is energetically favorable for the vortices to be localized in this region.

Our analysis of the resistive properties is done on the basis of pinning potentials of the following form (Fig. 2):

$$U_{pa}=\begin{cases} -F_{px}x, & 0\leqslant x\leqslant d \\ F_{px}(x-2d), & d\leqslant x\leqslant 2d, \\ 0, & 2d\leqslant x\leqslant a \end{cases}$$
$$U_{pb}=\begin{cases} -F_{py}y, & 0\leqslant y\leqslant d \\ F_{py}(y-2d), & d\leqslant y\leqslant 2d \\ 0, & 2d\leqslant y\leqslant b, \end{cases} \qquad (19)$$

where U_{0x} and U_{0y} are the depths of the potential wells of the pinning potentials, and $F_{px}=U_{0x}/d$, $F_{py}=U_{0y}/d$ are the pinning forces at the pinning centers along the directions of the vectors **x** and **y**, respectively. The regions of the pinning centers in potentials (19) correspond to wells of width $2d$, and the regions between pinning centers, to zero pinning potential. As parameters characterizing the concentration of pinning centers, we use the quantities $\varepsilon_x=2d/a$ and $\varepsilon_y=2d/b$ (more precisely, these are the fractions of the volume occupied by the pinning centers).

Substituting potentials (19) into formulas (11) for the probability functions ν_x and ν_y for a vortex to overcome the potential barriers of the pinning centers, we obtain the expression[16]

$$\nu(f,\tau,\varepsilon)=\frac{2f(f^2-1)^2}{2f(f^2-1)(f^2-1+\varepsilon)-\varepsilon\tau G}, \qquad (20)$$

where

$$G=[(3f^2+1)\cosh(f/(\tau\varepsilon))+(f^2-1)\cosh(f(1-2\varepsilon)/(\tau\varepsilon))-2f(f-1)\cosh(f(1-\varepsilon)/(\tau\varepsilon)-(1/\tau))-2f(f+1)\cosh(f(1-\varepsilon)/\tau\varepsilon)+(1/\tau)]/\sinh(f/(\tau\varepsilon)).$$

Here and below we have for the time being dropped the indices x and y from the physical quantities pertaining to the pinning potentials U_{pa} and U_{pb}, and formula (20) describes equally the pinning on both potentials (i.e., the indices are understood). Dimensionless quantities have been introduced for convenience of qualitative analysis of the formulas.

In formula (20) the effective external force F acting on a vortex in the direction perpendicular to the pinning center and causing the vortices to overcome the potential barriers of the pinning center (slipping) is characterized by the dimensionless parameter $f=Fd/U_0$, which specifies its ratio to the pinning force $F_p=U_0/d$, while the temperature is characterized by the dimensionless parameter $\tau=\tilde{T}/U_0$. The effect of the external force F acting on the vortices consists in a lowering of the potential barrier for vortices localized at pinning centers and, hence, an increase in their probability of escape from them. Increasing the temperature also leads to an increase in the probability of escape of the vortices from the pinning centers through an increase in the energy of thermal fluctuations of the vortices. Thus the pinning potential of a pinning center, which for $F,\tilde{T}\to 0$ leads to localization of the vortices, can be suppressed by both an external force and by temperature.

A quantitative and qualitative analysis of the behavior of $\nu(f,\tau,\varepsilon)$ as a function of all the parameters and its asymptotic behavior as a function of each are described in detail in Ref. 16. We will pay particular attention only to the typical curves of $\nu(f,\tau,\varepsilon)$ as a function of the parameters f and τ, which describe the nonlinear dynamics of the vortex system as a function of the external force acting on the vortices in the direction perpendicular to the pinning center and as a function of temperature (see Figs. 4 and 5 in Ref. 16). As we see from those figures, the form of the $\nu(f)$ and $\nu(\tau)$ curves is determined by the values of the fixed parameters τ and f. The monotonically increasing function $\nu(f)$ reflects the nonlinear transition of the vortex motion from the TAFF to the FF regime with increasing external force at low temperatures ($\tilde{T}\ll U_0$), while at high temperatures ($\tilde{T}\geqslant U_0$) the FF regime is realized in the entire range of variation of the

external force, at small forces because of the effect of thermal fluctuations on the vortices. The monotonically increasing function $\nu(\tau)$ reflects the nonlinear transition from a dynamical state corresponding to the value of the external force at zero temperature to the FF saturation regime. The character of the transition from the TAFF to the FF regime on the $\nu(f)$ and $\nu(\tau)$ curves is substantially different. With increasing τ the function $\nu(f)$ shifts leftward and becomes less steep (see Fig. 4 of Ref. 16). That is, the higher the temperature, the smoother the transition from the TAFF to the FF regime and the lower the values of the external force at which it occurs. With increasing f the $\nu(\tau)$ curve also shifts leftward, but it becomes steeper (see Fig. 5 of Ref. 16). Consequently, the greater the suppression of the potential barrier of the pinning center by the external force, the sharper the transition from the TAFF to the FF regime and the lower the temperatures at which it occurs. These graphs will be needed later on when we discuss the physical interpretation of the observed resistive and G-effect-related dependences. We also note that the dependence of the probability function $\nu(\varepsilon)$ on the concentration of pinning centers decreases monotonically from the value $\nu(0)\equiv 1$, which corresponds to the absence of pinning centers, and that it becomes steeper with decreasing fixed parameters f and τ, owing to the growth of the probability density for finding the vortices at the pinning centers with decreasing temperature and external force.

Let us now turn to the dimensionless parameters by which one can in the general case take into account the difference of the potentials U_{pa} and U_{pb}—specifically, the difference of their periods a, b and the potential well depths U_{x0}, U_{y0}. We introduce some new parameters: $\varepsilon=(\varepsilon_x\varepsilon_y)^{1/2}$ is the average concentration of pinning centers, $U_0=(U_{x0}U_{y0})^{1/2}$ is the average depth of the potential well, $k=(\varepsilon_y/\varepsilon_x)^{1/2}=(a/b)^{1/2}$, and $p=(U_{x0}/U_{y0})^{1/2}$, where the parameters k and p are measures of the corresponding anisotropies. The temperature will be characterized by a new parameter $\tau=\tilde{T}/U_0$, which specifies the ratio of the energy of thermal fluctuations of the vortices to the average potential well depth U_0. The current density will be measured in units of $j_c=cU_0/(\Phi_0 d)$. Then the dimensionless parameters f_x and f_y, which specify the ratio of the external forces perpendicular to the pinning centers, F_{Lx} and F_{Ly}, to the pinning forces $F_{px}=U_{0x}/d$ and $F_{py}=U_{0y}/d$ ($\nu_{x,y}$ are even functions of their respective arguments), have the form $f_x=F_{Lx}/F_{px}=p^{-1}j\cos\alpha$ and $f_y=F_{Ly}/F_{py}=-pj\sin\alpha$. The values of the external force $F=F_{px}$ and $F=F_{py}$ at which the heights of the potential barriers of potentials U_{pa} and U_{pb} vanish at $\tilde{T}=0$ correspond to the dimensionless critical currents $j_c^x(\alpha)=1/(p\sin\alpha)$ and $j_c^y(\alpha)=p/\cos\alpha$. In the general case of nonzero temperature the critical currents $j_c^x(\alpha)$ and $j^y(\alpha)$ correspond, at a specified angle α, to the change in the vortex dynamics from the TAFF regime to a nonlinear regime with respect to the systems of pinning centers with pinning anisotropy vectors **x** and **y**. The condition that determines the temperature region in which the concept of critical currents is physically meaningful is $0<\tilde{T}\ll U_0$ (for $\tilde{T}\geqslant U_0$ the transition from the TAFF to the nonlinear regime is smeared, and the concept of critical current loses physical meaning).

Let us also determine the principal critical currents (along the pinning anisotropy vectors **x** and **y**), which are given by $j_c^x\equiv j_c^x(\pi/2)=p^{-1}$, $j_c^y\equiv j_c^y(0)=p$ (for $\tilde{T}=0$). In analogy to the critical currents $j_c^x(\alpha)$ and $j_c^y(\alpha)$ we introduce the saturation currents $j_s^x(\alpha)$ and $j_s^y(\alpha)$ at which the nonlinear regimes of the vortex dynamics goes over to the FF regime at the respective systems of pinning centers ($j_s^x=j_s^x(\pi/2)$, $j_s^y=j_s^y(0)$ are the principal saturation currents along the pinning anisotropy vectors **x** and **y**, and $j_s^x(\alpha)=j_s^x/\sin\alpha$, $j_s^y(\alpha)=j_s^y/\cos\alpha$).

The main observable effects of the model investigated here are considered in Part II of this paper. A comprehensive study of the nonlinear G effect is made, and the observable magnetoresistivities $\rho_\parallel$ and $\rho_\perp$ are analyzed in the framework of this model. The polar diagrams $\rho(\alpha)$ of the total magnetoresistivity of the sample are investigated, and the main conclusions of the two Parts of the paper are stated.

*E-mail: Valerij.A.Shklovskij@univer.kharkov.ua

[1] S. Fleshler, W.-K. Kwok, U. Welp, V. M. Vinokur, M. K. Smith, J. Downey, and G. W. Grabtree, Phys. Rev. B **47**, 14448 (1993).
[2] A. A. Prodan, V. A. Shklovskij, V. V. Chabanenko, A. V. Bondarenko, M. A. Obolenskii, H. Szymczak, and S. Piechota, Physica C **302**, 271 (1998).
[3] V. V. Chabanenko, A. A. Prodan, V. A. Shklovskij, A. V. Bondarenko, M. A. Obolenskii, H. Szymczak, and S. Piechota, Physica C **314**, 133 (1999).
[4] H. Ghamlouch, M. Aubin, R. Gagnon, and N. Taillefer, Physica C **275**, 141 (1997).
[5] A. Casaca, G. Bonfait, C. Dubourdieu, F. Weiss, and J. P. Senateur, Phys. Rev. B **59**, 1538 (1999).
[6] C. Villard, G. Koren, D. Cohen, E. Polturak, B. Thrane, and D. Chateignief, Phys. Rev. Lett. **77**, 3913 (1996).
[7] H. Pastoriza, S. Candia, and G. Nieva, Phys. Rev. Lett. **83**, 1026 (1999).
[8] G. D'Anna, V. Berseth, L. Forro, A. Erb, and E. Walker, Phys. Rev. B **61**, 4215 (2000).
[9] J. Z. Wu and W. K. Chu, Phys. Rev. B **49**, 1381 (1994).
[10] G. Koren, E. Polturak, N. Levy, G. Deutscher, and N. D. Zakharov, Appl. Phys. Lett. **73**, 3763 (1998).
[11] É. B. Sonin and A. L. Kholkin, Fiz. Tverd. Tela (St. Petersburg) **34**, 1147 (1992) [Phys. Solid State **34**, 610 (1992)].
[12] V. A. Shklovskij, Fiz. Nizk. Temp. **23**, 1134 (1997) [Low Temp. Phys. **23**, 853 (1997)].
[13] V. A. Shklovskij, Fiz. Nizk. Temp. **25**, 153 (1999) [Low Temp. Phys. **25**, 109 (1999)].
[14] Y. Mawatari, Phys. Rev. B **56**, 3433 (1997).
[15] Y. Mawatari, Phys. Rev. B **59**, 12033 (1999).
[16] V. A. Shklovskiĭ, A. A. Soroka, and A. K. Soroka, Zh. Éksp. Teor. Fiz. **116**, 2103 (1999) [JETP **89**, 1138 (1999)].
[17] N. B. Kopnin and V. M. Vinokur, Phys. Rev. Lett. **83**, 4864 (1999).
[18] V. A. Shklovskij and A. A. Soroka, in *Proceedings of the 10th International Workshop on Critical Currents (IWCC-2001)*, June. 4–7, 2001, edited by C. Jooss, Göttingen, Germany (2001), p. 58.
[19] G. Blatter, M. V. Feigelman, V. B. Geshkenbein, A. I. Larkin, and V. M. Vinokur, Rev. Mod. Phys. **66**, 1125 (1994).
[20] O. V. Usatenko and V. A. Shklovskij, J. Phys. A **27**, 5043 (1994).
[21] B. Chen and J. Dong, Phys. Rev. B **44**, 10206 (1991).
[22] V. M. Vinokur, V. B. Geshkenbeĭn, A. I. Larkin, and M. Feĭgel'man, Zh. Éksp. Teor. Fiz. **100**, 1104 (1991) [JETP **73**, 610 (1991)].
[23] A. Hoffmann, P. Prieto, and Ivan K. Schuller, Phys. Rev. B **61**, 6958 (2000).
[24] M. J. Van Bael, K. Temst, V. V. Moshchalkov, and Y. Bruynseraede, Phys. Rev. B **59**, 14674 (1999).
[25] Z. Trajanovic, C. J. Lobb, M. Rajeswari, I. Takeuchi, C. Kwon, and T. Venkatesan, Phys. Rev. B **56**, 925 (1997).
[26] Y. Yuzhelevski and G. Jung, Physica C **314**, 163 (1999).

Translated by Steve Torstveit

Direct evidence for the occurrence of superconductivity in the magnetic compound YFe_4Al_8

V. M. Dmitriev*

Grenoble High Magnetic Field Laboratory, Max-Planck-Institut für Festkörperforschung; Centre National de la Recherche Scientifique, B.P. 166, F-38042 Grenoble Cedex 9, France; B. Verkin Institute for Low Temperature Physics and Engineering of the National Academy of Sciences of Ukraine, 47 Lenin Ave., Kharkiv 61103, Ukraine; and International Laboratory of High Magnetic Fields and Low Temperatures, 53-421 Wroclaw, Poland

L. F. Rybaltchenko

Grenoble High Magnetic Field Laboratory, Max-Planck-Institut für Festkörperforschung; Centre National de la Recherche Scientifique, B.P. 166, F-38042 Grenoble Cedex 9, France; and B. Verkin Institute for Low Temperature Physics and Engineering of the National Academy of Sciences of Ukraine, 47 Lenin Ave., Kharkiv 61103, Ukraine

P. Wyder and A. G. M. Jansen

Grenoble High Magnetic Field Laboratory, Max-Planck-Institut für Festkörperforschung

N. N. Prentslau

B. Verkin Institute for Low Temperature Physics and Engineering of the National Academy of Sciences of Ukraine, 47 Lenin Ave., Kharkiv 61103, Ukraine

W. Suski

International Laboratory of High Magnetic Fields and Low Temperatures, 53-421 Wroclaw, Poland and W. Trzebiatowski Institute of Low Temperatures and Structure Research, Polish Academy of Sciences, 50-950 Wroclaw, Poland

(Submitted December 28, 2001)
Fiz. Nizk. Temp. **28**, 374–377 (April 2002)

For the first time we present direct evidence for superconductivity in the ternary magnetic compound YFe_4Al_8 with the $ThMn_{12}$ type structure, found via point-contact (PC) experiments on contacts between a silver needle and single-crystal YFe_4Al_8, which reveal a distinct Andreev-reflection current. The spectra measured prove the existence of a normal–superconducting interface and exhibit a triangular-like shape in the vicinity of zero bias voltage, implying an unconventional type of superconductivity. The derived dependences of the order parameter versus temperature $\Delta(T)$ and magnetic field $\Delta(H)$ are presented. $\Delta(T)$ follows BCS theory, whereas $\Delta(H)$ does not satisfy any theoretical predictions. In some cases there exists noticeable superconductivity enhancement by a weak magnetic field. The data obtained imply a very inhomogeneous distribution of superconductivity over the sample volume in spite of its single-crystal structure. We assume that the reason is associated with inherent magnetic inhomogeneities of this material. The highest values for the critical temperature T_c, upper critical magnetic field H_{c2}, and ratio $2\Delta(0)/kT_c$ are 7.4 K, 5 T, and 7.2, respectively. © *2002 American Institute of Physics.* [DOI: 10.1063/1.1477359]

So far many materials have been discovered in which superconductivity and magnetism coexist in a wide temperature range. Among them, for example, are the ternary Chevrel phase and related systems,[1] borocarbide and boronitride compounds,[2] and the ruthenate cuprate family.[3] In this work we give, for the first time, direct evidence for the existence of superconductivity in the rare-earth ternary magnetic compound YFe_4Al_8 in an Andreev-reflection experiment.

The family of ternary magnetic compounds ReM_4Al_8 (Re is a rare earth, M is a transition metal) with the $ThMn_{12}$ type structure has been known for about two decades, and their physical properties have been investigated extensively.[4–6] However, weak signs of superconductivity in some of the compounds belonging to this family were discovered only recently in radio-frequency impedance and heat capacity experiments.[7,8] This is very surprising, because the compounds of this type have a complicated magnetic structure and their magnetic ordering is far from a completely compensated antiferromagnetic (AFM) order, for which superconductivity may coexist with magnetism. For compounds with a nonmagnetic Re element, like YFe_4Al_8, the incommensurate AFM structure consists of Fe moments in the (001) plane forming a rotating spiral structure. Besides, a migration of Fe atoms can create locally a noticeable excess of magnetic moments leading to the formation of a ferrimagnetic state or a spin-glass state.[4–6] These factors give rise to

 © 2002 American Institute of Physics

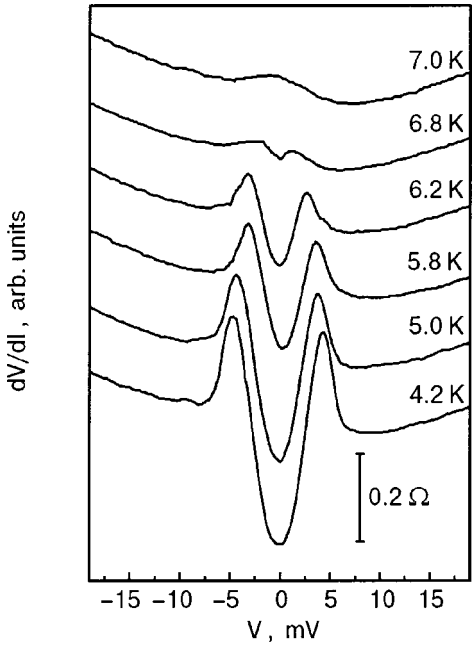

FIG. 1. $dV/dI(V)$ spectra at the different indicated temperatures for a point contact between an Ag needle and YFe_4Al_8 single crystal with normal contact resistance $R_n=27\ \Omega$. For clarity the curves are shifted vertically. The zero-bias structure disappears at a critical temperature $T_c=6.84$ K.

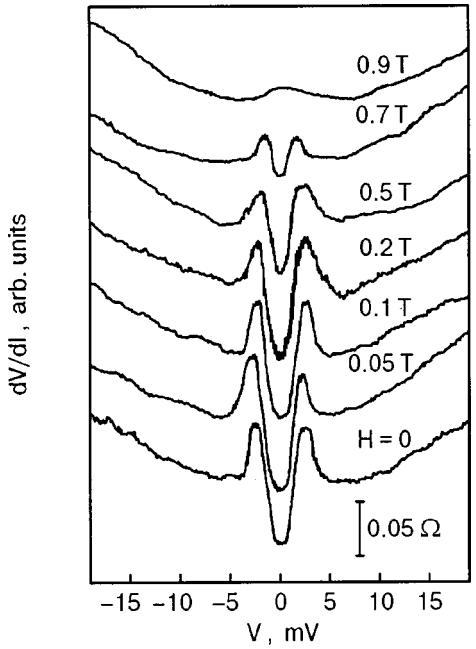

FIG. 2. $dV/dI(V)$ spectra at the different indicated magnetic fields for a point contact between an Ag needle and YFe_4Al_8 single crystal with normal contact resistance $R_n=5\ \Omega$ and critical temperature $T_c=6.15$ K. Temperature $T=4.2$ K. For clarity the curves are shifted vertically. The zero-bias structure disappears at a critical magnetic field $H_{c2}=0.87$ T.

significant uncompensated magnetic moments which in general prevent the possible occurrence of superconductivity in such systems.

For a more direct proof of superconductivity in YFe_4Al_8, we have undertaken an Andreev-reflection study using pressure-type point contacts (PC). As is well known, the Andreev reflection of the quasiparticles, passing a normal-metal/superconductor interface, leads to the lowering of the contact resistance for an applied voltage smaller than the superconducting order parameter Δ (i.e., $eV<\Delta$).[9] The measurements of the PC differential resistance characteristics, $dV/dI(V)$, were performed on contacts of the needle-anvil geometry with a silver needle as the normal electrode and freshly fractured surfaces of the YFe_4Al_8 single crystal as the superconducting counterelectrode. The contact sizes varied within 10–100 nm. The standard modulation techniques were used for the registration of $dV/dI(V)$ characteristics.

In some parts of fractured Y-compound surfaces (about 5%), we have found evident signatures of superconductivity. In Figs. 1 and 2 we present the typical spectra measured, respectively, at different temperatures and magnetic fields, which can be seen as the first direct evidence for superconductivity in this material. As one can see in Fig. 1, the weak zero-bias minimum, arising first on the 6.8 K curve and growing in amplitude with decreasing temperature, is a clear sign of probing the superconducting area. The relatively small reduction of $dV/dI(V)$ near $V=0$ implies that only a small part of the PC area goes to the superconducting state. Meanwhile, in some cases this reduction could reach about 30%, which indicates a very nonuniform distribution of superconductivity over the sample volume. It is seen that the triangular shape of the $dV/dI(V)$ minimum observed in the vicinity of zero voltage deviates strongly from the standard shape, i.e., that expected from BTK[9] theory for contacts with *s*-wave superconductors. In the latter case, the shape of this reduction should look like a double minimum characteristic, if electron scattering at the $N-S$ boundary occurs, or should have a flat bottom when this scattering is absent. The triangular shape of spectrum may be caused by a magnetic pair-breaking scattering intrinsic to the given compound or might reflect unconventional Cooper-pairing, like in UPt_3 (Ref. 10).

All the spectra are also characterized by the prominent horn structure which is often observed in low-Ohmic contacts. The reason for their appearance may be associated with the fast decrease of the Andreev-reflection current near $eV=\Delta$ and charge-imbalance processes. Besides, the superconducting clusters situated at the contact area periphery may result such horns.[11] In some measurements the spectra are not symmetrical, as is seen in Figs. 1 and 2. The reason for this phenomenon is not considered in the present paper.

Because of the unusual type of spectra measured, the standard BTK[9] theory for the description of the current–voltage characteristics cannot be used for finding the gap values. For qualitative estimation of the order parameter Δ and its temperature and magnetic dependences we define it as the half-width of the zero-bias minimum at the half-depth of the minimum. Apparently, the depth of this minimum also correlates with the order parameter and reflects its temperature and magnetic field dependences. Therefore, we also estimated the $R^0=R_n-R_s$ value, where R_n and R_s are the resistances at $V=0$ in the normal and superconducting states, respectively. The temperature dependences $\Delta(T)$ obtained in this manner for four series of PC spectra measured coincide well with BCS theoretical curve, as is seen from Fig. 3. The corresponding T_c are 5.85, 6.15, 6.84, and 7.40 K. The related $2\Delta(0)/kT_c$ ratios are 3.5, 4.0, 7.2, and 5.7, respectively.

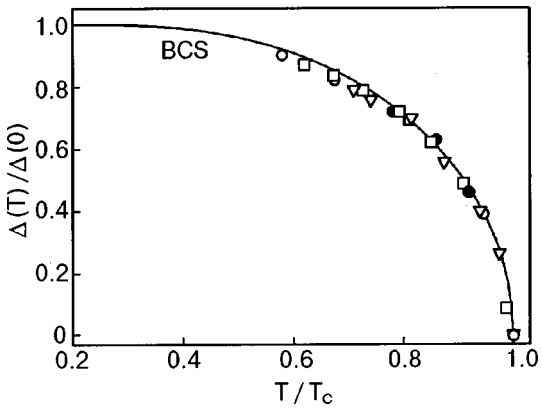

FIG. 3. The order parameter temperature dependences $\Delta(T)$ at zero magnetic field $H=0$ for four series of Ag-YFe_4Al_8 point contact measurements on different areas of the YFe_4Al_8 single-crystal surface. The corresponding critical temperatures T_c for different series are: 5.85 K (●), 6.15 K (△), 6.84 K (□), and 7.40 K (○). The related $2\Delta(0)/kT_c$ ratios are: 3.5 (●), 4.0 (△), 7.2 (□), and 5.7 (○). The corresponding critical magnetic fields H_{c2} are: 5 T (●), 0.87 T (△), 0.45 T (□), and 0.4 T (○). The solid line shows the BCS theoretical prediction.

In Fig. 2 one can see that both the width and depth of the minimum in the differential contact resistance decrease as the applied magnetic field increases, and they gradually disappear upon approaching about 0.9 T. In contrast to the temperature dependences, the magnetic field dependences for all the spectra measured do not follow any theoretical predictions. We have met two typical situations which are shown in Fig. 4. It is clearly seen that at field values higher than $H/H_{c2}\sim 0.5$ the experimental curves practically coincide. But at lower fields they are different. The curve represented by open triangles demonstrates noticeable (about 20%) enhancement of superconductivity by a weak magnetic field. At higher fields both curves deviate from the pair-breaking theoretical prediction[12] and indicate a much stronger pair-breaking influence of the field. The solid triangular points reflect the $R^0(H)$ dependence and correlate fairly well with the open triangles reflecting the $\Delta(H)$ dependence. Both types of data, obtained in the same experiment, unambiguously confirm the occurrence of the superconductivity enhancement effect. Earlier, enhancement of superconductivity in magnetic field was detected in the magnetic superconductor $HoNi_2B_2C$(Ref. 13) and in high-T_c materials containing magnetic impurities.[14] Probably all of these results are attributable to the reduction of the spin-disorder scattering due to the spin alignment improvement in an applied weak magnetic field, as was discussed in Ref. 13. Moreover, the existence of the negative magnetoresistance in ReM_4Al_8 compounds in weak magnetic fields at temperatures just before the superconducting transition[7,8] supports this suggestion.

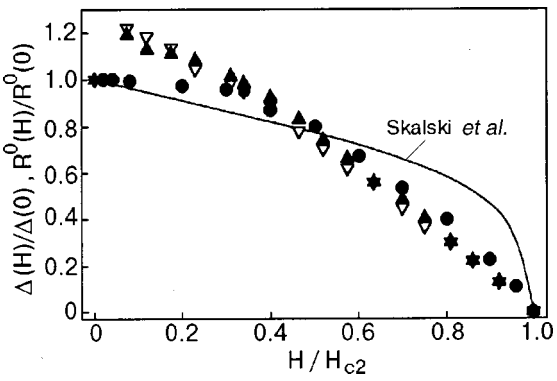

FIG. 4. The magnetic-field dependences of the order parameter $\Delta(H)$ at temperature $T=4.2$ K for two series of Ag-YFe_4Al_8 point-contact measurements. The corresponding parameters T_c, H_{c2}, and $2\Delta(0)/kT_c$ ratios for data marked by solid circles and open triangles are the same as in Fig. 3. The solid triangles show the magnetic-field dependence of the depth of the minimum $R^0=R_n-R_s$ and correlate well with the open triangles, reflecting the $\Delta(H)$ estimate for the same run of measurements. The solid line shows the pair-breaking-theory prediction of Skalski *et al.*

It was found that the superconductivity in YFe_4Al_8 can survive in rather high magnetic fields. The range of H_{c2} values measured at $T=4.2$ K lay within 0.4–5 T. The highest value $H_{c2}=5$ T measured at temperature $T=4.2$ K for the sample with $T_c=5.85$ K results in a coherence length of about 80 Å. We suppose that significant diversity in the T_c, H_{c2}, and Δ values obtained in our experiments is caused by variation of the magnetic states over the sample volume. In other words, magnetic inhomogeneities are inherent for such materials even in the single-crystal state.

In summary, we have presented the first direct evidence for the existence of superconductivity in the magnetic compound YFe_4Al_8 from measurements of Andreev reflection in point contacts of the N-S type. The anomalous shape of the Andreev-reflection spectra could point to an unconventional character of superconductivity in this compound or to magnetic pair-breaking resulting in quasiparticle states within the energy gap.

*E-mail: dmitriev@ilt.kharkov.ua

[1] M. B. Maple, in *Advances in Superconductivity*, edited by B. Deaver and J. Ruvalds, Plenum Press, New York (1983).
[2] R. J. Cava, H. W. Zandbergen, B. Batlogg, H. Eisaki, H. Tagaki, J. J. Krajewski, W. F. Peck, Jr., E. M. Gyorgy, and S. Uchida, Nature (London) **372**, 245 (1994).
[3] W. A. Fertig, D. C. Johnston, L. E. DeLong, R. W. McCallum, M. B. Maple, and B. T. Matthias, Phys. Rev. Lett. **38**, 987 (1977).
[4] P. Schobinger-Papamantellos, K. H. J. Buschow, and C. Ritter, J. Magn. Magn. Mater. **186**, 21 (1998).
[5] J. A. Paixão, S. Langridge, S. Aa. Sørensen, B. Lebech, A. P. Gonçalves, G. H. Lander, P. J. Brown, P. Burlet, and E. Talik, Physica B **234–236**, 614 (1997).
[6] I. Felner and I. Nowik, J. Magn. Magn. Mater. **54–57**, 163 (1986).
[7] A. M. Gurevich, V. M. Dmitriev, V. N. Eropkin, L. A. Ishchenko, N. N. Prentslau, and L. V. Shlyk, Fiz. Nizk. Temp. **25**, 15 (1999) [Low Temp. Phys. **25**, 10 (1999)].
[8] A. M. Gurevich, V. M. Dmitriev, V. N. Eropkin, B. Yu. Kotur, N. N. Prentslau, W. Suski, A. V. Terekhov, and L. V. Shlyk, Fiz. Nizk. Temp. **27**, 1308 (2001) [Low Temp. Phys. **27**, 967 (2001)].
[9] G. E. Blonder, M. Tinkham, and T. M. Klapwijk, Phys. Rev. B **25**, 4515 (1982).
[10] Y. de Wilde, J. Heil, A. G. M. Jansen, P. Wyder, R. Deltour, W. Assmus, A. Menovsky, W. Sun, and L. Taillefer, Phys. Rev. Lett. **72**, 2278 (1994).
[11] O. I. Shklyarevskii, A. M. Duif, A. G. M. Jansen, and P. Wyder, Phys. Rev. B **34**, 1956 (1986).
[12] S. Skalski, O. Betbeder-Matibet, and P. R. Weiss, Phys. Rev. **136**, A1500 (1964).
[13] L. F. Rybaltchenko, A. G. M. Jansen, P. Wyder, L. V. Tjutrina, P. C. Canfield, C. V. Tomy, and D. McK. Paul, Physica C **319**, 189 (1999).
[14] V. M. Dmitriev, L. A. Ishchenko, and N. N. Prentslau, Fiz. Nizk. Temp. **24**, 624 (1998) [Low Temp. Phys. **24**, 471 (1998)].

This article was published in English in the original Russian journal. Reproduced here with stylistic changes by AIP.

LOW-TEMPERATURE MAGNETISM

Magnetostriction of the antiferromagnet $NiCl_2$ in the homogeneous and multidomain states

V. M. Kalita, A. F. Lozenko,* and P. A. Trotsenko

Institute of Physics of the National Academy of Sciences of Ukraine, pr. Nauki 46, 03650 Kiev, Ukraine
(Submitted October 19, 2001)
Fiz. Nizk. Temp. **28**, 378–383 (April 2002)

Experimental data from measurements of the induced magnetostriction of the easy-plane two-sublattice layered antiferromagnet $NiCl_2$ in the homogeneous and multidomain states at $T=4.2$ K are analyzed. It is shown that the intersublattice magnetoelastic interactions are dominant in $NiCl_2$. The induced magnetostriction of the crystal in the single-domain state is due to canting of the spins of the sublattices toward the magnetic field direction. The induced magnetostriction in the multidomain state is due to a rearrangement of the domain structure and is independent of the small in-plane anisotropy. In both cases the values of the induced magnetostriction are directly proportional to the square of the value of the external magnetic field. © *2002 American Institute of Physics.* [DOI: 10.1063/1.1477360]

The magnetostriction of antiferromagnets (AFs) is due to processes of rearrangement of the multidomain state, changing of the orientation of the sublattice spins and of the magnitudes of the spins upon ordering, and the action of the magnetic field. In the $NiCl_2$ crystal the antiferromagnetic ordering is realized at temperatures below $T_N=49.6$ K.[1] In the antiferromagnetic state the crystal separates into domains, with the antiferromagnetic vector being uniform within a domain and having different directions in different domains.[2] $NiCl_2$ is an easy-plane two-sublattice AF with a layered structure and a small antiferromagnetic intersublattice (interlayer) exchange.[1] For $T=4.2$ K the spin-flip field of the sublattices in $NiCl_2$ is 129 kOe.[3]

In Refs. 4 and 5 the induced magnetostriction was investigated in the AF $CoCl_2$, the properties of which are close to those of $NiCl_2$. The value of the induced magnetostriction of $CoCl_2$ in the multidomain state is directly proportional to the square of the external magnetic field. This result was interpreted with the use of a magnetoelastic mechanism of the multidomain state.[4] The induced magnetostriction of $CoCl_2$ in the homogeneous state depends linearly on the square of the magnetic field[5] and was described in a model with magnetoelastic interactions, written with the use of the direction cosines of the sublattice spins.

According to the neutron-scattering data,[6] the spins in these AFs in the multidomain state are predominantly rotated by 120° in the different domains. In view of the symmetry of the crystals, the formation of this sort of multidomain state may be due to the presence of two sets of three twofold axes in the easy plane. The directions along the axes of one of these sets may be preferred by the spins. These preferred directions for the spins in the easy plane are an effect of the in-plane anisotropy. In Ref. 4 the magnetostriction of $CoCl_2$ in the multidomain state was described in the approximation of a continuous distribution of domains. In an antiferromagnetic resonance study reported in Ref. 7 it was noted that the in-plane anisotropy in $CoCl_2$ is small, and it was not taken into consideration in a description of the field dependence of the low-frequency branch of the antiferromagnetic resonance. According to the neutron diffraction data[6] and the domain structure proposed in Ref. 8, the effect of the in-aplane anisotropy cannot be ruled out.

In this paper we present and analyze observations of the induced magnetostriction of $NiCl_2$ in multidomain and homogeneous states in external magnetic fields up to 60 kOe at $T=4.2$ K. In analyzing the magnetostriction of the AF in the multidomain state the effect of a small in-plane anisotropy was examined; it was found that such an anisotropy could not affect the average value of the magnetostriction by acting on the distribution of the domains but left it independent of the magnetic field direction in the easy plane.

EXPERIMENTAL DEPENDENCE OF THE MAGNETOSTRICTION ON THE VALUE OF THE MAGNETIC FIELD

To eliminate the influence of the remanent striction,[9] we shall analyze the data from measurements of the induced magnetostriction of $NiCl_2$ during the first imposition of the magnetic field **H**. Figure 1 shows the relative elongations $\Delta l/l$ of the crystal along **H**. The magnetic field was oriented in the easy plane. In fields up to 10 kOe one is dealing with the magnetostriction of the multidomain state, and at higher fields, with the magnetostriction of the homogeneous state.

Figure 2 shows the dependence of $NiCl_2$ in the magnetostriction of the multidomain state of on the square of the external magnetic field H^2. In the multidomain state the magnetostriction is directly proportional to H^2. This dependence, as in the case of the $CoCl_2$ crystal,[4] can be represented in the form:

 © 2002 American Institute of Physics

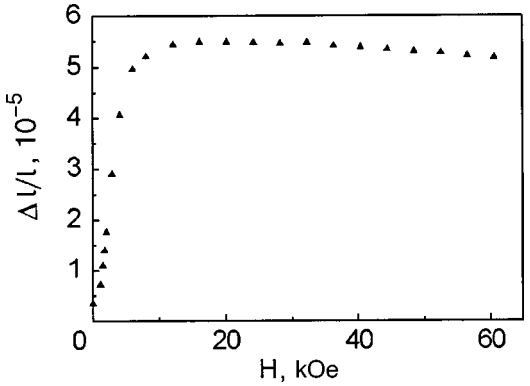

FIG. 1. Field dependence of the relative elongation of the $NiCl_2$ crystal, measured at $T=4.2$ K along the magnetic field, which was oriented in the easy plane.

$$\varepsilon=\varepsilon_s\frac{H^2}{H_d^2}, \tag{1}$$

where H_d^2 is a parameter having the value $H_d^2\approx 13$ kOe^2. A plot of relation (1) is shown by the solid line in Fig. 2.

The dependence of the magnetostriction of $NiCl_2$ on H^2 in the homogeneous state is presented in Fig. 3. The magnetostriction of the AF in the homogeneous state is described by the expression

$$\varepsilon=\varepsilon_s[1-\xi(H/H_{ff})^2], \tag{2}$$

where ξ is an experimentally determined parameter having the value ≈ 0.3, and H_{ff} is the spin-flip field of the sublattices. A plot of relation (2) is shown by the solid line in Fig. 3. The parameter ε_s in Eqs. (1) and (2) is equal to the spontaneous anisotropic magnetostriction in the homogeneous state at $H=0$, which is determined by extrapolating the $\varepsilon(H^2)$ curve in the homogeneous state to $H\to 0$.

INDUCED STRICTION OF THE CRYSTAL IN THE SINGLE-DOMAIN STATE

In describing the induced magnetostriction of the homogeneous state we specify the magnetoelastic contribution to the energy with the aid of the direction cosines of the sublattice spins.[5] We limit consideration to the planar problem.

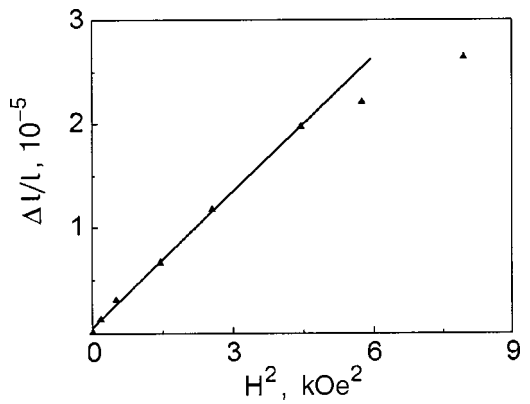

FIG. 2. Induced magnetostriction of $NiCl_2$ in the multidomain state versus the square of the magnetic field.

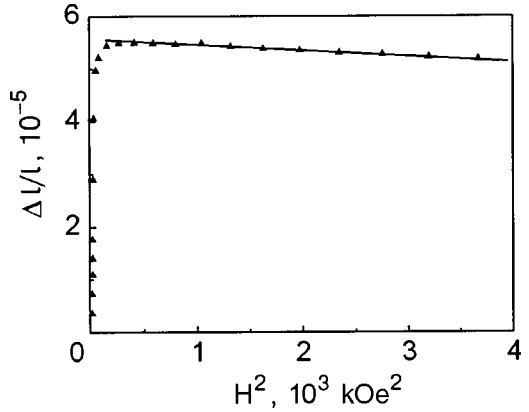

FIG. 3. Induced magnetostriction of the $NiCl_2$ crystal in the single-domain state versus the square of the magnetic field.

The equilibrium striction is determined by minimizing the sum of the magnetoelastic and elastic contributions to the energy:

$$\begin{aligned}E=&\sum_{\alpha\beta}\gamma_{\alpha\beta}(n_{\alpha x}n_{\beta x}-n_{\alpha y}n_{\beta y})(U_{xx}-U_{yy})\\&+\sum_{\alpha\beta}\lambda_{\alpha\beta}(n_{\alpha x}n_{\beta y}+n_{\beta x}n_{\alpha y})U_{xy}+\sum_{\alpha\beta}\delta_{\alpha\beta}(n_{\alpha x}^2\\&+n_{\alpha y}^2)(U_{xx}+U_{yy})+\frac{1}{2}C_{11}(U_{xx}^2+U_{yy}^2)+C_{12}U_{xx}U_{yy}\\&+(C_{11}-C_{12})U_{xy}^2,\end{aligned} \tag{3}$$

where $\alpha,\beta=1,2$ is the number of the sublattice, $\alpha\geqslant\beta$; γ, λ, and δ are magnetoelastic interaction parameters; $n_{\alpha x}$, $\eta_{\alpha y}$ and $n_{\beta x}$, $n_{\beta y}$ are the direction cosines of the sublattice spin vectors $\mathbf{s}_1$ and $\mathbf{s}_2$, respectively. The x and y axes are oriented in the easy plane. The first and second terms in (3) describe the anisotropic magnetoelastic interaction, and the third term describes the isotropic interaction in the layer. For $\alpha=\beta$ the parameters γ, λ, and δ specify the intralayer magnetoelasticity. When $\alpha\neq\beta$ one is talking about the interlayer (intersublattice) magnetoelasticity. In Eq. (3) the small in-plane anisotropy is not taken into account.

In a single-domain state $\mathbf{L}\perp\mathbf{H}$, and the spins of the sublattices are symmetric with respect to the magnetic field direction. The spin vectors $\mathbf{s}_1$ and $\mathbf{s}_2$ are at an angle φ to $\mathbf{H}$, the value of this angle being specified by the relation $\cos\varphi=H/H_{ff}$ (Ref. 10). From Eq. (3) we obtain an expression for the strain U_{yy} when $\mathbf{H}$ is oriented along the y or x axis:

$$U_{yy}(\mathbf{H}\|y,x)=A_0\mp A_{12}+(A_\rho\pm A_{11})\left[1-2\left(\frac{H}{H_{ff}}\right)^2\right], \tag{4}$$

where we have adopted the notation

$$\begin{aligned}A_0&=-\frac{2\delta_{11}}{C_{11}+C_{12}},\quad A_\rho=\frac{\delta_{12}}{C_{11}+C_{12}},\\A_{12}&=\frac{\gamma_{12}}{C_{11}-C_{12}},\quad A_{11}=\frac{2\gamma_{11}}{C_{11}-C_{12}}.\end{aligned} \tag{5}$$

In Eq. (4) the upper sign corresponds to orientation of $\mathbf{H}$ along the y axis, the lower sign to orientation along x. The terms containing A_{12} and A_{11} describe anisotropic striction

that depends on the direction of **H**. It changes sign when the field direction changes from the x axis to the y axis. The contribution to the spontaneous striction from A_ρ and A_0 is isotropic. It follows from a comparison of (4) with the experimental magnetostriction curves for **H** applied along x and then along y (Ref. 9) that the contribution to the magnetostriction from the terms containing A_ρ and A_0 can be neglected in $NiCl_2$. Then the expression for the striction in the homogeneous state can be written in the form

$$U_{yy}=\mp(A_{12}-A_{11})\left[1+\frac{2A_{11}}{A_{12}-A_{11}}\left(\frac{H}{H_{ff}}\right)^2\right]. \tag{6}$$

Comparing (6) with (2), we find that $\varepsilon_s=A_{12}-A_{11}$ and $\xi=2A_{11}/(A_{12}-A_{11})$. The modulus $|A_{11}|$ is less than A_{12}, so that $|A_{11}|\approx 0.13A_{12}$, and we have $A_{12}>0$ and $A_{11}<0$. In $NiCl_2$ the main contribution to the induced magnetostriction is given by the intersublattice magnetoelasticity, whereas in $CoCl_2$ (Ref. 5) the main contribution is from the intrasublattice magnetoelasticity.

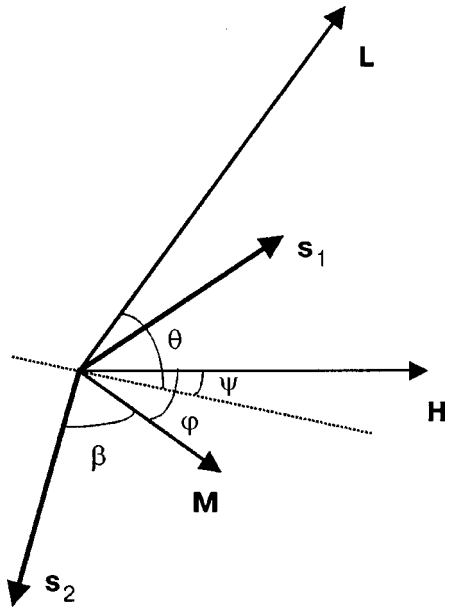

FIG. 4. Orientations of the sublattice spins $\mathbf{s}_1$ and $\mathbf{s}_2$, the magnetization vector **M**, and the antiferromagnetic vector **L** relative to the magnetic field **H**.

INDUCED STRICTION OF THE CRYSTAL IN THE MULTIDOMAIN STATE

We give a description of the induced magnetostriction of an AF in the multidomain state in accordance with the minimum free energy principle developed in Ref. 11, according to which the equilibrium multidomain state should correspond to a minimum of the free energy of the crystal. As in Ref. 4, we shall assume that the distribution of the domains is continuous. We find an expression for the free energy of the multidomain state, which we present in the form of a sum of the contributions from the reaction of the spin system to the introduction of a field with allowance for the in-plane anisotropy and the term characterizing the contribution to the free energy from the source of the multidomain character.

The spin energy per unit cell of a domain is written in the form of a sum of the intersublattice exchange, the in-plane anisotropy, and the Zeeman term:

$$e=zI_{12}\mathbf{s}_1\mathbf{s}_2+AL^6\cos 6\theta-\mathbf{H}\cdot(\mathbf{s}_1+\mathbf{s}_2), \tag{8}$$

where $\mathbf{s}_1$ and $\mathbf{s}_2$ are the sublattice spins, z is the number of nearest neighbors, I_{12} is the intersublattice exchange constant, L is the modulus of the antiferromagnetic vector $\mathbf{L}=\mathbf{s}_1-\mathbf{s}_2$, A is the anisotropy constant, θ is the angle between **L** and the crystallographic axis, which in Fig. 4 is indicated by a dotted line. We write the angle θ in the form $\theta=\pi/2+\psi-\varphi$, where ψ is the angle between **H** and the anisotropy axis, and φ is the angle between **H** and the magnetization vector $\mathbf{M}=\mathbf{s}_1+\mathbf{s}_2$. Assuming that the moduli of the vectors $\mathbf{s}_1$ and $\mathbf{s}_2$ are identical ($s=|\mathbf{s}_1|=|\mathbf{s}_2|$), that the angles between $\mathbf{s}_1$ and **M** and $\mathbf{s}_2$ and **M** are equal to β, and that the vector **M** is perpendicular to **L**, we write the energy (8) in the form

$$e=zI_{12}s^2(2\cos^2\beta-1)-AL^6\cos 6(\varphi-\psi)-2Hs\cos\beta\cos\varphi. \tag{9}$$

By minimizing (9) with respect to β, we determine the energy of a domain with orientation φ:

$$e=-\frac{H^2\cos^2\varphi}{2zI_{12}}-AL^6\cos 6(\varphi-\psi). \tag{10}$$

Taking (10) into account, we write the spin energy of the AF in the multidomain state in the form:

$$E=-\frac{V}{V_0}\sum_i P_i\left[\frac{H^2\cos^2\varphi_i}{2zI_{12}}+AL^6\cos 6(\varphi_i-\psi)\right], \tag{11}$$

where V and V_0 are the volume of the crystal and the volume of the unit cell. In Eq. (11) the summation is over domains with different orientation angles φ_i, the probability of which is denoted by P_i, where $P_i=V_i/V$, where V_i is the volume of domains of this orientation. The spin energy (11) can be written as an integral over φ:

$$E=-\frac{1}{\pi}\frac{V}{V_0}\int_{-\pi/2}^{\pi/2}\left\{p(\varphi)\left[\frac{H^2\cos^2\varphi}{2zI_{12}}+AL^6\cos 6(\varphi-\psi)\right]\right\}d\varphi, \tag{12}$$

where $p(\varphi)$ is the density of the distribution of the domains.

The expression for the free energy is written in the form a sum of the spin energy E and the contribution from the source of the multidomain character,[4]

$$F=\frac{1}{\pi}\frac{V}{V_0}\int_{-\pi/2}^{\pi/2}\left[p(\varphi)\left(\frac{H^2\cos^2\varphi}{2zI_{12}}+AL^6\cos 6(\varphi-\psi)\right)+f(p(\varphi))\right]d\varphi, \tag{13}$$

where f specifies the contribution to the free energy from the source of the multidomain character.

At $H=0$ and in the absence of anisotropy the domains are distributed equiprobably.[4] At low fields we introduce the

small deviation $\Delta p(\varphi)$ from the equiprobable domain distribution: $p(\varphi)=1+\Delta p(\varphi)$. With this deviation, Eq. (13) takes the form

$$F=\frac{1}{\pi}\frac{V}{V_0}\int_{-\pi/2}^{\pi/2}\left\{-\Delta p(\varphi)\left[\frac{H^2\cos^2\varphi}{2zI_{12}}+AL^6 \times\cos 6(\varphi-\psi)\right]+\frac{1}{2}\eta(\Delta p(\varphi))^2\right\}d\varphi, \quad (14)$$

where η is a positive parameter equal to the second derivative $\eta=d^2f/dp^2$ evaluated at $p=1$. In view of (13) and (14), anisotropy is not a necessary condition for the formation of a multidomain state. It is treated as an additional condition under which a rearrangement of the multidomain state occurs. By minimizing F, we find an expression for the density of the domain distribution for $H\neq 0$:

$$p(\varphi)=1+\frac{H^2}{2zI_{12}\eta}\left(\cos^2\varphi-\frac{1}{2}\right)+\frac{AL^6}{\eta}\left(\cos 6(\varphi-\psi)+\frac{\sin 6\psi}{3\pi}\right). \quad (15)$$

The in-plane anisotropy and the external magnetic field lead to anisotropy of the domain distribution. For $H=0$ the probability density has the form

$$p(\varphi)=1+\frac{AL^6}{\eta}\cos 6\varphi. \quad (16)$$

Such anisotropy in the distribution of domains at $H=0$ agrees with the data of neutron-diffraction observations.[6]

The rearrangement of the domain structure occurs at fields for which the contribution to the striction of a domain from the canting of the spins toward the field can be neglected. In this case the relative elongation ε along **H** of a domain with **L** not perpendicular to **H** in a multidomain state is given by

$$\varepsilon=\varepsilon_s(\cos^2\varphi-\sin^2\varphi)=\varepsilon_s\cos 2\varphi. \quad (17)$$

Averaging (17), we determine the average magnetostriction of the AF in the multidomain state:

$$\bar{\varepsilon}=\frac{1}{\pi}\int_{-\pi/2}^{\pi/2}\varepsilon_s\cos 2\varphi p(\varphi)d\varphi. \quad (18)$$

Substituting into (18) the expression for the probability density (15), we obtain an expression for the average magnetostriction of the crystal along the field **H** as a function of the field strength:

$$\bar{\varepsilon}=\varepsilon_s\frac{H^2}{8zI_{12}\eta}. \quad (19)$$

In the rearrangement of the multidomain state the magnetostriction is directly proportional to the square of the applied field, in agreement with the experimental data presented in Fig. 2. The value of the magnetostriction (19) does not depend on the value of the angle ψ, i.e., it is independent of the field orientation in the easy plane and of the value of the in-plane anisotropy.

CONCLUSION

The experimental relations (1) and (2) for the induced magnetostriction of the $NiCl_2$ crystal as a function of magnetic field are similar to those for the $CoCl_2$ crystal.[4,5] In the uniform region the induced magnetostriction of both crystals is determined by the orientation of the sublattice spins. The similarity of the magnetostriction in the crystals $NiCl_2$ and $CoCl_2$ upon rearrangement of the multidomain state is indicative of a common nature of the multidomain character of these crystals.

Because of the in-plane anisotropy the domain distribution in the multidomain state is anisotropic. This agrees with the data of neutron diffraction observations for the orientations of the domains. The induced magnetostriction of the crystal in the multidomain state (19) is independent of the orientation of the field in the easy plane.

The authors thank Prof. S. M. Ryabchenko for some comments made in a discussion of this study.

This study was done with the support of the Government Foundation for Basic Research of the Ministry of Education and Science of Ukraine, Grant 02.07/014.

*E-mail: lozenko@iop.kiev.ua

[1] P. A. Lingard, R. J. Birgenau, J. Als-Nielsen, and H. J. Guggenheim, J. Phys. C **8**, 1059 (1975).
[2] M. M. Farztdinov, Usp. Fiz. Nauk **84**, 611 (1964) [Sov. Phys. Usp. **7**, 855 (1964)].
[3] J. Gunzbourg, S. Papassimacopoulos, A. Mieden-Gros, and A. Allain, J. Phys. **32**, 125 (1971).
[4] V. M. Kalita and A. F. Lozenko, Fiz. Nizk. Temp. **27**, 872 (2001) [Low Temp. Phys. **27**, 645 (2001)].
[5] V. M. Kalita, A. F. Lozenko, and S. M. Ryabchenko, Fiz. Nizk. Temp. **26**, 671 (2000) [Low Temp. Phys. **26**, 489 (2000)].
[6] M. K. Wilkinson, J. W. Cable, E. O. Wollan, and W. C. Koehler, Phys. Rev. **113**, 497 (1959).
[7] A. F. Lozenko P. E. Parkhomchuk, S. M. Ryabchenko, and P. A. Trotsenko, Fiz. Nizk. Temp. **14**, 941 (1988) [Sov. J. Low Temp. Phys. **14**, 517 (1988)].
[8] V. M. Kalita and A. F. Lozenko, Fiz. Nizk. Temp. **27**, 489 (2001) [Low Temp. Phys. **27**, 358 (2001)].
[9] V. M. Kalita, A. F. Lozenko, S. M. Ryabchenko, and P. A. Trotsenko, Ukr. Fiz. Zh. **43**, 1469 (1998).
[10] L. Neel', Izv. Akad. Nauk SSSR, Ser. Fiz. **21**, 890 (1957).
[11] V. G. Bar'yakhtar, A. N. Bogdanov, and D. A. Yablonskiĭ, Usp. Fiz. Nauk **156**, 47 (1988) [Sov. Phys. Usp. **31**, 810 (1988)].

Translated by Steve Torstveit

Photoinduced magnetic linear dichroism in a YIG:Co film

O. V. Miloslavska,* Yu. N. Kharchenko, N. F. Kharchenko, and V. G. Yurko

B. Verkin Institute for Low Temperature Physics and Engineering of the National Academy of Science of Ukraine, 47. Lenin Ave., Kharkov 61103, Ukraine

A. Stupakiewicz and A. Maziewski

Laboratory of Magnetism, University of Bialystok, 15-424 Bialystok, Poland
(Submitted November 12, 2001)
Fiz. Nizk. Temp. **28**, 384–387 (April 2002)

The spectra of linear dichroism induced by a magnetic field are observed in a cobalt-doped yttrium iron garnet (YIG:Co) film grown in the (001) plane. The linear dichroism spectra are highly sensitive to the orientation of the magnetic field. The spectrum measured with the magnetic field directed along the crystallographic axis [100] turned out to have a form identical to the spectrum of the ''rigid'' photoinduced linear dichroism, known from earlier experiments. The similarity of these spectra may be regarded as evidence of the magnetic origin of the major part of the optical anisotropy induced by light with polarization $\mathbf{E}\|[100]$ in the nonmagnetized YIG:Co film. © *2002 American Institute of Physics.*
[DOI: 10.1063/1.1477361]

1. INTRODUCTION

Yttrium iron garnets $Y_3Fe_5O_{12}$ (YIG) doped with Co ions are interesting and promising objects for investigations and applications.[1–6] Substitution of the isotropic Fe^{3+} ions, which have zero orbital moment, by strongly anisotropic Co ions results in noticeable changes of the magnetic properties of the material, including the magnetic anisotropy, magnetorestriction, and the temperature behavior of the magnetization.[1,2] These substances are important as sensitive photomagnetic materials. Illumination of doped YIG films by visible or near-IR light often results in changes of their magnetic and nonmagnetic properties.[3–8] The appearance of light-induced anisotropic properties of the films is caused by the creation of highly anisotropic photosensitive centers when certain ions with valences different from the host ions are implanted in the YIG crystal lattice.[3,4] In films of yttrium iron garnet doped with cobalt (YIG:Co), especially strong photoinduced changes of the magnetic anisotropy and the magnetic hysteresis loops as well as switching of the magnetic domains by light have been revealed and studied by different methods.[3,5,6] The photoinduced effects in YIG:Co were stronger than in YIG crystals doped with Si atoms.[4,8] In Refs. 5 and 6 the photoinduced polarization-sensitive changes of the domain structure in epitaxial YIG:Co films have been investigated even at room temperature.

The light-induced optical linear dichroism was also observed in this film in Ref. 7. The spectra of linear dichroism induced by polarized light in a nonmagnetized epitaxial YIG:Co film were studied in the visible region. A dichroism spectrum with a prominent structure has been observed after irradiating the film by light with the plane of polarization along the [100] crystallographic axis of the film. No spectral features were observed when the irradiating light was polarized along [110]. The photoinduced dichroism spectrum could be considered as consisting of two components. The component called ''soft'' dichroism changes its sign when the plane of polarization of the irradiating light is rotated by 90°. The dichroism spectral bands, which do not change sign when the polarization axis of inducing light is rotated by 90°, compose the ''rigid'' component. The bands of the ''rigid'' LD spectrum could be observed after irradiation by [100]- or [010]-polarized light. The characteristic feature is the revealed memory phenomenon of the ''rigid'' dichroism: the photoinduced spectrum, which vanishes on heating up to 170 K through a change of magnetic order, is restored again after cooling back to 28 K without irradiation. The authors of Ref. 7 supposed that the ''rigid'' dichroism is a result of the photoinduced reorientation of the magnetic moments of the photoactive ions in the YIG:Co film and that the emergence of the photoinduced dichroism may actually be presented as a manifestation of the magnetooptic Voigt effect which is observed when the magnetic moments are oriented in the plane of the film in a definite way.

The aim of the present work was to verify the assumption about the magnetic origin of the changes of photoinduced optical anisotropy[7] by means of experimental studies of the magnetic dichroism spectra in a YIG:Co film in Voigt the geometry $\mathbf{H}\perp\mathbf{k}\|\mathbf{s}$, where $\mathbf{k}$ is the light propagation vector and $\mathbf{s}$ is the normal to the surface of the film.

2. EXPERIMENTAL RESULTS AND DISCUSSION

The garnet film of $Y_2CaFe_{3.9}Co_{0.1}GeO_{12}$ (YIG:Co) was grown by the method of liquid-phase epitaxy on a [001]-oriented substrate of $Gd_3Ga_5O_{12}$. The thickness of the YIG:Co film is 5.8 μm. The easy axis of YIG:Co changes its orientation with temperature.[9] In the temperature range between 125 K and 10 K three magnetic states can exist, with easy axis along [001], [100], and [110], either in stable or metastable form,[10] and at the temperature of the present experiment, $T=30$ K, the magnetic state with easy axis along [001] can be assumed to be dominant. The measurements of the magnetic linear dichroism spectra of YIG:Co were car-

 © 2002 American Institute of Physics

ried out in the spectral region 500–800 nm. We used a magnetooptical setup which comprised a monochromator, photoelastic modulator, cryogenic equipment, and superconducting solenoids. The spectral dependence of the quantity $(I_1 - I_2)/(I_1 + I_2)$ was measured using the modulation method, I_1 and I_2 being the intensities of light with the orthogonal orientations of the plane of polarization. The spectral measurements were performed with the electric vectors of the light oriented parallel to the magnetic field **H** for I_1 and perpendicular to **H** for I_2. The light coming from the monochromator had a rather low intensity and did not generate any noticeable photoinduced effect. The cryogenic technique allowed us to obtain temperatures as low as 10 K. The in-plane magnetic field was applied perpendicularly to the light propagation vector. The angle between the magnetic field vector and the cubic crystallographic axis [100] of the sample could be varied by rotation of the sample-holder around the normal to the YIG:Co film surface coinciding with the crystallographic axis [001].

A series of spectra of linear dichroism (LD) measured at different orientations of the magnetic field was obtained at a temperature near 30 K. The magnetic field was switched on after zero-field cooling (ZFC). The applied magnetic field strength was ~8.8 kOe. This value of the in-plane magnetic field was sufficient for uniform magnetization of the film. The orientation of the magnetic field was changed by rotating the sample around its [001] axis, that is, normal to the film surface, at the constant temperature. The LD spectra measured with the magnetic field oriented along the [100] and [110] axes and the spectrum at The magnetic field was switched on after zero-field cooling (ZFC). The applied magnetic field strength was ~8.8 kOe. This value of the in-plane magnetic field was sufficient for uniform magnetization of the film. The orientation of the magnetic field was changed by rotating the sample around its [001] axis, that is, normal to the film surface, at the constant temperature. The LD spectra measured with the magnetic field oriented along the [100] and [110] axes and the spectrum at zero magnetic field are shown in Fig. 1. The forms of the spectra are distinctly different for different orientations of magnetic field. The LD spectrum measured with the magnetic field directed along the [100] axis (Fig. 1a) has a well-defined structure, and the highest value of the magnetic linear dichroism is attained. We have not noticed any diversity in the spectra obtained in the [100]- and [010]- oriented magnetic fields. However, when the magnetic field was directed along an axis of the [110] type, the LD spectrum was quite different, and the linear dichroism value was lowered over almost all of the spectral region studied (Fig. 1b). At zero field, when the sample is not magnetically homogeneous, the LD is small (Fig. 1c).

A comparison of the spectrum of magnetic linear dichroism induced by **H**∥[100] with the LD spectrum induced by the action of polarized light with **E**∥[100] observed in Ref. 7 is shown in Fig. 2. The sample has been irradiated with linearly polarized light coming either from a white light source through a filter with $\lambda > 640$ nm or from a helium–neon laser with $\lambda = 632$ nm. The illumination was carried out for about 20 min, at a power about 0.4 W/cm^2 (Ref. 7).

The forms of both spectra are practically identical, but the value of the photoinduced LD is nearly 5 times smaller than that of the magnetic one.

The most noticeable changes of the magnetic LD at different orientations of the inducing magnetic field (Fig. 1) were observed in the region of the spectrum at wavelengths higher than 600 nm. The absorption spectra investigations[11] showed the presence of Co of both valences, Co^{2+} and Co^{3+}, in YIG:Co. The exact assignment of the experimentally observed spectral features to certain transitions in Co ions with a definite valence and in either a tetrahedral or octahedral crystallographic site is not an easy task, because in this region of the spectrum the Co bands are rather wide and overlapping.[11,12] Besides, the transitions in octahedral Co have an oscillator strength weaker than those for the tetrahedral ones, and in the spectral region under study the transitions in the Fe ions also contribute to the spectrum of YIG:Co.[13] The most prominent features originating from transitions in tetrahedral Co^{2+}, in octahedral Co of both valences, and in Fe^{3+} ions were determined using the results and analysis of Faraday rotation spectral studies in Refs. 12 and 13. For example, in Ref. 12 the bands near 590 nm and 630 nm were identified as arising from transitions in tetrahedral Co^{2+} and the spectral region near 700 nm as formed by

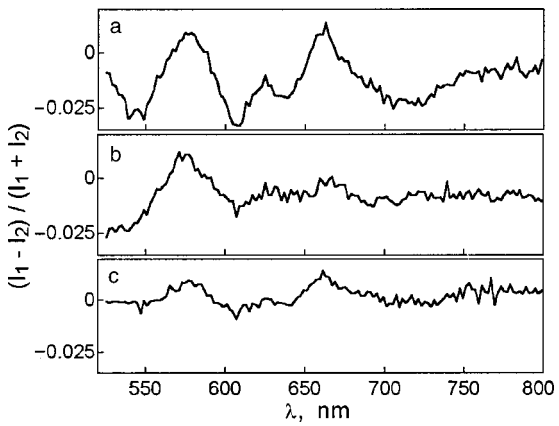

FIG. 1. Magnetic linear dichroism spectra measured after ZFC at $H = 8.8$ kOe ($T = 30$ K) for different orientations of the magnetic field: **H**∥[100] (a); **H**∥[110] (b); and at zero field, $H = 0$ (c).

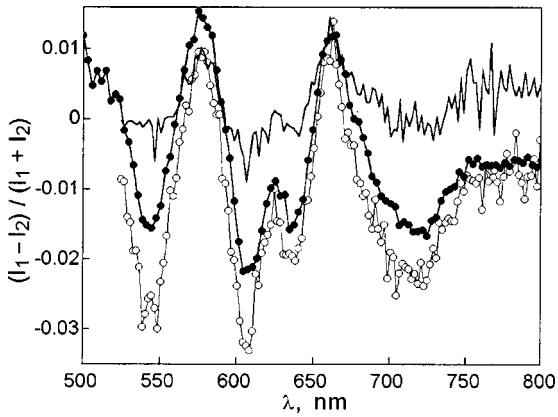

FIG. 2. The spectra of magnetic linear dichroism at $H = 8.8$ kOe without irradiation (open circles) at $T = 30$ K (the present experiment) and of the photoinduced LD after irradiation with **E**∥[100] (solid symbols) at $T = 28$ K.[7] The latter has been multiplied by five. The line without symbols shows the LD at $H = 0$ and without irradiation.

transitions in octahedral Co^{2+} and Co^{3+}. The analysis of absorption and Faraday rotation spectra of pure YIG crystals and films, performed in Ref. 13, as well as magnetic circular dichroism spectra analysis in Ref. 14, allowed attribution of the band near 543 nm to a transition of tetrahedral Fe^{3+} and the band in the region of 625 nm to a transition in octahedral Fe^{3+}.

The coincidence of the photoinduced dichroism spectrum with the magnetic dichroism spectrum indicates that photoinduced LD, like its rigid component, is actually magnetic dichroism. The light-induced linear dichroism arises as a result of reorientation of magnetic moments after a photoinduced change of magnetic anisotropy.

As has already been proposed in many earlier papers,[5–7] light polarized along a certain direction acts on the Co centers in the definite crystallographic positions and causes effective electron transfer between Co ions. This process, in turn, results in a change of Co valences and further redistribution of the Co ions with definite valences among crystallographic sites[5–7] involving the centers in a preferred direction. The process of rearrangement of Co ions then leads to changing magnetic anisotropy in the film. At $T \sim 30$ K the easy axis of the sample is near the [001] crystallographic axis,[9,10] whereas under the action of the [100]- and [010]-polarized light the easy axis turns into a hard axis. The easy axis now becomes directed close to any of the [100] or [010] crystallographic axes which are slightly nonequivalent in the real film. As a result, after irradiation the magnetic moments of the magnetic sublattice become oriented along a direction close to any of the cubic axes of the [100] type. The same orientation of magnetic moments results from the action of a magnetic field directed along [100]. It looks quite natural to expect the dichroism spectra to be similar in the two cases, and that is proved by the present experimental observations.

The effect of light with a definite polarization may be therefore presented as the action of an effective magnetic field, with a definite direction, on the YIG:Co film.

It should be noted that the proposed mechanism of induced anisotropy could be considered as rather local processes. It is shown that the photoinduced linear dichroism is five times less than that induced by magnetic field, and this fact may be due to the reason that the action of the light could be nonuniform, and its effect will be determined by the same factors that make the [100] and [010] directions nonequivalent in the film. Inhomogeneously distributed Co ions as well as impurities, deformations, and elastic stresses may manifest themselves in such a way that in different regions of the sample the easiest axes could take the direction [100] or [010]. This will result in a nonuniform orientation of magnetic moments in the irradiated film and in the formation of small domains in which the preferred dichroism axes will be oriented perpendicularly. This fact will result in the effective compensation of the dichroism, which in the experiment is to be measured in a region much larger than the characteristic size of the inhomogeneities. In the case of the action of a magnetic field, the magnetic moments are oriented rather uniformly, if the magnetic field is of a sufficiently high value.

3. CONCLUSION

Spectra of magnetic linear dichroism sensitive to the orientation of the external magnetic field has been observed in a YIG:Co film. The form of the magnetic LD spectrum for an orientation of the magnetic field along the [100] axis turned out to be similar to the LD spectrum induced by linearly polarized light with polarization along the [100] axis. This similarity of the induced LD spectra leads to the conclusion that the so-called ''rigid'' component of the photoinduced optical anisotropy in YIG:Co films is of a magnetic origin.

*E-mail: miloslavskaya@ilt.kharkov.ua

[1] S. Geller, G. Balestrino, A. K. Ray, and A. Tucciarone, Phys. Rev. B **27**, 326 (1983).
[2] A. Maziewski, J. Magn. Magn. Mater. **88**, 325 (1990).
[3] A. B. Chizhik, S. N. Lyakhiments, A. Maziewski, and M. Tekielak, J. Magn. Magn. Mater. **140-144**, 2111 (1995).
[4] E. F. Kovalenko and É. L. Nagaev, Usp. Fiz. Nauk **148**, 561 (1986) [Sov. Phys. Usp. **29**, 297 (1986)].
[5] A. B. Chizhik, I. I. Davidenko, A. Maziewski, and A. Stupakiewicz, Phys. Rev. B **57**, 14366 (1998).
[6] A. Stupakiewcz, A. Maziewski, I. I. Davidenko, and V. Zablotskii, Phys. Rev. B **64**, 64405 (2001).
[7] A. A. Milner, N. F. Kharchenko, A. Maziewski, and J. M. Desvignes, J. Magn. Magn. Mater. **140-144**, 2113 (1995).
[8] J. F. Dillon, Jr., E. M. Gyorgy, and J. P. Remeika, Phys. Rev. Lett. **22**, 643 (1969).
[9] M. Tekielak, W. Andra, A. Maziewski, and J. Taubert, J. Phys. IV **7C**, 461 (1997).
[10] M. Tekielak, A. Stupakiewicz, A. Maziewski, and J. M. Desvignes, J. Magn. Magn. Mater. (2002) (to be published).
[11] D. L. Wood and J. P. Remeika, J. Chem. Phys. **46**, 3595 (1967).
[12] Z. Šimša, J. Šimšova, P. Görnert, and A. Maziewski, Acta Phys. Pol. A **6**, 277 (1989).
[13] W. Wettling, B. Andlauer, P. Koidl, J. Schneider, and W. Tolksdorf, Phys. Status Solidi B **59**, 63 (1973).
[14] R. V. Pisarev, B. Antonini, P. Paroli, and A. J. Tucciarone, J. Magn. Magn. Mater. **54-57**, 1391 (1986).

This article was published in English in the original Russian journal. Reproduced here with stylistic changes by AIP.

LOW-DIMENSIONAL AND DISORDERED SYSTEMS

Features of the x-ray bremsstrahlung in the scattering of intermediate-energy electrons on atoms of inert elements

É. T. Verkhovtseva and E. V. Gnatchenko*

B. Verkin Institute for Low Temperature Physics and Engineering, National Academy of Sciences of Ukraine, pr. Lenina 47, 61103 Kharkov, Ukraine

(Submitted January 4, 2002; revised February 4, 2002)
Fiz. Nizk. Temp. **28**, 388–399 (April 2002)

The results of experimental and theoretical studies of the differential x-ray bremsstrahlung spectra emitted in the scattering of intermediate-energy electrons on atoms of inert elements are presented in generalized form. The experimental studies were done using the low-temperature gas-jet method of generation of electromagnetic radiation. The features of the bremsstrahlung and the relationships governing the novel form of bremsstrahlung due to polarization effects are established. It is shown that the Born approximation is inapplicable for considering the bremsstrahlung cross sections in the scattering of electrons of intermediate energies on atoms of inert elements. © *2002 American Institute of Physics.*
[DOI: 10.1063/1.1477362]

INTRODUCTION

In recent years the low-temperature gas-jet method of generating electromagnetic radiation has been actively employed in the physics of electron–atom collisions. In this method an electron-beam-excited supersonic jet in vacuum is used as a dense gaseous target.[1–3] Thanks to the formation of a jet with a large Mach number ($M \approx 10$) and the low temperature of the gas in the jet (around 10 K), due to its isentropic expansion into vacuum, the velocity of directed motion of the particles of the jet in the axial direction is much greater than the radial velocities of the random thermal motion. As a result, a dense gas jet–target with sharp boundaries with the vacuum is obtained in the vacuum chamber, making it possible to study subtle effects in the interaction of the electron beam with the particles of the jet target. The use of this low-temperature method has led to substantial progress in the physics of bremsstrahlung as a result of the observation of a novel type of bremsstrahlung—polarization bremsstrahlung (PB).[2,3]

According to current theoretical ideas,[4] bremsstrahlung, which arises in the scattering of a charged particle by a target particle (an atom or ion), is formed by two mechanisms. In the first case the photons are emitted by the incoming charged particle as it is braked in the static field of the target particle; this is ordinary bremsstrahlung (OB). It was discovered around 80 years ago in connection with the discovery of x rays. OB is characterized by a smooth spectral distribution of the photons and is well described by the Bethe–Heitler/Sauter (BHS) theory,[5,6] which is based on a screening approximation. According to that approximation, the electron shell of the atom or ion is replaced by the electrostatic field that it creates. The BHS theory was generally accepted until recently, and numerous calculations of the radiation spectra of fast particles passing through matter, the emission and absorption spectra of plasmas, etc., have been done in the framework of that theory.

In the period of 1970–1980, however, the physics of bremsstrahlung was reborn. A group of theorists[7–10] predicted another mechanism of bremsstrahlung formation, which was observed in specially designed experiments.[2,3] Essentially, in this mechanism the photons of the continuum are emitted not by the scattered particle, as in the first mechanism, but by electrons of the target particle as a result of its dynamic polarization by the field of the incoming particle. The bremsstrahlung formed by this mechanism has been given the name polarization bremsstrahlung (PB). Unlike the process described by the BHS theory, the electrons of the target are now treated as a dynamical system having internal degrees of freedom. Theoretical studies[4] have established that taking the influence of the electron shell of the atoms or ions into account will in a number of cases lead to substantially different results. The difference lies in different frequency and angular characteristics of the radiation and also in the a radiation probability that is independent of the mass of the incoming particle.

Thus the traditional BHS theory is strictly applicable only to individual ''structureless'' particles (e.g., the radiation emitted by an electron scattered on a proton) or to particles that emit at extremely high frequencies. In the technologically important optical and x-ray frequency regions, polarization effects have a substantial influence and can sometimes even play the governing role.

The important role of the polarization mechanism of bremsstrahlung is attested to by the fact that taking it into account makes it possible to explain a number of experimental facts that could not be explained in the framework of the BHS theory. These facts include, e.g., the breakdown of alkali metal vapor by laser radiation,[11] the appearance of ''giant'' maxima in the spectra of photons emitted in the bom-

 © 2002 American Institute of Physics

barding of rare-earth and transuranic metals by fast electrons,[12–14] the high x-ray intensity produced when a solid target is irradiated by fast protons,[15] the appearance of a band of continuum radiation above the band gap when cryocrystals of inert elements are irradiated by fast electrons,[16] etc.

Direct observation of PB was first achieved in the ultrasoft x-ray region of photon energies 70–220 eV in the scattering of 0.6-keV electrons on Xe atoms.[2,3] The PB was manifested as a wide band with a structure close to that of the ''giant'' resonance in the photoabsorption spectrum of Xe atoms. The successful completion of experiments on the observation of PB was made possible by the development of a low-temperature gas-jet method of generating electromagnetic radiation[17] and the creation of a unique low-temperature experimental apparatus utilizing that method.[18] It should be noted that the gas-jet method can be used to study PB in electron-scattering processes not only on atoms but also on clusters, which occupy an intermediate position between atoms and solids. The proposed program of research on PB therefore includes investigation of the spectra in the scattering of electrons both on atoms and on clusters of inert elements.

In this paper we present generalized results of experimental and theoretical research on the differential spectra of PB in the ultrasoft x-ray region in the scattering of electrons of intermediate energies on atoms of inert elements.

GAS-JET METHOD OF GENERATING ELECTROMAGNETIC RADIATION

In the gas-jet method of generating electromagnetic radiation, a spatially bounded supersonic gas jet formed in a vacuum chamber and pumped out by cryogenic pumps is excited by an electron beam. The crossing region where the jet and electron beam intersect is a source of electromagnetic radiation in a wide range of wavelengths, including the ultrasoft x-ray (USX), vacuum ultraviolet (VUV) ($\lambda < 200$ nm), near ultraviolet (200–400 nm), visible, and infrared regions of the spectrum.

The gas-jet method has several important features. The first is that the gas flow in the subsonic part of the nozzle is at close to room temperature and essentially contains only atoms of the gas, but after passing into the supersonic part of the nozzle the gas expands isentropically and is cooled to a temperature of ~ 10 K and is found in a supersaturated state. For this reason, in certain regimes of flow the homogeneous condensation of the gas in the jet will be accompanied by the formation of clusters (aggregations of atoms bound by van der Waals forces).[19]

At low pressures P_0 and high temperatures T_0 of the gas at the entrance to the nozzle, conditions can be created in which the jet has a purely atomic composition. However, with increasing pressure P_0 (at $T_0 = \text{const}$) or with decreasing gas temperature T_0 (at $P_0 = \text{const}$) the formation of clusters containing from two to hundreds of thousands of atoms will occur.[20] Thus the gas-jet method offers a real opportunity for studying PB in qualitatively new processes, specifically, in collisions of electrons with clusters of different sizes.

The second important feature of the gas-jet method consists in the following. Thanks to the relatively sharp boundaries of the jet with the vacuum, placing the electron gun close to the supersonic jet will make it possible to obtain the emission spectra of atoms and clusters as the electron beam successively probes the electron shells of the atom from the valence to the innermost K shell. By varying the electron energy, one can create favorable experimental conditions for studying bremsstrahlung, specifically, to study a region of bremsstrahlung photon energies in which the bremsstrahlung spectrum does not have any atomic emission lines superimposed on it.

Finally, the third feature of the gas-jet method is the possibility of delivering the generated radiation into a high-vacuum chamber at a pressure of 10^{-5}–10^{-6} Pa in a large solid angle without the use of optical windows. This possibility is particularly important for the relatively inaccessible VUV and USX regions of spectroscopy, for which there are no mechanically tough transparent materials and the systems along the propagation path of the radiation must be evacuated. And it is in those regions where polarization effects are most clearly manifested.[4]

These features have brought the gas-jet method of generating electromagnetic radiation into wide use for solving some pressing scientific problems in the fields of gas dynamics, cluster physics, the physics of atomic and electron collisions, and VUV and USX spectroscopy.[3,20–23]

CHOICE OF OBJECTS FOR STUDYING POLARIZATION BREMSSTRAHLUNG

In the scattering of a fast electron on an atom, the spectral distribution of bremsstrahlung photons $d\sigma(\omega)$ in the logarithmic approximation has the form ($e=\hbar=m=1$):[10]

$$d\sigma(\omega)=\frac{16}{3}\left(\frac{z^2}{c^3p^2\omega}\ln\frac{2p}{z^{1/3}}+\frac{\omega^3|\alpha(\omega)|^2}{c^3p^2}\ln\frac{p}{\omega\tau_0}\right)d\omega, \tag{1}$$

where p is the momentum of the incoming electron, ω is the photon energy, $\alpha(\omega)$ is the dynamic polarizability of the atom, z is the nuclear charge, and τ_0 is the radius of the subshell giving the largest contribution to the polarizability of the atom. The first term in (1) describes ordinary bremsstrahlung, i.e., the emission of a photon by a fast electron as it is braked in the static field of the atom. OB is characterized by a smooth spectral distribution of photons, proportional to $1/\omega$. The intensity of the spectrum of OB, proportional to $\omega d\sigma(\omega)/d\omega$, is independent of the energy of the emitted photon. The second term in (1) describes polarization bremsstrahlung, i.e., the emission of a photon by the atom on account of its dynamic polarization by the field of the incoming electron. According to Eq. (1), PB, unlike OB, is characterized by a nonmonotonic frequency dependence, which basically repeats the trend of the frequency dependence of the dynamic polarizability of the atom and gives the largest contribution in those parts of the spectrum where the dynamic polarizability of the atom is large. On the other hand, the imaginary part of the dynamic polarizability of an atom, $\mathrm{Im}\,\alpha(\omega)$, can be expressed, according to the optical theorem, as[24]

$$\mathrm{Im}\,\alpha(\omega)=\frac{c}{4\pi\omega}\sigma_j(\omega). \tag{2}$$

Here $\sigma_j(\omega)$ is the photoabsorption cross section, which for many atoms has a ''giant'' resonance in the USX region of the spectrum above the threshold for ionization of the $4d$ subshell.[25–27] From an analysis of (1) and (2), even before calculating $\mathrm{Re}\,\alpha(\omega)$, we can conclude that a powerful resonance in the photoabsorption cross section will correspond to an analogous structure in the bremsstrahlung spectrum in the same region of photon energies. On this basis we have chosen Xe from among the inert elements as the main object for studying PB, as it has a ''giant'' resonance in the photoabsorption spectrum in the region of photon energies 70–150 eV.[25]

EXPERIMENTAL APPARATUS AND MEASUREMENT TECHNIQUE

A diagram of the experimental apparatus for studying bremsstrahlung is shown in Fig. 1. It consists of an x-ray tube with a supersonic gas jet as the anode and an RSM-500 spectrometer–monochromator.[18] The working principle of the apparatus is as follows. The gas to be studied flows out of a high-pressure cylinder into a heat exchanger *1*. Having acquired the specified temperature of the heat exchanger, the gas is formed by a conical nozzle *2* into a jet *9* flowing into the vacuum chamber. The diameter of the nozzle throat is 0.38 mm, and the ratio of the area of the exit section to the area of the throat is 35.4. A liquid-hydrogen-cooled cryogenic pump *4* is used to pump out the gas brought in by the jet. Thanks to the sharp boundaries of the supersonic gas flow with the vacuum (10^{-3} Pa), the electron gun *3* is placed only 40 mm from the jet, forming a beam with energy from 100 to 2000 eV and current density from 0.1 to 1 A/cm^2. The electron beam crosses the jet at a distance of 5 mm from the exit section of the nozzle, perpendicular to its axis. The radiation that arises is focused by a spherical mirror *8* onto the entrance slit *7* of the RSM-500 spectrometer–monochromator and is then dispersed into a spectrum by a gold-coated diffraction grating *5* having 600 lines/mm. Beyond the exit slit of the RSM-500 spectrometer–monochromator the radiation is registered by a proportional counter *6* of the SRPP-203 type, filled with methane to a pressure of 1.5×10^4 Pa. A nitrocellulose film is used as the window on the counter.

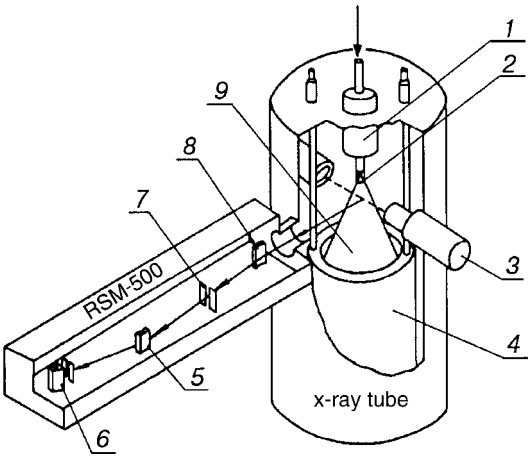

FIG. 1. Diagram of the experimental apparatus: *1*—heat exchanger, *2*—supersonic conical nozzle, *3*—electron gun, *4*—cryogenic pump, *5*—diffraction grating, *6*—proportional counter, *7*—entrance slit of the spectrometer–monochromator, *8*—mirror, *9*—supersonic gas jet.

The bremsstrahlung experiments were done in the single-collision region, as is attested to by the linear trend of the dependence of the bremsstrahlung intensity on the current density of the electron beam. The experiments were done under the following conditions.

1. The range of photon energies studied was 60–220 eV.

2. The spectral resolution was 1 Å.

3. The range of variation of the energy of the excited electrons was 0.3–0.9 keV, which made it possible to avoid ionization of the $3d$ subshell of Xe and the consequent appearance of multiple-line spectra in the investigated region of photon energies.[28]

4. The gas pressure ($P_0=3\times10^4$ Pa) and the temperature at the entrance to the nozzle ($T_0=650$ K) ensured:

—a monatomic composition of the jet;

—a density of atoms equal to 8×10^{15} cm^{-3} at the crossing region of the jet and electron beam;

—not more than 5% self-absorption of the radiation by the Xe atoms.

5. Solid angle of collection of the radiation equal to $d\Omega=1.7\times10^{-3}$ sr.

It should be noted that there are both bremsstrahlung spectra integrated over emission directions and differential spectra specified by the angle between the direction of motion of the electron and the direction of the emitted photon.[4] In the present studies we measured the differential spectra of the bremsstrahlung. Here the angle between the direction of motion of the incoming electrons and the direction of the analyzed photons was $\chi=97°$.

For comparison of the experimental and theoretical spectra it is important to know the true shape of the spectrum. Here we took into account the distortions introduced in the spectrum by the efficiency of the RSM-500 spectrometer by the method described in Ref. 28. In converting from the number of photons measured in the wavelength interval $N_\lambda d\lambda$ to the number of photons in the frequency interval $N_\omega d\omega$ we introduced a normalizing coefficient $N_\omega=\lambda^2 N_\lambda$.

Two series of experiments were done. In the first series the profile of the bremsstrahlung spectra was investigated for different electron energies. This was done by measuring the spectral distribution of the bremsstrahlung intensity in the scattering of electrons with energies of 0.3, 0.6, and 0.9 keV on Xe atoms (at different electron beam currents). The spectra obtained were averaged over 8–10 measurements. The energy position of the maximum of the intensity of the spectra was determined to an error of ±2 eV. The error of determination of the relative intensity of the bremsstrahlung spectra, including the random and systematic errors of measurement, was 10%.

In the second series of experiments we studied the dependence of the intensity of the bremsstrahlung spectrum on the energy of the electrons scattered on Xe and Ar atoms. This was done by measuring the spectral distribution of the bremsstrahlung intensity in the scattering of electrons with energies of from 0.3 to 0.9 keV on Xe atoms and with ener-

gies of 0.3 to 2 keV on Ar atoms (at a constant electron beam current).

RESULTS OF THE INVESTIGATIONS

Differential bremsstrahlung spectra in the scattering of electrons of intermediate energies on Xe atoms

Figure 2 shows the photoabsorption spectrum of Xe in the region of the $4d$ ionization threshold and the bremsstrahlung spectra obtained in the scattering of electrons with energies of 0.3, 0.6, and 0.9 keV on Xe atoms. It follows from an analysis of the results that the bremsstrahlung spectrum recorded at a fixed electron beam energy is significantly different from the spectrum of ordinary bremsstrahlung described by the BHS theory. In fact, as we have said, the intensity of the OB spectrum is independent of the photon energy, i.e., the spectral distribution of the intensity should be a straight horizontal line. However, instead of a horizontal line one observes a broad emission band with a pronounced maximum, the profile of which in its general features is similar to the profile of the ''giant'' resonance in the photoabsorption spectrum (see Fig. 2). The observed band is polarization bremsstrahlung and is formed by virtual transitions of electrons of the Xe atom to states of the continuum above the $4d$ ionization threshold.[3]

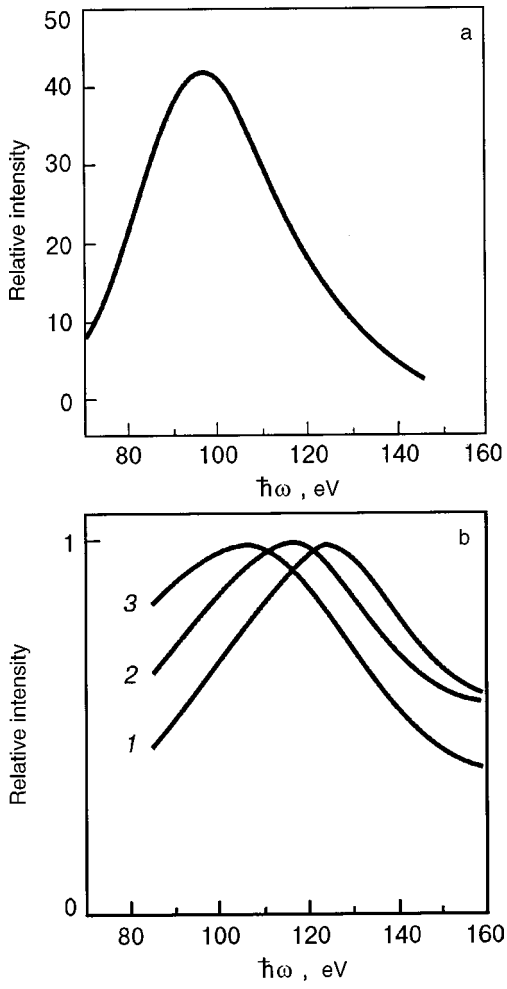

FIG. 2. Photoabsorption spectrum of Xe from Ref. 25 (a); bremsstrahlung spectra obtained in the scattering, on Xe atoms, of electrons of various energies E [keV]: 0.3 (*1*), 0.6 (*2*), and 0.9 (*3*). Each spectrum is normalized to its maximum (b).

The clearest feature of the spectra is the shift of the spectral curve of the bremsstrahlung to lower photon energies as the electron energy increases, i.e., the bremsstrahlung curve approaches that of the resonance in the photoabsorption spectrum.

To explain the cause of the shift of the bremsstrahlung spectrum with changing electron energy, Zon and co-workers investigated the differential bremsstrahlung spectra theoretically[1] for the conditions of our experiments as to the energies of the incoming electrons and the angle χ. The studies were done in the Born approximation. Calculations of the atomic characteristics were done by the method of the relativistic local electron density functional[29] (with all the atomic electrons taken into account), in which the correlation effects are treated phenomenologically.[30,31] Calculation of the OB cross section $d\sigma_e$ shows that it is a smooth function of the emitted photon frequency and varies by not more than 10%.[1] Therefore the shift of the bremsstrahlung spectrum with changing electron energy cannot be due to the BO cross section. For this reason only the PB cross section $d\sigma_a$ was analyzed in Ref. 1.

The differential cross section of PB in the Born approximation has the form[1]

$$\frac{d\sigma_a(\chi,\omega)}{\sin\chi d\chi}=\frac{\alpha}{\pi v^2c^2}|\omega^2\alpha(\omega)|^2 \times\left\{[\varepsilon\sin^2\chi+2(1+\varepsilon)\cos^2\chi]L-2(1-\varepsilon) \times\left(\cos^2\chi-\frac{1}{2}\sin^2\chi\right)\right\}\frac{d\omega}{\omega}. \quad (3)$$

In particular, for $\chi=\pi/2$ (close to the experimental value $\chi=97°$) it was found in Ref. 1 that

$$\frac{d\sigma_a(\pi/2,\omega)}{d\chi}=\frac{\alpha}{\pi v^2c^2}|\omega^2\alpha(\omega)|^2(1+\varepsilon L)\frac{d\omega}{\omega}, \quad (4)$$

where the parameters $\varepsilon\equiv m\hbar\omega/p^2\ll 1$, and $L\equiv\ln(\gamma v^2/(\omega^2R_a^2))$. Here $\alpha=e^2/\hbar c\approx 1/137$, $R_a\approx\hbar/mv_a$ is the characteristic size of the electron shell of the atom, γ is a factor of the order of unity, the indeterminacy of which is due to the indeterminacy of the scattering angle $\Theta_a\approx v_a/v$ (v is the velocity of the incoming electron, and v_a is the velocity of the electrons of the atom). Since $|\alpha(\omega)|^2$ is a rather symmetric curve in the neighborhood of the maximum, we can describe it by a Lorentzian function:

$$|\alpha(\omega)|^2=\alpha_0^2\frac{\omega_0^2}{(\omega-\omega^0)^2+\Gamma^2}, \quad (5)$$

where ω_0 determines the position of the maximum and Γ is the half-width of the curve of $|\alpha(\omega)|^2$.

The position of the frequency $\omega_{\max}$ corresponding to the maximum of the cross section $\omega d\sigma_a/(d\chi d\omega)$ is easily obtained after substituting (5) into (4).

TABLE I. Experimental and theoretical values of the positions of the maxima on the polarization bremsstrahlung spectra.

Electron energy E, keV	Position of the maximum, $\hbar\omega_{max}$, eV	
	Experiment	Calculation
0.3	123	126
0.6	115	114
0.9	105	113

Neglecting the frequency dependence of the parameter L and assuming that $\omega_{max}=\omega_0+q$, $q\ll\omega_0$, the authors in Ref. 1 obtained a simple expression for q:

$$q=\frac{2\Gamma^2}{\omega_0}\,\frac{1+5\varepsilon L/4}{1+[1-5(\Gamma/\omega_0)^2/2]\varepsilon L}. \tag{6}$$

In calculating the parameter L it was assumed that $\omega=\omega_0$, $\gamma=1$, and $R_a=0.2\times10^{-8}$ cm (the size of the $4d$ subshell of Xe), and for calculating q the theoretical values of ω_0 and Γ obtained in Ref. 1 were used: $\hbar\omega_0=100$ eV, $\Gamma=24$ eV.

Table I gives the values of the positions of the maxima in the PB spectra as obtained experimentally and as calculated with the use of formula (6).

It is seen from the table that formula (6), which contains the parameter $\varepsilon\equiv m\hbar\omega/p^2$, correctly conveys the character and order of magnitude of the variation of ω_{max} with electron energy: $\propto p^2$. We note that according to expression (3), the formula (6) for the calculation of q will have a different form for different angles χ. This means that the position of the maximum on the PB curve ($\omega_{max}=\omega_0+q$) will also depend on the angle between the direction of motion of the electrons and the direction of the emitted photons.

On the basis of the given results of experimental and theoretical studies of the differential spectra of the bremsstrahlung emitted in the scattering of electrons of intermediate energies on Xe atoms, one can draw the following conclusions.

1. The maximum observed in the bremsstrahlung spectrum in the region of the ''giant'' resonance in the photoabsorption spectrum of the Xe atom is due to the polarization mechanism of bremsstrahlung.

2. The position of the maximum on the PB dispersion curve depends on the energy of the incoming electrons and the angle between the direction of motion of the electrons and the direction of emission of the bremsstrahlung photons.

3. In the asymptotic Born limit the dispersion curves of the photoabsorption and PB are qualitatively similar. However, there is a slight difference in the positions of the maxima of these spectra. This difference is mainly due to the fact that the photoabsorption is governed by the imaginary part of the dynamic polarizability of the atom, while the PB is governed by its absolute value.

4. The position of the maximum of the experimental dispersion curves of the bremsstrahlung is satisfactorily described in the Born approximation and is consistent with the calculations of the atomic characteristics by the relativistic local electron density functional method.

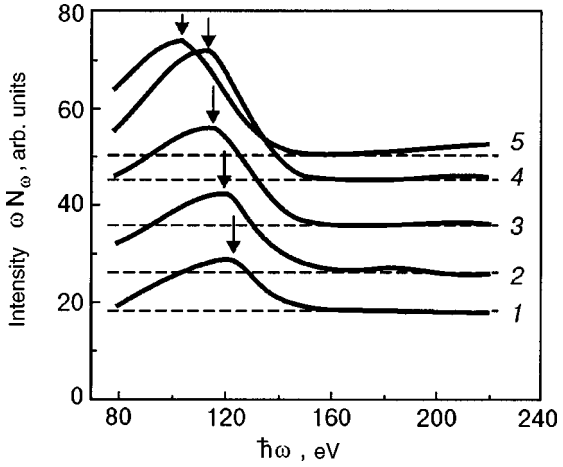

FIG. 3. Total bremsstrahlung spectra for different energies of the scattered electrons E [keV]: 0.3 (*1*), 0.4 (*2*), 0.5 (*3*), 0.6 (*4*), and 0.9 (*5*). The arrows indicate the position of the maxima of the dispersion curves of the polarization bremsstrahlung [eV]: 123 (*1*), 120 (*2*), 117 (*3*), 115 (*4*), 105 (*5*); the dashed lines show the extrapolated intensity of the ordinary bremsstrahlung.

Dependence of the intensity of the differential bremsstrahlung spectra on the energy of the electrons scattered on Xe atoms

The spectral distributions of the bremsstrahlung intensity for different energies of the scattered electrons are shown in Fig. 3.

It should be noted that in these experiments the density n of Xe atoms, the electron beam current i, and the geometric dimensions L of the excitation region of the jet were the same for all the electron energies studied.[32] Therefore, the changes of the spectral distribution of the intensity of the differential bremsstrahlung spectra $I(\hbar\omega)$ for different values of the electron energy E reflect the changes of the spectral distribution of the differential bremsstrahlung cross section $d\sigma/d\omega d\Omega$ with electron energy according to the equation

$$\frac{d\sigma}{d\omega d\Omega}=\frac{I(\hbar\omega)}{n(i/e)\hbar\omega}\,\frac{1}{L}. \tag{7}$$

It follows from Fig. 3 that in the region of photon energies $\hbar\omega>160$ eV, in which the contribution of the PB is insignificant, the spectral distribution of the bremsstrahlung intensity is independent of the photon energy, i.e., it has the same trend as the curve of the OB intensity. However, in the region of photon energies $\hbar\omega<160$ eV, in which the dynamic polarizability of the Xe atom is large, a substantial contribution to the bremsstrahlung intensity is given by the PB in addition to the OB. Indeed, if the intensity of the OB spectrum is extrapolated into the region of lower photon energies (the dashed straight lines in Fig. 3), then the intensity of the bremsstrahlung spectrum at the maximum is larger than the intensity of OB by a factor of approximately 1.6. The wide bands with pronounced peaks above the dashed lines are the PB spectra for the different electron energies.

An analysis of the results given in Figs. 3 and 4 reveals an important feature—the intensity of the bremsstrahlung spectra increases with increasing electron energy, even though, according to the Born approximation, the intensity of both the differential[1] and integrated [formula (1)] brems-

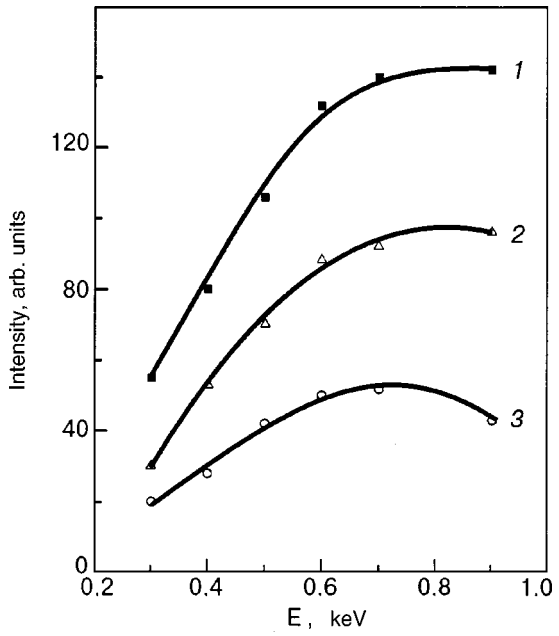

FIG. 4. Intensity at the maxima of the bremsstrahlung (1), ordinary bremsstrahlung with a photon energy of 117.1 eV (*2*), and polarization bremsstrahlung (*3*) versus the energy of the scattered electrons.

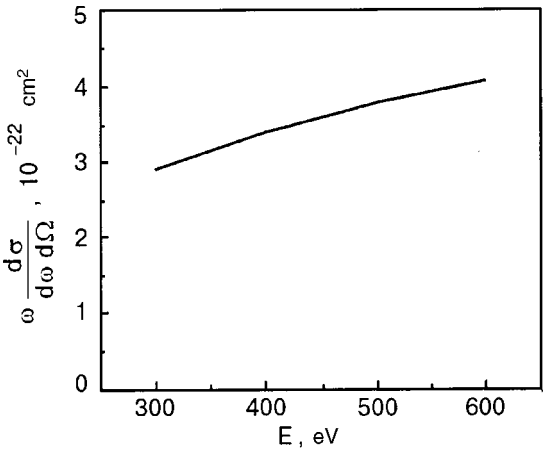

FIG. 5. Theoretical dependence of the differential bremsstrahlung cross section ($\hbar\omega = 177.1$ eV) on the energy of the incoming electron.[33]

strahlung spectra should decrease with increasing electron energy. Growth of the intensity is characteristic for both the OB in the region of photon energies $\hbar\omega > 160$ eV and for the PB in the region $\hbar\omega < 160$ eV (see Fig. 4), but in contrast to the OB the $I(E)$ curve for PB has a maximum in the region 0.6–0.8 keV.

Before turning to a discussion of the results, we should note that there are different types of collisions between an electron and an atom which can lead to the emission of a bremsstrahlung photon.[4] The most highly radiative processes are those in which the atom remains in the ground state after the collision (elastic bremsstrahlung). However, other processes, in which the atom changes its original state as a result of the collision and emission of the bremsstrahlung photon, i.e., is excited or ionized (inelastic bremsstrahlung), are also possible. It should be emphasized that the well-known expressions for the bremsstrahlung cross sections, describing a decrease of the cross sections with increasing energy of the scattered electrons, were obtained for elastic bremsstrahlung processes.[4] There have as yet been no consistent calculations of the cross sections for the inelastic bremsstrahlung processes.

From what we have just said, the growth of the bremsstrahlung intensity in the scattering of electrons of intermediate energies on Xe atoms may be due to an increase in the number of opened excitation or ionization channels accompanying the braking effect. This was the point of view expressed in Ref. 33, where the low-energy theorem[34] was used to explain the experimentally observed growth of the intensity of OB as the electron energy increases from 0.3 to 0.9 keV (see Fig. 4). According to the low-energy theorem, for photons whose energy energy is significantly less than the energy of the incoming electron, the bremsstrahlung cross section σ is expressed in terms of the ''non-braking'' scattering cross section σ_0^e as[33,34]

$$\frac{d\sigma}{d\omega d\Omega} \approx \frac{\alpha v^2}{4\pi^2 c^2 \omega}\left[1+\frac{2}{3}\left(1-\frac{1}{2}\cos^2\chi\right)\right]\sigma_0^e, \tag{8}$$

where α is the fine structure constant, v is the velocity of the incoming electron, ω and Ω are the frequency and solid angle of the emitted bremsstrahlung photon, and χ is the polar angle of emission of the photon with respect to the incident electron. For the geometry of our experiment (with the angle χ close to 90°), expression (8) assumes the simpler form[33]

$$\frac{d\sigma}{d\omega d\Omega} \approx \frac{5\alpha v^2}{12\pi^2 c^2 \omega}\sigma_0^e. \tag{9}$$

To take into account the contributions of both the elastic and inelastic bremsstrahlung, Zon[33] calculated the differential cross sections according to formula (9) using the experimental values of the total cross sections for the scattering of electrons on Xe atoms from Ref. 35, which take into account the contributions of all elastic and inelastic ''non-braking'' scattering processes.

Figure 5 shows the theoretical dependence of the differential cross section of ordinary bremsstrahlung (with a photon energy 177.1 eV) on the energy of the incoming electron, according to formula (9). We see that a smooth growth of the bremsstrahlung cross section (and, hence, of the intensity) is observed as the electron energy increases from 0.3 to 0.6 keV. It is of interest here to ascertain the behavior of $I(E)$ for bremsstrahlung in a wider range of electron energies. However, to do such experiments by the scattering of electrons on Xe atoms is impossible, since increasing the electron energy E above 0.9 keV leads to the efficient ionization of the $3d$ subshell of the Xe atom and to the appearance of a multiple-line spectrum in the investigated region of photon energies 60–220 eV.[28] Therefore, in these experiments we used argon as the working substance of the jet. This made it possible to measure the $I(E)$ curve in a broader range of electron energies, 0.3–2 keV, and thereby to obtain information about the dependence of the energy of the bremsstrahlung spectra on the electron energy.

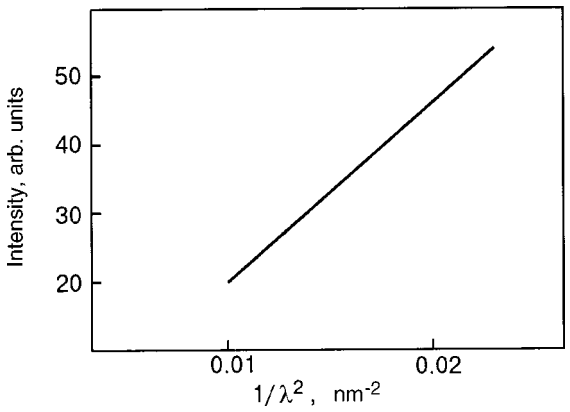

FIG. 6. Bremsstrahlung spectrum at an energy of the incoming electrons of 1 keV. For convenience of comparison with the data of Ref. 37 the curve is plotted versus $1/\lambda^2$.

Dependence of the intensity of the differential bremsstrahlung spectra on the energy of the electrons scattered on Ar atoms

Experiments were done on an argon jet of atomic composition with a particle density of 2.3×10^{16} cm^{-3} for energies of the scattered electrons in the interval 0.3–2 keV and photon energies in the range 124–191 eV (10–6.5 nm), where the dynamic polarizability of the Ar atom is small.[36] In this region of photon energies the spectrum is free of superimposed characteristic emission lines of the Ar atom. The remaining experimental conditions are the same as for the scattering of electrons on Xe atoms.

As an example, in Fig. 6 we show the bremsstrahlung spectrum obtained in the wavelength interval 6.5–10 nm at an electron energy of 1 keV. Analogous spectra are obtained for the other electron energies in the range 0.3–2 keV. The spectrum shown is characterized by a smooth distribution of intensity, which varies with wavelength in proportion to $1/\lambda^2$. This result agrees with the data[37] for the OB of a thin anode.

The dependence of the OB intensity on the electron energy E is shown in Fig. 7 for several wavelengths in the interval 6.5–10 nm. We see that the bremsstrahlung intensity I increases $\propto E^{1/2}$ as the electron energy increases from 0.3 to 0.7 eV, and upon further increase of the electron energy to 2 keV it decreases $\propto 1/E^{1/2}$.

It should be noted that the $I(E)$ curves of the bremsstrahlung spectra obtained in the scattering of electrons of intermediate energies on the Ar and Xe atoms are in good agreement with each other in the electron energy region 0.3–0.7 keV: in both cases one observes a growth of the bremsstrahlung intensity with increasing electron energy, in disagreement with the $I(E)$ curve obtained in the Born approximation.[1,10]

The observed increase in the bremsstrahlung intensity as the electron energy increases from 0.3 to 0.7 keV is apparently due to an increase in the number of opened excitation or ionization channels accompanying the braking effect, i.e., to an increase in the contribution of inelastic bremsstrahlung processes. To take the contributions of both the elastic and inelastic processes to the formation of the bremsstrahlung into account we calculated the differential bremsstrahlung

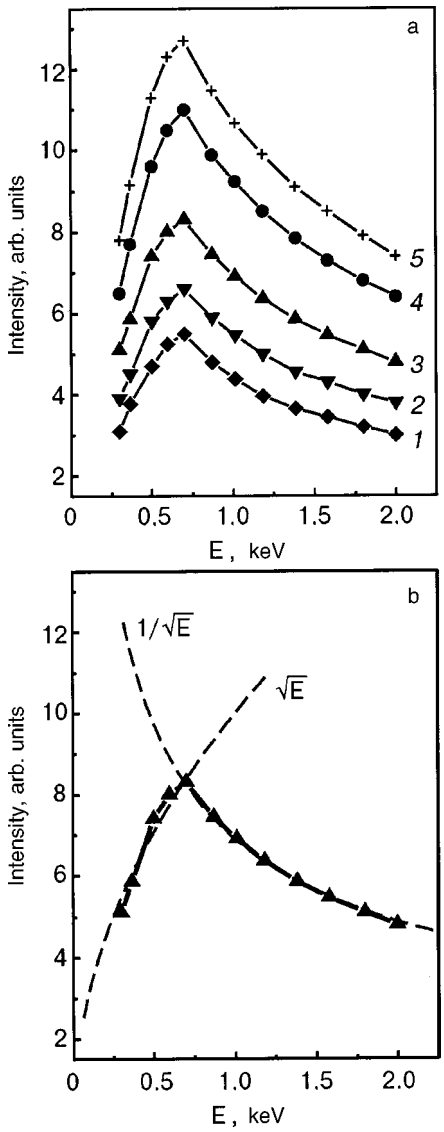

FIG. 7. Dependence of the bremsstrahlung intensity on the electron energy for different wavelengths: *1*—10 nm (124 eV), *2*—9 nm (137.8 eV), *3*—8 nm (155 eV), *4*—7 nm (177.1 eV), *5*—6.5 nm (190.8 eV) (a). The experimental dependence of the intensity at a wavelength of 8 nm on the electron energy. The dashed curves vary as $\sqrt{E}$ and $1/\sqrt{E}$ (b).

cross sections using Eq. (9). In the calculations we used the experimental values of the total cross sections for electron scattering on Ar atoms from Ref. 38, which take into account the contributions of all the elastic and inelastic process of ''non-braking'' scattering.

Figure 8 shows the experimental curve of the emission intensity at a photon energy of 177.1 eV as a function of the electron energy, normalized to the maximum intensity at energy $E=0.7$ keV. Also shown on the same figure is the theoretical curve of the differential bremsstrahlung cross section for a photon energy of 177.1 eV, normalized to the value of the cross section at $E=0.7$ keV. Since under the conditions of our experiments the intensity of the bremsstrahlung spectrum is proportional to the bremsstrahlung cross section [see Eq. (7)], the normalized intensity curve $I(E)/I_{\max}$ is the experimental dependence of the normalized bremsstrahlung cross section

$$\omega(d\sigma/d\omega d\Omega)[\omega(d\sigma/d\omega d\Omega)]^{-1}_{E=0.7\ \text{keV}},$$

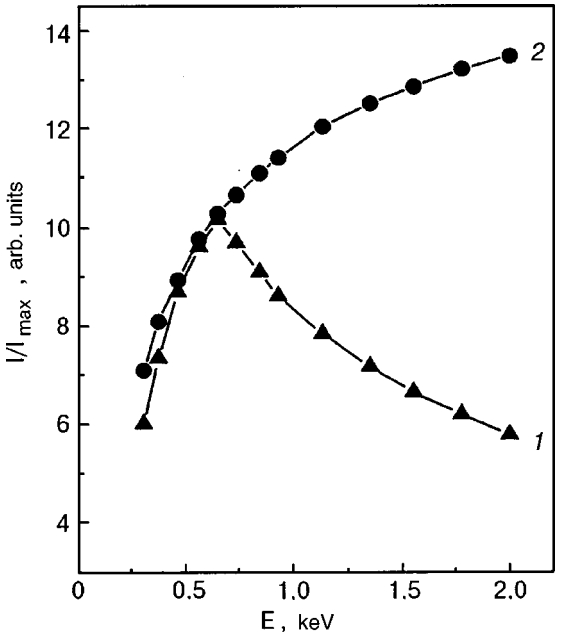

FIG. 8. Experimental dependence of $I/I_{\max}$ on the electron energy (*1*) and the theoretical dependence of $\omega(d\sigma/d\omega d\Omega)[\omega(d\sigma/d\omega d\Omega)]^{-1}_{E=0.7\ \mathrm{keV}}$ on the electron energy (*2*).

on the electron energy.

It follows from the data shown that the low-energy theorem [Eq. (9)] describes well that part of the experimental curve that reflects the growth of the bremsstrahlung intensity with increasing electron energy. This fact confirms the point of view that inelastic processes contribute to the increase in the bremsstrahlung intensity. We attribute the subsequent decline of the intensity with increasing electron energy from 0.8 to 2 keV to the decreasing number of excitation or ionization channels accompanying the braking effect. Here it should be noted that the decay of the intensity $I(E) \propto 1/\sqrt{E}$ does not agree with the corresponding decay of the bremsstrahlung intensity obtained in the Born approximation.[1] It follows that the Born approximation is inapplicable to the description of the bremsstrahlung cross sections in the scattering of electrons of intermediate energies on Ar atoms. Therefore additional theoretical studies are needed in order to achieve good agreement of the theory with experiment.

CONCLUSION

Analysis of the differential spectra of bremsstrahlung emitted in the USX region of the spectrum in the scattering of electrons of intermediate energies on atoms of inert elements have permitted us to observe experimentally and to elucidate the behavior of a novel type of bremsstrahlung, which is due to polarization effects. We have shown that the contribution of the polarization bremsstrahlung to the total bremsstrahlung spectrum is substantial in parts of the spectrum where the dynamic polarizability of the target atom is large. Studies of the differential PB spectra in the neighborhood of the ''giant'' resonance in the $4d$ photoabsorption spectrum of xenon show that the position of the maximum on the dispersion curve of the PB depends on the energy of the scattered electrons and on the angle between the direction of motion of the electrons and the direction of emission of the x rays. In the asymptotic Born limit the dispersion curves of the photoabsorption and PB of xenon match up with each other in a qualitative way.

Our studies have revealed an important feature—growth of the intensity of the differential bremsstrahlung spectra with increasing electron energy, due to the contributions of inelastic bremsstrahlung processes.

We have also established that the Born approximation used together with calculations of the atomic characteristics satisfactorily describes the experimentally observed position of the maximum of the bremsstrahlung dispersion curves. However, this approximation is inapplicable for describing the cross section (and, hence, the bremsstrahlung intensity) in the scattering of electrons of intermediate energies on atoms of Ar and Xe.

Based on what we have said, it is urgent and timely to do a theoretical investigation of bremsstrahlung in the scattering of intermediate-energy electrons on atoms and other particles, taking both elastic and inelastic bremsstrahlung processes into consideration. In addition, as we know, the spectrum of PB emission is governed by the internal structure of the colliding particles, and its study can yield additional and, at present time, unique information about this structure. In this connection it is important to study the influence (and manifestations) of the internal structure of atoms on the PB spectra arising in the interaction of electrons with polyatomic formations (clusters).

In closing we express our gratitude to Prof. V. V. Eremenko for his steady interest in and support of this work, and to Prof. B. A. Zon and Dr. V. N. Samovarov for fruitful discussions.

*E-mail: egnatchenko@ilt.kharkov.ua

[1] É. T. Verkhovtseva, E. V. Gnatchenko, B. A. Zon, A. A. Nekipelov, and A. A. Tkachenko, Zh. Éksp. Teor. Fiz. **98**, 797 (1990) [Sov. Phys. JETP **71**, 443 (1990)].
[2] É. T. Verkhovtseva, E. V. Gnatchenko, and P. S. Pogrebnyak, in *Abstracts of the VI All-Union Conference on the Physics of Vacuum Ultraviolet Radiation and the Interaction of Radiation with Matter* [in Russian], Moscow (1982), p. 50.
[3] E. T. Verkhovtseva, E. V. Gnatchenko, and P. S. Pogrebnjak, J. Phys. B **16**, L613 (1983).
[4] M. Ya. Amus'ya, V. M. Buĭmistrov, B. A. Zon, V. N. Tsytovich, V. A. Astapenko, E. B. Kleĭman, A. V. Korol', Yu. A. Kratov, A. B. Kukushkin, V. S. Lisitsa, I. M. Oĭringel', A. V. Solov'ev, and V. I. Kogan, Polyarizatsionnoe tormoznoe izluchenie chastits i atomov, Nauka, Moscow (1987).
[5] H. Bethe and W. Heitler, Proc. R. Soc. London, Ser. A **146**, 83 (1934).
[6] F. Sauter, Ann. Phys. (Leipzig) **9**, 217 (1931).
[7] V. N. Tsytovich, Tr. Fiz. Inst. Akad. Nauk SSSR **66**, 191 (1973).
[8] V. M. Buĭmistrov and L. I. Trakhtenberg, Zh. Éksp. Teor. Fiz. **69**, 108 (1975) [Sov. Phys. JETP **42**, 54 (1975)].
[9] M. Ya. Amus'ya, A. S. Baltenkov, and A. A. Paĭziev, JETP Lett. **24**, 332 (1976).
[10] B. A. Zon, Zh. Éksp. Teor. Fiz. **73**, 128 (1977) [Sov. Phys. JETP **46**, 65 (1977)].
[11] J. E. Rizzo and R. C. Klewe, J. Appl. Phys. **17**, 1137 (1966).
[12] T. M. Zimkina, V. A. Fomichev, and S. A. Gribovskiĭ, Fiz. Tverd. Tela (Leningrad) **15**, 2685 (1973) [Sov. Phys. Solid State **15**, 1786 (1973)].
[13] I. I. Lyakhovskaya, V. M. Ipatov, and T. M. Zimkina, Zh. Strukt. Khim. **18**, 668 (1977).
[14] T. M. Zimkina, A. S. Shu akov, and A. P. Braĭko, Fiz. Tverd. Tela (Leningrad) **23**, 2006 (1981) [Sov. Phys. Solid State **23**, 1171 (1981)].
[15] K. Ishii and S. Morita, Phys. Rev. A **30**, 2278 (1984).
[16] A. G. Belov, I. Ya. Fugol', and E. M. Yurtaeva, Fiz. Nizk. Temp. **21**, 238 (1995) [Low Temp. Phys. **21**, 183 (1995)].

[17] É. T. Verkhovtseva, Ya. M. Fogel', B. I. Verkin, V. S. Osyka, and V. N. Sokolov, ''Means of obtaining continuous emission spectra of inert gases in the ultraviolet region'' [in Russian], Inventor's Certificate (USSR) No. 226927; publ. Byul. Izobret., No. 29 (1968); É. T. Verkhovtseva, E. A. Bondarenko, and Yu. S. Doronin, ''Means of obtaining the emission spectra of inert gases in the vacuum ultraviolet region'' [in Russian], Inventor's Certificate (USSR) No. 1278611; publ. Byul. Izobret., No. 47 (1986).
[18] É. T. Verkhovtseva and P. S. Pogrebnyak, *Apparatus and Methods of X-Ray Analysis* [in Russian], ONPO ''Burevestnik,'' Mashinostroenie, Leningrad (1980), p. 153.
[19] D. Golomb, R. E. Good, and M. R. Busby, J. Chem. Phys. **57**, 3844 (1972).
[20] S. I. Kovalenko, D. D. Solnyshkin, E. T. Verkhovtseva, and V. V. Eremenko, Chem. Phys. Lett. **250**, 309 (1996).
[21] É. T. Verkhovtseva, in *Progress in Spectroscopy*, Vol. 1 [in Russian], Council on Spectroscopy of the Academy of Sciences of the USSR, Moscow (1978), p. 87.
[22] É. T. Verkhovtseva, Izv. Akad. Nauk SSSR **48**, 675 (1984).
[23] E. T. Verkhovtseva, E. A. Bondarenko, V. I. Yaremenko, and Yu. S. Doronin, *Rarefied Gas Dynamics*, Vol. 2, Plenum Press, New York and London (1985), p. 1063.
[24] R. Karaziya, *Introduction to the Theory of X-Ray and Electron Spectra of Free Atoms* [in Russian], Mokslas, Vilnius (1987).
[25] R. Haensel, G. Keitel, P. Schreiber, and C. Kunz, Phys. Rev. **188**, 1375 (1969).
[26] T. M. Zimkina and S. A. Gribovskiĭ, J. Phys. (Paris) **32**, Colloq. C4, 282 (1971).
[27] J. P. Connerade, B. Drerup, and M. W. D. Mansfield, Proc. R. Soc. London, Ser. A **348**, 235 (1976).
[28] E. T. Verkhovtseva, E. V. Gnatchenko, P. S. Pogrebnjak, and A. A. Tkachenko, J. Phys. B **19**, 2089 (1986).
[29] D. A. Liberman and A. Zangwill, Comput. Phys. Commun. **32**, 75 (1984).
[30] S. Lundqvist and N. H. March (Eds.), *Theory of Inhomogeneous Electron Gas*, Plenum Press, New York (1983).
[31] S. A. Zapryagaev and A. V. Mogilev, Opt. Spektrok. **59**, 730 (1985) [Opt. Spectrosc. **59**, 441 (1985)].
[32] A. A. Tkachenko, E. V. Gnatchenko, and É. T. Verkhovtseva, Opt. Spektrosk. **78**, 208 (1995) [Opt. Spectrosc. **78**, 183 (1995)].
[33] B. A. Zon, Zh. Éksp. Teor. Fiz. **107**, 1176 (1995) [JETP **80**, 655 (1995)].
[34] V. B. Berestetskiĭ, E. M. Lifshitz, and L. P. Pitaevskiĭ, *Relativistic Quantum Theory*, 2nd ed. [Pergamon Press, Oxford (1982); Nauka, Moscow (1980)].
[35] A. Zecca, G. Karwazg, R. Brusa, and R. Grisenti, J. Phys. B **24**, 2737 (1991).
[36] E. V. Gnatchenko, A. A. Tkachenko, and E. T. Verkhovtseva, in *Abstracts of the 13th International Conference on Vacuum Ultraviolet Radiation Physics, VUV-13*, Trieste, Italy (2001), p. TU 162.
[37] T. J. Peterson Jr. and D. A. Tomboulian, Phys. Rev. **125**, 235 (1962).
[38] A. Zecca, S. Oss, G. Karrovasz, R. Grisenti, and R. S. Brusa, J. Phys. B **20**, 5157 (1987).

Translated by Steve Torstveit

Field emission microscopy of the cluster and subcluster structure of a Zr–Ti–Cu–Ni–Be bulk metallic glass

A. S. Bakaĭ,* I. M. Mikhailovskij, and T. I. Mazilova

Kharkov Physicotechnical Institute National Research Center, ul. Akademicheskaya 1, 61108 Kharkov, Ukraine

N. Wanderka

Hahn-Meitner Institut, Glienickerstrasse 100, D-14109 Berlin, Germany
(Submitted February 7, 2002)
Fiz. Nizk. Temp. **28**, 400–405 (April 2002)

The cluster structure of a Zr–Ti–Cu–Ni–Be bulk metallic glass is investigated by the methods of high-resolution field emission microscopy. Internal interfaces are revealed, having a density of $\sim 10^6$ cm^{-1} and a width of approximately 1 nm. It is shown that the binding energy of the atoms at the intercluster boundaries is lower by 0.13–0.43 eV than in the interior of a cluster. Subcluster heterogeneities of the structure of the bulk amorphous alloy are observed, with a characteristic scale of the short-range order equal to 1.5–3 nm, attesting to the diversity of the short-range order in glassy melts. © *2002 American Institute of Physics.*
[DOI: 10.1063/1.1477363]

INTRODUCTION

Questions of the structure and structural defects of metallic glasses are widely discussed in the literature. The experimental data on the structure and properties of metallic glasses are usually interpreted using the two most highly developed models of the structure—the model of random close packings of spheres,[1] and the polycluster model.[2,3] These models have the following important difference: In the model of random close packing of spheres it is assumed that a homogeneous topological and compositional disorder is present, and numerical simulations indicate that both point and extended defects are unstable in these structures. The polycluster structures are formed by locally regular noncrystalline clusters, and the intercluster boundaries are stable; these structures contain coincident and noncoincident sites as in high-angle intercrystallite boundaries.[4] According to the estimates obtained in Refs. 2 and 3, the average binding energy of the atoms in the boundary layers is, in order of magnitude, 0.1 eV lower than in the interior of a cluster.

The question of the existence of internal interfaces in metallic glasses is important because defects of that kind determine the mechanical properties, low-temperature anomalies of the specific heat and thermal conductivity, and the kinetics of diffusion and crystallization of metallic glasses. A number of previous studies[5–7] by the methods of field emission microscopy have revealed internal interfaces in rapidly quenched amorphous alloys of the metal–metal and metal–metalloid type, the characteristic sizes of the cluster being of the order of 10 nm. Structural heterogeneities of subcluster sizes, 1–2 nm, have been observed in rapidly quenched amorphous alloys and identified as paracrystallite regions of medium-range order.[3,6,8]

Of particular interest are the observation and study of internal interfaces in bulk alloys[9,10] obtained by slow cooling of multicomponent melts. With a comparatively homogeneous compositional and topological disorder, one expects that the bulk alloys obtained by slow cooling will be have fewer defects and that the characteristic sizes of the clusters in them will be much larger than in rapidly quenched alloys. If the sizes of the cluster in a bulk glass and a rapidly quenched alloy turn out to be comparable, that would mean that the melts are appreciably inhomogeneous and that the heterogeneities are preserved upon glass formation, independently of the rate of cooling, and their scales do not depend strongly on the composition of the melt. The internal interfaces in highly disordered systems have not yet been investigated experimentally, primarily because of the complexity of deciphering the microdiffractograms. In this paper we report the application of high-resolution methods of combined field emission microscopy[7,11] to the study of the internal interfaces in the bulk of an amorphous alloy with the composition $Zr_{41}Ti_{14}Cu_{12.5}Ni_{10}Be_{22.5}$.

EXPERIMENTAL TECHNIQUE

We studied knifelike and axisymmetric tips prepared by electrochemical etching of amorphous foils and rods of a quenched bulk amorphous alloy with the composition $Zr_{41}Ti_{14}Cu_{12.5}Ni_{10}Be_{22.5}$. The alloy was prepared by induction melting of the pure components in a levitation device in an argon atmosphere with a subsequent quenching to room temperature. The alloy was quenched at a rate of the order of 10 K/s by placing it in contact with a water-cooled copper surface. The material was remelted in a quartz crucible and poured under pressure into a copper mold. The rods obtained had a length of 60 mm and diameters from 3 to 15 mm and, according to x-ray diffraction data, were amorphous with a macroscopically uniform structure. Examination by transmission electron microscopy revealed that the alloy contained a small number of primary crystals formed during quenching, with transverse sizes of the order of 10 μm. The composition of the primary crystals, which had an orthorhombic structure, corresponded to the phase $ZrBe_2$ with

 © 2002 American Institute of Physics

small admixtures of Ti, Cu, and Ni.[12] However, in our analysis with a field ion microscope no such crystallites were detected, possibly because of their preferential etching during the electrochemical preparation of the sharpened samples.

Shafts with a length of 10–15 mm and a cross section of 0.2×0.2 mm were cut from the rods using a diamond cutter. Needlelike tips with a radius of curvature of 10–200 nm were prepared by electrochemical polishing with a dc voltage of 5–15 V in a 10% solution of perchloric acid in ethyl alcohol. In experiments on anodic oxidation of the surface layers we used sharp-tip samples that had been additionally etched in this same electrolyte at a voltage of 2–3 V.

Studies were done in a two-chamber field emission (ion and electron) microscope.[13] As the imaging gas we used hydrogen and a mixture of 90% helium and 10% hydrogen at a pressure of $(4-8)\times10^{-3}$ Pa. In the experiments on decoration of the interfaces by anodic oxidation the imaging gas used was nitrogen at a pressure of 2×10^{-3} Pa. The surface of the samples after mounting in the microscope were cleaned by field desorption. Then a forming of the surface by field evaporation was carried out at 78 K to a depth of 10–50 nm. During the evaporation process a surface microtopography corresponding to the distribution of local threshold values of the evaporating electric field was formed.

To detect the internal interfaces in the amorphous alloy we used the techniques of band contrast of ion microscope images of knifelike samples,[5,6] prepared by field etching stimulated by active gases,[14] and decoration of the interfaces in anodic oxidation of the surface layers. The bands of contrast were formed on the emission ion microscope images in regions where the interface comes out to the surface as a result of the formation of a specific microrelief (localized saddle-shaped depressions with negative curvature of the surface) and the corresponding ion-optical effects. This method can be used to study the size distribution of structural heterogeneities in nonaxisymmetric samples prepared from thin foils. The technique of selective field etching was used to reveal the configuration of the interfaces, which were characterized by a lowered stability against evaporation stimulated by active gases.

EXPERIMENTAL RESULTS AND DISCUSSION

Field emission images of knifelike samples of the order of 10 nm thick were characterized by the presence of distinct bands of contrast which were preserved in the process of field evaporation (Fig. 1). In analyzing the band contrast we took into account the dependence of the local linear magnification on the angle coordinates. In particular, a preferential orientation of the contrast bands along the normal to the surface of the foil, which can be seen in Fig. 1, is due to the substantial difference of the local magnifications in the planes of the principal sections of the surface near the tips of nonaxisymmetric samples. The distances between bands are from 5 to 15 nm. The thickness of the evaporated layer was estimated from the change of the working voltage with an accuracy of up to 50%. Within these limits it agrees with the average distance between contrast bands. A study of the band contrast at the interfaces in knifelike samples by the methods of field ion microscopy of thin foils[5,6] showed that their origin lies in a developed network of internal two-dimensional

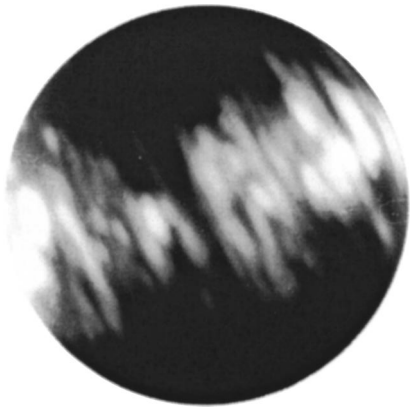

FIG. 1. Bands of bright contrast in the field ion microscope image of a bulk amorphous alloy with the composition $Zr_{41}Ti_{14}Cu_{12.5}Ni_{10}Be_{22.5}$.

interfaces in the rapidly quenched amorphous alloys. The presence of distinct contrast bands is due to local variations of the magnification around places where the internal interfaces come out to the surface. Analysis of the band contrast and its evolution in the course of field evaporation shows that the investigated $Zr_{41}Ti_{14}Cu_{12.5}Ni_{10}Be_{22.5}$ bulk alloy contains internal interfaces (intercluster boundaries) having an average density equal in order of magnitude to 10^6 cm^{-1}.

During the electropolishing of the sharpened samples of the alloy at low voltages (up to 2 V) we observed oxidation of the tips with the formation of an insulating surface film. This is indicated by the fact that increasing the voltage did not result in a smooth increase in the field emission current in accordance with the Fowler–Nordheim relation:[15] the emission increased in a jump, and, as a rule, vacuum breakdown was initiated. Analysis of the composition of the films on the surfaces of the electropolished tips of the $Zr_{41}Ti_{14}Cu_{12.5}Ni_{10}Be_{22.5}$ amorphous alloy by the atomic probe method showed that they are oxide layers. The morphology of these surface layers is characterized by a cellular structure (Fig. 2). The inhomogeneity of the structure of the film shows up with the highest contrast when nitrogen is used as the imaging gas. The cells had an irregular polygonal shape with transverse dimensions ranging from 2 to 15 nm, edged by boundaries with a high emission contrast. Within the error of determination of the linear dimensions (around 30%), the size distribution of the cells was the same as

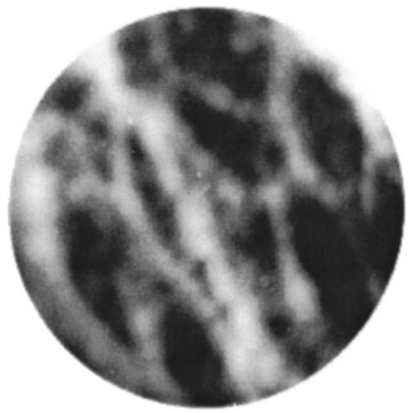

FIG. 2. Ion microscope image of intercluster boundaries, decorated by anodic oxidation, in a bulk metallic glass.

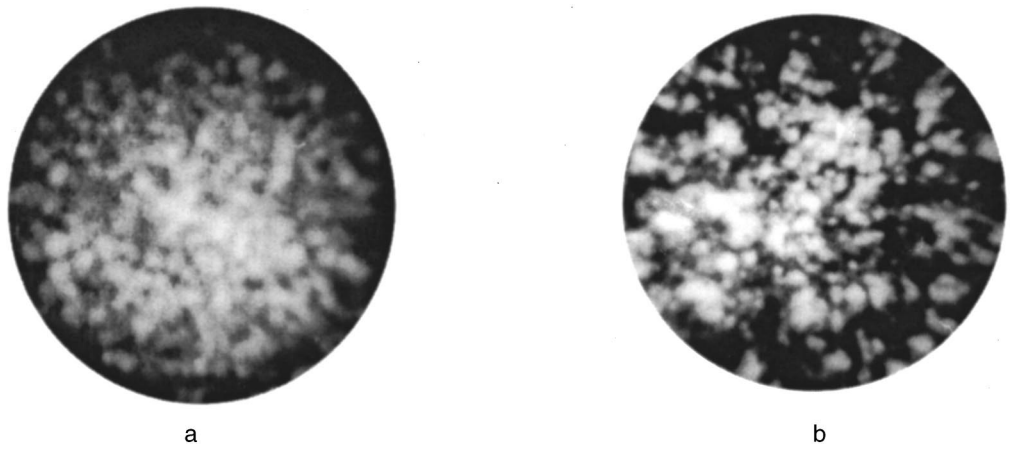

FIG. 3. Field ion microscopic image of the surface of a Zr–Ti–Cu–Ni–Be bulk amorphous alloy, obtained as a result of pulsed field evaporation (a) and stimulated field etching (b) in hydrogen.

the distribution of distances between contrast bands on the ion microscope images of the knifelike samples of the Zr–Ti–Cu–Ni–Be amorphous alloy. The observed picture attests to the fact that oxidation of the surface occurs preferentially at places where the intercluster boundaries emerge on the surface.

Typical ion microscopic images of axisymmetric samples prepared from amorphous alloys and formed by low-temperature field evaporation in high vacuum are characterized by an isotropic distribution of bright emitting centers, corresponding to irregularly distributed surface atoms.[6,7] In the case of pulsed field evaporation in a medium of active gases at a rate above 1 nm/s the ion image of the amorphous alloy is also an irregular set of emission centers (Fig. 3a). When the rate of field evaporation is decreased and hydrogen is used as the imaging gas, a selective field etching occurs which reveals the structural heterogeneities of the amorphous alloy (Fig. 3b). One observes compact nanometer atomic complexes—subclusters—surrounded by regions with a reduced image brightness. The high packing density of the atoms in these complexes is manifested, in particular, in the absence of point contrast, as is typical for ion microscope images of the most densely packed groups of atoms on the surface of the object under examination.[14] The observed reduction of the image brightness of the material at the periphery of subclusters indicates a lowering of the threshold values of the electric field for stimulated evaporation, which is accompanied by the formation of nanogroves of preferential field etching. The size distribution of the subclusters is shown in Fig. 4. Here we see the smeared maximum in the interval of 1.5–3 nm. We note that the previously observed regions of medium-range ordering in metallic glasses (see Refs. 3 and 8) have the same sizes. We see that the structure of the clusters which are separated by boundaries is inhomogeneous. The clusters consist of subclusters with different degrees of ordering of the atoms, as is attested to by the presence of selective field etching stimulated by active gases.

Analysis of the structure of the Zr–Ti–Cu–Ni–Be amorphous alloy by the method of field emission microscopy[11] revealed local variations of the energy of evaporation, with a characteristic scale of the order of 10 nm, which indicates the presence of structural heterogeneities. Figure 5b shows a typical field-emission image of a surface that has been formed by low-temperature field evaporation for a needlelike sample of a $Zr_{41}Ti_{14}Cu_{12.5}Ni_{10}Be_{22.5}$ bulk metallic glass with a polycluster structure. It is of particular interest to find the quantitative energy parameters characterizing these structural heterogeneities. The method of determining the field evaporation energy Q of a material from the result of a study of the morphology of needlelike samples formed by low-temperature field evaporation is as follows. In the framework of the field-evaporation model proposed in Ref. 14, one obtains the following expression for Q:

$$Q=(ne)^{3/2}F^{1/2}, \tag{1}$$

where n is the ionization (charge) state of the evaporated atom, F is the electric field of activationless evaporation, and e is the charge of the electron. For a sample surface that has been preliminarily formed by field evaporation, the variations of the local electric field on the surface when the microscope is operated in a field-emission mode are determined by the inhomogeneity of the distribution of the field-evaporation energy. Thus for calculating the local variations of the field-evaporation energy one can use the Fowler–Nordheim relation, which describes the dependence of the field-emission current density j on the strength of the electric field.[15] It follows directly from the Fowler–Nordheim relation that the logarithmic derivative of j with respect to the

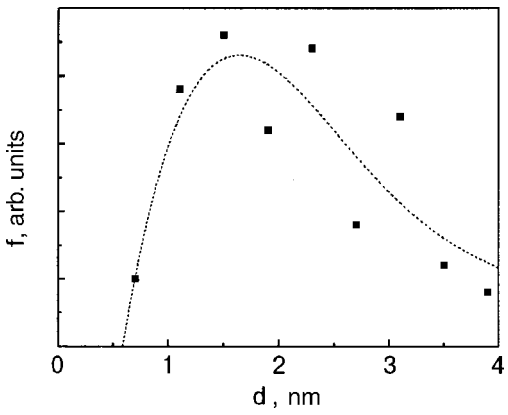

FIG. 4. Size distribution of subclusters in the bulk metallic glass.

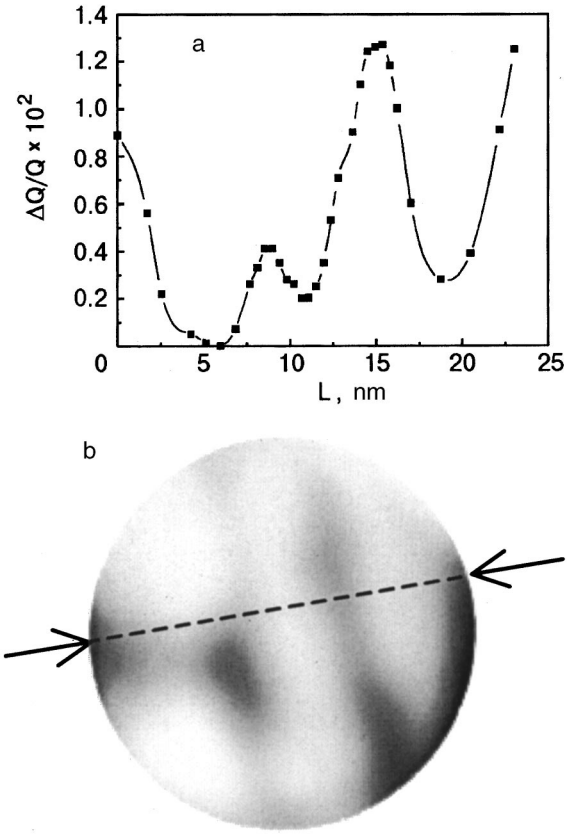

FIG. 5. Variation of the field evaporation energy of a polycluster metallic glass (a) in the cross section indicated by arrows on the field emission image of this surface (b).

reciprocal of the electric field is constant to within 5–7% in the interval $2.5\ \text{V/nm} < F < 4\ \text{V/nm}$ used in field-emission microscopy. With allowance for this circumstance it is easily shown that

$$\frac{\Delta Q}{Q} = \frac{1}{2\chi}\frac{\Delta j}{j}, \tag{2}$$

where χ is the field-sensitivity factor of the field emission, equal to (17 ± 3). Upon exponentiation of the field-emission image on photographic film in the linear region of optical blackening density the quantity $\Delta j/j$ can be obtained by a microphotometric method. Figure 5a shows the curve calculated according to formula (2) for the variation of the field-evaporation energy of an amorphous sample, $\Delta Q/Q$, in a cross section passing through three clusters (Fig. 5b). It follows from Figs. 5a and 5b that the minimum field evaporation energy corresponds to the boundaries of the clusters.

It is difficult to determine the absolute value of the energy of activationless field evaporation from formula (1) because of the complexity of the field evaporation spectrum of an alloy. Analysis of the evaporation spectrum with the aid of a field ion microscope—the atomic probe described in Ref. 12—showed that beryllium, copper, titanium, and nickel evaporated predominantly in the form of doubly charged ions, while zirconium evaporated as doubly and triply charged ions. The average value of the charge state n of the evaporated ions is close to two. The absolute value of the electric field for evaporation of the central part of the clusters can be determined by comparing the voltage for activationless evaporation of the alloy (at 78 K) with the best-image voltage in neon, which corresponds to a field of 35 V/nm.[14] The electric field determined by this method turns out to be equal to (39 ± 5) V/nm, and, accordingly, the field evaporation energy $Q = 33$ eV. The lowering of the evaporation energy in the region of the intercluster boundaries in the quenched amorphous Zr–Ti–Cu–Ni–Be alloy studied was from 0.13 to 0.43 eV. The values obtained for the difference of the binding energy of atoms to the intercluster boundaries and in the interior of the cluster are comparable in magnitude to the difference of the binding energies of atoms at high-angle intercrystallite boundaries and in the interior of the grains of metallic alloys.[4]

CONCLUSION

By a number of methods of high-resolution field emission microscopy we have observed internal interfaces with a density of $10^6\ \text{cm}^{-1}$ in a Zr–Ti–Cu–Ni–Be bulk metallic glass. Since similar structures with the same dimensions and density are observed in rapidly quenched amorphous alloys, the glass-forming melts must be compositionally and structurally inhomogeneous, and the heterogeneities are preserved in the glasses, their scales depending weakly on the composition and rate of cooling.

The atoms in the intercluster boundaries layers have a binding energy that is 0.13–0.43 eV lower than in the interior of the cluster. Since this value is comparable to the binding energy deficit of atoms in intercrystallite boundaries, it can be concluded that the microscopic structures of the intercluster and intercrystallite boundaries are similar, in spite of the lack of translational invariance of the noncrystalline structure of the clusters.

It is natural to assume that the two-level systems responsible for the low-temperature anomalies of the thermal conductivity, specific heat, sound absorption, etc. are located at the intercluster boundaries, i.e., belong to two-dimensional extended defects. The presence of subcluster heterogeneities of the structure of the bulk amorphous alloy attests to the diversity of short-range order in the melts and indicates that the characteristic scale of the short-range order is 1.5–3 nm.

This study was supported in part by the NATO International Program No. SA (PST.CLG.976376)5437 and the NTTsU, Project Nos. 1804 and 655.

*E-mail: bakai@kipt.kharkov.ua

[1] P. H. Gaskell, in *Glassy Metals II*, edited by H.-J. Güntherodt and H. Beck, Vol. 58 of Topics in Applied Physics, Springer, Berlin (1983).
[2] A. S. Bakaĭ, *Polycluster Amorphous Solids* [in Russian], Énergoizdat, Moscow (1987).
[3] A. S. Bakai, in *Glassy Metals III*, edited by H. Beck and H.-J. Güntherodt, Springer, Heidelberg (1994), p. 209.
[4] A. P. Sutton and R. W. Balluffi, *Interfaces in Crystalline Materials*, Clarendon Press, Oxford (1995).
[5] A. S. Bakaĭ, I. M. Mikhaĭlovskiĭ, P. Ya. Poltinin, and L. I. Fedorova, Vopr. At. Nauki Tekh. Ser. Fiz. Radiats. Povrezh. Radiats. Materialoved. (Kharkov), No. 3(45), 44 (1988).

[6] I. M. Mikhaĭlovskiĭ, L. I. Fedorova, and P. Ya. Poltinin, Fiz. Met. Metalloved. **76**, 123 (1993).
[7] A. S. Bakai, V. V. Kul'ko, I. M. Mikhailovskij, V. B. Rabukhin, and O. A. Velikodnaya, J. Non-Cryst. Solids **182**, 315 (1995).
[8] Y. Hirotsu, M. Uehara, and M. Ueno, J. Appl. Phys. **59**, 3081 (1986).
[9] A. H. Okumura, A. Inoue, and T. Masumoto, Acta Metall. Mater. **41**, 915 (1993).
[10] A. Peker and W. L. Johnson, Appl. Phys. Lett. **63**, 2342 (1993).
[11] A. S. Bakaĭ, N. Vanderka, M.-P. Makht, I. M. Mikhaĭlovskiĭ, and T. I. Mazilova, Metallofiz. Noveĭshie Tekhnol. **20**, 58 (1998).
[12] N. Wanderka, U. Czubayko, P. Schubert-Bischoff, and M.-P. Macht, Mater. Sci. Engin. A **270**, 44 (1999).
[13] B. G. Lazarev, V. A. Ksenofontov, and I. M. Mikhaĭlovskiĭ, O. A. Velikodnaya, Fiz. Nizk. Temp. **24**, 272 (1998) [Low Temp. Phys. **24**, 205 (1998)].
[14] E. W. Müller and T. T. Tsong, *Field Ion Microscopy: an Introduction to Principles, Experiments, and Applications* [American Elsevier, New York (1969); Metallurgiya, Moscow (1972)].
[15] A. Modinos, *Field, Thermionic and Secondary Electron Emission*, Plenum, New York (1984).

Translated by Steve Torstveit

QUANTUM EFFECTS IN SEMICONDUCTORS AND DIELECTRICS

Excitons in the layered insulators ZnI_2 and CdI_2:Zn

O. N. Yunakova and V. K. Miloslavsky*

N. V. Karazin Kharkov National University, pl. Svobody 4, 61077 Kharkov, Ukraine

E. N. Kovalenko

Physicotechnical Research Center of the Ministry of Education and Science and National Academy of Sciences of Ukraine, ul. Novgorodskaya 1, 61145 Kharkov, Ukraine

(Submitted November 20, 2001)
Fiz. Nizk. Temp. **28**, 406–413 (April 2002)

The fundamental electronic absorption spectra in the layered compounds ZnI_2 and Zn-doped CdI_2 are investigated in the spectral interval 3–5.9 eV. The samples are thin grain-oriented films deposited on quartz substrates. It is found that ZnI_2, unlike CdI_2, is a direct-gap insulator, despite the similarity of the crystal structures of these compounds. The introduction of Zn atoms into the cation sublattice of CdI_2 at concentrations $x \geqslant 1\%$ leads to the vanishing of the absorption from indirect transitions and to the appearance of a strong exciton band at the fundamental absorption band edge. The parameters of the exciton bands (spectral position, half-width Γ, oscillator strength f) are measured in the temperature interval 80–330 K. The measured temperature dependence of Γ in both compounds is typical for three-dimensional excitons. In ZnI_2 the oscillator strength decreases with increasing T because of the Debye–Waller factor, while in CdI_2:Zn it increases. This last result is evidence of the forbidden character of the direct optical transition at the interband absorption edge in CdI_2, which is partially allowed because of the exciton–phonon interaction. © *2002 American Institute of Physics.*
[DOI: 10.1063/1.1477364]

INTRODUCTION

The compounds CdI_2 and ZnI_2 are layered insulators consisting of close-packed I–Me–I ''packets'' within which the ionic bonding predominates, coupled to other packets by a weak van der Waals interaction. The layered structure of the compounds is responsible for many of their physical and chemical properties: strong anisotropy of the mechanical, thermal, and optical properties, and the capacity for intercalation of various atoms and molecules. The crystal structure of CdI_2 has been studied repeatedly. It has been established that this compound has a tendency toward the formation of polytypes owing to the weak bonding between packets. The most common polytypes are $2H$ and $4H$.[1] the most stable polytype is $4H$; all the other polytypes are transformed into $4H$ when the crystals are annealed. Both polytypes have a hexagonal unit cell with $a=4.24$ Å, with $c=6.24$ Å for the $2H$ polytype and $c=13.68$ Å for the $4H$ polytype (with 2 molecules per unit cell). The structure of ZnI_2 is less studied. According to the data of Ref. 2, ZnI_2 has the structure of the $2H$ polytype of CdI_2, with $a=4.25$ Å and $c=6.54$ Å, while, according to Ref. 3, ZnI_2 forms in a crystal lattice of the $CdCl_2$ type with three molecules per unit cell.

In a number of studies[4–7] the fundamental electronic spectrum of CdI_2 has been investigated by the methods of optical spectroscopy. It has been established that CdI_2 is an indirect-gap insulator,[5,7] with a wide gap $E_g=3.473$ eV (1.7 K), while the energy gap corresponding to direct transitions between the valence and conduction bands is close to 4 eV. The electronic spectrum of CdI_2 has been calculated theoretically by the tight-binding method[8,9] and by the augmented spherical waves method with the relativistic corrections and the spin–orbit interaction taken into account.[10] The calculations show that the upper valence band of CdI_2 is formed by the $5p$ states of iodine, and the lower conduction band by the $5s$ states of cadmium. A calculation of the optical constants and the complex dielectric permittivity in the spectral interval 4–10 eV is given in Ref. 11. By virtue of the difference of the coordination numbers for the cation and anion, the width of the $4s$ conduction band of cadmium is narrower (around 2.5 eV)[6] than the $5p$ valence band of I (4.9 eV). The calculations predict, in agreement with experiment, that the minimum of the conduction band and the maximum of the valence band lie at different points of the Brillouin zone and thus that the optical spectrum will have an indirect-transition region. The data of different authors place the smallest energy gap corresponding to direct transitions at different points of the Brillouin zone: at Γ (Refs. 9 and 11), A (Ref. 8) and L (Refs. 6 and 10). According to the data of Refs. 6 and 10, the transition at the L point is forbidden by parity and is partially allowed on account of the electron–phonon interaction.

The influence of isoelectronic impurities on the absorption spectrum of CdI_2 has been little studied. In Refs. 12 and 13 the impurity band of Pb^+ in CdI_2 was observed at 3.23 eV.

In contrast to CdI_2, the fundamental electronic spectrum

 © 2002 American Institute of Physics

and optical absorption in ZnI_2, as a consequence of the hygroscopic nature of the compound, have hardly been studied. In Ref. 14 the spectral position of the exciton band was indicated ($E_{ex}=4.5$ eV, 77 K), but there was no other information about the electronic spectrum of the compound.

The goal of the present study was to investigate the electronic spectrum and excitons in ZnI_2 and in CdI_2 doped with Zn^{2+} ions. The objects of study were thin films of the compounds. The absorption spectra were measured in the spectral interval 3–6 eV. The excitonic absorption bands and their parameters were studied in the temperature interval 80–330 K.

THIN FILMS OF ZnI_2 AND CdI_2:Zn, THEIR PREPARATION, AND MEASUREMENT OF THE SPECTRA

Thin films of ZnI_2 were prepared by the vacuum deposition of ZnI_2 powder on quartz substrates heated to 80 °C. Because of the high hygroscopicity of ZnI_2, strong light scattering arises in films removed from the vacuum chamber and cooled to room temperature. To avoid this, the samples were transferred in the heated state to a vacuum optical cryostat, the copper finger of which had been heated beforehand to 70 °C. After the cryostat was pumped down and flooded with nitrogen, the films remained transparent and suitable for spectral measurements. The absence of light scattering in the films was monitored from their transmission spectra in the transparency region. After flooding with nitrogen the temperature of the sample (80–90 K), monitored by a copper–Constantan thermocouple, was maintained for a long time to permit measuring the absorption spectra in a wide frequency interval. The thickness of the films was determined from the transmission spectra in their transparency region by the optical interference method described in Ref. 15. The chosen film thickness (around 100 nm) was dictated by the necessity of measuring the spectrum in the region of large absorption coefficients. The intermediate temperatures were achieved by using baths of liquids that freeze at $T<273$ K and mixtures of these liquids with small amounts of nitrogen and were maintained to within ± 2 K for 20 min; in this case the absorption spectrum was measured in a narrower frequency interval which encompassed the low-frequency exciton band.

In measuring the absorption spectrum of ZnI_2 we unexpectedly encountered the following difficulty. At $T\geqslant 195$ K the exciton band is strongly shifted to higher frequencies and is weakened, although the sample remains non-scattering. The reason for this shift was found to be release of CO_2 from the carbon adsorption pump of the cryostat (the sublimation temperature of CO_2 is 194.5 K). We attribute the shift of the exciton band by 0.5 eV to the intercalation of carbon dioxide molecules into the layered compound ZnI_2. A similar shift of the exciton band has been observed in PbI_2 upon its intercalation by pyridine.[16] For this reason the ZnI_2 spectrum was measured in the temperature interval 285–330 K, and then the sample was cooled to nitrogen temperature and the measurements were made in the interval 80–195 K.

Thin films of CdI_2:Zn were obtained by evaporation of a mixture of CdI_2 and ZnI_2 powders of specified molar composition on quartz substrates heated to 80 °C. The Zn concentration varied from 0.5% to 10%. This method of preparation apparently ensures the formation of the $4H$ polytype of CdI_2 (Ref. 1). Since the method of preparation of the CdI_2 films is similar to that described in Ref. 17, where structural studies were done, the films have a high structural perfection. The crystallites, several microns in size, were oriented with their **c** axis perpendicular to the substrate. The CdI_2:Zn films are not hygroscopic in the concentration range indicated, and no intercalation effects were observed in the measurements of the absorption spectra.

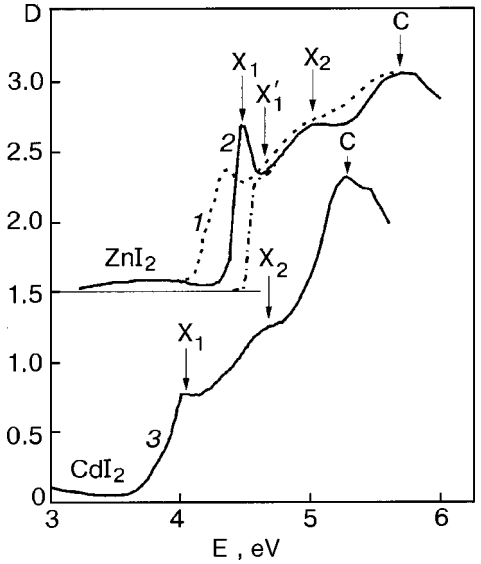

FIG. 1. Absorption spectra of ZnI_2 at 290 K (*1*) and 90 K (*2*) and of CdI_2 at 90 K (*3*). The dot-and-dash curve shows the absorption edge after the exciton band X_1 has been subtracted off.

ABSORPTION SPECTRA OF ZnI_2 AND CdI_2:Zn FILMS AND THEIR DISCUSSION

The absorption spectra of impurity-free ZnI_2 and CdI_2 films are presented in Fig. 1. The absorption spectrum of ZnI_2 has a strong exciton band X_1 at 4.48 eV (80 K) and a more smeared band X_2 with a maximum at 5.02 eV. Both bands were smeared out and shifted to lower frequencies as the temperature was raised to room temperature. A broad C band, located at 5.7 eV, is less sensitive to the change in temperature. The slight increase in the optical density at 3.5 eV is due to optical interference in the thin film in the transparency region. The absorption spectrum of CdI_2 also exhibits the X_1 (4.03 eV), X_2 (4.62 eV), and C (5.48 eV) bands, in agreement with the data of other authors.[17] We see that to a first approximation the absorption spectrum of ZnI_2 is similar to that of CdI_2 and is shifted to higher energies. However, there is a substantial difference in the spectra: in ZnI_2 the exciton band X_1 is strong and has a steeply falling long-wavelength edge, while in CdI_2 the X_1 band is considerably weaker and has a smeared edge at $E<4.03$ eV. This smearing of the long-wavelength edge of the absorption band is caused by the well-established existence of indirect transitions in the interval 3.5–4 eV.[5,7]

The appearance of a strong and comparatively narrow exciton band in the absorption spectrum of ZnI_2 indicates that this compound is a direct-gap insulator, i.e., the exciton band X_2 is adjacent to the edge of direct allowed interband transitions. Evidently, in ZnI_2, as in CdI_2, the upper valence

band is formed by the $5p$ states of iodine, while the lower conduction band is formed by the $4s$ states of zinc. The maximum of the valence band and the minimum of the conduction band lie at the same point of the Brillouin zone. To determine the parameters of the X_1 band (the spectral position, half-width, and oscillator strength) we approximated it by a symmetric contour in the form of a linear combination of a Lorentzian and a Gaussian by the method proposed in Ref. 18. After the exciton band X_1 at 4.6 eV was substracted off, a step (the X_1' band) was observed, which we ascribe to the superimposition of a weaker $2s$ exciton band on the edge. From the spectral position of the $1s$ and $2s$ exciton bands we can determine the exciton binding energy using the model of a Wannier–Mott exciton:

$$E_B = k(E_{\mathrm{ex},n=2} - E_{\mathrm{ex},n=1}), \tag{1}$$

where $E_{\mathrm{ex},n}$ is the spectral position of the X_1 and X_1' bands, and k is a coefficient in the range $9/8 \leqslant k \leqslant 4/3$; the value $k = 4/3$ corresponds to an isotropic three-dimensional exciton, and $k = 9/8$ corresponds to a two-dimensional exciton. For layered crystals of the ZnI_2 type the Bohr radius of the excitons is small, with a size close to the width of an I–Me–I packet, i.e., the excitons in them exhibit more of a three-dimensional character.[4] As will be shown below, the three-dimensional character of the excitons in ZnI_2 is confirmed by the temperature dependence of the half-width of the exciton band. Assuming that $k = 4/3$, we find $E_B = 0.16$ eV, and from the formula

$$E_g = E_{\mathrm{ex},n=1} + E_B \tag{2}$$

we obtain a value of $E_g = 4.62$ eV for the band gap of ZnI_2. As in CdI_2, the appearance of the X_2 band in ZnI_2 is due to the spin–orbit splitting of the valence band. The value of the splitting $\Delta_{LS} = E_{X_2} - E_{X_1} \approx 0.54$ eV and is close to the corresponding value in CdI_2 ($\Delta_{LS} = 0.59$ eV). This value is somewhat lower than Δ_{LS} for a free iodine atom ($\Delta_{LS} = 0.67$ eV),[10] possibly because of a small admixture of the $4d$ state of Cd in the valence band of the compound. Assuming that in both crystals the width of the C band, with a maximum at E_C, corresponds to optical transitions between centers of the upper valence band and the $5s$ conduction band, we find the total width of the allowed bands adjacent to the forbidden band as

$$\Delta E = 2(E_C - E_h), \tag{3}$$

which gives $\Delta E = 2.16$ eV for ZnI_2 and, with allowance for the indirect transitions, $\Delta E = 4.02$ eV for CdI_2. The considerably smaller value of ΔE in ZnI_2 correlates with the larger value of E_g in that compound. The decrease of ΔE in ZnI_2 in comparison with CdI_2 is apparently due to the "flattening out" of the lower cationic $4s$ conduction band. The decrease in the width of the $4s$ band is indicated by the fact that the ionic radius of Zn^{2+} (1.31 Å) is smaller than that of Cd^{2+} (1.48 Å), while the lattice parameter a of the two compounds is only slightly different.

Judging from the method used to prepare the thin films of CdI_2:Zn and the closeness of the crystal structure of the two compounds, the introduction of Zn to CdI_2 leads to the formation of solid solutions of substitution $Cd_{1-x}Zn_zI_2$, with the Zn^{2+} ions substituting for Cd^{2+} in the cation sublattice.

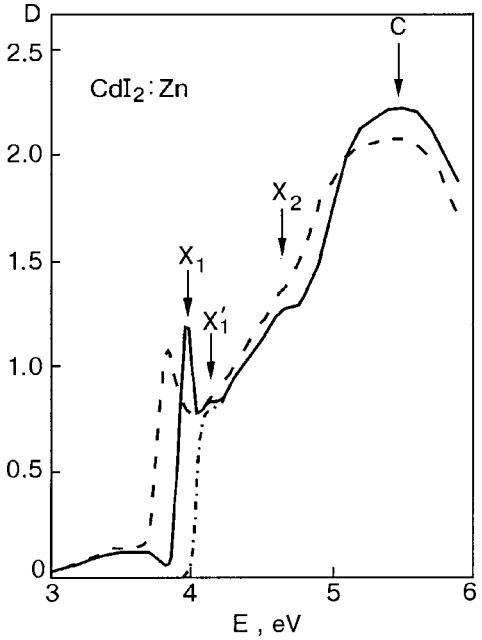

FIG. 2. Absorption spectrum of CdI_2 activated by Zn^{2+} ions ($x = 0.05$) at 290 K (dashed curve) and 90 K (solid curve); the dot-and-dash line shows the absorption edge after the exciton band X_1 has been subtracted off.

As is seen in Fig. 2, the introduction of Zn^{2+} ions in CdI_2 leads to a fundamental rearrangement of the absorption edge: an exciton band with a maximum at 3.965 eV ($x = 0.05$) appears at the long-wavelength edge of the fundamental absorption band of CdI_2, and the gradual tail due to indirect transitions disappears. In the concentration interval investigated ($0.005 < x < 0.1$) the new X_1 band exists down to $x = 0.01$; for $x < 0.01$ the strong band vanishes, and the absorption spectrum acquires the typical form for pure CdI_2 (Fig. 1). The X_1 absorption band in CdI_2:Zn is shifted to longer wavelengths relative to the X_1 band in CdI_2 ($E_m = 4.03$ eV). With increasing x the exciton band X_1 shifts weakly to higher energies by the linear law:

$$E_{\mathrm{ex}}(x) = (3.93 + ax) \ \text{eV}, \tag{4}$$

where $a = (0.5 \pm 0.05)$ eV. It follows from Eq. (4) that in the indicated concentration interval the new band occupies a lower-frequency position than the X_1 band in pure CdI_2 (4.03 eV). The shift of the exciton bands in the absorption spectra of solid solutions is typical for many insulators. For example, in the layered insulator PbI_2, where the absorption edge corresponds to direct transitions, one also observes a shift of the exciton band to shorter wavelengths when the Pb^{2+} ions are substituted by Cd^{2+} (Ref. 12), but in contrast to CdI_2:Zn, the shift of the exciton band in PbI_2:Cd is accompanied by a weakening of the band.

According to the data of Refs. 6 and 10, direct optical transitions in CdI_2 occur between the top of the valence band, located at the Γ point, and the bottom of the conduction band, at the L point of the Brillouin zone. On the other hand, the smallest energy gap corresponding to direct transitions ($\cong 3.8$ eV) is also located at the L point. Apparently, the introduction of Zn^{2+} ions in CdI_2 leads to a shift of the bottom of the conduction band to higher energies, and so increasing the Zn^{2+} concentration causes the absorption

edge due to indirect transitions to be shifted to higher frequencies, and for $x \geqslant 0.01$ the energy gap corresponding to the indirect transitions becomes larger than the gap for direct transitions. Consequently, for $x \geqslant 0.01$, CdI_2 becomes a direct-gap insulator.

It should be mentioned that in accordance with the energy band calculations,[9,10] the direct transition at the L point is forbidden by the selection rules for $\mathbf{E} \perp \mathbf{c}$ ($L_3^+/L_4^+ \rightarrow L_3^+/L_4^+$ transition, $2H$ polytype, band calculation with the LS coupling taken into account). The CdI_2:Zn films apparently belong to the $4H$ polytype. If it is assumed that in the $4H$ polytype, the top of the valence band, as in the $2H$ polytype, is formed at the L point by the $5p_z$ atomic orbitals of iodine, then the direct optical transition in $4H$-CdI_2 should remain forbidden. However, in spite of its being forbidden by the selection rules, optical absorption occurs at this point for a number of reasons. First, the forbiddenness is partially lifted when vibrations of the crystal lattice are taken into account. The lifting of the forbiddenness on the optical transition for Ag^+ and Cu^+ impurity centers in alkali halide crystals, which affects the temperature dependence of the oscillator strength of the bands, has long been known.[19] Second, the Zn^{2+} ions, because of their smaller radius, lead to a displacement of the iodine atoms in their nearest neighborhood, and for this reason the Cd^{2+} ions in the neighboring octahedra acquire an off-center position, which also leads to a growing oscillator strength of the band.[20] It is also possible that the shift to lower energies of the X_1 band, which lies at 4.03 eV in the spectrum of pure CdI_2, is due to an increase in the Cd–I interatomic distance in neighboring octahedra. However, it is hard to follow the dynamic shift of the X_1 band in the concentration interval $0.005 < x < 0.01$ because of the unavoidable scattering in the concentration over the thickness of the film.

As in ZnI_2, in CdI_2:Zn a weak X_1' band (at 4.12 eV) is observed on the short-wavelength side of the X_1 band. Attributing this band to to a $2s$ exciton, we find, using Eq. (1), an exciton binding energy $E_B = 0.2$ eV and, using Eq. (2), a band gap $E_g = 4.17$ eV for CdI_2 containing 5% Zn. The total width of the allowed bands adjacent to the gap is estimated from Eq. (3) as 2.62 eV, considerably less than the value of ΔE in pure CdI_2.

TEMPERATURE DEPENDENCE OF THE PARAMETERS OF THE LONG-WAVELENGTH EXCITONIC ABSORPTION BANDS IN ZnI_2 AND CdI_2:Zn

In referring to the parameters of the exciton bands we mean the position of the maximum E_m, the half-width Γ, and the oscillator strength f of the band. All three of these characteristics depend on the temperature. In ionic crystals, of which ZnI_2 and CdI_2 are examples, the temperature dependence of the parameters is determined mainly by the interaction of the excitons with longitudinal optical (LO) phonons, and the strongest temperature dependence of the parameters occurs for $\hbar\omega_{LO} \leqslant kT$. The energy of the LO phonons in CdI_2 is equal to 21.7 meV, while the value of $\hbar\omega_{LO}$ in ZnI_2 is unknown. However, if we assume that the ratio of the frequencies ω_{LO} for the ZnI_2 and CdI_2 crystals is the same as the ratio of the frequencies of the asymmetric stretching vibrations of the molecules ($\rho = 1.28$),[21] then we can find $\hbar\omega_{LO} = 27.8$ meV.

The exciton–phonon interaction leads to a temperature shift of the X_1 band to longer wavelengths by the linear law:

$$\text{for} \quad ZnI_2 \quad dE_m/dT = -7.7 \times 10^{-4} \text{ eV/k}$$

$$\text{for} \quad CdI_2\text{:Zn} \quad dE_m/dT = -6.2 \times 10^{-4} \text{ eV/k}$$

In order of magnitude such a shift of the bands is typical for the majority of ionic crystals. The value of dE_m/dT obtained for CdI_2:Zn is somewhat larger than the value $dE_m/dT = -4 \times 10^{-4}$ eV/K found from the shift of the absorption edge at 4 eV in CdI_2 films.[22]

At the same time, the temperature dependence of the half-width Γ in the two compounds is nonlinear (Fig. 3a). Analysis of the temperature dependence of Γ yields additional information about the dimensionality of the excitons in layered crystals. In Ref. 23 the temperature dependence $\Gamma(T)$ was investigated theoretically for excitons of different dimensionality d ($d = 1,2,3$):

$$\Gamma(T) \approx \left[\frac{\pi D^2}{\gamma(d/2)(2\pi B)^{d/2}} \right]^{2/4-d}, \tag{5}$$

where $\gamma(d/2)$ is the d-dependent gamma function, $D^2 = 0.5C^2\hbar\omega_{LO}\coth(\hbar\omega_{LO}/kT)$, where $C^2/2$ is the energy of relaxation of the lattice upon excitation of an exciton, and B is the width of the exciton band. In processing the experimental $\Gamma(T)$ curves one should take into account the shape of the contour of the exciton band and the contribution to Γ from the residual broadening $\Gamma(0)$ due to lattice defects. For ZnI_2 at nitrogen temperature the shape of the band, found from its long-wavelength edge, is a linear combination of a Lorentzian and a Gaussian, but the Gaussian component becomes stronger with increasing temperature. For CdI_1:Zn the

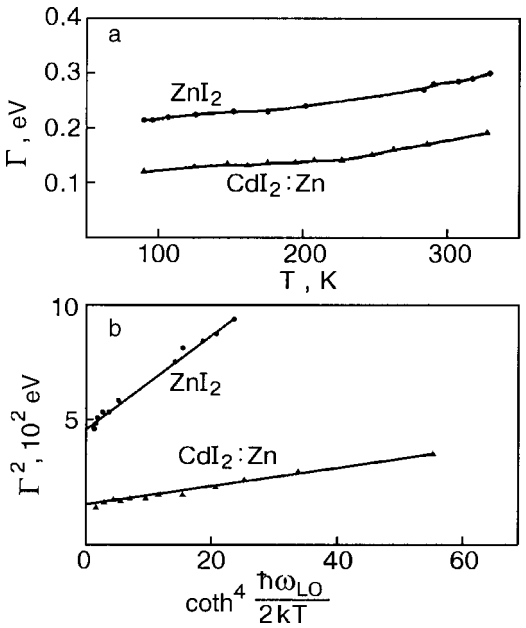

FIG. 3. Temperature dependence of the half-width Γ of ZnI_2 and CdI_2:Zn (a); temperature dependence of Γ in the coordinates Γ^2 versus $\coth^2(\hbar\omega_{LO})/kT$) in ZnI_2 and CdI_2:Zn (b).

shape of the band is Gaussian in the entire temperature interval studied. In the case of a Gaussian contour the total half-width is given by the relation

$$\Gamma=[\Gamma^2(0)+\Gamma^2(T)]^{1/2}, \tag{6}$$

where $\Gamma(T)$ obeys Eq. (5) with an unknown temperature-independent factor A. A processing of the experimental dependence of Γ on T showed that the best agreement with formula (5) is achieved for $d=3$. Then $\Gamma(T)=A\coth^2(\hbar\omega_{LO}/kT)$, and a plot of $\Gamma(T)$ in coordinates of Γ^2 versus $\coth^4(\hbar\omega_{LO}/kT)$ is linear (Fig. 3b). A least-squares processing of this dependence gives:

in ZnI_2 $\Gamma_1(0)=(0.214\pm0.002)$ eV,

$A_1=(4.36\pm0.07)\times10^{-2}$ eV,

in CdI_2:Zn $\Gamma_2(0)=(0.125\pm0.002)$ eV,

$A_2=(1.9\pm0.05)\times10^{-2}$ eV.

The width of the exciton band in these compounds is unknown. However, if the energy of the lattice relaxation upon excitation of an exciton is assumed to be the same in ZnI_2 and CdI_2:Zn, then the value of A is proportional to $(\hbar\omega_{LO})^2B^{-3}$. Using the ratio of the values obtained for A_1 and A_2 and the corresponding energies of the LO phonons, we find for the ratio of the exciton bandwidths of the two compounds $B_1/B_2=0.89$, i.e., the exciton band in ZnI_2 is 10% narrower than in CdI_2:Zn. This value of the ratio B_1/B_2 is in fair agreement with the ratio of the total widths of the electronic bands adjacent to the band gap, $\Delta E_1/\Delta E_2=0.82$, in view of the error of determination of ΔE and A.

In the temperature interval from 90 to 330 K the oscillator strength of the exciton bands in ZnI_2 and CdI_2:Zn was determined with allowance for the mixing of the Gaussian and Lorentzian contours according to the formula

$$f=(mv/4\pi e^2h^2)\varepsilon_{2m}E_m\Gamma[1-\alpha(1-\pi\ln 2)^{-1/2})], \tag{7}$$

where v is the volume per molecule in the lattice; ε_{2m} is the imaginary part of the complex dielectric permittivity at the maximum of the band, $\varepsilon_{2m}\equiv\varepsilon_2(E_m)$; the value of ε_{2m} was found by calculating the optical constants of the film by the method proposed in Ref. 18; α is the Gaussian-component fraction of the total contour of the exciton band. A numerical analysis shows that replacing the Voigt contour (which is a convolution of a Lorentzian contour with a Gaussian distribution) by a mixed contour with same parameters gives an error of determination of f of not more than 1%. It is found that the value of $f(T)$ calculated according to Eq. (7) is a decreasing function of T in ZnI_2, while in CdI_2:Zn an appreciable growth of the oscillator strength with temperature is observed.

The decrease of $f(T)$ with increasing T is a hallmark of the temperature behavior of a zero-phonon band. In the absence of noticeable dispersion of the frequency ω_{LO} the oscillator strength of a zero-phonon band decreases on account of the Debye–Waller factor according to the law[24]

$$f(T)=f_0\exp[-g_0(2n_{\rm ph}+1)], \tag{8}$$

where $n_{\rm ph}$ is the distribution function of the LO phonons, $n_{\rm ph}=[\exp(\hbar\omega_{LO}/k_BT)-1]^{-1}$, and g_0 determines the Debye–Waller factor at 0 K. A least-squares processing of the curve of $\ln f(T)$ versus $2n_{\rm ph}+1$ (Fig. 4a) gives $f_0=0.22\pm0.003$ and $g_0=0.17\pm0.01$.

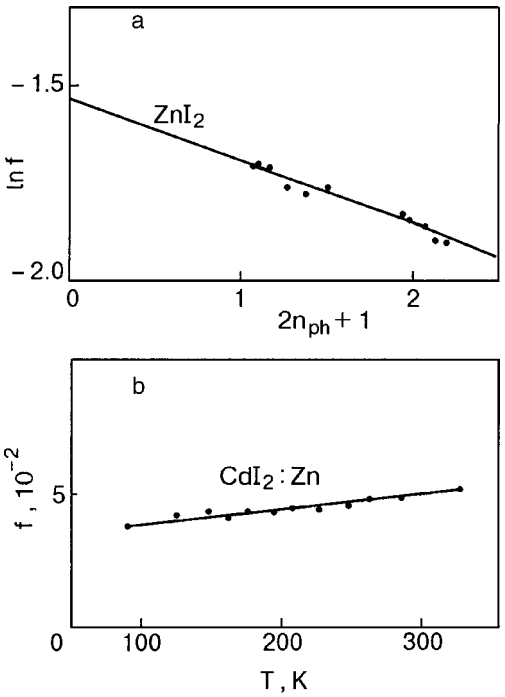

FIG. 4. Temperature dependence of the oscillator strength in ZnI_2, in the coordinates $\ln f(T)$ versus $2n_{\rm ph}+1$ (a), and in CdI_2:Zn (b).

In CdI_2:Zn the oscillator strength increases with increasing T, from 0.038 at 90 K to 0.046 at 330 K by a linear law (Fig. 4b). The growth of f with temperature for the exciton band in CdI_2:Zn is a sign that the direct optical transition between the valence band edge and the conduction band edge adjacent to the exciton band is partially forbidden, since for excitons of the Wannier–Mott type the oscillator strength of the exciton band is proportional to the square of the matrix element of the momentum operator, $|P_{cv}(\mathbf{k}_0)|^2$, constructed on the wave functions of the conduction band and valence band at the given point of the Brillouin zone. The forbiddenness is lifted on account of the exciton–phonon interaction, which increases with increasing T. This result agrees with the conclusion of Refs. 6 and 10 that the minimum band gap for direct transitions lies at the L point of the Brillouin zone, where the optical transition for the polarization $\varepsilon_0\perp\mathbf{c}$ is forbidden by the selection rules. That the transitions in CdI_2:Zn are partially forbidden is also indicated by the oscillator strength of the exciton band, which at 90 K is substantially smaller (by a factor of 5) than that in ZnI_2, where $f=0.182$ at that same temperature.

CONCLUSION

In summary, a study of the absorption spectra of thin films of ZnI_2 has established that the exciton band in this compound is adjacent to the edge of direct interband allowed transitions, i.e., unlike CdI_2, the compound ZnI_2 is a direct-gap insulator. Studies of the temperature dependence of the parameters of the exciton band indicate that the excitons in this compound have a three-dimensional character. It is also established that the introduction of Zn^{2+} ions in the crystal

lattice of CdI_2 transforms that compound to a direct-gap insulator, as is attested to by the appearance of a strong, narrow exciton band at edge of the fundamental electronic absorption band of CdI_2. The exciton band in CdI_2:Zn is adjacent to the edge of direct interband transitions at the L point of the Brillouin zone, where the optical transition is forbidden. The forbiddenness is lifted on account of the exciton–phonon interaction and the distortion of the crystal lattice of CdI_2 in the nearest neighborhood of the Zn^{2+} impurity ions.

*E-mail: Vladimir.K.Miloslavsky@univer.kharkov.ua

[1] G. C. Trigunayat and G. K. Chadha, Phys. Status Solidi A **4**, 9 (1971).
[2] Landolt-Bornstein, *Tabellen 4 Teil, Kristalle* (1955).
[3] Z. G. Pinsker, L. I. Tatarinova, and V. A. Novikova, Zh. Fiz. Khim. **20**, 1401 (1946).
[4] M. R. Tubbs, Phys. Status Solidi **49**, 11 (1972); **67**, 4 (1975).
[5] Y. Takemura, T. Komatsu, and Y. Kaifu, Phys. Status Solidi **72**, 87 (1975).
[6] I. Pollini, J. Thomas, R. Coehoorn, and C. Haas, Phys. Rev. B **8**, 5747 (1986).
[7] H. Nacagawa, T. Jamada, H. Matsumoto, and T. Hayashi, J. Phys. Soc. Jpn. **56**, 1185 (1987).
[8] J. V. McCanny, R. H. Williams, R. B. Murray, and P. C. Kemeny, J. Phys. C **10**, 4255 (1977).
[9] J. Robertson, J. Phys. C **12**, 4753 (1979).
[10] R. Coehoorn, G. A. Sawatzky, C. Haas, and R. A. de Groot, Phys. Rev. B **31**, 6739 (1985).
[11] Ya. O. Dovgiĭ and I. V. Kityk, Ukr. Fiz. Zh. **29**, 884 (1984).
[12] A. I. Rybalka, V. K. Miloslavskiĭ, L. A. Ageev, and V. B. Blokha, Fiz. Tverd. Tela (Leningrad) **17**, 2180 (1975) [Sov. Phys. Solid State **17**, 1444 (1975)].
[13] T. Goto and M. Ueta, J. Phys. Soc. Jpn. **29**, 1512 (1970).
[14] M. R. Tubbs, Phys. Status Solidi **28**, 135 (1968).
[15] V. K. Miloslavskiĭ, A. I. Rybalka, V. M. Shmandiĭ, Opt. Spektrosk. **48**, 619 (1980) [Opt. Spectrosc. **48**, 341 (1980)].
[16] A. I. Rybalka, V. K. Miloslavskiĭ, Opt. Spektrosk. **41**, 252 (1976) [Opt. Spectrosc. **41**, 147 (1976)].
[17] D. K. Wright and M. R. Tubbs, Phys. Status Solidi **37**, 551 (1970).
[18] V. K. Miloslavskii, O. N. Yunakova, Sun Tsya-Lin, Opt. Spektrosk. **78**, 436 (1995) [Opt. Spectrosc. **78**, 391 (1995)].
[19] K. Fussgaenger, K. Martienssen, and H. Bilz, Phys. Status Solidi **12**, 889 (1965).
[20] S. A. Payne, Phys. Rev. B **36**, 6125 (1987).
[21] K. S. Krasnov (ed.), *Molecular Constants of Inorganic Compounds. A Handbook* [in Russian], Khimiya, Leningrad (1979).
[22] A. D. Brothers and J. T. Pajor, Phys. Rev. B **14**, 4570 (1976).
[23] M. Schreiber and Y. Toyozawa, J. Phys. Soc. Jpn. **51**, 1528 (1982).
[24] A. S. Davydov, *Theory of the Solid State* [in Russian], Nauka, Moscow (1976).

Translated by Steve Torstveit

LATTICE DYNAMICS

IR spectra of cryocondensates of an isotopic water mixture on thermocycling

A. Aldijarov, A. S. Drobyshev,* and S. S. Sarsembinov

Kazakh State National University, Tole bi, 96, 480012 Almaty, Kazakhstan
(Submitted September 28, 2001; revised November 19, 2001)
Fiz. Nizk. Temp. **28**, 414–420 (April 2002)

The IR spectra are measured for thin films of vacuum condensates of an isotopic water mixture in the proportions H_2O (10%), HDO (50%), and D_2O (40%). The condensation was done on an Invar metal mirror in the temperature interval 30–130 K at a pressure of the gas phase during cryocondensation of 6.7×10^{-4} Pa. Warming of these cryocondensates is accompanied by structural transformations which lead to a change of the energy of the hydrogen bonds between molecules. Calculations for the various types of stretching vibrations of the mixture show that this corresponds to a decrease of the enthalpy of the hydrogen bond with increasing temperature. Increasing the temperature of the cryocondensates formed at 30 K leads to a significant decrease of the frequencies of the absorption bands corresponding to deformation vibrations of the D_2O and HDO molecules. In the frequency range of the librational vibrations a substantial change of the spectrum of the cryocondensate of the isotopic water mixture is observed with increasing temperature. The cause of this is apparently thermally stimulated proton–proton and deuteron–deuteron exchange between the D_2O and HDO molecules. © *2002 American Institute of Physics.* [DOI: 10.1063/1.1477365]

INTRODUCTION

One of the fundamental problems of modern physics is the problem of self-organization and evolution of open systems, in which metastable intermediate states can exist. The degree of stability of these states is largely determined by the thermodynamic conditions of phase formation and the intramolecular structure of the investigated substance. As to the thermodynamic conditions, the region of low-temperature gas–solid transformations is the most suitable for studying these systems. Low rates of condensation and substantial supercoolings with respect to the equilibrium parameters significantly shorten the lifetime of the molecules in the adsorbed layer, and that leads the formation of real cryocrystals. This is particularly characteristic for substances whose molecules have some sort of features such as an intrinsic dipole moment. Water and heavy water are typical representatives of that class of molecules. Moreover, the presence of a long-range intermolecular interaction, due to the hydrogen bond, stimulates processes of formation of polyaggregates of water molecules, and that in large measure determines the macroscopic characteristics of the solid phase formed during cryocondensation. Thus a determination of the influence of the parameters of the intramolecular structure and the forces of intermolecular interaction, in particular, the hydrogen bond, on the formation of vacuum condensates of water can promote our understanding of the mechanisms of formation and the principles of behavior of open unstable systems.

From what we have said it becomes clear that the temperature of formation and the existence of cryocrystals is the most important factor determining the structure of the solid phase that forms. The studies reported in Ref. 1 revealed a substantial temperature dependence of the IR spectra of water and heavy water. Those studies were done on rather thick samples (more than 3 μm thick). In that case the fine structure of the characteristic absorption bands corresponding to the main intramolecular vibrations were not analyzed. Meanwhile, it is known[2] that processes such as cluster formation and the interaction via hydrogen bonds can be manifested in the spectra in the form overtones against the background of the fundamental frequencies. Moreover, the presence of a static field due to the formation of hydrogen bonds in the crystal leads to a perturbation of the fundamental intramolecular and lattice vibrations, and that affects their frequency shifts and the absorption amplitudes. Thus analysis of the IR spectra of cryovacuum condensates formed at different thermodynamic parameters can yield information about the change in the character of the intermolecular interaction in the crystal. The presence of stable isotopes of water (D_2O and HDO) makes it possible to obtain more-complete information about the problem, since it becomes possible to determine experimentally the influence of the features of the intramolecular structure on the properties of cryocrystals. With this goal, in the present study we have investigated the influence of temperature on the IR spectra of thin layers of cryocondensates of an isotopic water mixture.

EXPERIMENTAL APPARATUS AND MEASUREMENT TECHNIQUES

The measurements were made on the experimental apparatus described in detail in Ref. 3. The object of study was water consisting mainly of HDO and D_2O. The isotopic composition of the water was monitored by mass-spectrometric measurements with the use of an IPDO-1

 © 2002 American Institute of Physics

meter for measuring the partial pressures of the residual gases. On the basis of the mass spectra obtained, the mass composition of the water was calculated to be 10% H_2O, 50% HDO, and 40% D_2O. The error of measurement was 3–5%.

The temperature-stabilizing system used previously did not allow us to achieve the desired precision of temperature regulation. We therefore upgraded the temperature stabilization system of the cryostat of the device described in Ref. 3. Additional heaters controlled by a computer made it possible to maintain the temperature of the condensation surface to a precision of 0.05 K or better. The cryostat used in the apparatus was mounted on the upper low-temperature flange of the microcryogenic machine of a Gifford–MacMahon system.

The IR reflection spectra were measured on an IKS-29 spectrometer. In the updating of the apparatus we mounted an optical bypass channel that made it possible to operate in a double-beam mode. As a result, the quality of the IR spectra was improved and their processing was simplified. The measurement accuracy was 0.75 cm^{-1}, with a resolution $R = 850$, according to the documentation for the spectrometer. At the same time, some of the results presented here were obtained in the single-beam mode prior to the updating of the apparatus; special note of this is made in the discussion.

The measurements were made by the following procedure. A sample of thickness $d = 0.12$ μm was condensed at a substrate temperature of 30 K and a pressure of 6.7×10^{-4} Pa. Then the IR reflection spectrum of the cryocrystal–substrate system was taken. The curves obtained correspond to the absorption spectra recorded in a double passage of the optical signal through the cryocrystal film. After the measurement of the spectra at the condensation temperature the substrate temperature was raised at a rate of not more than 0.05 K/s. When the specified temperature was reached, the temperature stabilization system was turned on, and the IR spectrum was measured. Then the substrate temperature was again lowered to 30 K and the reflection characteristics were measured.

RESULTS AND DISCUSSION

Numerous spectral studies of ices have shown that the intramolecular vibrational frequencies of water are temperature and pressure dependent. This is a consequence of the structural diversity of the solid phase of water. In the thermodynamic existence region of the so-called vacuum condensates (low temperatures and pressures) the ground state of water has the hexagonal structure Ih. In the low-temperature existence region of Ih ice, metastable forms of it can appear. At condensation temperatures below 100 K an amorphous phase forms, which with increasing temperature[4] is irreversibly transformed to another metastable form of hexagonal ice—the so-called cubic ice Ic. This transition does not have a strictly defined temperature and is observed in an interval from 120 to 160 K.[5] Further increase of the temperature of cubic ice leads to its irreversible transformation to hexagonal ice. This transition also has smeared temperature boundaries, from 140 K (Ref. 4) to 200 K (Ref. 6). The causes of this indeterminacy of the temperature boundaries of the existence regions of the structural modifications of vacuum condensates of water have still not been conclusively established. It has been conjectured[7] that this is due not only to the different condensation temperature but also to the different rates of growth and heating of the films and also to the particular temperature pre-history of the samples. In our view, the cause is much deeper and is due to the fundamental disorder of hexagonal increase in respect to the protons (deuterons). These considerations motivated us to do the studies whose results are reported below.

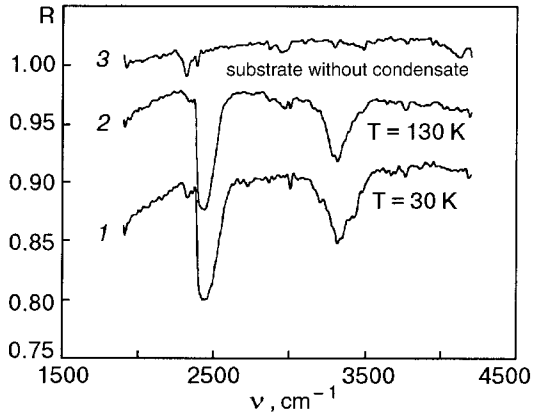

FIG. 1. IR spectrum of 0.12-μm thick cryocondensates of an isotopic water mixture at different substrate temperatures. The curves have been shifted along the vertical by 0 (*1*), +0.06 (*2*), and +0.07 (*3*) (*R* is the reflection coefficient).

The IR spectra of cryocondensates of our isotopic water mixture at temperatures of 30 and 130 K are presented in Figs. 1–5. For convenience of analysis the spectra have been shifted along the vertical while preserving the scale. The thickness of the samples in the majority of the experiments was 0.12 μm. This was sufficient for the formation of the main absorption bands, while still permitting analysis of the fine structure of the spectra.

The general conclusion that can be drawn from an analysis of the spectra shown is that changing the substrate temperature leads to significant transformations of the spectra in the regions of the characteristic frequencies. One observes a shift of the absorption bands and changes of their width and fine structure.

For detailed analysis below we shall consider narrower parts of the spectra, corresponding to some particular types of vibrations.

1. The 3000–3500 cm^{-1} range. The absorption peak in this range is formed mainly on account of the characteristic O–H stretching vibrations of the HDO molecule.[8] As we see in Fig. 2, warming the film leads to substantial changes in the spectrum, which becomes smoother and has a less-pronounced fine structure. In addition, the band narrows on warming and is shifted to lower frequencies by an amount equal to the half-width of the absorption. It can be assumed that this process corresponds to structural transformations during the annealing and the transition of the sample to a more stable state, which should lead to a change in the energy of the hydrogen bonds O–H...O between HDO molecules. According to Badger and Bauer,[7] this frequency shift is related to the energy of the hydrogen bonds by the simple relation

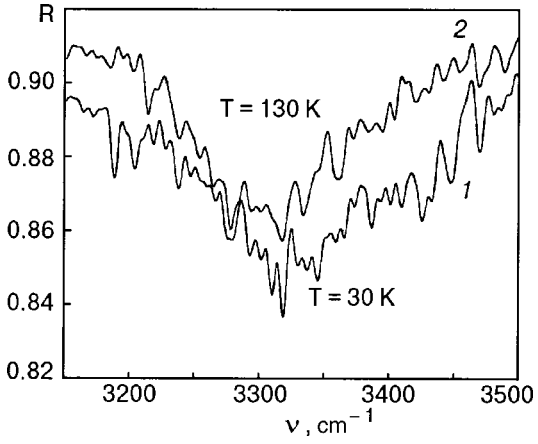

FIG. 2. IR spectrum of 0.12-μm thick cryocondensates of an isotopic water mixture at different substrate temperatures. The curves have been shifted along the vertical by 0 (*1*) and -0.013 (*2*).

$$\Delta\nu_{\mathrm{OH}} = -\frac{\Delta H}{0.024},$$

where ΔH is the change in enthalpy of the O–H valence bond in the static field of the hydrogen bond.

We used this relation to calculate the change in enthalpy of the hydrogen bond as a result of the increase in temperature of the film for frequencies corresponding to the values at the half-width of the absorption band, equal to $\nu_{T=30\ \mathrm{K}} = 3340\ \mathrm{cm}^{-1}$ and $\nu_{T=130\ \mathrm{K}} = 3316\ \mathrm{cm}^{-1}$. The value of the frequency shift on warming from 30 to 130 K is $\Delta\nu = 24\ \mathrm{cm}^{-1}$, and the corresponding change in enthalpy of the hydrogen bond for O–H vibrations of the HDO molecule is $\Delta H = -3.96$ J/mole. Thus, increasing the temperature leads to a decrease in the energy of the hydrogen bond for this type of vibration of the molecule.

2. The 2350–2600 cm^{-1} range. This is the range of the stretching vibrations of D_2O and of the D–O bond of the HDO molecule. The absorption peak is clearly a superposition of these vibrations (Fig. 3). We see that annealing the sample leads to a smoothing of the spectrum and makes it significantly narrower than for the cryocondensate formed at 30 K. We had previously obtained analogous results for thicker films of D_2O cryocondensates.[1] The substantial narrowing of the stretching band of absorption when the sample is warmed was also observed in Ref. 1. These results agree qualitatively with those in Ref. 8, even though both the temperature regimes and the sample preparation conditions were substantially different.

In analogy with the calculations given above, we calculated the change in enthalpy of the hydrogen bond on warming of the film for this type of vibrations also. The frequencies corresponding to the different temperatures are equal to $\nu_{T=30\ \mathrm{K}} = 2459\ \mathrm{cm}^{-1}$ and $\nu_{T=130\ \mathrm{K}} = 2450\ \mathrm{cm}^{-1}$. Thus the value of the frequency shift on heating of the sample from 30 to 130 K is $\Delta\nu = 9\ \mathrm{cm}^{-1}$, and the corresponding change in enthalpy of the hydrogen bond for the O–D vibrations is $\Delta H = -2.58$ J/mole. Consequently, as in the case of the O–H bond in the HDO molecule, increasing the temperature leads to a decrease of the energy of the hydrogen bond, although the value of the change is considerably less. This is apparently due to the difference in the masses of the proton and deuteron.

3. The 800–1400 cm^{-1} range. This range corresponds to the so-called "scissors" vibrations of the D_2O and HDO molecules. The results of the measurements of the IR spectra in this range are shown in Fig. 4 (they were obtained in the single-beam mode of the spectrometer). The spectra shown were measured at three temperatures: 30 K (condensation temperature, spectrum *1*), 90 K (the first warming step, spectrum *2*), and 130 K (the second warming step, spectrum *3*).

As we see in the figure, annealing of the sample leads to significant changes in the character of the spectrum. First, as the temperature is raised there is a substantial shift of the spectrum to lower frequencies of the absorption band corresponding to the bond-angle vibration of the heavy-water molecule. The frequencies at the absorption maximum are: $\nu_{2(T=30\ \mathrm{K})} = 1236\ \mathrm{cm}^{-1}$, $\nu_{2(T=90\ \mathrm{K})} = 1229\ \mathrm{cm}^{-1}$, and $\nu_{2(T=130\ \mathrm{K})} = 1227\ \mathrm{cm}^{-1}$.

Such a frequency difference is indicative of structural transformations occurring in the crystal during the temperature evolution. It must be noted that these frequencies are found in good agreement with the data for ices with the *Ih* structure.[8] Here the values are given for the deformation vi-

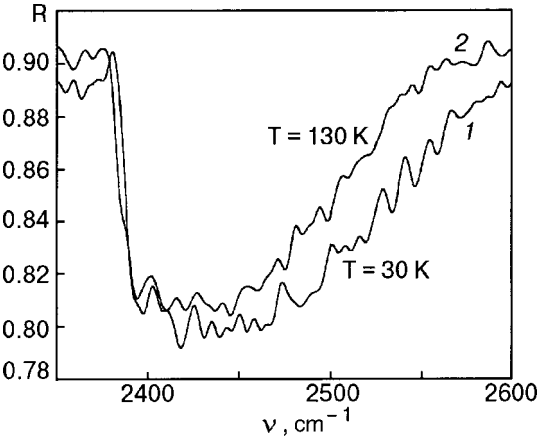

FIG. 3. IR spectra of a crystal 0.12 μm thick in the region of D–O stretching vibrations. The measurements were made at the condensation temperature 30 K (*1*) and after annealing to 130 K (*2*). The curves are shifted along the vertical by 0 (*1*) and -0.025 (*2*).

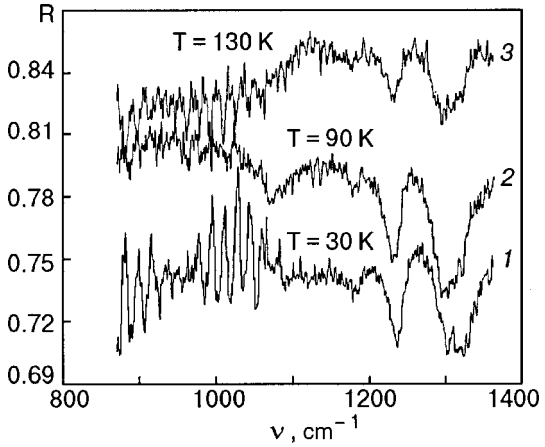

FIG. 4. IR spectrum of 0.12-μm thick cryocondensates of an isotopic water mixture at different substrate temperatures. The curves have been shifted along the vertical by 0 (*1*), 0.03 (*2*), and 0.1 (*3*).

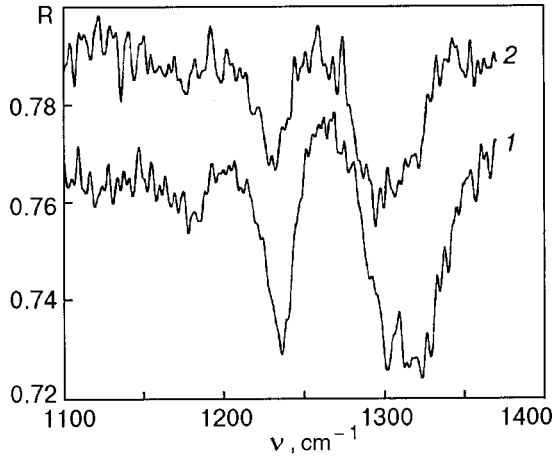

FIG. 5. IR spectra of a 0.12-μm thick crystal of an isotopic water mixture during thermocycling. The measurements were made at the condensation temperature 30 K (*1*) and after annealing to 130 K (*1*). The curves are shifted vertically by 0 (*1*) and 0.04 (*2*).

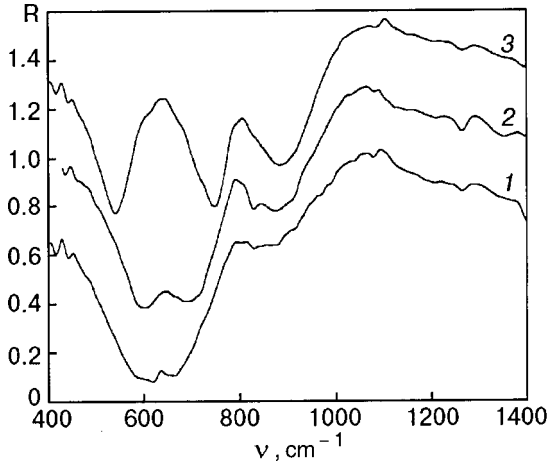

FIG. 6. IR spectrum of a 2-μm thick crystal of an isotopic water mixture at different temperatures: at the condensation temperature 30 K (*1*), after annealing to 100 K (*2*), and directly after condensation at a temperature of 100 K (*3*). The curves are shifted vertically by 0 (*1*), 0.3 (*2*), and 0.7 (*3*).

brations $\nu_{2(Ih)}=1210\ \mathrm{cm}^{-1}$. The discrepancy between the numerical values and our results is apparently due to both the difference in the methods of preparing the samples and differences in the temperature regimes. In Ref. 8 the samples were obtained by pulverizing ordinary ice *I*, and the measurements were made in the temperature interval 110–180 K. Nevertheless, our data show a tendency for the deformation frequency to decrease with increasing temperature and are clearly drawing closer to data of Ref. 8.

The behavior of the absorption peak at frequencies near $1300\ \mathrm{cm}^{-1}$ can serve as a manifestation of the temperature dependence of the frequency of the deformation vibrations. It corresponds to the O–D deformation vibration of the HDO and D_2O molecules and is also very sensitive to temperature variations of the sample. Thus for different temperatures and types of vibrations the frequencies at the half-width of the absorption band (Fig. 5) have the values:

$$\nu^{\mathrm{OH}}_{2(30K)}=1234\ \mathrm{cm}^{-1},\quad \nu^{\mathrm{OH}}_{2(130K)}=1231\ \mathrm{cm}^{-1},$$

$$\nu^{\mathrm{OD}}_{2(30K)}=1313\ \mathrm{cm}^{-1},\quad \nu^{\mathrm{OD}}_{2(30K)}=1303\ \mathrm{cm}^{-1},$$

At the same time, it should be noted that the effect seen here is somewhat at odds with the results of Refs. 9 and 10, where they speak of a weak dependence of the deformation vibrations on temperature and on the change in energy of the hydrogen bond. In particular, the calculations of Pimentel and Zimmerman[9] indicate a very weak decrease in the peak frequency of the vibration with increasing temperature, while the lattice vibrations display a large dependence on temperature. This led the authors to conclude that the deformation and translational vibrations in ices are not coupled, but this view is not universally accepted.[8,11]

In addition to the shift of the absorption band with increasing temperature of the film a substantial narrowing of this band (Fig. 5) and a decrease of the absorption amplitude are observed. These facts can be interpreted fully as being the result of structural transformations in the cryocondensate of the isotopic water mixture during warming.

4. The $400-1200\ \mathrm{cm}^{-1}$ range. Previously we obtained results attesting to the unusual behavior of the absorption spectra in the frequency range of the lattice and librational vibrations for samples of various thicknesses. These features are clearly manifested at relatively large sample thicknesses ($\approx 1.5-2\ \mu$m). In this connection we measured the spectra of 2-μm thick cryocondensates of our isotopic water mixture at various temperatures (Fig. 6). The measurements were made in the following order. At a substrate temperature of 30 K a sample was deposited and the reflection spectrum was taken (curve *1*). Then the substrate temperature was increased to 100 K and the IR spectrum was measured again (curve *2*). Curve *3* is the spectrum of a sample directly condensed at a temperature of 100 K. We see that during the warming of the sample its IR spectrum undergoes substantial changes (curves *1* and *2*). The broad absorption band with a maximum at $\nu\approx 600\ \mathrm{cm}^{-1}$ splits into two bands. The manifestations of fine structure are transformed into individual peaks, as is especially noticeable in spectrum *3*. It is clear that films found at the same temperature but having different temperature ''biographies'' are structurally different, and this is reflected in the IR spectra.

The frequency range considered corresponds to the librational vibrations of the D_2O molecule, and for the analogous vibrations of the HDO molecule the frequency region is $800-950\ \mathrm{cm}^{-1}$. In this range one also observes significant transformations of the spectrum as the temperature is raised. The broad but low-intensity absorption band at $T=30$ K is accentuated as the temperature is increased to 100 K, but even in this range the spectra of samples at the same temperature but obtained under different conditions of cryocondensation are substantially different.

The reason for this behavior of the IR spectra of an isotopic water mixture in the range of librational vibrations is most likely due to the interaction of the D_2O and HDO molecules. The point is that the nature of librations lies in the hopping of protons (deuterons) from one O...H–O bond to an adjacent bond, which is analogous to a rotation of the molecule by 120°. This leads to the creation of so-called *L* and *D* defects, where, in the first case, there is no proton (deuteron) between oxygen atoms, and, in the second case, a bond with two protons (deuterons) is formed. A consequence of this is the appearance of the negative ions OH^- and OD^+

and also positive ions of the types D_3O^+, D_2HO^+, H_2DO^+, and H_3O^+. Increasing the temperature of the sample facilitates this type of hopping, and that ultimately leads to a change of the absorption spectra.

CONCLUSIONS

The main conclusion is that changing the substrate temperature leads to significant transformations of the spectra in the regions of the characteristic frequencies. A shift of the absorption band and changes in its width and fine structure are observed. These are expressed in the following typical manifestations.

1. Warming of the cryocondensates of an isotopic water mixture is accompanied by structural transformations that lead to a change in energy of the hydrogen bonds between molecules. This is indicated by the change in the bandwidth of the stretching vibrations and by a shift of these vibrations to lower frequencies. Calculations done for different types of stretching vibrations of the mixture showed that this corresponds to a decrease of the enthalpy of the hydrogen bond with increasing temperature.

2. Increasing the temperature of cryocondensates formed at $T=30$ K leads to a substantial decrease of the frequencies of the absorption bands corresponding to deformation vibrations of the D_2O and HDO molecules. This can serve as an indication of structural transformations occurring in the crystal during the temperature evolution.

3. Annealing of the sample leads to significant smoothing out of the fine structure of the stretching vibrations. In addition, increasing the temperature decreases the amplitude of the absorption in the regions of the stretching and deformation vibrations.

4. In the frequency range of librational vibrations one observes a change of the spectra of cryocondensates of an isotopic water mixture with changing temperature. The reason is apparently the thermally stimulated proton–proton and deuteron–deuteron exchange between D_2O and HDO molecules, giving rise to *L* and *D* defects in the samples.

*E-mail: drobyshev@nursat.kz

[1] A. S. Drobyshev and D. N. Garipogly, Fiz. Nizk. Temp. **22**, 1064 (1996) [Low Temp. Phys. **22**, 812 (1996)].
[2] H. Ogasawara, J. Yoshinobu, and M. Kawai, J. Chem. Phys. **111**, 70038 (1999).
[3] A. S. Drobyshev and T. A. Prokhodtseva, J. Low Temp. Phys. **119**, 431 (2000).
[4] L. C. Dowell and A. P. Rinfret, Nature (London) **188**, 1144 (1960).
[5] M. Blackman and N. D. Lisgarten, Adv. Phys. **7**, 189 (1958).
[6] R. H. Beaumont, H. Chihara, and J. A. Morrison, J. Chem. Phys. **4**, 1456 (1961).
[7] G. N. Zatsepina, *Physical Properties and Structure of Water* [in Russian], Izd. MGU, Moscow (1987).
[8] J. E. Bertie and E. Whalley, J. Chem. Phys. **4**, 1637 (1964).
[9] R. Zimmerman and G. Pimentel, *Advances in Molecular Spectroscopy*, New York (1962).
[10] G. Pimentel and A. L. McClellan, *The Hydrogen Bond*, Freeman, San Francisco (1960).
[11] J. E. Bertie and E. Whalley, J. Chem. Phys. **40**, 1646 (1964).

Translated by Steve Torstveit

LETTER TO THE EDITOR

On the role of Jahn–Teller vibrations in the mechanism of high-T_c superconductivity of intercalated C_{60} fullerite films with *p*-type conductivity

V. M. Loktev*

N. N. Bogolyubov Institute of Theoretical Physics, National Academy of Sciences of Ukraine, ul. Metrologicheskaya 14-b, 03143 Kiev, Ukraine

É. A. Pashitskiĭ

Institute of Physics of the National Academy of Sciences of Ukraine, pr. Nauki 46, 03650 Kiev, Ukraine

(Submitted September 24, 2001)
Fiz. Nizk. Temp. **28**, 421–425 (April 2002)

An attempt is made to explain the high values of the superconducting transition temperature observed in intercalated fullerite films. The approach is based on the fact that charged C_{60} molecules in hexagonal lattices have degenerate electronic terms which are strongly coupled to the Jahn–Teller intramolecular vibrations. Certain other effects leading to enhancement of the superconductivity in molecular metals are also discussed. © *2002 American Institute of Physics.* [DOI: 10.1063/1.1477366]

1. In a series of studies by Batlogg *et al.*,[1–3] by injecting holes into thin films of C_{60} fullerite by means of an external electric field the critical temperature T_c of the superconducting transition was raised from $T_c=52$ K for the pure single-crystal film to $T_c=84$, 117, and 146 K in films intercalated with $CHCl_3$, $CHBr_3$, and CHI_3 molecules, respectively. The highest value $T_c=146$ K is a record for all known high-T_c superconductors, including the cuprates Bi–Sr–Ca–Cu–O,[4] Tl–Ba–Ca–Cu–O,[5] and Hg–Ba–Ca–Cu–O[6] at normal pressure.

The monotonic growth of T_c in C_{60} films with increasing radius of the halogen atom G=Cl, Br, I, just as in the metal-doped crystals A_3C_{60} (A=K, Rb, Cs, Tl),[7–11] finds a natural explanation in the framework of the BCS theory,[12] according to which T_c is determined by the dimensionless electron–phonon coupling constant $\lambda_{\rm ph}=N(\varepsilon_F)g_{\rm ph}^2$, where $g_{\rm ph}$ is the matrix element of the electron–phonon interaction (EPI), and $N(\varepsilon)$ is the density of states at the Fermi level ε_F, which depends on the degree of doping and also on either the width W_c of a partially filled conduction band or (in the case of *p*-type conductivity) the width W_v of the valence band. With increasing size of the molecules CHG_3 or atoms A, the lattice constant of the C_{60} crystal increases and the overlap of the π orbitals of adjacent molecules decreases, leading to a narrowing of the conduction band and an increase in the density of states. The fact that T_c is higher in *p*-type fullerite films than in *n*-type films[2] is, we believe, simply explained by the fact that $W_v<W_c$ by virtue of the smaller overlap of the wave functions of the deeper electronic states of the fullerene. This should be true in all such cases.

On the basis of the standard BCS model one cannot, however, understand the absence of superconductivity in the crystals A_3C_{70} and $A_3(C_{60})_y(C_{70})_{1-y}$ (Ref. 13) and the low T_c recently observed in C_{70} films,[14] even though the phonon spectrum in these molecular systems is governed mainly by intramolecular vibrations and in C_{70} is even richer than in C_{60}.

2. Previously[15] we have conjectured that in cubic A_3C_{60} crystals with *n*-type conductivity the superconductivity is due to the high symmetry of both the lattice itself and of the C_{60} molecule (icosohedral group Y_h). The first excited state t_{1u}, which is degenerate in the molecule, creates three bands in the crystal, the lowest of which is twofold degenerate and has valleys at the symmetric L points of the Brillouin zone.[16,17]

In A_3C_{60} compounds all the C_{60} molecules are located on average in a triply charged state, C_{60}^{3-}, forming either a spin doublet with Jahn–Teller deformations and a complete splitting of all the levels or a spin quartet with the recovered symmetry of the free C_{60} fullerene.[18] However, in the conducting phase these molecules, which form a narrow-band molecular metal with degenerate itinerant electrons, are found in indefinite (fluctuating) charge and spin states. Transitions between different electronic terms of the C_{60} molecules are accompanied by Jahn–Teller deformations which correspond to specified (as a rule, quadrupolar) intramolecular vibrations.[1)]

The electron–phonon interaction in a fullerite with Jahn–Teller intramolecular vibrations is described in the site representation by the Hamiltonian[15]

$$H_{\text{el-ph}}=\sum_{\mathbf{n},\sigma}\sum_{\lambda_1,\lambda_2}\chi_{\mathbf{n}}^{\lambda_1\lambda_2}a_{\mathbf{n}\lambda_1\sigma}^{+}a_{\mathbf{n}\lambda_2\sigma}Q_{\mathbf{n}}^{\lambda_1,\lambda_2}, \tag{1}$$

where $\chi_{\mathbf{n}}^{\lambda_1\lambda_2}$ is the electron–phonon coupling constant, and $a_{\mathbf{n}\lambda\sigma}^{+}$ and $a_{\mathbf{n}\lambda\sigma}$ are the Fermi creation and annihilation operators for an electron in state λ with spin σ at the **n**-th site. An important feature of the operator (1) is the one-site character of the EPI, which distinguishes it from its counterpart in ordinary metals. According to Ref. 15, the EPI with Jahn–

 © 2002 American Institute of Physics

Teller intramolecular vibrations which are described by the generalized coordinate $Q_{\mathbf{n}}^{\lambda_1,\lambda_2}$ distinguishes the cubic crystals A_3C_{60} from the systems A_3C_{70}, which have a lower symmetry at low temperatures[19] and which all the electronic states are split and the Jahn–Teller effect is absent. In the second order of perturbation theory the EPI (1) can give rise to a rather strong electron–electron attraction at the C_{60} sites and to superconductivity characterized by values $T_c \approx 19-48$ K.[7–11] This is also promoted by the many-valley structure of the conduction band,[16,17] which enhances the EPI by a factor equal to at least the number of equivalent valleys.[15]

3. In contrast to the cubic crystals A_3C_{60} the lattice of C_{60}/CHG_3 films belong to the hexagonal system.[2] In this case the crystalline field has a uniaxial character,[20] so that all of the electronic states of the fullerene conserve the L_Z projection of the orbital angular momentum **L** onto the axis of the C_6 lattice, splitting into doublets $\pm L_Z$ (except for the state with $L_Z=0$).

Then the Hamiltonian of the fullerene in the crystalline field of the fullerite C_{60}/CHG_3, where the role of the ligands for each molecule is played by the same, similarly charged C_{60} molecules surrounding it,[21] can be written in the form

$$H_{\mathrm{mol}}=B_2^0\sum_{\mathbf{n}}(L_{\mathbf{n}}^Z)^2+B_4^0\sum_{\mathbf{n}}(L_{\mathbf{n}}^Z)^4, \tag{2}$$

in which the B_n^m are parameters of this field. The first excited state of each of the molecules in the crystal is the doublet $L_Z=\pm 1$, which begins to be filled at hole concentrations per molecule $n_h \geqslant 2$. The transition to this state is directly related to the quadrupolar intramolecular vibrations, which cause a rhombic Jahn–Teller deformation of the C_{60} molecules and lift the degeneracy of the doublet. The Hamiltonian of the corresponding EPI can be represented by the expression

$$H_{\text{el-ph}}=B_2^2\sum_{\mathbf{n}}[(L_{\mathbf{n}}^X)^2-(L_{\mathbf{n}}^Y)^2]Q_{\mathbf{n}}^{\mathrm{rh}}, \tag{3}$$

in which $Q_{\mathbf{n}}^{\mathrm{rh}}$ is the normal coordinate of the intramolecular vibrations of symmetry D_{2h}. Here it is fundamental that, in analogy to the EPI (2), the coupling of the carriers with the vibrations is also realized at the molecule, i.e., it has a one-site character. The only intermolecular (in other words, inter-site) operator is

$$H_{\mathrm{tun}}=\sum_{\mathbf{n},\rho,\sigma}\sum_{\lambda_1,\lambda_2}t^{\lambda_1\lambda_2}a_{\mathbf{n}\lambda_1\sigma}^{+}a_{\mathbf{n}+\rho\lambda_2\sigma} \tag{4}$$

for the hopping (tunneling) of fermions between neighboring C_{60} molecules separated by a vector ρ and found in states λ_1 and λ_2, and $t^{\lambda_1\lambda_2}$ specifies the amplitude of these hops.

It is readily seen that the operator of the crystal can be put in the form[22]

$$H=H_{\mathrm{mol}}+H_{\mathrm{tun}}+H_{\text{el-ph}},$$

$$H_{\mathrm{mol}}=\sum_{\mathbf{n},\lambda}\varepsilon_\lambda a_{\mathbf{n}\lambda\sigma}^{+}a_{\mathbf{n}\lambda\sigma}+\sum_{\mathbf{n}}\omega_{\mathrm{rh}}b_{\mathbf{n}}^{+}b_{\mathbf{n}}, \tag{5}$$

$$H_{\text{el-ph}}=\frac{1}{\sqrt{N}}\sum_{\mathbf{n},\mathbf{q},\sigma}\sum_{\lambda_1,\lambda_2}\chi_{\mathbf{n}}^{\lambda_1\lambda_2}(\mathbf{q})a_{\mathbf{n}\lambda_1\sigma}^{+}a_{\mathbf{n}\lambda_2\sigma}\varphi_{\mathrm{rh}}(\mathbf{q}),$$

where ε_λ is the energy of the molecular terms, $\chi_{\mathbf{n}}^{\lambda_1\lambda_2}(\mathbf{q})$ is the electron–phonon coupling constant with the Jahn–Teller modes, $\varphi_{\mathrm{rh}}(\mathbf{q})$ is the Fourier transform of the operator of rhombic intramolecular displacement of the term proportional to $b_{\mathbf{n}}^{+}+b_{\mathbf{n}}$, and $b_{\mathbf{n}}^{+}$ and $b_{\mathbf{n}}$ are Bose creation and annihilation operators for quanta of the intramolecular vibrations.

It must be noted that $H_{\text{el-ph}}$ in (5) is formally the same as the operator of the EPI in manganites (see Ref. 23), where it is also of a Jahn–Teller nature, and its main consequence is polaron narrowing of the band of free motion of the carriers in the undeformed lattice. It is known[22] that the Hamiltonian H with an EPI operator $H_{\text{el-ph}}$ of the form (5) admits diagonalization by a unitary transformation $\exp\hat{S}$ in which the anti-Hermitian operator $\hat{S}$ is determined from the condition that the restructured Hamiltonian $\tilde{H}$ not contain terms linear in the Bose operators. Omitting the standard manipulations (see Refs. 22 and 23), we write the renormalized Hamiltonian of fullerite as

$$\tilde{H}=\sum_{\mathbf{n},\lambda,\sigma}\varepsilon_\lambda a_{\mathbf{n}\lambda\sigma}^{+}a_{\mathbf{n}\lambda\sigma}+\sum_{\mathbf{q}}\omega_{\mathrm{rh}}(\mathbf{q})b^{+}(\mathbf{q})b(\mathbf{q})$$

$$+\sum_{\mathbf{n},\rho,}\sum_{\lambda_1,\lambda_2}\tilde{t}^{\lambda_1\lambda_2}a_{\mathbf{n}\lambda_1\sigma}^{+}a_{\mathbf{n}+\rho\lambda_2\sigma}$$

$$-\frac{1}{2}\sum_{\mathbf{n},\mathbf{m}}V_{\mathbf{nm}}^{\lambda_1\lambda_2}a_{\mathbf{n}\lambda_1}^{+}\uparrow a_{\mathbf{n}\lambda_1}\uparrow a_{\mathbf{m}\lambda_2}^{+}\downarrow a_{\mathbf{m}\lambda_2}\downarrow. \tag{6}$$

In this expression

$$\tilde{t}^{\lambda_1\lambda_2}=t^{\lambda_1\lambda_2}\exp\left(-\frac{1}{N}\sum_{\mathbf{q}}\left|\chi^{\lambda_1\lambda_2}(\mathbf{q})\right|^2/\omega_{\mathrm{rh}}^2(\mathbf{q})\right) \tag{7}$$

is the renormalized (by the aforementioned effect) polaron narrowing of the amplitude of the hops of holes between molecules, and

$$V_{\mathbf{nm}}^{\lambda_1\lambda_2}=\frac{1}{N}\sum_{\mathbf{q}}\chi_{\mathbf{n}}^{\lambda_1\lambda_2}(\mathbf{q})\chi_{\mathbf{m}}^{\lambda_2\lambda_1}/\omega_{\mathrm{rh}}(\mathbf{q}) \tag{8}$$

is the effective interfermion attraction, which in the limit of weak dispersion (or no dispersion) of the optical crystal modes generated by the intramolecular vibrations, turns out to be practically local. As a result, unlike the kinetic terms of the Hamiltonian (6), for example, it does not depend (or depends relatively weakly) on the intermolecular distance. It also follows from (6)–(8) that the greatest contribution to the significant (exponential) decrease of the ''bare'' width of the conduction band (which in this case is just the valence band) and, hence, to the growth of the density of states and the increased tendency toward superconductivity is that due to the soft ''shear'' modes $\omega_{\mathrm{rh}}(\mathbf{q})$ corresponding to the ordinary low-frequency Jahn–Teller intramolecular vibrations.[2)]

Finally, in the hexagonal lattices of fullerite systems the Jahn–Teller intramolecular vibrations should be manifested at a number of holes per molecule $n_h>2$. It is at such concentrations of the injected carriers that one observes the steep growth of T_c in both pure and intercalated C_{60} films.[2] On the other hand, the observation of superconductivity in hexagonal C_{70} films,[14] where the Jahn–Teller effect is also possible,

provides yet another argument in favor of the validity of the ''molecular'' approach proposed in Refs. 15 and 21 for the description of the properties of fullerites.

4. Other effects also promote a high T_c. One such effect is the nonadiabaticity of the EPI in a narrow-band molecular metal, when the actual frequencies $\omega_{\rm rh}$ of the intramolecular vibrations are comparable to ε_F, violating the validity criterion of the Migdal theorem[24] as to the smallness of correction to the zeroth phonon vertex $\Gamma_{\rm ph}^{(0)}=1$. In application to A_3C_{60} this question is discussed in Ref. 25, where only the first-order corrections to the normal and anomalous self-energy parts were taken into account, leading to a renormalization of the electron–phonon coupling constants $\lambda_{\rm ph}\to\tilde{\lambda}_{\rm ph}=\lambda_{\rm ph}(1+2\lambda_{\rm ph}P)$, where $\lambda_{\rm ph}$ is given in paragraph 1 above, and P is some integral characteristic of the electron and phonon spectra. In our case $g_{\rm ph}^2\sim|\chi_{\mathbf{n}}^{\lambda_1\lambda_2}|^2/\omega_{\rm rh}n_{\rm car}$ ($n_{\rm car}$ is the density of carriers (electrons or holes) in the conduction or valence band).

However, the above renormalization of $\lambda_{\rm ph}$ is insufficient if the EPI is not small. In the general case it is necessary to take all of the diagrams into account, which leads to a multiplication of the electron–phonon coupling constant, which determines T_c, by $\Gamma_{\rm ph}^2$ (where $\Gamma_{\rm ph}>1$);[26] here $\tilde{\lambda}_{\rm ph}=\lambda_{\rm ph}(1+\lambda_{\rm ph}P)^2$. Ultimately, with allowance for strong coupling effects,[27] the value of T_c can be estimated from the formula[28]

$$T_c\approx\overline{\omega}_{\rm ph}\exp\left\{-\frac{1+\lambda_{\rm ph}}{\tilde{\lambda}_{\rm ph}-\mu_C(1+0.5\lambda_{\rm ph})}\right\}, \tag{9}$$

where $\overline{\omega}_{\rm ph}\approx\omega_{\rm rh}$, and the dimensionless screening of the Coulomb repulsion, $\mu_C=N(\varepsilon_F)\overline{V}_C/[1+2N(\varepsilon_F)\overline{v}_c]$ at $\tilde{\omega}_{\rm ph}\sim\varepsilon_F$ and does not exceed its limiting value $\mu_c\approx0.5$ at $N(\varepsilon_F)\overline{V}_C\gg1$ ($\overline{V}_C$ is the matrix element of the Coulomb interaction of the carriers).

Expression (9) shows that the growth of the density of states leads to an increase of $\lambda_{\rm ph}$ and $\tilde{\lambda}_{\rm ph}$, and the growth, quadratic in $\lambda_{\rm ph}$, of the renormalized electron–phonon coupling constant $\tilde{\lambda}_{\rm ph}$ ''overpowers'' the increase of the Coulomb repulsion $\mu_C(1+\lambda_{\rm ph})$ and, accordingly, brings about a monotonic increase of T_c. As a result, for $\lambda_{\rm ph}\gg1$ for Eq. (9) we have $T_c\approx\omega_{\rm ph}\exp(-\lambda_{\rm ph}/\tilde{\lambda}_{\rm ph})$, so that for $P\approx1$ we find that $T_c^{\max}\sim\overline{\omega}_{\rm ph}\approx\omega_{\rm rh}$. This, in turn, gives a rather optimistic estimate for the critical temperature: $T_c^{\max}\approx300-400$ K.

5. Thus in molecular metals of the C_{60}/CHG_3 type with anomalously narrow (owing to phonon renormalization) bands and substantial nonadiabatic effects of the ''local field'' for $\overline{\omega}_{\rm ph}\sim\varepsilon_F$ and $\lambda_{\rm ph}\gg1$ it is possible to achieve extremely high superconducting transition temperatures T_c. Here the observed dependence of the critical temperature on the intermolecular distance is direct evidence of the local character of the attraction in these compounds, actually confirming the pairing mechanism proposed above (and also in Ref. 15). The bell-shaped behavior of T_c as a function of n_h may be due to effects of filling of the split term[21] and, in principle, to weakening of the Jahn–Teller effect as L_Z increases.

The work of V.M.L. was supported in part by a grant from the Swiss Science Foundation (SCOPES Project 7UKPJ062150.00/1). É.A.P. thanks the Royal Academy of Sciences (Swedish KVA) and the Department of Applied Physics at the Chalmers University of Technology and the Göteborg University for partial financial support.

*E-mail: vloktev@bitp.kiev.ua

[1)]For example, numerical calculations have shown[18] that the transition between the aforementioned quartet and doublet states of C_{60}^{3-} fullerene is accompanied by distortion of the latter with an elliptical distortion of $\approx9.2\%$ and an average frequency $\overline{\omega}_{\rm ph}\approx533$ cm^{-1} of the quadrupolar intermolecular vibration of symmetry H_g; the transition between the quartet of C_{60}^{3-} and the triplets of C_{60}^{2-} or C_{60}^{4-} corresponds to a distortion of $\approx5.3\%$ and average frequencies $\overline{\omega}_{\rm ph}\approx556-559$ cm^{-1}; the transition between the quartet of C_{60}^{3-} and the singlet of C_{60}^{2-} corresponds to a distortion of 11.7% and $\overline{\omega}_{\rm ph}\approx498$ cm^{-1}.

[2)]It is apropos to mention here that the frequencies of the completely symmetric intramolecular vibrations, as a rule, are much higher, and, consequently, their role in the phenomenon of superconductivity in the fullerite should, generally speaking, be less important.

[1] J. H. Schön, Ch. Kloc, and B. Batlogg, Nature (London) **408**, 549 (2000).
[2] J. H. Schön, Ch. Kloc, and B. Batlogg, Science **293**, 2432 (2001).
[3] Perspectivnye Tekhnologii, edited by S. T. Koretskaya **8**, 1 (2001).
[4] M. A. Subramanian, S. S. Torrardi, J. C. Calabresc *et al.*, Science **239**, 1015 (1988).
[5] Z. Z. Sheng and A. M. Hermann, Nature (London) **332**, 138 (1988).
[6] S. N. Putilin, E. V. Antropov, O. Chmaissem, and M. Marezio, Nature (London) **362**, 226 (1993).
[7] A. F. Hebard, M. I. Rosseinsky, R. C. Haddon, D. W. Murphy, S. H. Glarum, T. T. M. Palstra, A. P. Ramirez, and A. R. Kortan, Nature (London) **350**, 600 (1991).
[8] K. Tanigaki, T. W. Ebessen, S. Saito, J. Mizuki, J. S. Tsai, Y. Kubo, and S. Kuroshima, Nature (London) **352**, 222 (1991).
[9] M. J. Rosseinsky, A. P. Ramirez, S. H. Glarum, D. Murphy, R. C. Haddon, A. F. Hebard, T. T. M. Palstra, A. R. Kortan, S. M. Zahurat, and V. Makhija, Phys. Rev. Lett. **66**, 2830 (1991).
[10] K. Holezer, O. Klein, S.-M. Huang, R. D. Kaner, K.-J. Fu, R. L. Wetten, and F. Diederich, Science **252**, 1154 (1991).
[11] Z. Igbal, R. H. Baughman, B. I. Ramakrishna, S. Khare, N. S. Murphy, H. J. Bornemann, and D. E. Morris, Science **254**, 826 (1991).
[12] J. R. Schrieffer, *Theory of Superconductivity* [Benjamin, New York (1964); Mir, Moscow (1971)].
[13] A. A. Zakhidov, A. Ugawa, K. Imeda, K. Yakushi, and H. Inokuchi, Solid State Commun. **79**, 939 (1991).
[14] J. G. Schön, Ch. Kloc, T. Siegrist, M. Steigerwald, C. Svensson, and D. Batlogg, Nature (London) **413**, 831 (2001).
[15] V. M. Loktev and E. A. Pashitskiĭ, JETP Lett. **55**, 478 (1992); Zh. Éksp. Teor. Fiz. **103**, 594 (1993) [JETP **76**, 297 (1993)].
[16] Y. Huang, D. F. R. Gilson, and I. S. Butler, J. Phys. Chem. **95**, 5723 (1991).
[17] S. Saito and A. Oshiyama, Phys. Rev. Lett. **66**, 2637 (1991).
[18] W. H. Green, S. M. Forum, G. Fitzgerald, P. W. Fowler, A. Ceulemans, and B. C. Titeca, J. Phys. Chem. **100**, 14892 (1996).
[19] A. P. Isakina, A. I. Prokhvatilov, M. A. Strzhemechnyĭ, and K. A. Yagotintsev, Fiz. Nizk. Temp. **27**, 1406 (2001) [Low Temp. Phys. **27**, 1037 (2001)].
[20] C. A. Al'tshuler and B. N. Kozyrev, *Electron Paramagnetic Resonance* [in Russian], Nauka, Moscow (1972).
[21] V. M. Loktev, Fiz. Nizk. Temp. **27**, 561 (2001) [Low Temp. Phys. **27**, 414 (2001)].
[22] A. S. Davydov, *Theory of Molecular Excitons* [Plenum Press, New York (1971); Nauka, Moscow (1968)].
[23] V. M. Loktev and Yu. G. Pogorelov, Fiz. Nizk. Temp. **26**, 271 (2000) [Low Temp. Phys. **26**, 171 (2000)].
[24] A. B. Migdal, Zh. Éksp. Teor. Fiz. **34**, 1438 (1958) [JETP **7**, 996 (1958)].
[25] L. Pietronero, Europhys. Lett. **17**, 365 (1992).
[26] O. V. Dolgov and E. G. Maksimov, Usp. Fiz. Nauk **138**, 95 (1982) [Sov. Phys. Usp. **25**, 688 (1982)].
[27] G. M. Éliashberg, Zh. Éksp. Teor. Fiz. **38**, 966 (1960) [Sov. Phys. JETP **11**, 696 (1960)].
[28] V. L. Ginzburg and D. A. Kirzhnits (eds.), *Problems of High-Temperature Superconductivity* [in Russian], Nauka, Moscow (1977).

Translated by Steve Torstveit